Dynamic Measurement of Residual Strains by X–Ray Diffraction in a Metal Matrix Composite During Rapid Temperature Cycling

by

Gijsbertus (Guy) Langelaan

A thesis submitted to the Department of Materials and Metallurgical Engineering in conformity with the requirements for the degree of Master of Science (Engineering)

Queen's University
Kingston, Ontario
September, 1997

Abstract

One of the demands facing the automotive industry is the reduction of a vehicle's weight, and light–weight, high–strength materials are necessary to meet this demand. Use of light–weight metals, such as aluminum, in the engine is limited by their high temperature strength. Although the advent of metal matrix composites (MMC) can alleviate this limitation the residual stresses which develop due to the mismatch of the thermal expansion coefficients can affect the performance and lifetime of a component made from an MMC. The role of residual stresses must therefore be well evaluated before entering service.

This study was undertaken to characterize the temperature dependence of the residual stresses in an AA339 Al alloy reinforced with 23%(vol.) Kaowool short fibres. This material is being considered for service in a piston head by General Motors Corp. An experiment was designed to measure the residual stresses by x–ray diffraction dynamically during isothermal stress relaxations at 100°C and 300°C with rapid temperature ramping of 200°C/min between the two states. This simulates the thermal cycling conditions between an idling engine (100°C) and an accelerating one (300°C).

A linear position sensitive detector was used to measure a peak profile in 5 seconds, and a novel high temperature stage was developed with a very low thermal mass and thermal expansion. The x–ray experiments were supplemented by an elastic model to examine the strain distribution due to a periodic array of cuboidal inclusions.

Stress relaxations at 100°C after rapid cooling from 300°C were observed in some of the runs. It was found that a slow rate thermal cycle (5°C/min heating and cooling) eliminated the relaxations in cycles immediately following it. Several rapid cycles were required after which the relaxations reappeared. This behaviour can be attributed to the development of a fine dispersion of incoherent precipitates. These can be redissolved in a slow cycle, but are stable during rapid ones. High stresses developed during low temperature cooling unpin dislocations from their coherent precipitates and this unpinning reduces the elastic stresses when these particles become incoherent.

Acknowledgements

I am endebted to Prof. Shigeo Saimoto for his supervision and mentorship without which this thesis could not have been completed.

I am also most grateful for the support and love of my family (Willem, Aureel, Jack & Mia) who have always been with me through all of my endeavours, Dank jullie wel!

To the other students in Shig's group, Brad, Jian, Bill, James and Don who have helped me in a variety of ways either by interesting discussions (especially Bill & Brad) or nasty questions (Don) or by finding various papers and articles for me, I thank all of you.

I have been given the luxury of having had wonderful housemates over the years, but I am especially grateful to my housemate of this summer, Panya, who was staying in Kingston to learn English. I would be much thinner without his delicious cooking during the writing stage of this project. Thank you very much!

To Joyce, thanks for putting up with my indecisive scheduling and all around inability to plan more than one x–ray scan ahead of time.

Thank you's are also due to Messrs. Mike Phaneuf for taking the FIB images, to Darryl Dietrich for building the high temperature stage, and to Charlie Cooney for his help with the optical micrograph.

To Prof. J.D. Boyd, I am endebted by his loan of a computer during the last few weeks of writing this thesis: mine had undergone the catastrophic phase transformation from a working computer to an electric doorstop.

I am also very grateful for the generous loan of equipment from CANMET MTL.

Lastly, also to General Motors for providing us with such an interesting and challenging opportunity.

Table of Contents

List of Figures

Appendix 2

Chapter 1
Introduction

The paradigm of engineering materials for structural applications is to produce high strength, light weight materials. In particular, for the transportation industry, this is very important to minimize fuel consumption while maintaining a safe, reliable vehicle.

This mandate has led to the development of novel, high performance composite materials which combine the ideal properties of different classes of materials by joining them together in one component. Perhaps the most common composite materials are the polymer matrix ones reinforced with glass, carbon or polymer (i.e. Kevlar or Aramid) fibre reinforcement phases. These materials offer excellent performance at low temperatures, however at higher temperatures, metal or ceramic based materials become more appropriate.

The improvement in properties of a composite are due to the interaction between the two phases and by balancing the desired properties, such as ductility versus high strength. In a polymer matrix–carbon fibre composite for example, the the high strength and stiffness of the carbon fibres is complemented by the high toughness of the polymer. The result is a material with strength greater than that of the polymer alone, but with a somewhat reduced fracture toughness. The same principle is applied to metal matrix composites (MMC) which are usually reinforced by small ceramic particles or short fibres (whiskers) rather than the long, continuous fibre reinforcement typical of polymer matrix composites.

Metal matrix composites have been of great interest for many applications because of the formability of the metal combined with the high strength and stiffness of the ceramic reinforcement. The high temperature strength of ceramics adds to the scope of potential applications for MMC's. A recent text by Clyne & Withers[1] describes extensively the behaviour and applications of MMC's including a discussion about the role of the residual stress state.

Because of the different thermoelastic properties of the two phases, residual stresses may develop in both phases. The different moduli result in residual stresses under loading and the different coefficients of thermal expansion generate residual stresses if the processing temperature is different from the operating temperature. These residual stresses may enhance the bulk properties, but could also cause failure of one of the phases if the residual stresses become too large. The interaction between the two components of the composite must therefore be carefully characterized prior to its use.

In an internal combustion engine, reducing the weight of the moving components such as the piston head can greatly improve performance and fuel efficiency. However, lower density materials such as aluminum have poor high temperature strength, hence the combustion conditions must be changed to reduce the temperature. Unfortunately, this decreases the thermodynamic efficiency and hence a compromise must be reached. By using an aluminum based metal matrix composite, the high temperature strength can be improved while maintaining the desired light weight. Before such a material can be implemented however, the response of the material to the thermal cycling conditions must be characterized. The residual stresses due to the different coefficients of thermal expansion play an important role in defining the properties and service life of the component.

This study was undertaken to characterize the behaviour of the residual stresses during rapid thermal cycling in an AA339 aluminum alloy reinforced with 23%(vol.) Kaowool whiskers. This material is being considered for use in a piston head by General Motors Corp. The aim of this project was to examine the isothermal stress relaxations at 100°C and 300°C after rapid temperature changes of 200°C/min. This simulates the thermal cycling conditions predicted to occur between the states of an idling engine (100°C) and an accelerating one (300°C).

The residual stresses were deduced from strain measurements made by x-ray diffraction techniques and the high temperature control was achieved using a novel high temperature stage developed for in situ x-ray measurements.

Chapter 2
Literature Review and Theoretical Background

This review comprises several different topics: firstly, the theory of strain measurements by diffraction techniques; secondly, the use of position sensitive detectors in residual strain measurements; and lastly the micromechanics of residual stresses in discontinuously reinforced materials.

2.1 Theory of Strain Measurements by Diffraction Techniques

The general theory of strain measurements has been discussed in great detail by many authors; in particular the book by Noyan and Cohen[2] covers the topic comprehensively. In this discussion a brief review of the principle of the diffraction technique will be presented and then followed by a more detailed discussion about penetration depth and elastic anisotropy effects which are very important to this study.

2.1.1: Review of general strain measurement theory

Diffraction techniques measure the spacing between crystallographic planes. The general relation between the interplanar spacing and the coherent scattering angle is given by Bragg's law:[3] $\lambda=2d\sin\theta$, where λ is the wavelength of the radiation, d is the interplanar spacing and $90°-\theta$ is the angle between the plane normal and the incident beam. If the volume of material being examined has a stress applied to it, then there will be a corresponding elastic strain. This elastic strain changes the spacing between the crystallographic planes. Hence, if the position of the diffracted peak is measured precisely, then elastic strains can be registered. This can be shown by taking the partial derivative of Bragg's law $\partial d/\partial\theta$.

$$\left.\frac{\partial d}{d}\right|_{\lambda} = -\left.\frac{\partial \theta}{\tan\theta}\right|_{\lambda} \tag{2.1}$$

Note that the LHS is a strain and hence the change in peak position is directly a measurement of the strain in the diffracting volume. This equation can also be interpreted as an experimental parameter, that is the minimum strain that can be resolved by the instrumentation. The precision and accuracy with which a peak position can be registered ($\partial\theta$) gives the minimum strain that can be resolved. Since the resolution increases with increasing scattering angle, strain measurements are typically made at high angles. Making measurements at high angles also has the advantage of increasing the depth of penetration and hence surface effects can be minimized. This is further discussed in the following sections. Unfortunately, high angle 'reflections' tend to have lower scattering efficiencies and hence measurement times are increased.

Simply measuring the strain from one reflection is not generally sufficient to provide useful information about the stress state in the specimen. Strain measurements must be made in at least six different independent orientations to obtain all six components of the strain tensor.[4] The different orientations refer to the angles of the diffracting plane normals with respect to the specimen co-ordinates. The definitions of these angles are shown in Figure 2.1, where ψ is the angle between the specimen normal and the diffracting plane normal, and φ is a rotation about the specimen normal.

Since the parameter of interest is not the strain in various (φ,ψ) orientations but the stress tensor, the relationship between the measured strains and the stress tensor must be solved. The principle is to rotate the measured strains to the specimen co-ordinate system (they are measured in the laboratory co-ordinate system) and to use Hooke's Law to calculate the

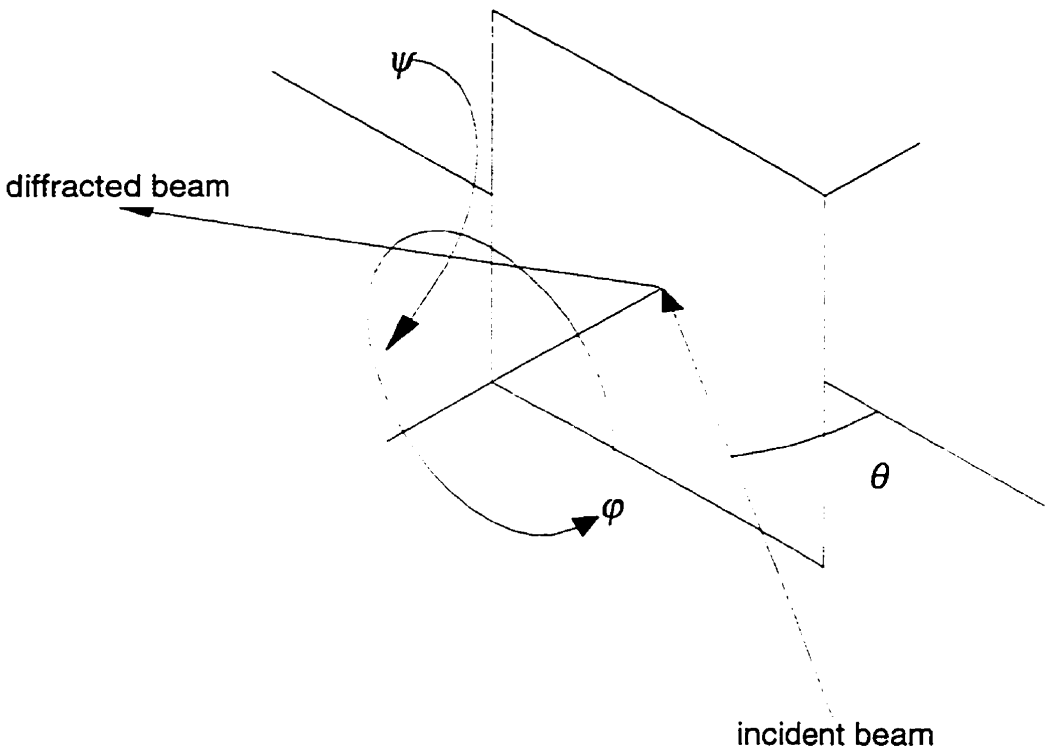

Figure 2.1: Definitions of x–ray angles θ, φ, ψ

stresses. By combining these two steps into one, an expression for the relationship between the measured strains and the stress tensor is obtained:[2]

$$\varepsilon(\varphi,\psi)=S_1(\sigma_{11}+\sigma_{22}+\sigma_{33})+\frac{1}{2}S_2\left\{\begin{matrix}\left(\sigma_{11}\cos^2\varphi+\sigma_{12}\sin 2\varphi+\sigma_{22}\sin^2\varphi-\sigma_{33}\right)\sin^2\psi\\+\sigma_{33}+\left(\sigma_{13}\cos\varphi+\sigma_{23}\sin\varphi\right)\sin 2\psi\end{matrix}\right\} \tag{2.2}$$

S_1 and $S_2/2$ are the appropriate elastic constants and for elastic isotropy they reduce to $S_1=-\frac{\nu}{E}$ and $\frac{1}{2}S_2=\frac{1+\nu}{E}$, and where the 3rd direction is normal to the specimen surface, ν is Poisson's ratio, E is Young's modulus and the measured strain is defined as:

$$\varepsilon(\varphi,\psi)=\frac{d(\varphi,\psi)-d_o}{d_o} \tag{2.3}$$

To obtain accurate stress values it is of utmost importance to accurately know the unstressed lattice parameter, d_o. In general this must be measured separately using a specially prepared specimen of some sort, either by preparing an identical piece that did not undergo the processing such as shot peening, or some filings of the original specimen from which long range stresses are removed resulting in a situation where all small scale or micro–stresses cancel. In a biaxially stressed specimen (σ_{i3}=0), there is a (φ,ψ) orientation at which the strain vanishes and therefore preparing a separate specimen is not necessary. The d_o can now be obtained either by direct measurement, or by interpolation. The assumption that the normal stresses are negligible is an often–made approximation since these stresses must vanish at the free surface and the penetration depth of x–rays is typically only a few micrometres. In some cases however, this approximation is not valid and a triaxial stress analysis must be performed. In principle, it is better to assume that a triaxial stress state exists since any stress state can be calculated. If, for example, the stress state were biaxial then a triaxial analysis would

merely show that the normal stresses were zero. Performing a biaxial analysis on a specimen which does have significant stresses normal to the surface, can lead to erroneous results.

Lastly, from equation 2.2, the strain is linear with $\sin^2\psi$ if no shear stresses are present and this is an often made approximation. The following two sections discuss other effects which may result in non–linear behaviour.

2.1.2: Effects of penetration depth on strain measurements

As mentioned above, the penetration depth of x–rays is an important consideration in strain measurements. In particular, the requirement that the stresses normal to the surface must vanish at the surface can result in stress gradients if there are such stresses present below the surface. Since the penetration depth of the radiation varies with the tilt of the specimen, it is difficult to perform measurements which are not affected by stress gradients. Because of this inherent effect, a number of studies have been published which examine the effect both experimentally and theoretically.[5,6,7,8] The presence of stress gradients in itself is not problematic, but because of the depth change with changing specimen tilt, different stress states are measured at each tilt! The result of this is that the d vs. $\sin^2\psi$ plot is no longer linear but has some curvature. Typically, the approach is to assume some sort of gradient function which attempts to describe the rate at which the normal stresses, σ_{i3}, relax near the surface.[9,10,11] These are then used to describe the curvature observed in the data.

More recently, attempts have been made to characterize the gradient by measuring the spacing at different depths. Predecki *et al.*[12,13] proposed three techniques to physically define the diffraction volume. The first used a grazing incidence technique which relies on the refractive index of the specimen to assist in changing the penetration depth with only small changes

in the incident angle. The other two techniques rely on using masks to confine the incident and diffracted beams. The latter two techniques are similar to those commonly used in neutron diffraction experiments to control the measurement volume being studied. In a subsequent paper,[14] Ballard *et al.* showed that the first technique could be used to measure the stress state in a Mo film deposited on a vycor substrate with depth from 250Å to 1250Å, indicating that this technique is only useful for measuring gradients very near the surface.

Genzel[7,8] proposed a method to measure gradients which extend over a longer range. Rather than using the tilt angle, ψ, as a parameter to vary the penetration depth, he defines a third axis of rotation, η, which is a rotation about the diffracting plane normal. Rotations about η maintain the (φ,ψ) orientations and hence no corrections are necessary when computing the stress tensor. The penetration depth is now given by:[8]

$$\tau_\eta = \frac{\sin^2\theta - \sin^2\psi + \cos^2\theta\sin^2\psi\sin^2\eta}{2\mu_{abs}\sin\theta\cos\psi}, \tag{2.4}$$

where the mass absorption coefficient is μ_{abs}. Hence by varying η, strain profiles can readily be measured as a function of depth. This therefore allows the complete stress tensor to be determined at different depths, eliminating the need for assumptions about the gradients of the stresses normal to the surface.

In considering the complex stress state in composite materials, it is difficult to make assumptions about the stress state measured by x–rays. Hanabusa *et al.*[15] argued that a triaxial stress state exists if the x–ray penetration depth is greater than the characteristic dimension of the reinforcement phase. Previous work has measured distinct triaxial stress states, in particular with the same material being examined in this study.[16,17]

2.1.3: Effects of texture on strain measurements

Preferred orientations, or texture, are very common in metallic materials and can greatly affect the properties of the product. Anisotropy of the elastic constants and the yield locus can be greatly exaggerated by texture for example. During x–ray measurements, the most noticeable effect of texture is the non–uniform Debye rings in powder diffraction spectra. It is this effect that is used to quantitatively evaluate the crystallographic texture present in a material. Typically, diffracted intensities are measured at many (φ,ψ) orientations for several *hkl* reflections. Each 'pole figure' measurement can be plotted on a stereographic projection, showing the intensity measured at different orientations with respect to the specimen co–ordinates. The data from the pole figures can be used to determine the so-called orientation distribution function (ODF), a mathematical description of the texture which describes the rotations of crystallites with respect to the specimen co–ordinates. From the ODF, the mean values of properties which vary with crystallographic orientation can be determined for the specimen in the bulk (specimen) co-ordinates. A very detailed discussion about texture and ODF's can be found in the book by Bunge.[18] The presence of a non–random texture results not only in changes in intensity for different orientations, but because of elastic anisotropy, the stress/strain states in different orientations may be different.

The presence of texture may thus lead to difficulties in performing the so-called d vs. $\sin^2\psi$ technique to measure residual stresses since the d vs. $\sin^2\psi$ curve becomes non–linear. This is due to the anisotropic elastic constants of most materials. Only random textured materials will always yield linear curves.[19] In particular, residual stresses due to plastic deformation yield non–uniform stress states among neighbouring grains and the stress state is dependent on the amount of deformation experienced by each grain. The

usual approach is to measure the d–spacing at many ψ orientations to obtain a good estimate of the curvature. By characterizing the elastic constants (possibly from an ODF measurement and the single crystal elastic constants to obtain a bulk average) equation (2.2) can be modified and fitted to the data to obtain the stresses. Van Houtte & de Buyser[19] and Noyan & Cohen[2] both discuss methods for calculating the appropriate elastic constants for different stress states. In particular, assumptions about the nature of the stress state are very important. The distinction to be made is whether the stresses are assumed homogeneous and the strains vary from grain to grain (Reuss model), or that the strains are constant from grain to grain and the stresses vary (Voigt model).[19] There are also a number of intermediate models which offer self–consistent solutions to satisfy the compatibility condition. The difficulty in performing residual stress analysis is determining which model applies to the specimen being studied. Since the strain is given by the peak position, the measurement technique automatically averages the strain in the diffraction volume. The usual method of measuring the strain at many tilts then measures the strains in many grains and since the grains have different orientations with respect to the specimen, the stress/strain state in each may be different. As mentioned above, the diffraction measurement yields the average strain state in the diffracting volume. Thus if a technique could be developed which measures the same grains at each tilt, then the stress/strain state measured for the different orientations should be the same. Such a technique has been developed and treats the diffraction volume as a single crystal. The technique has been described by Korhonen & Paszkiet in 1989, and was applied to residual stresses in metallization films.[20] The important result of this analysis (reproduced in **Appendix 1** for a triaxial stress state) is that the strain varies linearly with $\sin^2\psi$ and is independent of the *hkl* reflection used,

unlike the techniques described by Van Houtte & de Buyser which may depend on the reflection used.[18] In treating the specimen as a single crystal, only the ideal orientations which are geometrically associated with the grains being studied can be used in the measurement otherwise, other grains with different orientations will be measured and the single crystal analysis does not apply. In principle, the technique could be used to measure the residual strains in different texture components, component by component. Such a study has been applied to examining ridging in rolled steels.[16]

2.2 Use of Position Sensitive Detectors in Strain Measurements

Position sensitive detectors (PSD) have been used for residual strain measurements as early as 1973,[21] since they allow much quicker data acquisition. In particular, they are used extensively in portable systems for 'on–site' strain measurements. This advantage of the rapid data acquisition is essential in this study. Hence some discussion about the techniques adopted for using PSDs is presented here. The discussion begins by presenting the operating principles of proportional counters in general, and is then followed by that of position sensitive proportional counters (PSPC). The discussion then considers the geometrical considerations in using a linear PSPC for strain measurements.

2.2.1: Operation principles of proportional counters

Proportional counters have been discussed in great detail by a number of authors,[22,23,24] and hence only a rather brief review is presented here. A proportional counter detects radiation by measuring the ionization of a gas in an electric field. Typically, the field is generated between an anode wire and a cathode plate. The anode is at a large positive potential with respect to the

cathode. When an x-ray photon enters the chamber, it may strike an outer shell electron of a gas atom and ionize the atom. The electron is attracted to the anode wire and accelerates towards it. In doing so, it may strike another atom and ionize it. In a proportional counter, the electric field is large enough that the free electrons gain enough kinetic energy between collisions to ionize an atom in each collision. This results in an avalanche effect and amplifies the original signal by approximately 10^4.[22,24] For a proportional counter, the charge which reaches the wire is linearly proportional to the energy of the incident photon. Since the anode is usually a fine conducting wire, the electric field is high enough to cause the avalanche very near the wire and the avalanche volume is very small, hence position information may be resolved from a proportional counter. If the potential across the chamber is increased, then the avalanche effect is so large that the signal is no longer proportional to the energy of the radiation. The potential is also then typically large enough that other atoms are not ionized but are raised to excited states and emit ultraviolet radiation, which can ionize other atoms throughout the detector. Detectors which operate in this region are known as Geiger-Mueller counters and cannot operate effectively as position sensitive counters, since the avalanche is no longer sharply localized.[24]

2.2.2: Position resolution for a proportional counter

While there are a number of different methods for achieving position resolution, many position sensitive counters use a highly resistive anode wire (typically a carbon coated quartz wire only a few tens of microns in diameter) so that when a charge is generated on the wire, the signal is split and travels to both sides of the wire. The position on the wire is determined by measuring the difference in the arrival times at the ends of the wire. Very

good position resolution can be achieved by this technique with relatively simple electronic signal processing.

The primary drawback of this design however is that the anode wire can be damaged by very high intensities.[23] When too many x-rays strike the detector in a particular location, the ion density may become so high that the chamber 'arcs' (high voltage breakdown). This may remove some of the carbon coating on the wire and hence degrade the detector performance. If the damage is very severe then all of the carbon may be locally removed and the detector wire is an open circuit. For less severe damage, only some of the carbon is locally removed and the detector will have a reduced efficiency at that point.

2.2.3: Geometrical corrections applicable to linear PSD's

When using position sensitive detectors, in particular linear ones, corrections due to deviations from ideal geometry must be considered. This discussion shall deal only with corrections appropriate to small linear detectors. There are two geometrical considerations to be considered: defocussing due to deviations from the Bragg–Brentano criterion, and peak position corrections due to the deviation from the diffractometer circle.

Considering first the position corrections due to the linear detector not matching the diffractometer circle, the problem has been analyzed by James & Cohen.[25] The geometry of the problem is shown in Figure 2.2 and the angle $\delta 2\theta$ is given by $\delta 2\theta = \tan^{-1}(nz/R)$ as shown in the figure, where n is the number of channels from the centre and z is the width of a channel. The correction required is the difference between $\delta 2\theta$ and nz/R. That is, the true 2θ position at which some intensity is $2\theta_o+\delta 2\theta$, while the detector records the intensity at $2\theta_o+\kappa(nz)$, where κ is the calibration constant converting the multichannel

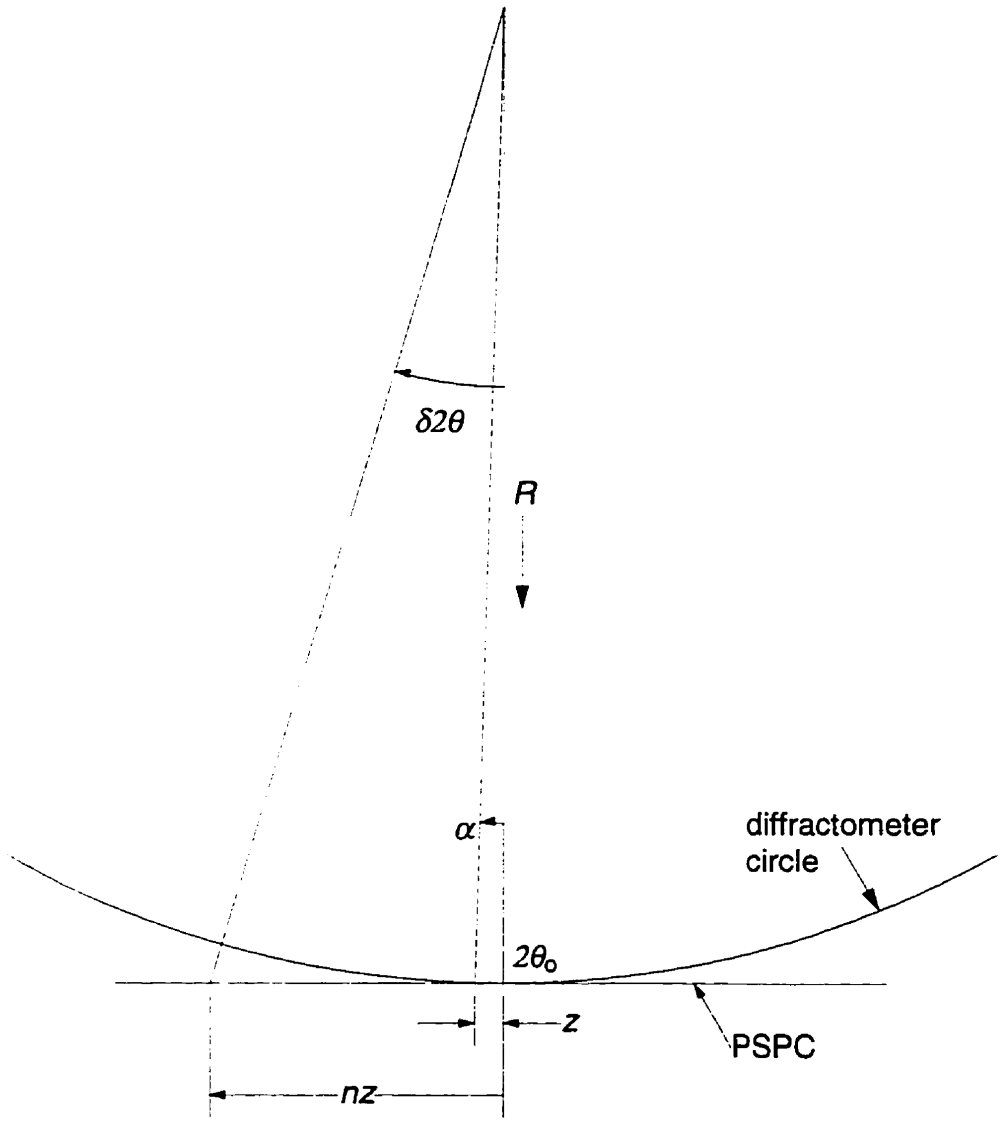

Figure 2.2: Geometry for the corrections due to deviations from the diffractometer circle for a linear PSD. z is the physical width of a 'channel' in the MCA and the calibration constant is $\kappa=\alpha/z$

analyzer channel number to position on the detector in angular units (i.e. degrees 2θ per channel). James & Cohen point out that the difference between the two is less than 0.001° 2θ within ±2.25° of $2\theta_0$ and hence can be neglected when examining only one diffraction peak on the detector which is moderately well centred.

Errors due to defocussing have also been discussed by James & Cohen,[25] but are also discussed by Heizmann & Laruelle[26] and reviewed by Wcislak & Bunge[27] and Wcislak *et al.*[28] The latter three papers discussed using PSD's to measure several pole figures simultaneously. The analysis of James & Cohen for a divergent beam show that at high angle, the defocussing error is very small: less than 0.002° 2θ for offsets of 6° from the point of tangency. At low angles, the defocussing can be significant, resulting in peak position errors of ~0.035° 2θ for similar offsets with the detector tangent at 45° 2θ. While James & Cohen show that the error varies with ψ, they aligned the ψ rotation axis with the θ axis, and hence the size of the focussing circle is a function of ψ. This is not the case for a 4–circle goniometer design, and hence these errors become independent of ψ.

The treatment by Heizmann & Laruelle considers only a parallel beam geometry and considers the loss in intensity when the Debye cone becomes wider than the receiving slits (for non-position sensitive detectors) which causes the measured integrated intensity to drop compared to the true integrated intensity. Wcislak *et al.* find that defocussing errors due to deviations from the Bragg–Brentano geometry are insignificant for PSD's whose angular widths are less than ~9° 2θ.

2.3 Micromechanics of Residual Stresses in Metal Matrix Composites

The interaction between the reinforcement and the matrix is of great importance to the bulk properties of a composite. The stress distributions and the relaxation mechanisms are critical to the mechanical behaviour such as the fatigue life. In the following discussion the stress relaxation mechanism of dislocation punching in discontinuously reinforced metals is described.

The primary mechanism of relieving the misfit stress in metal matrix composites is to punch prismatic dislocation loops from the interface. Dislocation punching has been studied as early as 1950,[29,30] and was first applied to the question "when does a growing coherent precipitate become semi- or incoherent". These studies examined the minimum stress required to punch a dislocation. As will be discussed, the results showed that very large strains were required to form a prismatic dislocation loop in an otherwise perfect crystal. This is of great relevance to metal matrix composites, since the large difference in coefficients of thermal expansion between the reinforcement and the matrix indicate that very large strains may be present.

These studies were concerned with the onset of dislocation punching, and all began with the following assumptions: the matrix behaved according to the laws of linear, isotropic elasticity of the matrix, and the matrix near the precipitate can be treated as a perfect crystal. Also, the elastic constants of the precipitates are usually assumed to be the same as the matrix, but in some cases this assumption has not been made to keep the study more general. These assumptions are reasonable in light of real systems, with the exception of isotropic elasticity.

Weatherly[31] derived the punching criterion for the general case of an ellipsoidal particle by using Eshelby's method to calculate the stress/strain field near the precipitate and then determined the maximum shear stress on

a slip plane. For needle shaped precipitates and for lenticular precipitates, Weatherly obtained the following maximum shear stresses on glide planes:

$$\tau_{needle}(\max) = \sqrt{\frac{3}{2}}\mu e_{11}^{T} \text{ and } \tau_{disc}(\max) = \frac{3\mu e_{33}^{T}}{2}. \quad (2.5)$$

The shear modulus of the matrix is μ and for the needle, the 3rd direction is parallel to the long axis and is assumed to be aligned in the crystal to the direction of minimum strain, i.e. ε_{33}=0. For the disc, the 3rd direction is normal to the short axis and the disc is assumed to lie in the plane of minimum strain, ε_{11}=ε_{22}=0. It is interesting to note that this result is independent of particle size, in agreement with Eshelby, and is solely dependent on the misfit strain between the two lattices of the precipitate and the matrix. The critical stress to punch a prismatic loop is the theoretical shear strength of the glide plane. Using Kelly's result,[32] Weatherly obtains critical strains on the order of ~10^{-2}. That these strains are so large at first seems unlikely compared to typical bulk yield strains, however it must be remembered that the matrix is effectively a perfect crystal and that the dislocation must be nucleated. The more common forms of dislocation slip and multiplication to relieve the stress do not operate since glissile dislocations are assumed to be not present.

Ashby and Johnson[33] provided an alternate nucleation mechanism in which a glide dislocation is first nucleated and allowed to cross slip on other slip planes and is rejoined by cross slip again on a plane parallel to the initial plane. Their paper also calculated the shape of the punched out dislocations based on the shear stress distribution near the spherical particle and predicted a near circular shape, intersecting the particle at 90°. This prediction is in excellent agreement with the electron microscope observations of Gulden and Nix.[34]

Rather than use the theoretical strength requirement as Weatherly did, Ashby and Johnson used a strain energy criterion for the critical misfit to nucleate a shear loop. They define the nucleation criterion as the condition under which the energy of the system is reduced by the presence of a shear loop. The contributions considered in this derivation are the work done by the misfit stress and the self–energy of the nucleated loop. From the above definition, two limits can be delineated for the nucleation: the first that there is no energy barrier to nucleation, and the second that the total energy can be reduced by the presence of a shear loop. This second limit has an energy barrier much larger than thermal fluctuations and hence can only be realized by an externally applied stress or by radiation induced vacancies and dislocation loops.[35] The former case is similar to Weatherly's criterion and the critical strain for such spontaneous nucleation is also of the order of 10^{-2}. Ashby and Johnson's lower limit is strongly size dependent and for particles greater than a few micrometers the critical strain at which a shear loop reduces the energy of the system is now less than 10^{-3}.

In metal matrix composites, numerous studies[36–45] have found punched loops from the ceramic–metal interface experimentally, and the theoretical discussions have typically followed energy minimization criteria. Since the problem is essentially identical to the one discussed above, the same principles apply. This discussion therefore proceeds from the precipitation hardened materials to MMCs, for which many of the same experimental techniques (i.e. TEM imaging of the dislocations) have continued to be used. An important advance in microscope technology has been the improved image quality which prevented the earlier studies such as Brown *et al.* [35] from performing experiments at high temperature. With the newer TEM microscopes, Arsenault and co–workers have published several studies

which examined the formation of punched loops in situ during high temperature annealing. In particular, by using high voltage microscopes, thicker foils could be used to minimize the effects of the surfaces. High dislocation densities observed by Arsenault and Fisher[36] in 1983 were shown in later studies[37,38,39] to be due solely to the thermal mismatch between the SiC reinforcement and the Al matrix. Arsenault and Shi[37] proposed a model to predict the dislocation densities due to the mismatch based on the following simple assumptions: both the SiC and the Al are elastically isotropic, the shear stress to move a dislocation is small, the reinforcement is simplified to parallelepiped particles and lastly, prismatic punching occurs equally on all faces. By calculating the length of dislocation necessary to relax the misfit and ignoring particle–dislocation and dislocation– dislocation interactions, they obtain the following expression for the dislocation density:[37]

$$\rho = \frac{B f_V \varepsilon^*}{b(1-f_V)} \frac{1}{t}, \tag{2.6}$$

where B is a geometrical parameter related to the shape of the particle, f_V is the volume fraction of the reinforcement, b the Burger's vector and t is the smallest dimension of the particle. Lastly, ε^* is the misfit strain between the matrix and the particle. The dislocation densities predicted by this model are in excellent agreement with the TEM observations. While the observations measure slightly lower dislocation densities than the model predicts, the thin TEM specimens are not a good representation of the bulk behaviour because the stress normal to the foil must be very small due to continuity requirements at the interface. Hence slightly higher dislocation densities could be expected in the bulk, improving the agreement with the model.

That this model is so successful is rather surprising since it does not take into account the effects of the crystallography of dislocations. That is, the effects due to orientation of a particle (in particular, whiskers or platelets) with the crystallographic orientation of the surrounding matrix were ignored. Since dislocations can only be punched in particular directions, the matrix–particle orientation relationship should strongly affect the dislocation density. Because Al has an fcc structure, the multiplicity of the slip systems is rather high, so the effects of such misorientations is minimized. Thus, Arsenault and Shi's model is not expected to accurately predict dislocation densities in composites whose matrix material has a lower crystal symmetry, such as hcp.

Taya, Mori *et al.*[40,41,42] have also proposed analytical models for criteria of dislocation punching and have in particular studied the number of punched loops necessary to relax the strain and the distance the loops are punched from the interface. In their model for relaxation in short fibre MMC's, Taya and Mori[40] assumed that misfit dislocations were already present at the interface and then calculated the distance N dislocations would punch to relax the stress field. Writing the potential energy of the composite as the elastic energy due to the misfit and a work term due to the friction stress of dislocation motion, the relaxed state can be defined as the force balance:

$$\nabla U_{elastic} + \nabla W_{friction} = 0. \tag{2.7}$$

Considering only punching in the direction parallel to the long (c) axis of the fibres, the problem becomes essentially one dimensional. Performing numerical calculations, Taya and Mori find that the punching distance increases with increasing misfit strain (increasing $|\Delta T|$) and decreases with increasing fibre aspect ratio. The first conclusion is expected, but the second is perhaps a bit surprising. The second conclusion does not state that no punching is predicted for long fibres, but rather that longitudinal punching

becomes energetically unfavourable. Thus for long fibres, only transverse punching is expected to occur. Dunand and Mortensen[43] found that this model overestimated the punching distance and proposed a similar model, but relaxed some of the constraints. Taya and Mori's model required that the punched dislocations exactly relax the stress field: the modification proposed by Dunand and Mortensen allowed the dislocations to over or under relax the stress field. Again finding the minimum energy, they now find that there will be an excess of punched dislocations in a smaller plastic volume. The results of the modified model were found to be in better agreement with experimental results.[43,44]

Shibata *et al.*[41] performed a similar analysis for spherical particles, but with a different dislocation array. While the short fibre model considered prismatic dislocation loops which were coaxial with the fibre axis, the new model for spherical reinforcement assumed the dislocations can be considered as rings surrounding the particle. The plastic region was predicted to grow via a dissociation–glide–recombination mechanism but seems to violate the crystallographic geometry of dislocations. It is not clear why the authors chose such a model while the dislocation geometry for the short fibre case should be applicable to the spherical case, with the modification that the punching is equally preferred along any axis. This would then be similar to the model of Arsenault and Shi described above. Since they treated the problem from a continuum mechanics viewpoint, the end result for the size of the punched volume may still be valid. For a spherical particle with identical elastic constants to the infinitely extending matrix, the punching radius was found to be:[41]

$$R = a\left[\frac{1+\nu}{2(1-\nu)}\frac{\mu}{K}\left|\varepsilon^*\right|\right]^{1/3}, \tag{2.8}$$

where the particle radius is a, ν is Poisson's ratio, μ the shear modulus, K the dislocation flow stress and ε^* is again the misfit strain. For a uniform distribution of particles in the matrix, the punching radius is limited by the volume fraction and particle size: $R \leq a(f_V)^{-1/3}$. The limit is imposed by the constraint that the punched volumes not overlap.

The research performed by the two groups discussed above (Arsenault *et al.* and Taya *et al.*) examined punching from a continuum mechanical perspective. While these studies have provided considerable insight into the criteria for dislocation punching and the range of punching, they did not consider effects due to crystal geometry on punching modes. Dunand and Mortensen[43] have examined experimentally a model system which simulates a metal matrix composite to study in detail the crystallography of dislocation punching. Their studies have focussed on whisker reinforced materials and hence are directly relevant to this study. The experimental approach was to examine a model system which simulated a metal matrix composite[44] by using glass or alumina fibres in AgCl (which has an NaCl structure). They were able to decorate the dislocations with Ag precipitates and examine the structure in a high resolution optical microscope. AgCl is transparent, hence 0.1mm thick specimens could be prepared and viewed using transmitted light. They were then able to discuss the resultant structures in light of the residual stress fields and dislocation theory. By using this model system, the extensive specimen preparation necessary for TEM studies of metals could be avoided. In particular the effects of the thin foil geometry on the stress state are eliminated, hence more 'realistic' dislocation behaviour can be achieved.

Dunand and Mortensen[45] did not model the thermodynamical criteria for nucleating a prismatic loop (as Ashby, Weatherly, *et al.* did), but considered instead a shear lag and dislocation theory based approach. Rather than treat

fibres as prolate spheroids, they are treated instead as cylinders, and consider punching only in the longitudinal direction.[45] The shear lag model adopted is based on the work of Cox[46] who examined the load transfer from the matrix to a fibre. While Cox considered externally applied loads, the stress field due to the mismatch is equally applicable to this technique. The analysis of Dunand and Mortensen indicates that the stress state of the fibre is a strong function of its length and changes along the length of the fibre. They define three classes: elastic only stress state for short fibres, elastic–plastic for longer fibres, and lastly elastic–plastic–unstrained for very long fibres.[45] The unstrained region refers to the middle section of very long fibres and it is the interfacial shear stress which is zero, the longitudinal stress in the fibre is still high, but has reached a maximal value. The authors mention that the elastic analysis has been found to agree with the experimental results of other workers. They defined the elastic limit as the condition when the interfacial shear stress reaches the matrix flow stress. The critical fibre length is then:

$$L_p = \frac{2}{\beta}\tanh^{-1}\left[\frac{4\tau_c}{\beta E_f d\varepsilon^*}\right], \tag{2.9}$$

where

$$\beta = \left[\frac{8\mu_m}{E_f d^2 \ln\left(f_V^{-1/2}\right)}\right]^{1/2}.$$

The controlling parameter is not so much the misfit strain as it is the flow stress, τ_c. While Ashby and Johnson[33] and Weatherly[31] showed that in a perfect crystal, the flow stress is very high and hence critical punching strains are on the order of 10^{-2}, experimental evidence indicates that punching occurs at much lower strains. Despite Arsenault *et al.*'s TEM observations[37,38] that all dislocations disappear at high temperatures, which agrees with the perfect crystal assumption, there must be some easy mechanism for the nucleation of

punched loops. Perhaps roughness on the interface acts as stress concentrations, or perhaps dislocations in the fibre act as sources similar to the threading dislocation mechanism[47] in epitaxial films. Dislocation sources at interfaces, especially Shockley partials, have been reported by Malis *et al.*[48] in 99.98% pure nickel.

The genesis of dislocation evolution and elimination during recovery is most important during thermal cycling of MMC's. Depending on the time–temperature cycle, the accumulated damage could lead to void or crack formation. The mechanics of dislocations punching to relieve stresses and the recovery of loops may be indirectly assessed by measurement of mean residual stresses during time–temperature cycling.

Chapter 3
Experimental Apparatus and Procedures

This chapter describes the design of the experiments for this study, and presents the calibration and alignment procedures which were developed specifically for the use of the position sensitive detector. The design of a new low thermal mass high temperature stage and the techniques used for sample preparation are described. Lastly, a simulation of the strain distribution in a hypothetical model is derived.

3.1 Experimental Design Criteria

Since the purpose of this study is to examine the dynamic behaviour of residual stresses during a simulation of the thermal cycling of the piston head, a hot stage which can meet the heating and cooling rates required is necessary. Likewise, a detection system which can record the information quickly and frequently is required to obtain the dynamic information.

The conditions for this simulation were that the specimen be heated or cooled in one minute between intervals at 100°C and 300°C. Heating was performed at a constant heating rate of 200°C/min and the cooling was achieved by air quenching.

3.1.1: X-ray peak detection requirements

In order to determine the dynamic behaviour of the stress state, the diffracted peak position must be recorded quickly. From previous work, it was found that during continuous thermal cycling, peak measurements should be made in a time such that the temperature change during the measurement was kept to less than 15°C.[49] This keeps the broadening of the peak to within acceptable limits for an accurate determination of the peak location. Thus for

dynamic information to be obtained with reasonable accuracy during the rapid temperature ramping, x–ray measurement time must be kept to less than 5s. The use of a scintillation counter which measured the Bragg peak position is not suitable for this study since measurement times cannot practically be made in less than approximately 30s. This limitation is due to the time required to physically move the detector throughout the width of the diffracted peak in addition to the time to collect the x–ray intensity at each position. Hence it is clear that a frame grabber aspect of position sensitive detection is required.

Such a detector must meet the following requirements: position resolution sufficiently fine to achieve the required angular resolution, an energy discrimination mode to reduce background noise, a high quantum efficiency to keep counting times short and lastly a detector to span a wide range of 2θ.

3.1.2: High temperature stage requirements

The simulation requires rapid changes in temperature, hence a design with a large heating and cooling power to thermal mass ratio is the dominant criterion. The stages used in previous studies[16,17,49,50] were designed to have a very wide x–ray window so that measurements could be made at high ψ angles at low 2θ reflections. The stages were also designed to have a very low thermal expansion to minimize z–displacement of the specimen which affects the measured peak position. Rapid temperature changes was not a requirement for this previous design and consequently it had a large thermal mass to improve the stability of the temperature control.

As stated above, the current study requires a stage which can meet the rapid thermal cycling. The stage should also meet the requirement of a low thermal expansion to minimize the peak shift errors due to specimen

displacement. A wide x-ray window is also necessary for measurements at high ψ orientations.

3.2 Measurement of the Peak Position

This section covers a rather broad range of topics, but all are important issues in accurately and precisely measuring the lattice parameter. The detection apparatus and calibration procedures are discussed first. Secondly, a method for correctly balancing the $K_{\alpha 1}$ and $K_{\alpha 2}$ intensities for textured materials is presented and lastly, techniques for making reliable measurements using materials with large grain sizes is discussed.

3.2.1: TEC model 205 PSPC

The TEC model 205 position sensitive proportional counter (PSPC),† was found to meet the performance criteria required for this study. The measurement window is 50 mm wide and 10 mm tall which allows for an effective angular window at a 350 mm working distance of 8.1° 2θ. The energy resolution inherent to a proportional counter is very useful in removing background noise and peaks due to diffraction from the K_β radiation. The small size allows measurements to be made even at very high angle reflections. The detector is a sealed chamber, and thus eliminates the difficulties associated with installing hoses for a gas flow system. The sealed design therefore also permits easier use of a wide range of 2θ. The detector is however sensitive to very high intensities and the wire can be damaged by arcing in the chamber. Because of this, great caution must be exercised to prevent damaging the detector, in particular considering the high intensity source being used. For textured specimens, the risk of damaging the detector is again increased since strong diffracted peaks are present at some

† obtained from TEC Corp. of Knoxville, Tennesee

orientations. Thus if very strong peaks are suspected, then a filter should be used or the power of the x-ray source reduced. In particular, caution should be exercised when examining thin films on a single crystal substrate, such as metallization films on Si wafers as the Si will diffract very strongly at some orientations.

To minimize such damage, 1 cm on each side of the PSPC window was covered by 0.5 mm Pb foil. Since less than 5° is required to measure the peak shape and position with the accuracy required, no loss of signal was observed. The Pb foil served only to protect the outer regions, and does not offer any protection to the central region. The principle for using the foil was to prevent damage from strong K_β reflections from other phases present in a specimen (a Si wafer substrate, for example). If a high background is still suspected or observed, then the use of an appropriate filter may improve the signal to noise ratio and minimize damage. It was found that with the specimens used in this study, the background contributions were sufficiently small and that a vanadium filter (appropriate for the Cr x–ray source) was not needed. The use of a V filter would also have decreased the intensity and longer counting times would have been required. From the above discussion about the PSPC detector itself, it follows that the electronics which amplify and analyze the signal should now be discussed.

3.2.2: Detector signal processing

The electronics will be presented in sequence, tracing the signal from the moment at which it is detected in the chamber to the computer which collects the data and controls the experiment.

Figure 3.1 shows the schematic circuit diagram, and the settings for each instrument are listed in **Appendix 4**. The PSPC 'head' requires a high voltage supply (the bias for the chamber) and a +12V and -12V pre-amp power supply.

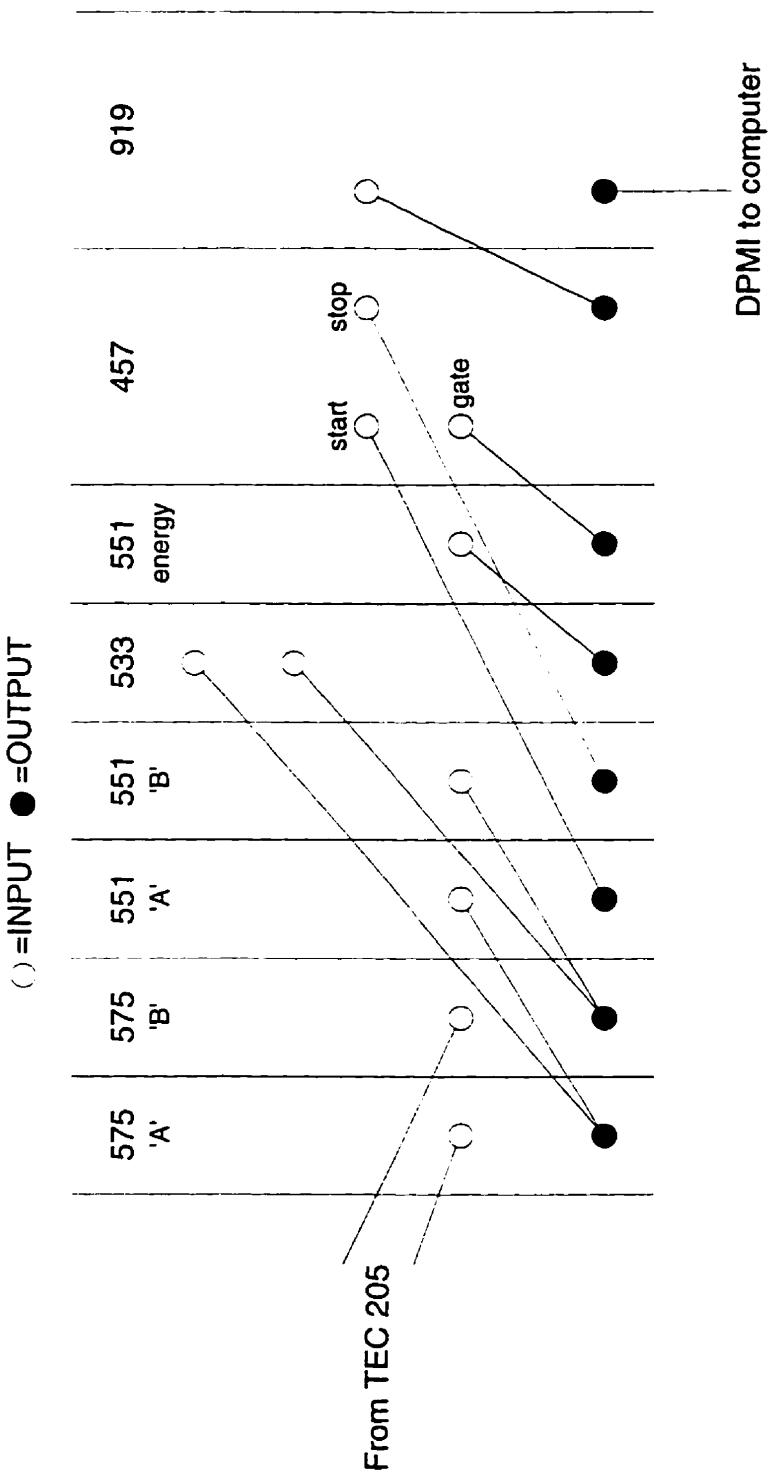

Figure 3.1: Schematic diagram of the circuit used for the signal processing for the TEC 205 position sensitive detector. The high voltage source and the preamplifier power supply for the detector are not shown.

The pre-amplifier is built into the detector head and consists of two separate units. Each amplifies only one of the signals from the two ends of the wire. From the pre-amps, the two signals are each received by a 575† amplifier which outputs a positive leading bipolar pulse. Each of these is then sent to a 551 timing single channel analyzer and together to the 533 Dual Sum and Invert amplifier. The output from a 551 is set to a sharp negative pulse with a rapid exponential decay. The output pulse is emitted after the zero crossing of the input bipolar pulse and a known (adjustable) delay. The signals from these two are accepted as the start pulse and the stop pulse for the 457 Biased Time to Pulse Height Converter. The output from the 533 Dual Sum and Inverting Amplifier is split with one signal to the energy discriminator (the third 551) and the other to a ratemeter. The ratemeter thus measures all detected photons and not exclusively those of a particular energy range. By monitoring the ratemeter, damage can be minimized or prevented.

The output from the energy discriminator is a positive square pulse and is sent to the 457 as a gate signal. That is, the 457 only gives an output when a gate signal is received and is coincident with a start/stop pulse pair. The output of the 457 is a square pulse whose amplitude is proportional to the time difference between the start pulse and stop pulse. An interesting and very useful feature of the 457 is the biased amplifier, since it allows a region of time differences to be considered while ignoring both large and small differences in time. This means that the signals measured near the edges of the detector can be ignored completely, while improving the position resolution in the central region! The 457 accepts a positive square pulse as a gate from the third 551 Timing Single Channel Analyzer. This 551 serves as

† EG&G Ortec product number

the energy discriminator so that only x–rays which have an energy similar to the Cr K_α are counted by the multichannel analyzer (MCA).

The MCA converts the analog pulse height signal to a digital signal and adds a 'count' to a register which correlates to the height of the pulse. The MCA communicates with the computer control via a dual port memory interface.

3.2.3: Detector calibration

Having introduced the detector, it is appropriate to discuss the calibration and alignment procedures particular to the PSPC. There are two separate steps in the calibration: determining the conversion factor of MCA channel number to 2θ angle, and the measurement of the centre channel with respect to the centre of the detector.

Calibration of the conversion factor (number of channels per degree 2θ) was performed by measuring the change in peak position on the detector for several known 2θ offsets imposed by the 2θ motor drive. Peak positions in the MCA were measured using the built-in peak measurement function of the *Maestro II*™ software package from EG&G Ortec. The software package performs a linear least squares fit of the data to a Gaussian after background subtraction.[51] Results of the calibration are shown in Figure 3.2 and the conversion factor was found to be 223 channels per degree 2θ. This was repeated several times during the study, and no drift was observed.

Calibration of the centre channel is equivalent to determining the true zero for the 2θ axis. This calibration can therefore be incorporated into the usual alignment procedure (discussed in **Appendix 3**). For this study, specimen and beam alignment were performed using the scintillation counter. Thus determining the centre channel for the PSPC was relatively

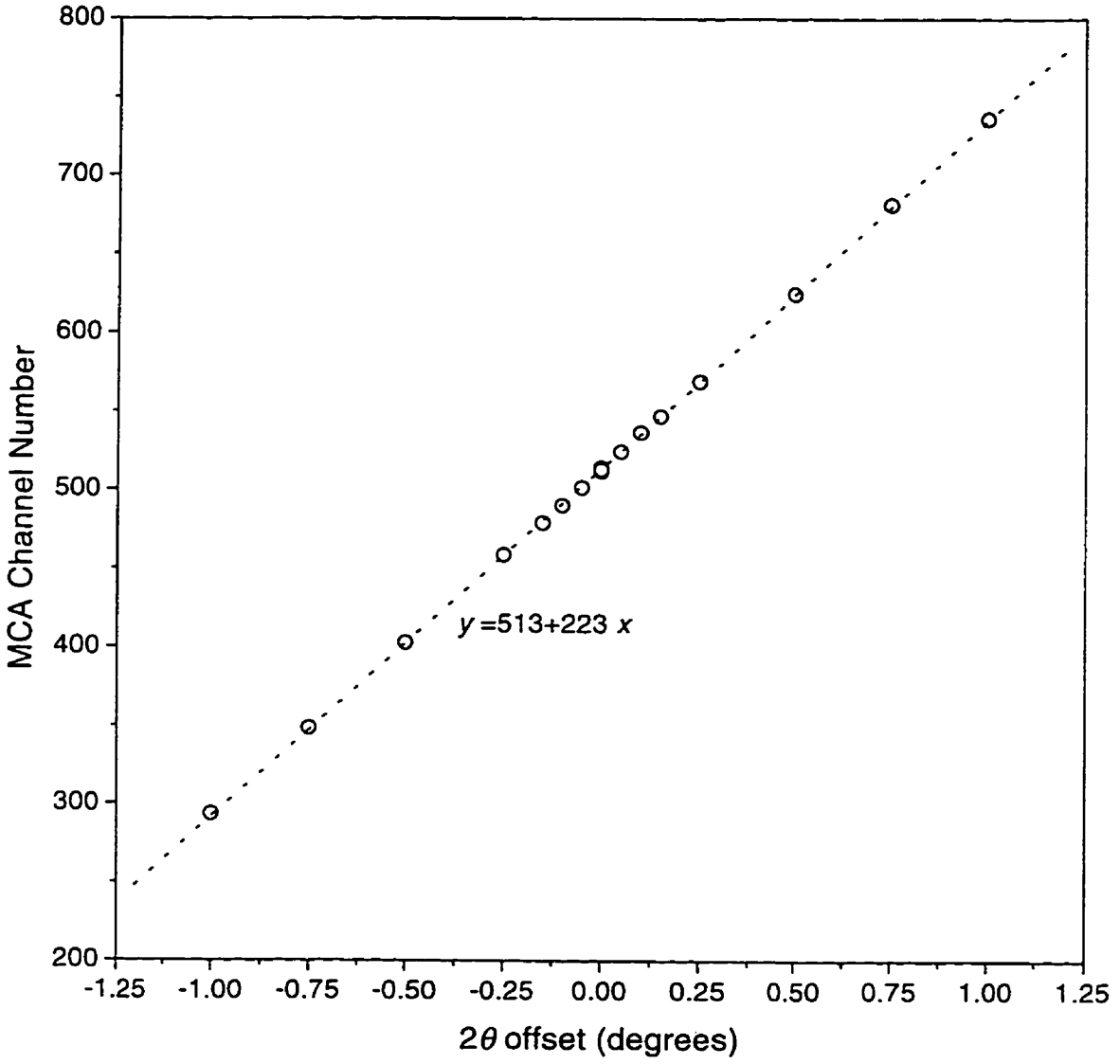

Figure 3.2: Plot of multichannel analyzer peak channel vs. 2θ offset, the slope of the line gives the channels/degree calibration constant

simple. For a specimen with random texture and which is free of stresses, the lattice parameter is independent of (φ,ψ) orientation and of the *hkl* reflection. If the measured lattice parameter is not constant for different reflections and the specimen and beam are both correctly aligned, then the difference is solely due to the detector being offset from the true 2θ zero position. For the PSPC, the difference can be corrected by either changing the centre channel in the data collection program, or by physically changing the zero position of the detector. The zero is correctly set when the measured lattice parameter at low 2θ reflections is identical to that measured at high 2θ reflections. Since the high angle reflections are much less sensitive to zero offsets than those for low angle ones, it is easy to determine whether the offset is negative or positive.

3.2.4: Peak profile corrections for strongly textured materials

At high 2θ reflections (the {311} position for Al using a Cr target is at ~139.5°), the $K_{\alpha 1}$ and $K_{\alpha 2}$ diffraction peaks are rather well separated. The two peaks are ~0.5° apart in 2θ space. This means that for textured materials, keeping the θ angle constant during a measurement could bias either of the two peaks. This is because the diffraction condition would be met for only one of the wavelengths. For random–textured, fine–grained materials this does not occur because there would be some grains oriented with the diffracting plane at a slightly different (φ,ψ) orientation and would still diffract. With strongly textured materials, such grains may not be present. Thus, like a single crystal, the diffraction condition is met more strongly for one of the wavelengths than the other, and the usual treatment of the intensity ratio of the $K_{\alpha 1}/K_{\alpha 2}=2$ would not hold. Since the specimens being studied have a strong <001> fibre texture, this could result in distorted peak shapes and hence a poor estimate of the peak position. This effect was observed in an

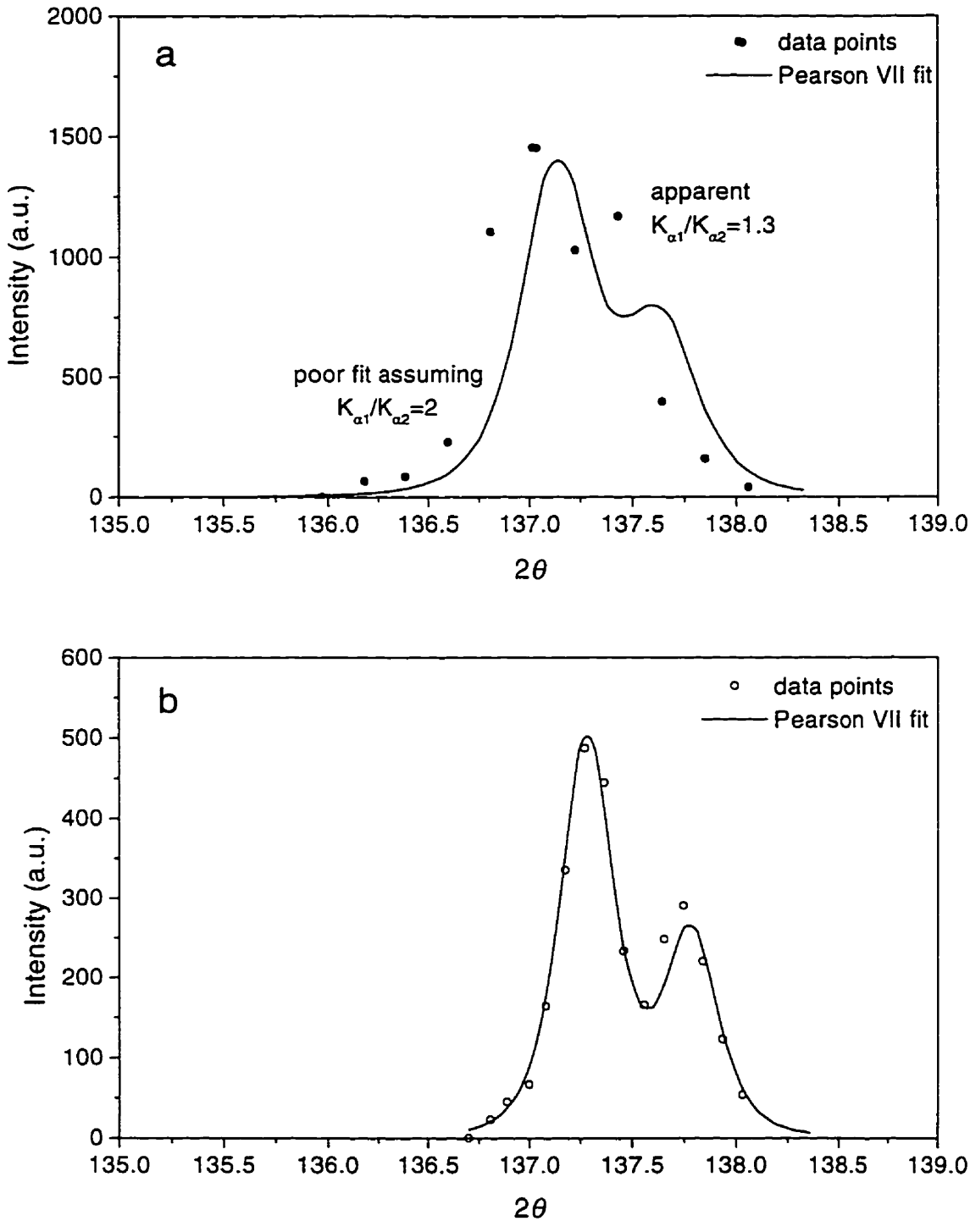

Figure 3.3: Peak profiles for (**a**) a peak measured without rocking θ showing a biased $K_{\alpha1}/K_{\alpha2}$ ratio and a poor peak fit, and (**b**) a peak measured using the rocking technique with the correct ratio and a good fit

early part of this study and an example is shown in Figure 3.3. This effect becomes even more deleterious during continuous temperature cycling, since the lattice parameter changes and hence the peak shifts during the measurement.

The solution to this problem is to ensure that both $K_{\alpha 1}$ and $K_{\alpha 2}$ wavelengths are allowed to diffract equally. To achieve this, the data collection program was modified to rock θ during each measurement. The rocking angle was calculated from the peak width information of the previously measured peak. The modification was developed so that the specimen would be rocked continuously during a measurement. The rocking speed was calculated to match the rocking angle to the exposure time, and the rocking was synchronized to begin slightly before the beginning of the exposure. By setting the rocking angle based on the width of the combined peaks, rather than the angular spacing between the $K_{\alpha 1}$ and $K_{\alpha 2}$, biasing of the $K_{\alpha 1}$ and $K_{\alpha 2}$ intensities is minimized during dynamic temperature cycling. With the modification in place, all peaks showed the expected balance of the intensities and good fits to the peaks were obtained. This rocking technique is commonly used for single crystal measurements,[52] and hence it is not surprising that its necessity become apparent in strongly textured materials.

3.2.5: Reliable lattice parameter measurements for large grained materials

The unreinforced standard from which the stress-free lattice parameter is obtained is a slice from a casting, as previously described.[17] The microstructure was found to be dendritic and the grain size was found to be very large: on the order of millimetres. Hence at most only one or two grains would meet the diffraction condition for any (φ, ψ) orientation. This is not in itself problematic. In fact the large diffracting volume results in high

intensities. The difficulty in dealing with such large grains is that a systematic error in the peak position is obtained when the diffracting grain is not centered in the beam. Figure 3.4a shows this effect schematically for a parallel beam geometry. The error in peak position due to such an offset is similar to that of a displacement parallel to the specimen normal. The systematic error in the peak position due to an offset in the horizontal position of the grain for a parallel beam geometry was derived to be:

$$\delta(2\theta) = \frac{\delta x \cos\theta}{R} \tag{3.1}$$

Where δx is the distance from the goniometer centre to the centre of the diffracting grain along the specimen surface and radius of the goniometer is R. This is a very large effect for even moderate misalignments. Thus the parallel beam geometry is not well suited for precise lattice parameter measurements of very large grained materials. For the Bragg-Brentano focussing geometry, the effect is much less because of the beam divergence, which has the effect of partially self correcting the misalignment of a grain in the beam. The error in the peak position (assuming an ideal point source) is derived as:

$$\delta(2\theta) = \left[\frac{\delta x \sin\theta}{R} - \tan^{-1}\left(\frac{\delta x \sin\theta}{R - \delta x \cos\theta}\right)\right] \tag{3.2}$$

and the geometry of this design is shown in Figure 3.4b. These effects are not often documented since only in very few cases is the grain size large enough to result in non-uniform diffraction from the irradiated volume.

The above discussion refers only to offsets in the diffraction plane, however the grain being examined must also be vertically aligned in the

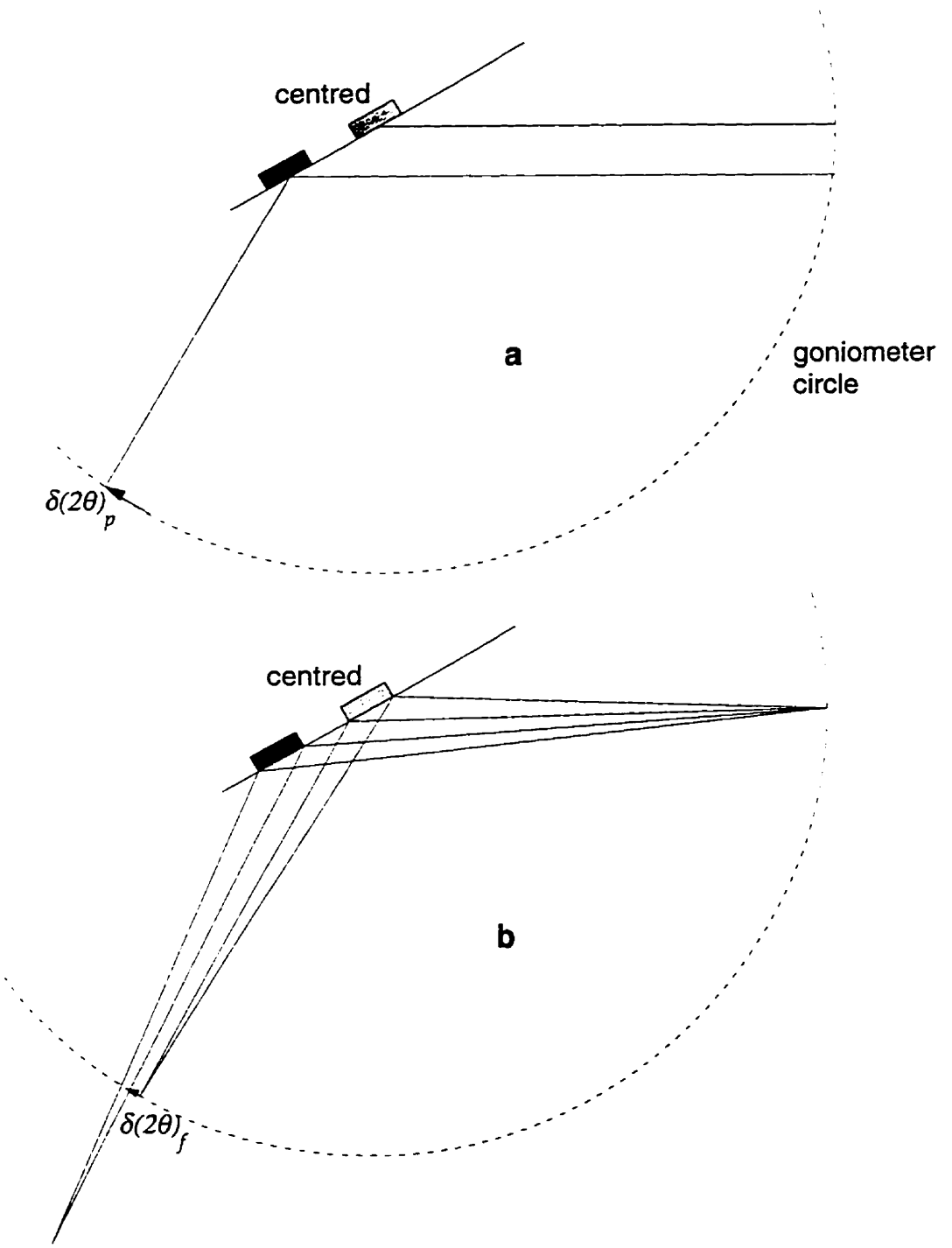

Figure 3.4: Schematic representation of the systematic errors in peak position due to an off centre grain for the parallel beam geometry (**a**) and for the Bragg–Brentano focussing geometry (**b**)

beam: a misalignment in this direction is equivalent to a beam misalignment. Hence positioning of the centre of the grain must be similarly close to the horizontal centre line of the beam. If the grain is similar in size or larger than the effective height of the beam on the specimen, then this is no longer a problem so long as the grain fills the beam height.

Alignment procedures for centering the grain in the beam can be easily achieved using the new hot stage mounted on the oscillating sample holder. It should be noted that oscillating the stage is not recommended during the actual measurement since the result would be to only broaden the measured peak. The oscillating stage is useful however during the initial alignment to find a suitably oriented grain.

3.2.6: Software control for peak detection and analysis

Since the peak position shifts with the changing temperature, the peak analysis can be optimized by moving the detector to track the peak shifts. While the detector is stationary during a measurement, the data collection software was written to move the detector between measurements to follow the peak shifts. This kept the peak position near the centre of the detector and hence good peak shapes were obtained and defocusing errors were minimized. Peak positions were calculated by fitting two Pearson VII functions to the data after background subtraction. The fitting technique is described in more detail in reference[16].

3.3 Low Thermal Mass, Zero Thermal Expansion High Temperature Stage

As mentioned above, the requirements for the high temperature stage are that the thermal expansion is kept to a minimum, that the x–ray window is as large as possible and that the heating and cooling power to thermal mass ratio is a maximum.

This third requirement rejects the previous hot plate design since the thermal mass of the heating wires and the plate itself are in themselves large. To keep the thermal mass to a minimum, the stage should be designed so that (ideally) only the specimen is heated. This implies that heating should be localized to as small a volume of material as possible.

3.3.1: Implementation of an infrared spot heater

Infrared heating lamps can provide very efficient heating for samples with even a moderate emissivity. They have the advantage of a very small thermal mass (only the filament) and can be focused to heat a selected area on a specimen. Since the radiant energy is proportional to T^4, even small changes in the temperature of the filament greatly affect the heating efficiency. This makes temperature control difficult since the characteristic time constant will be very small. This does however give the advantage of increasing the cooling rate: the heat source can be very quickly turned off.

A 50 mm diameter infrared spot heater manufactured by Research Incorporated which focused the light from the filament to a 5mm x 8mm ellipse was found to provide efficient heating to the specimens used in this study. A Variac transformer was used to provide 22V AC supply for the lamp. The reflector and housing of the lamp was cooled using continuous air flow from a small blower.

To improve the focussing of the spot heater, a stainless steel truncated cone was developed. This polished cone mounts onto the lamp and directs stray light back towards the specimen without interfering with the x–ray beam path. Initial work showed that without the cone, heating efficiency was very poor and insufficient to heat the specimen to 300°C. With the cone in place, the spot heater could very easily heat the specimen to the required temperatures. (The programmable temperature controller indicated that the

heater could maintain the reinforced specimens at 300°C using approximately 30% power.) A second stainless steel cone was developed to fit behind the specimen to redirect light which passed around the edges of the sample to the back of the sample. It also may have reduced convective heat loss behind the specimen.

The heater was mounted on an arm which was bolted to the goniometer. This kept the spot heater correctly directed at the specimen at all (φ,ψ,θ) orientations. To keep the spot heater out of the beam path at high angle reflections, the heater was positioned above the incident slits and directed downwards onto the specimen. The angle at which the light struck the specimen was estimated to be approximately 45° from the normal. Despite the decrease in heating efficiency due to the incident angle the high temperatures could still be easily controlled.

3.3.2: Design of the zero expansion stage

The design criteria of low thermal expansion and low thermal mass were realized simultaneously by a novel approach. The stage was designed such that the front (irradiated) surface was the reference plane. Figure 3.5 is a schematic representation of the new stage and the spot heater. A ceramic 'C-Shell' which could be mounted onto the oscillating pole figure stage was developed, to support an aluminum specimen holder so that the front surface is pressed against the inner ledge. The holder was made with a rectangular cut–out for the specimen, and two glass plates were bolted to the front of the holder. The specimen is pressed against the 'under side' of the glass plates by spring clips. Thus the irradiated surface of the specimen is co-planar with the front surface of the Al holder. Since the spot heater can be focused onto the specimen, heating of the stage itself is kept to a minimum. Also because the front surface is the reference plane, any thermal expansion

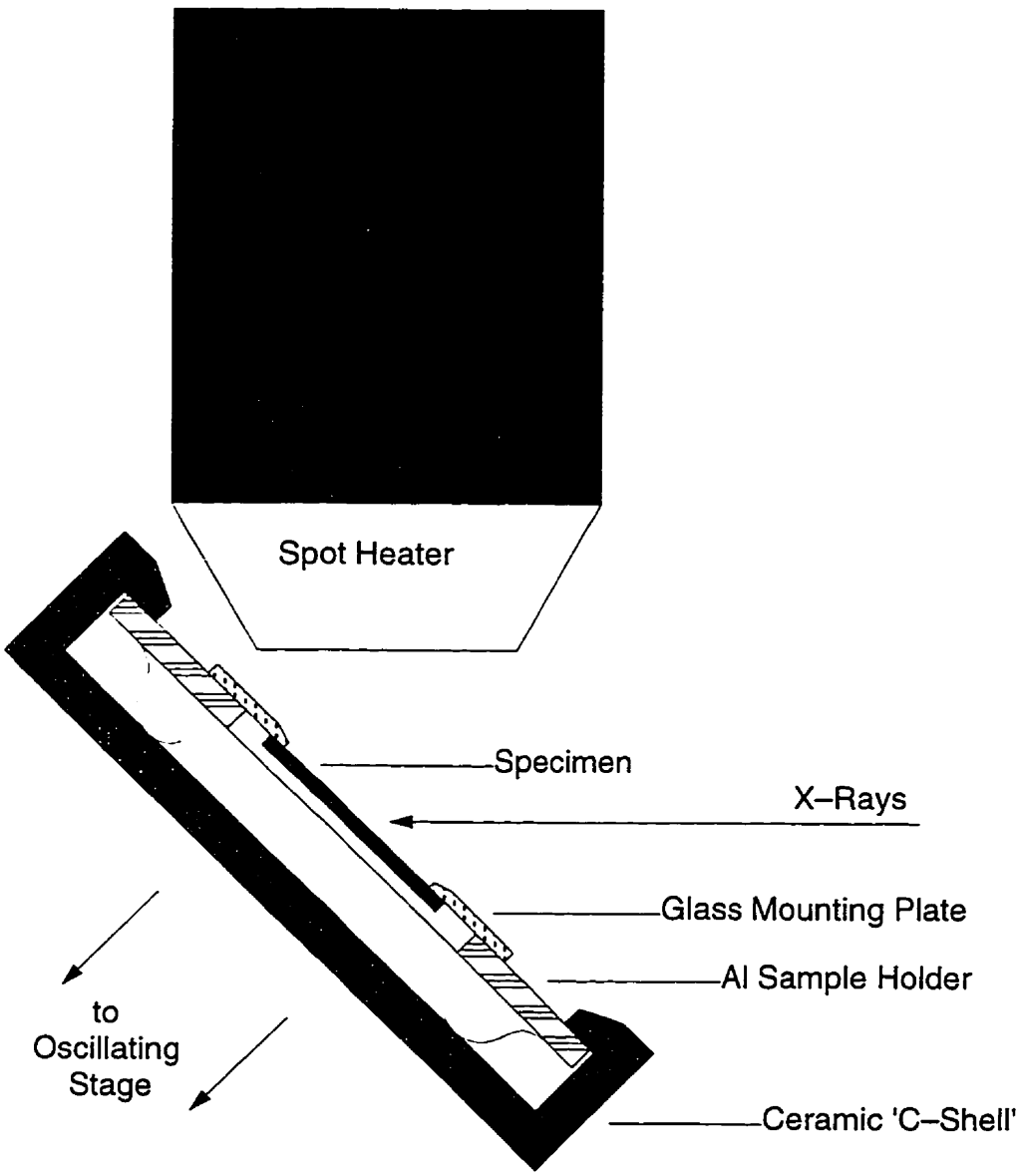

Figure 3.5: Schematic representation of the low thermal mass, zero expansion high temperature stage and the spot heater, the oscillating stage (not shown) shuttles the stage in the plane of the specimen

of the holder (and the specimen) is directed into the shell. Thus the stage is designed to have zero net thermal expansion!

Having met the requirement for a low thermal expansion, the stage is also directly designed to have a low thermal mass. This is achieved by focussing the spot heater on the specimen and by a poor thermal contact between the specimen and the stage. Heat from the sample must flow through the spring clips to the Al holder or through the glass plates to the holder. Thus the thermal mass is effectively limited by the size of the specimen.

Temperature control was achieved using a Eurotherm 818 programmable temperature controller. The specimen temperature was measured using a type K thermocouple contact welded to the back surface of the specimen but away from the edges, making the thermocouple an integral part of the specimen. Furthermore since the specimen was less than 1 mm thick, the temperature variation between the irradiated surface and the measured is expected to be smaller than the undulations due to the on/off cycle of the infrared heater. Welding the thermocouple to one of the spring clips was found to result in low measured temperatures due to heat loss through the clip. Since the thermal conductivity of aluminum is rather large, temperature gradients from the irradiated surface to the back surface were expected to be small. Positioning the thermocouple on the back surface was also expected to be more appropriate since it would not interfere with the x-ray beam path, and would eliminate over estimation of the temperature from the thermocouple potentially being heated more efficiently than the specimen due to differences in emissivity.

3.3.3: Calibration of the stage expansion

The expansion of the high temperature stage was calibrated by performing the specimen z-alignment procedure at two temperatures. The alignment procedure was performed using a 1.0μm Al film deposited on (100) Si. The film has a strong {111} fibre texture and thus the d-spacing must be linear

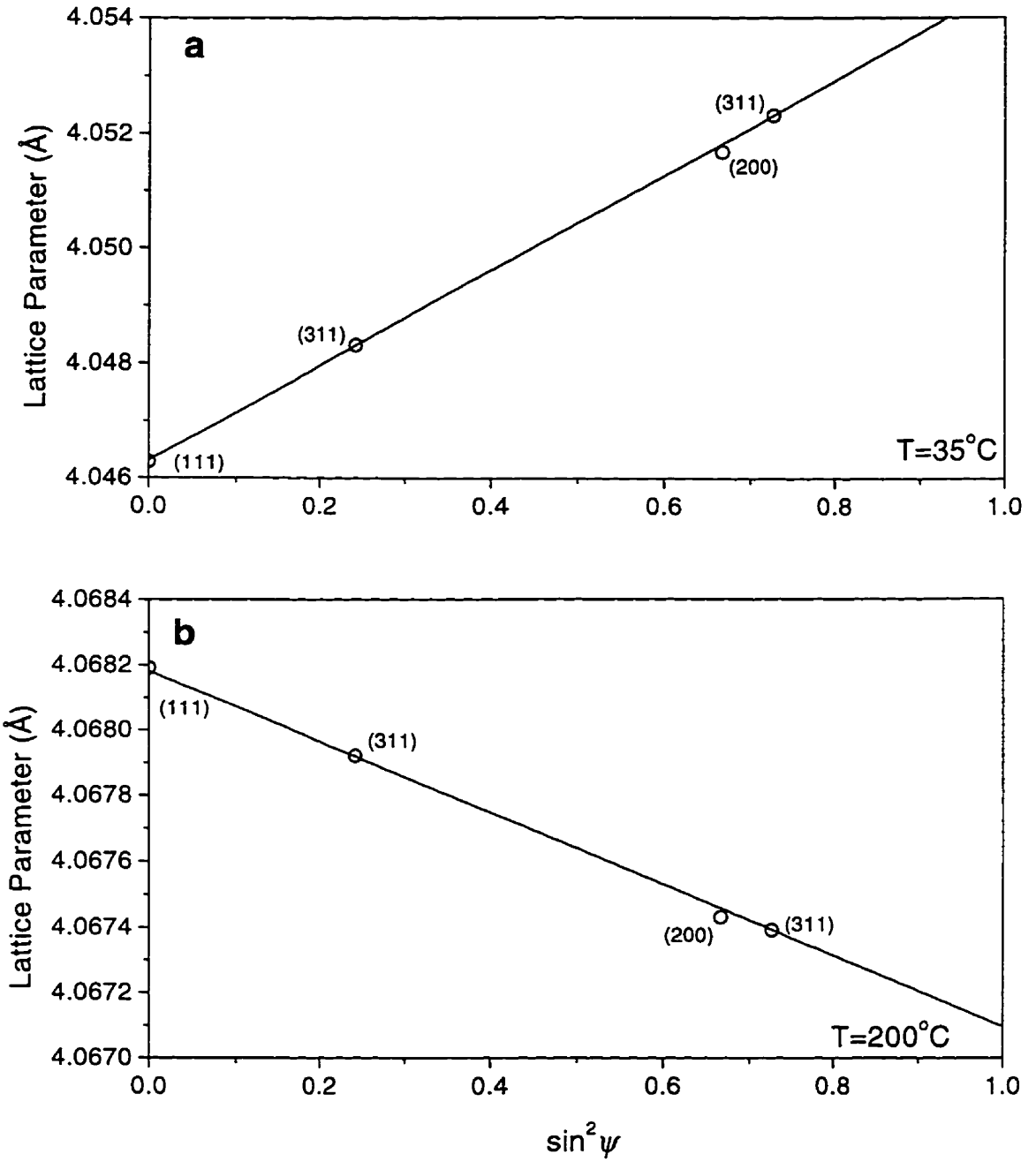

Figure 3.6: d vs. $\sin^2\psi$ plots at (**a**) 35°C and (**b**) 200°C for a 1μm Al blanket film on a (100) Si wafer. The linearity in both indicate good alignment at both temperatures, demonstrating a thermal expansion less than the measurement limit. The reflections used are given beside the data points.

with $\sin^2\psi$ based on the single crystal treatment. The stress state is biaxial plane stress in the film plane and the stress can be calculated from the slope of the d vs. $\sin^2\psi$ line. Alignment procedures were performed at 35°C and at 200°C. The results of the alignment, shown in Figure 3.6, indicate that there is no measurable change in specimen position which confirms the zero expansion design. A misalignment arising from a z–direction change as small as 5μm can be measured by this technique.[16]

The temperature of the Al holder was also measured during one of the slow cycles up to 300°C and it was found that the holder reached a maximum temperature of 80°C after 20 min at 300°C, demonstrating that the spot heater does not efficiently heat the stage. Thus the thermal mass is kept to a minimum. This was further confirmed by the cooling rates achieved: the specimens used, when 'step' cooled from 300°C the time to reach 100°C was approximately 50 to 55s. The initial cooling rates were exceptionally rapid, reaching 200°C in less than approximately 15s.

3.4 Summary of Experimental Design

Having discussed the details of the experiment, the design can now be clearly summarized. A photograph of the x–ray strain measurement system is shown in Figure 3.7. From left to right in the photo: the TEC 205 PSPC with the leaded plexiglas cover, the Euler cradle, the spot heater is illuminating a specimen on the zero expansion high temperature stage, the primary beam collimating slits and lastly the rotating anode x–ray source.

3.5 Sample Preparation

Specimens were received from General Motors North American Operations (GMNAO) Research & Development Center. Two cylindrical castings, one reinforced with the kaowool fibres, and the other an unreinforced casting which simulated the aluminum matrix composition

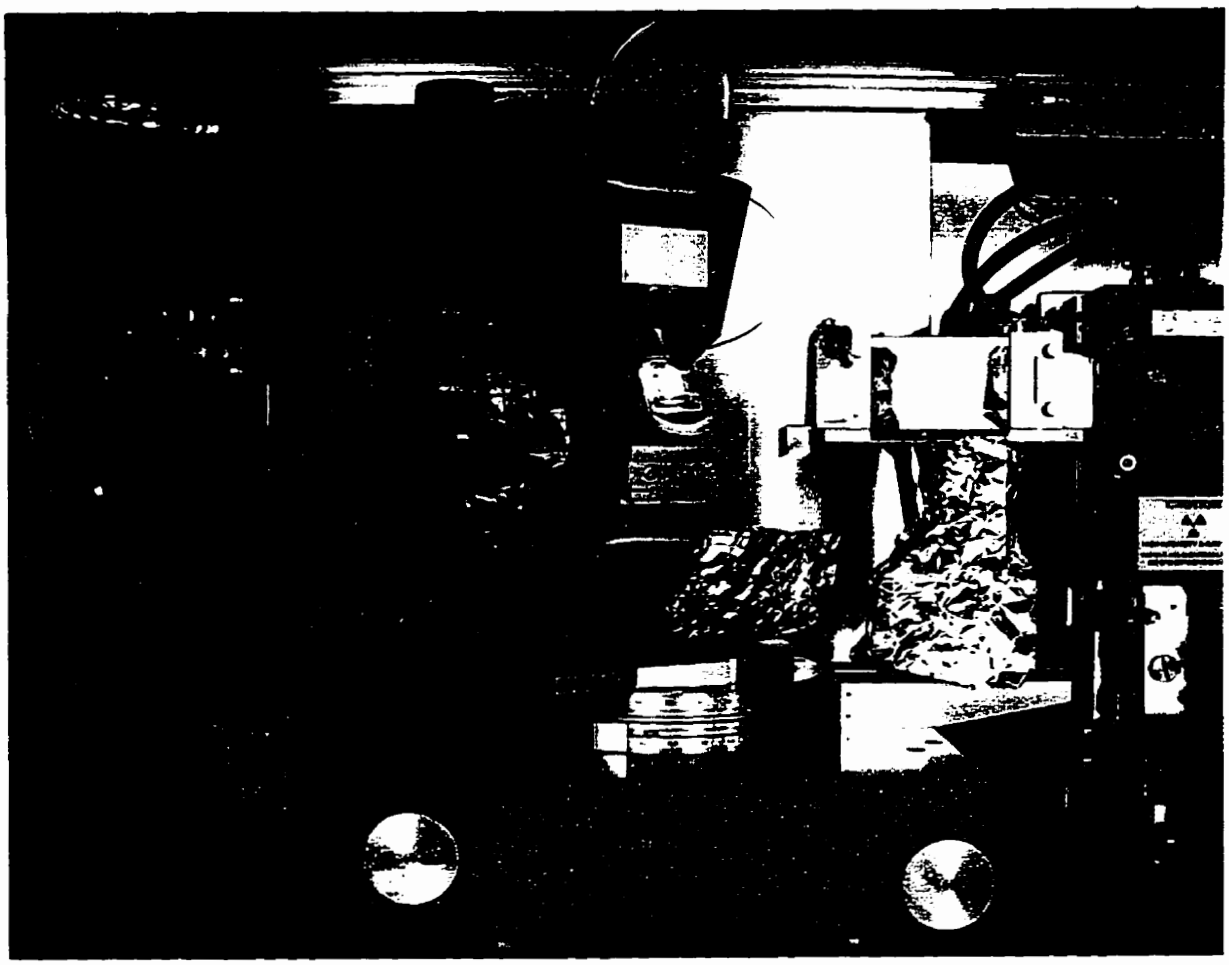

Figure 3.7: Photograph of the x–ray diffraction apparatus, showing (L–R) the TEC 205 PSPC, the Euler cradle, the high temperature stage and spot heater, the incident beam collimating slits and the high intensity x–ray source.

were electro-discharge cut into slices parallel to the cast face. The specimens were then hand ground and polished to 6μm diamond polish.

Because of the geometry of the new high temperature stage, it was essential to ensure that the polished surfaces were also planar. Non–flat specimens could result in deviations from the goniometer centre to which they must be aligned. To achieve this, the specimens were mounted on a flat plate using double sided tape during grinding and polishing. Good flatness at each stage of grinding can be observed by examining the scratches during the grinding steps.

A specimen is flat to the 'resolution' of the grinding paper if the scratches are uniform over the specimen surface. The specimens were ground at each grinding paper, starting with 220 then 320, 400 and finally 600 grit SiC papers, until the abrasion was uniform across the surface. Lastly, the specimens were polished using an aqeous suspension of 6μm diamond powder. Flatness of the specimens was confirmed by laying them down on an optically flat glass plate. No light was visible passing between the specimen and the plate. It is estimated that deviations as small as ~20μm would allow light to pass between the sample and the plate and be detected by this technique. This flatness is sufficient for the measurements to be made at the {311} peak.

Some stresses from the grinding–polishing steps are expected to be generated and these must be removed. The relaxation of these stresses can be readily achieved by annealing the specimens.[17] The annealing treatment used was to heat the specimens at 5°C/min to 300°C and hold for 30 minutes. The specimens were then cooled at 5°C/min to ambient temperature. It was found that two such cycles were sufficient to remove the stresses.

All specimens used were prepared using the methods described above and underwent two annealing cycles to remove the damage induced by the

grinding and polishing. The source of the reinforced specimens used in this study are shown in Figure 3.8.

The unreinforced specimen was taken from the cast surface to try to obtain the random textured, fine grained structure near the cast face. However, after grinding and polishing, the microstructure showed large dendrites indicating the columnar region. That the chill zone is thin and that the dendrites are large indicate a slow cooled casting. Thus the techniques described above in §3.2.5 were required to measure the lattice parameter with temperature.

3.6 Thermal History of the Kaowool Specimens

3.6.1: Specimen composition and casting method

The MMC specimen is an AA339 Al alloy reinforced with 23% (vol.) Kaowool fibres. The composition of the alloy is (wt.%) 12 Si, 1 Mg, 1 Cu, 1 Ni, 0.5 Fe and the balance Al. In the previous study,[17] the microstructure was found to contain two types of precipitates: Si rich ones and intermetallic ones. Section §4.2 discusses the microstructure of the specimens observed by focussed ion beam microscopy for the reinforced specimens and by optical microscopy for the stress free standard. The composition of the matrix (0.6 Si, 0.25 Mg, 0.6 Cu (wt.%)) was measured in the previous study by electron microprobe analysis so that a suitable stress free specimen could be cast with a composition similar to the matrix solid solution. This reduces the uncertainties in the stress free lattice parameter due to the compositional variation.

Both the reinforced and stress free specimens were prepared in the same squeeze casting apparatus. This is especially necessary for the reinforced sample since the molten alloy must infiltrate the Kaowool fibre preform and eliminate porosity.

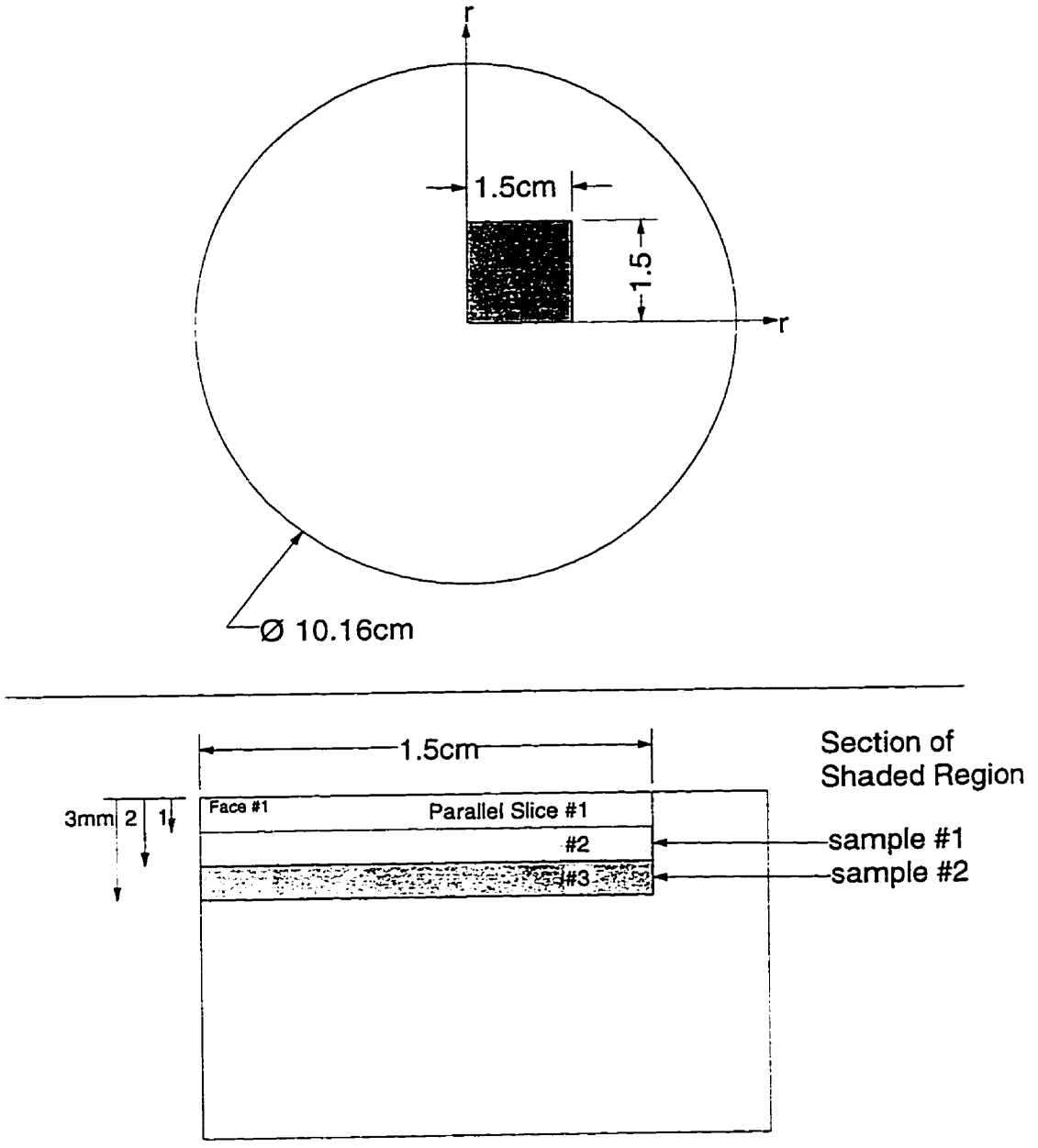

Figure 3.8: Location in the casting from which the reinforced specimens were removed.

3.6.2: Thermo–mechanical history of the reinforced specimens

Since the prior thermo–mechanical history is very important in the development of the stress state at any point in time, the complete thermo-mechanical history must be presented. This section therefore is a bibliography of the specimens used in this study, after their receipt from the GMNAO Research & Development Center.

The specimens were prepared as described above and the thermal history is given in the table below using the following notation: the temperature and time for an isothermal hold is temp(time), i.e. 100(20) is a 20 minute anneal at 100°C. The ramp rate between such steps is given as /rate>, i.e. /5> is a ramp rate of 5°C/min. Thus the heat treatments to relieve the polishing stresses becomes in this notation: *Amb./5>300(30)/5>Amb.* which is a heating rate of 5°C.min from ambient temperature to 300°C and isothermally held for 30 minutes. The specimen was then cooled at 5°C/min back to ambient temperature. The notation /Q> represents a quench from the high temperature to the lower temperature. Runs 18 and 19 contain rapid, short hold time cycles which were repeated 10 times. This is represented as a loop with the following notation: $\left|cycle\right|_n$, where *cycle* refers to the treatment used and n is the number of times this was repeated.

Table 3.1: Thermal history of the 1st reinforced specimen

Run #	Heat Treatment
stress removal #1	Amb. /5> 300(30) /5> Amb.
stress removal #2	Amb. /5> 300(30) /5> Amb.
1	Amb. /5> 300(20) /5> Amb.
2	Amb. /5> 300(20) /5> Amb.

Table 3.1 cont.

Run #	Heat Treatment
3	Amb. /5> 300(20) /5> Amb.
4	Amb. /5> 100(15) /200> 300(10) /Q> 100(20)/200> 300(10) /Q> 100(20) /5> Amb.
5	Amb. /5> 100(15) /200> 300(10) /Q> 100(20)
6	100(10) /200> 300(10) /Q> 100(20) /5> Amb.
7	Amb. /5> 100(10) /200> 300(10) /Q> 100(20) /5> Amb.
8	Amb. /5> 100(10) /200> 300(10) /Q> 100(20) /5> Amb.
9	Amb. /5> 100(20) /200> 300(10) /Q> 100(20) /5> Amb.
10	Amb. /5> 100(20) /200> 300(10) /Q> 100(20) /5> Amb.
11	Amb. /5> 100(20) /200> 300(10) /Q> 100(20) /5> Amb.
12	Amb. /5> 100(20) /200> 300(10) /Q> 100(20) /5> Amb.
13	Amb. /5> 100(20) /200> 300(10) /Q> 100(20) /5> Amb.
14	Amb. /5> 100(20) /200> 300(10) /Q> 100(20) /5> Amb.
15	Amb. /5> 100(20) /200> 200(3) /200> 300(20) /Q> 200(3) /Q> 100(20) /200> 200(3) /200> 300(10) /Q> 200(3) /Q> 100(20) /5> Amb.
16	Amb. /5> 100(20) /200> 200(3) /200> 300(20) /Q> 200(3) /Q> 100(20) /200> 200(3) /200> 300(10) /Q> 200(3) /Q> 100(20) /5> Amb.
17	Amb. /5> 300(20) /5> Amb.
18	Amb. /5> 100(20) /200> 300(20) /Q> 100(8) $\left\|\text{/200> 300(3) /Q> 100(8)}\right\|_{10}$ /200> 300(20) /Q> 100(20) /5> Amb.
19	Amb. /5> 100(20) /200> 300(20) /Q> 100(8) $\left\|\text{/200> 300(3) /Q> 100(8)}\right\|_{10}$ /200> 300(20) /Q> 100(20) /5> Amb.

The other specimen used in this study was also used in the previous study,[17] and was examined for comparison of methodologies. The thermal history of this specimen is presented only for the heat treatments performed in this study and is given below in Table 3.2. The temperature control for runs 1–3 for specimen #2 underestimated the temperature by approximately 10% due to a poor thermocouple junction at the specimen and the high temperature was therefore estimated to reach 330°C.

Table 3.2: Thermal history for specimen #2 for cycles performed in this study

Run #	Heat Treatment
1	Amb. /5> 330(20) /5> Amb.
2	Amb. /5> 330(20) /5> Amb.
3	Amb. /5> 330(20) /5> Amb.
4	Amb. /5> 300(20) /5> Amb.
5	Amb. /5> 300(20) /5> Amb.

3.7 Simulation of Strain Distributions in a Metal Matrix Composite

This simulation was undertaken to add physical insight of the strain fields in two phase materials. This simple model is useful in interpretting the measured mean residual stresses in an MMC. The strain distribution in a reinforced material is not uniform, but varies with the distance from the interface separating the two phases. Here, an elastic analysis of a very simple system is presented to demonstrate the non-uniform distribution of the strains and to elucidate the difference between the measured mean strain given by the position of the Bragg peak and the measured strain distribution

given by the shape of the diffracted peak. Much work has been done to model the strain distribution, usually by finite element methods which also consider the plastic deformation.[1] For this simulation, however, an analytical elastic solution is sufficient to demonstrate the non–uniform distribution. Moreover, since only elastic strains can be measured by diffraction techniques an elastic analysis is a reasonable approximation to the contributions to the shape and position of a diffracted peak. The example is a hypothetical case of a periodic distribution of cuboidal strain centres. To examine this, Mura's derivation[53] is followed. The analysis is based on Eshelby's approach to elastically modelling inclusions.[54] Here the inclusions, or strain centres, are considered to have the same elastic constants as the matrix. In essence, the inclusion is modelled in the following manner. The inclusion is removed from the homogeneous parent block and allowed to undergo some transformation, i.e. some phase transformation, or its temperature changed so that its volume changes. Next stresses are applied to the inclusion such that it returns to its original shape (elastically) and it is re-inserted into the parent block. The inclusion is 'welded' into the block and the applied tractions are removed. The block and inclusion are then allowed to accommodate the relaxation elastically.

In this example, the inclusions are cubes of characteristic size $2a$ and are uniformly separated in all 3 directions by a distance $2L$. The arrangement is shown in Figure 3.9. Since the array is periodic, the solution can be obtained using a Fourier series method. If the origin is aligned to the centre of one of the cubes, then the displacement in the x_3 direction can be expressed as:[53]

$$u_3(\mathbf{x}) = 8\kappa \sum_{p,q,r=1}^{\infty} \frac{\sin\left(\frac{p\pi a}{L}\right)\sin\left(\frac{q\pi a}{L}\right)\sin\left(\frac{r\pi a}{L}\right)}{pq\left(p^2+q^2+r^2\right)} \cos\left(\frac{p\pi x_1}{L}\right)\cos\left(\frac{q\pi x_2}{L}\right)\sin\left(\frac{r\pi x_3}{L}\right) \quad (3.3)$$

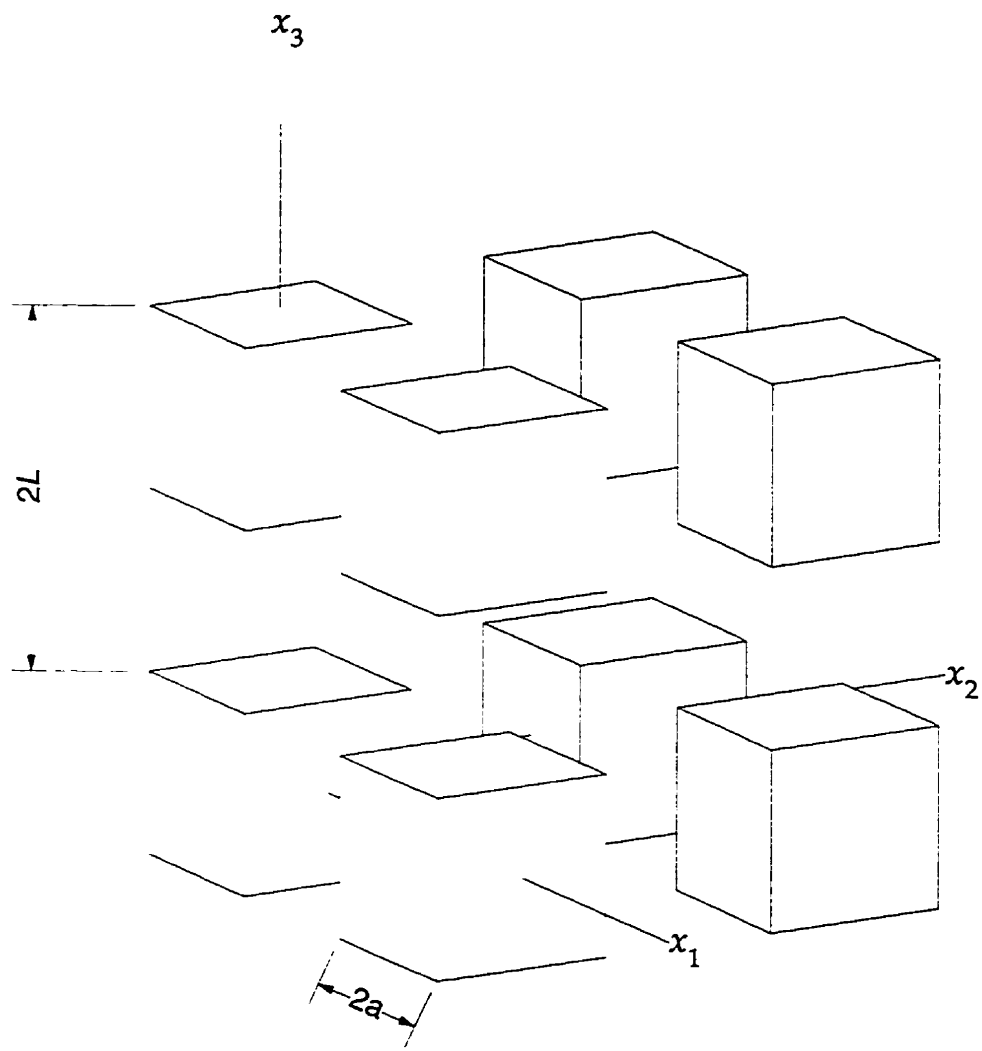

Figure 3.9: Definition of the coordinate system used for the simulation and the positions of the inclusions, showing the particle size $2a$ and the period $2L$.

where

$$\kappa = \frac{3\lambda + 2\mu}{\lambda + 2\mu}\frac{Le^*}{\pi^4}$$

λ and μ are the Lamé constants and e^* is the eigenstrain applied to the cuboidal regions. The other two displacements can be obtained by cyclic permutations of the indices and ordinates. The eigenstrain applied for this example is purely dilatational: $\varepsilon_{ij}^* = \delta_{ij} e^*$. The strains are obtained from the displacements by half the sum of the partial derivatives:

$$\varepsilon_{ij} = \frac{1}{2}\left(\frac{\partial u_i}{\partial x_j} + \frac{\partial u_j}{\partial x_i}\right), \tag{3.4}$$

and for example,

$$\varepsilon_{33}(\mathbf{x}) = \frac{8\pi}{L}\kappa \sum_{p,q,r=1}^{\infty} \frac{r \sin\left(\frac{p\pi a}{L}\right)\sin\left(\frac{q\pi a}{L}\right)\sin\left(\frac{r\pi a}{L}\right)}{pq\left(p^2+q^2+r^2\right)} \cos\left(\frac{p\pi x_1}{L}\right)\cos\left(\frac{q\pi x_2}{L}\right)\cos\left(\frac{r\pi x_3}{L}\right). \tag{3.5}$$

To proceed further, it is now necessary to define the volume fraction of the inclusions and to define the eigenstrain applied. For simplicity, a volume fraction of 12.5% is chosen. This corresponds to $a/L=1/2$ and greatly simplifies the series expansion since all even terms vanish and the odd terms are conveniently ±1. A program was written using Borland Turbo BASIC to calculate the strains at 1024 points (32x32) in the x_1–x_2 plane over the domain of (-1..+1,-1..+1) at $x_3=0$, which corresponds to one cycle of the periodic distribution. This was also performed for the strains ε_{11}, ε_{12} and ε_{31}. It is not necessary to calculate ε_{22} and ε_{23} separately, since by symmetry they are equivalent to ε_{11} and ε_{31} respectively but with the x_1 and x_2 axes interchanged.

Chapter 4
Results and Discussion

4.1 Simulation of Strain Distribution

This simulation modelled the strain distribution due to a periodic distribution of cuboidal inclusions with moduli identical to the matrix, but with a different coefficient of thermal expansion. The computer calculations of equation (3.5) and the equivalent ones for the other ε_{ij} were performed using a compressive eigenstrain of 10^{-3} and the elastics constants for aluminum. The results of the calculations were plotted as isostrain contour graphs using *Microcal Origin 4.10* with the *3–D and Contour Module* and are shown in Figures 4.1 through 4.4. All calculations were performed on the plane x_3=0 (see Figure 4.1a) except ε_{31} which vanishes on this plane, hence ε_{31} was calculated at its maximum on the x_3=0.5 plane (see Figure 4.4a). From Figures 4.1 and 4.2 it can be seen that the strain normal to the interface is discontinuous at the interface, while the strains parallel to an interface are continuous. The non-uniform strain distribution is clearly demonstrated in these figures and is reinforced by the distribution of the shear strains shown in Figures 4.3 and 4.4. With the applied strain of 10^{-3} in the inclusions, the magnitude of the strains in the matrix is clearly rather low. While for most metal matrix composites the reinforcement is much stiffer than the matrix, the modulus of the Kaowool (mullite)[55] is very close to that of the matrix and hence the strains are potentially similar to those of the experimental system. The large normal strains near the interface support the requirement of prismatic dislocation punching of interstitial discs or vacancy discs. That all

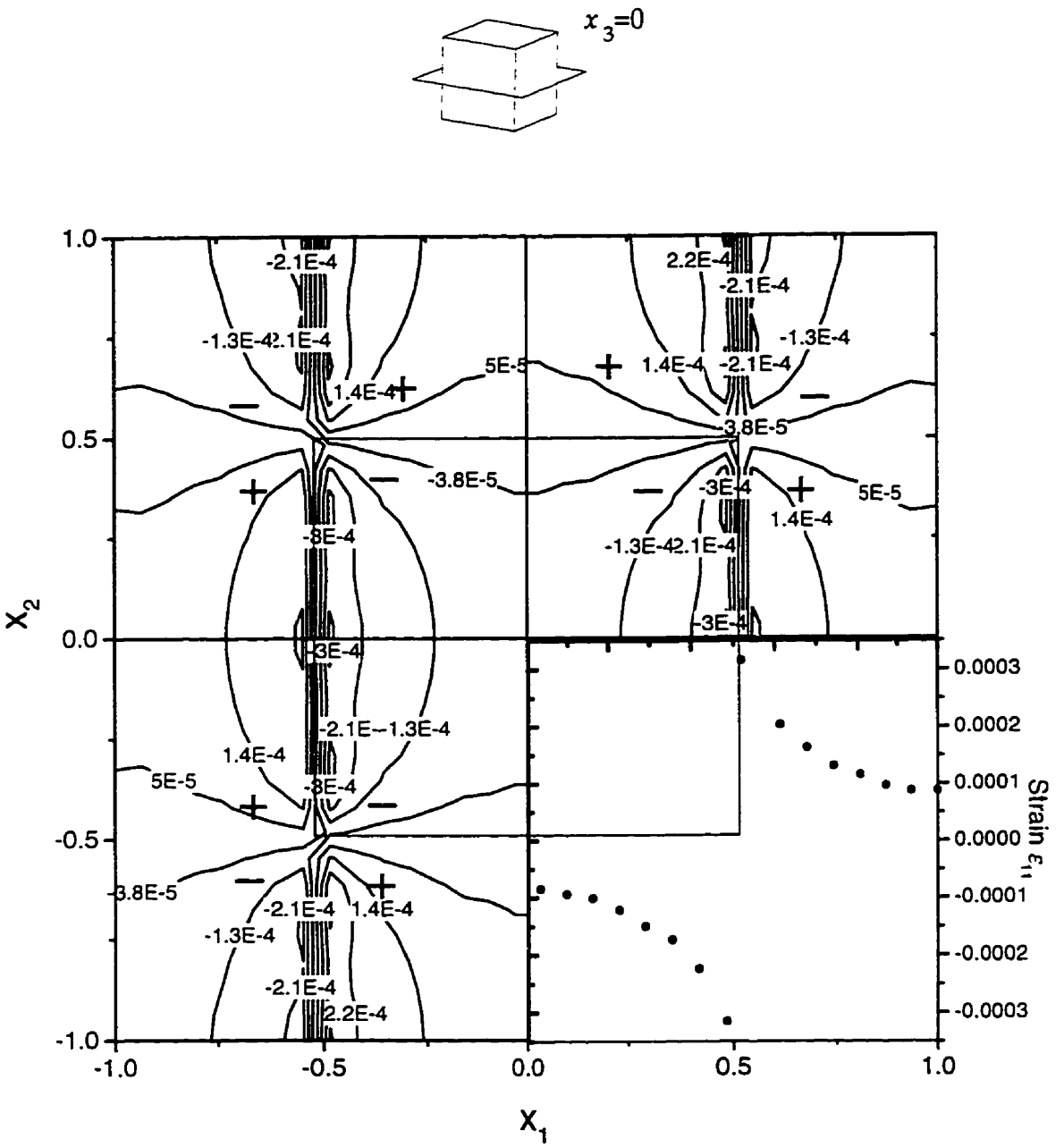

Figure 4.1: Isostrain contours of ε_{11} on the x_3=0 plane. The inset (bottom right) shows the discontinuity of ε_{11} along the x_2=0 line. Positive and negative signs show the pattern of the distribution, and the gray square defines the intersection of the inclusion and the matrix.

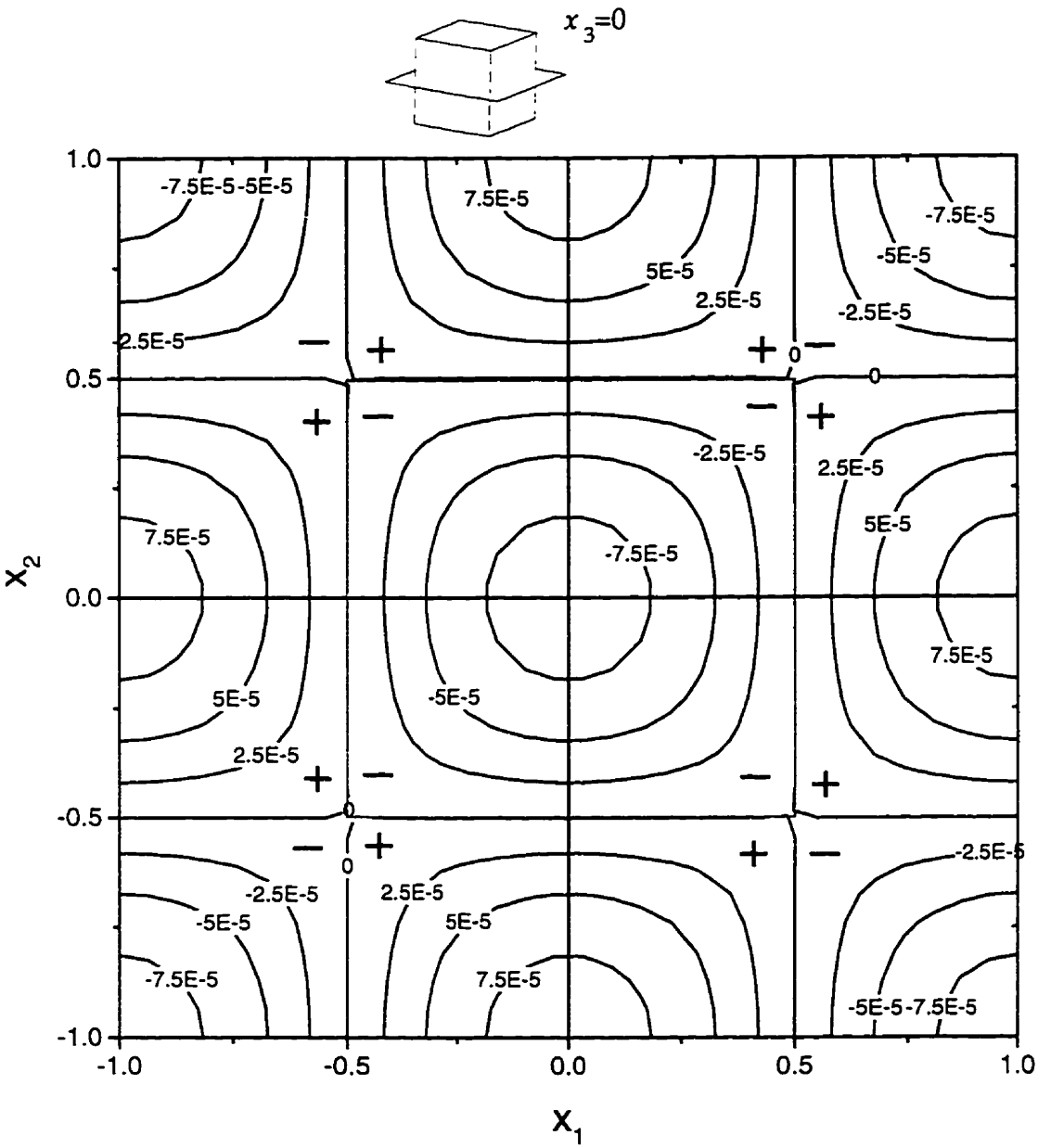

Figure 4.2: Isostrain contours of ε_{33} on the x_3=0 plane. Positive and negative signs show the pattern of the distribution, and the gray square defines the intersection of the inclusion and the matrix.

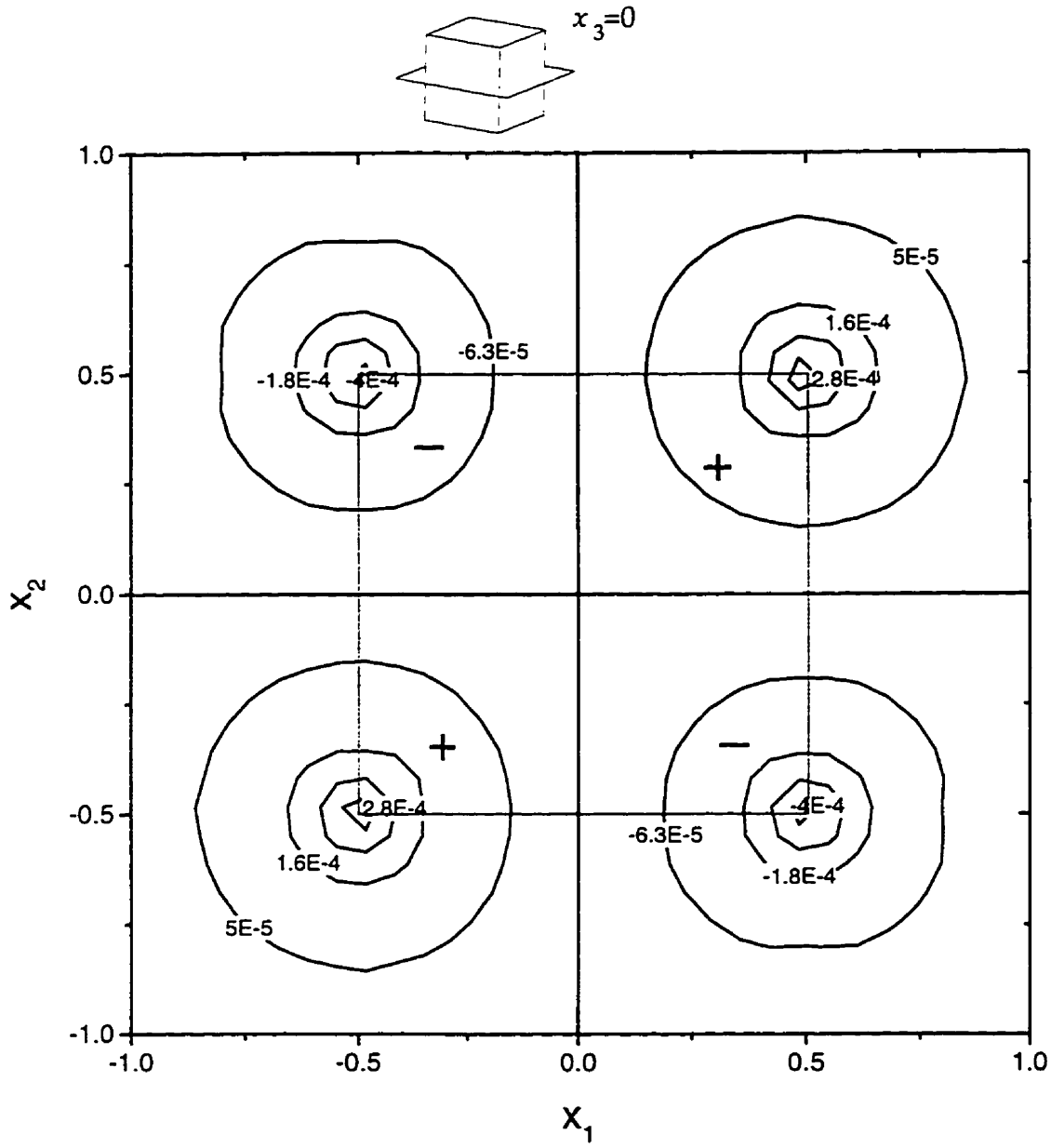

Figure 4.3: Isostrain contours of ε_{12} on the x_3=0 plane. Positive and negative signs show the pattern of the distribution, and the gray square defines the intersection of the inclusion and the matrix.

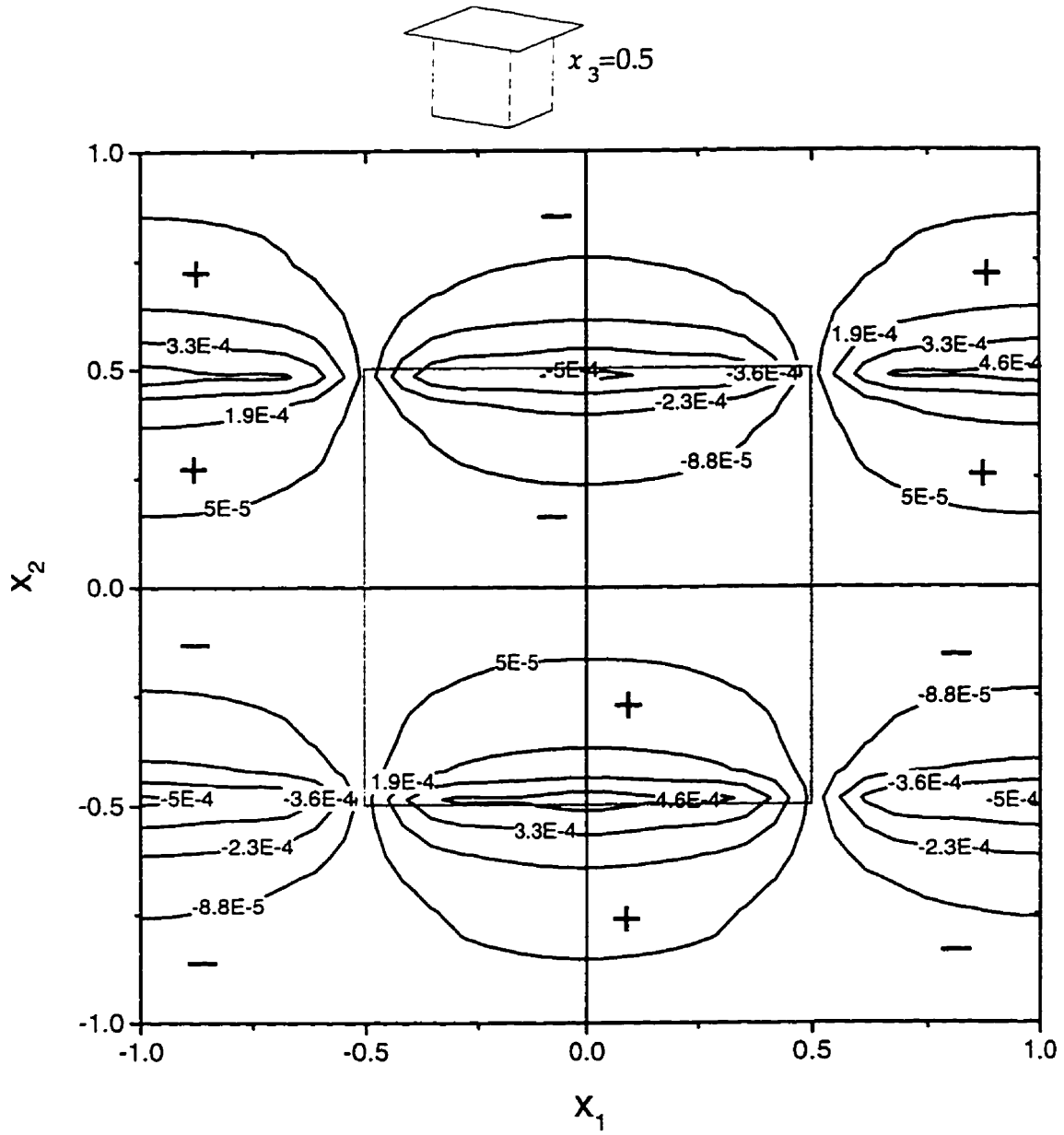

Figure 4.4: Isostrain contours of ε_{31} on the x_3=0.5 plane. Positive and negative signs show the pattern of the distribution, and the gray square defines the intersection of the inclusion and the matrix.

strains ε_{ij} approach zero at the corners of the cubes is due to the continuity requirement; that is, the strain distribution is mathematically continuous everywhere.

Considering the shear strains (Figures 4.3 and 4.4) it can be seen that they are greatest on the cube edges. A significant result obtained from this simulation is that the shear strains appear to cancel: that is the mean shear strain in the matrix volume is zero. This is an important result since it supports the assumption of a simple stress state in the derivation in **Appendix 1.** It must be noted that the presence of the shear strains would contribute to the width of the diffracted peak, but they do not affect the position of the peak. In contrast, it can be seen from Figures 4.1 and 4.2 that the normal strains in the matrix do not cancel and hence there is a net peak shift and the inhomogeneous distribution also contributes to the broadening of the peak. These observations can be confirmed by calculating analytically the expectation values of the strains in the volume of one period (and hence the total volume). The expectation value is given by

$$\langle \varepsilon_{ij} \rangle = \frac{\int_V \varepsilon_{ij} dV}{\int_V dV}. \tag{4.1}$$

The volume of the matrix in one period is defined by the domain, $-1 \le x_i < 1$ without $-0.5 \le x_i \le 0.5$. Hence the expectation values for ε_{33} and ε_{12} from equations (3.3) and (3.4) become

$$\langle \varepsilon_{33} \rangle = \frac{8\pi}{7L^4} \kappa \sum_{p,q,r=1}^{\infty} \frac{1}{p^2 q^2 \left(p^2 + q^2 + r^2\right)} \neq 0 \tag{4.2a}$$

and

$$\langle \varepsilon_{12} \rangle = \frac{8\pi}{7L^4} \kappa \sum_{p,q,r=1}^{\infty} \frac{\sin\left(\frac{p\pi a}{L}\right)\sin\left(\frac{q\pi a}{L}\right)\sin\left(\frac{r\pi a}{L}\right)}{p^2 q^2 \left(p^2 + q^2 + r^2\right)} \left\{ \begin{array}{l} \int_{-1}^{1} \sin(p\pi x_1) dx_1 \int_{-1}^{1} \sin(q\pi x_2) dx_2 \int_{-1}^{1} \cos(r\pi x_3) dx_3 - \\ \int_{-0.5}^{0.5} \sin(p\pi x_1) dx_1 \int_{-0.5}^{0.5} \sin(q\pi x_2) dx_2 \int_{-0.5}^{0.5} \cos(r\pi x_3) dx_3 \end{array} \right\}$$

$$\therefore \langle \varepsilon_{12} \rangle = 0 \tag{4.2b}$$

By symmetry, these equations are identical for the other components of the strain tensor. Equation (4.2a) shows that the unrelaxed misfit strain e^* can be estimated from the measured mean strains if there has been no plastic response. Since the experiments performed were those of rapid temperature changes, the initial strains observed after cooling may be a good estimate of this case since the diffusion necessary to form the prismatic loops is likely to be rather slow. Again since this simulation assumes that the elastic constants are homogeneous throughout the composite, the result is expected to be inaccurate.

Since equation (4.2b) proves that the net shear strain (and hence stress) is zero, the assumption of a simple stress state in the diffraction volume made in **Appendix 1** is appropriate. The presence of shear stresses in the matrix would introduce a $\sin 2\psi$ term to (A1.1) which is present in the more general equation (2.2). This would have made experimental measurements more difficult since the two tilt method would yield large errors in the calculated stresses.

The other important issue that can be examined from this model is the magnitude of the maximum stress. From Figures 4.1 and 4.3, it can be seen that the highest strains are at the interface and these are the normal strains, while the tangential strains are small. The model gives the strain exactly at the interface (0.500,0,0) as zero, hence the maximum strain can be obtained by solving for the normal strain at a small distance from the interface. Solving for the ε_{11} at (0.512,0,0) yields a strain of $\varepsilon_{11}(max)=3.5\text{x}10^{-4}$. That the distance of maximum strain is rather far from the interface is likely an artifact of the model. Considering now the mean strain calculated from equation (4.2a), a ratio of the maximum strain to the mean strain can be deduced. This gives

some insight into the x–ray measurements since some information about interface can be obtained from the bulk behaviour. Defining the strain ratio as

$$\Re_\varepsilon = \frac{\varepsilon_{max}}{\langle \varepsilon \rangle}, \tag{4.3}$$

and substituting the appropriate values, the strain ratio is

$$\Re_\varepsilon = \frac{3.50 \times 10^{-4}}{4.24 \times 10^{-5}} = 8.26.$$

This value seems reasonable and can be used to estimate the punching stress in the specimens studied experimentally. This ratio is dependent on the volume fraction of inclusions and decreases with increasing volume fraction (it must approach unity when the volume fraction of particles is 1). Since the tangential stresses are small near the interface, wheras the normal strain is large, it can be assumed that the stress state is uniaxial, which greatly simplifies the analysis presented in §4.5.

4.2 Micrographs

Figure 4.5 is an optical micrograph of the unreinforced specimen used to obtain the stress–free lattice parameter. The dendrites are clearly very large and the grain size is approximately 2mm. This is in agreement with the x-ray observations of large grain size effects.

The micrograph in Figure 4.6a is an ion image produced by focussed ion beam (FIB) scanning performed by Mr. M. Phaneuf of Fibics Inc. using the Micrion 2500 FIB. The large, light gray features are the Kaowool reinforcement and a precipitate phase can be seen. Figure 4.6b is the corresponding secondary electron image (SEI) and the fibres are now black. The micrographs were taken at room temperature and hence microstructural features present at this temperature may be different from those present at higher temperatures. The Kaowool reinforcement consists primarily of ellipsoidal fibres 2–3μm in diameter and 10–30μm in length together with occasional particulates about 20μm in size. While the FIB images seem to

indicate only one type of precipitate, the previous study showed that there were two types: a Si rich one and an intermetallic one. These precipitates are rather large and widely spaced. They are not likely therefore to contribute strongly to dislocation pinning.

Figure 4.5: Optical micrograph of unreinforced specimen, showing the large dendritic grains at 20× magnification

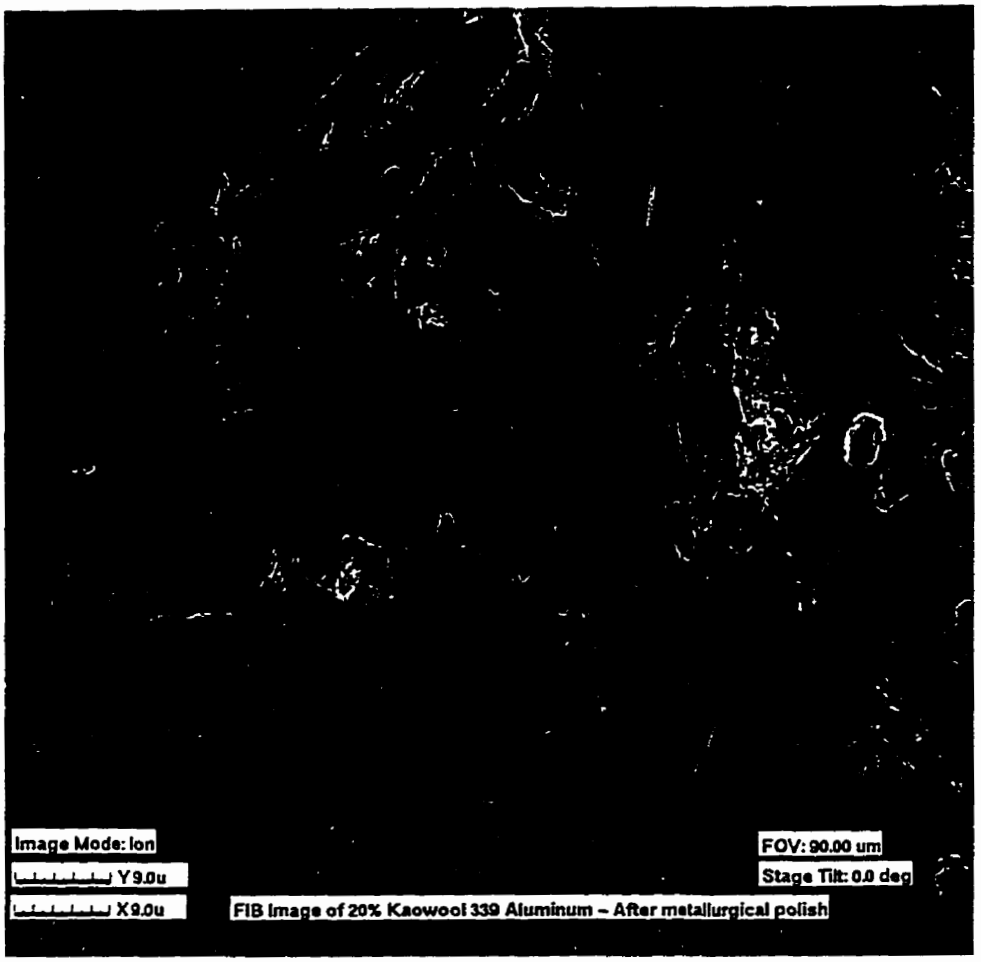

Figure 4.6a: ion image micrograph from ion scanning of the MMC specimen. The Kaowool fibres are the large light gray features. Image taken near room temperature.

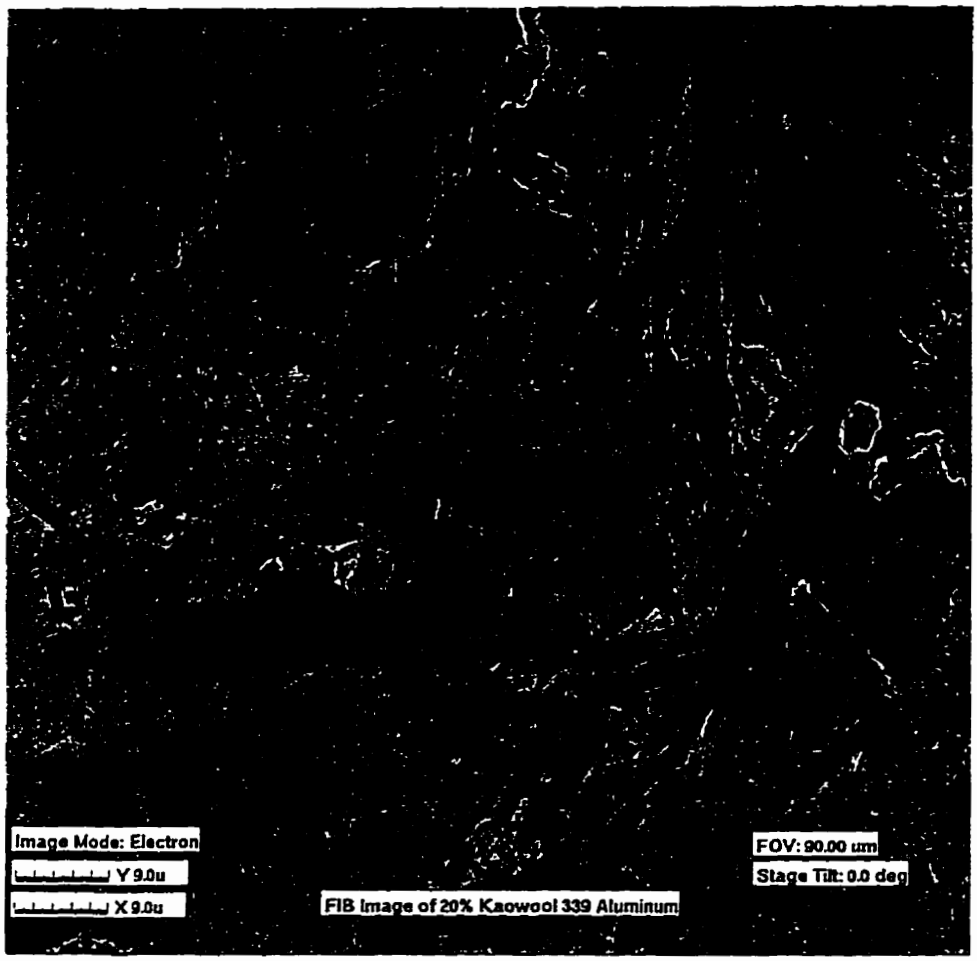

Figure 4.6b: SEI micrograph from ion scanning of the MMC specimen. The Kaowool fibres are the large black features. Image taken near room temperature.

4.3 Unstressed Lattice Parameter

As discussed in §2.1.1, the unstressed lattice parameter is very important to obtain a reliable measurement of the strain in the material. The alignment procedure previously described in §3.25 to centre a suitable grain was used to measure the lattice parameter during temperature cycling for a {311} peak. As demonstrated in §3.2.5, this reduces the errors due to an offset. The heating and cooling rates used were 5°C/min for the thermal cycling. The results of the measurements are shown in Figure 4.7. A second order polynomial was fitted by the least squares method to the data, yielding the following expression for the unstressed lattice parameter as a function of temperature:

$$a_0(T) = 4.04696 + 8.44 \times 10^{-5} T + 5.29 \times 10^{-8} T^2 \text{ Å}, \qquad (4.4)$$

where the temperature is in degrees Celsius.

The lack of hysteresis between the heating portion and cooling portion of the cycle indicates that any stresses induced by grinding and polishing had been removed by the previous cycles. The error in measured lattice parameter is primarily due to counting statistics, and is approximately the size of the data points in the figure.

4.4 Slow Cycle Data and Cool Downs

Comparison of current data with previous work by Clarke and Saimoto[17] should reveal differences if the methodology affected the determinations. The reduced data collected in this study for a slow rate temperature cycle are shown in Figure 4.8 and results from the earlier work using the identical specimen for a similar cycle are shown in Figure 4.9. The in–plane stresses ($\sigma_{\|}$) at low temperature and at 300°C agree well, but in this study larger normal stresses ($\sigma_{\perp}$) were measured. Secondly, the maximum stress observed in this study were found near 80°C and reached 80MPa. This was not observed in the previous study. This stress behaviour was also observed in other

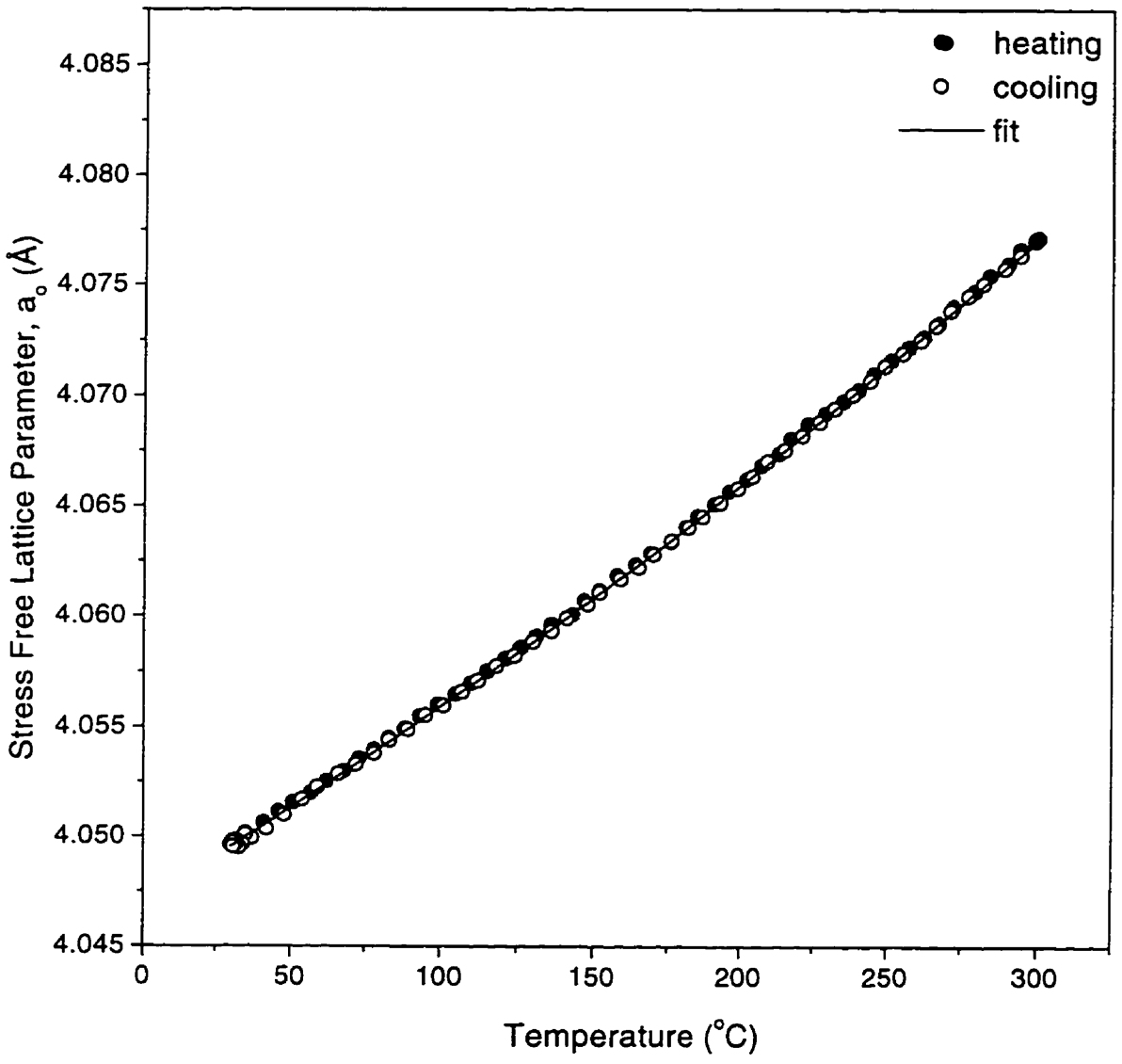

Figure 4.7: Unstressed lattice parameter vs. temperature, heating and cooling rate of 5°C/min

experiments in this study and will be discussed later. Considering again the difference in the normal stresses between the current work and the previous study, the difference can be attributed to a z–alignment error[16] in the earlier work. This is likely due to the difficulty in obtaining specimens of identical thickness and to the difficulty in alignment using the large grained unreinforced specimens. This latter effect was not recognized in the previous study, hence is a likely source of the discrepancy.

Figure 4.10 is a stress–temperature plot of a slow cycle run of the second specimen subsequently used for the rapid cycle studies. Comparing the results with the other specimen (Figure 4.8) show that the agreement is reasonable, indicating that the casting is macroscopically homogeneous. This also shows the characteristic hump in the stress on cooling near 80°C although less pronounced than for the first specimen. The cooling portions of other cycles are shown in Figure 4.11 and are similar in character. An arrest or plateau may exist in the 50–40°C range but due to the estimated ±7MPa scatter further aspects of microstructural changes should be pursued by other means. The non–existence of the 1st hump in the Clarke & Saimoto[2] study is possibly due to much longer hold times (8 to 20 hours compared to 20 min in this study) at 300°C. The heating and cooling rate for that study was also slower, 4°C/min, compared to the 5°C/min for the low temperature heating and cooling rates in this study. Experience (Clarke *et al.*[49] and Langelaan *et al.*,[50])has shown that the cooling rates below 100°C for the hot stage used in previous work was limited by the heat capacity of the stage and by 60°C the maximum cooling rate achievable was only 2°C/min. While this slower cooling rate may have an effect, the rates are already rather slow, hence the difference is most likely due to the longer hold times at 300°C. The longer anneals could completely dissolve some of the precipitates in the matrix, while the shorter anneals might only partially dissolve them. These would act as pre-existent nuclei on cooling and the precipitate size would then be larger and with a coarser

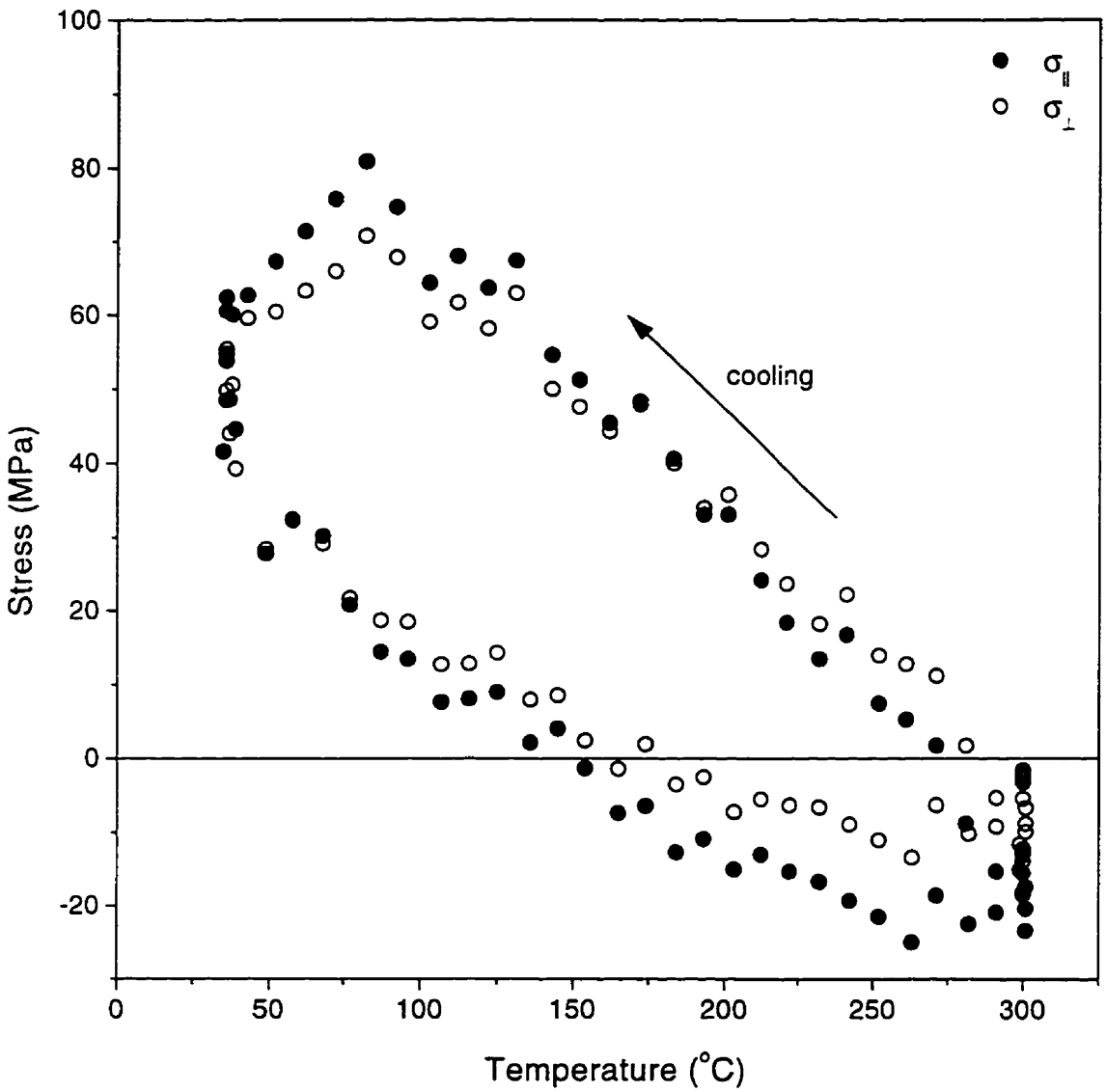

Figure 4.8: Stress vs. temperature obtained using the identical specimen used by Clarke & Saimoto.[17]

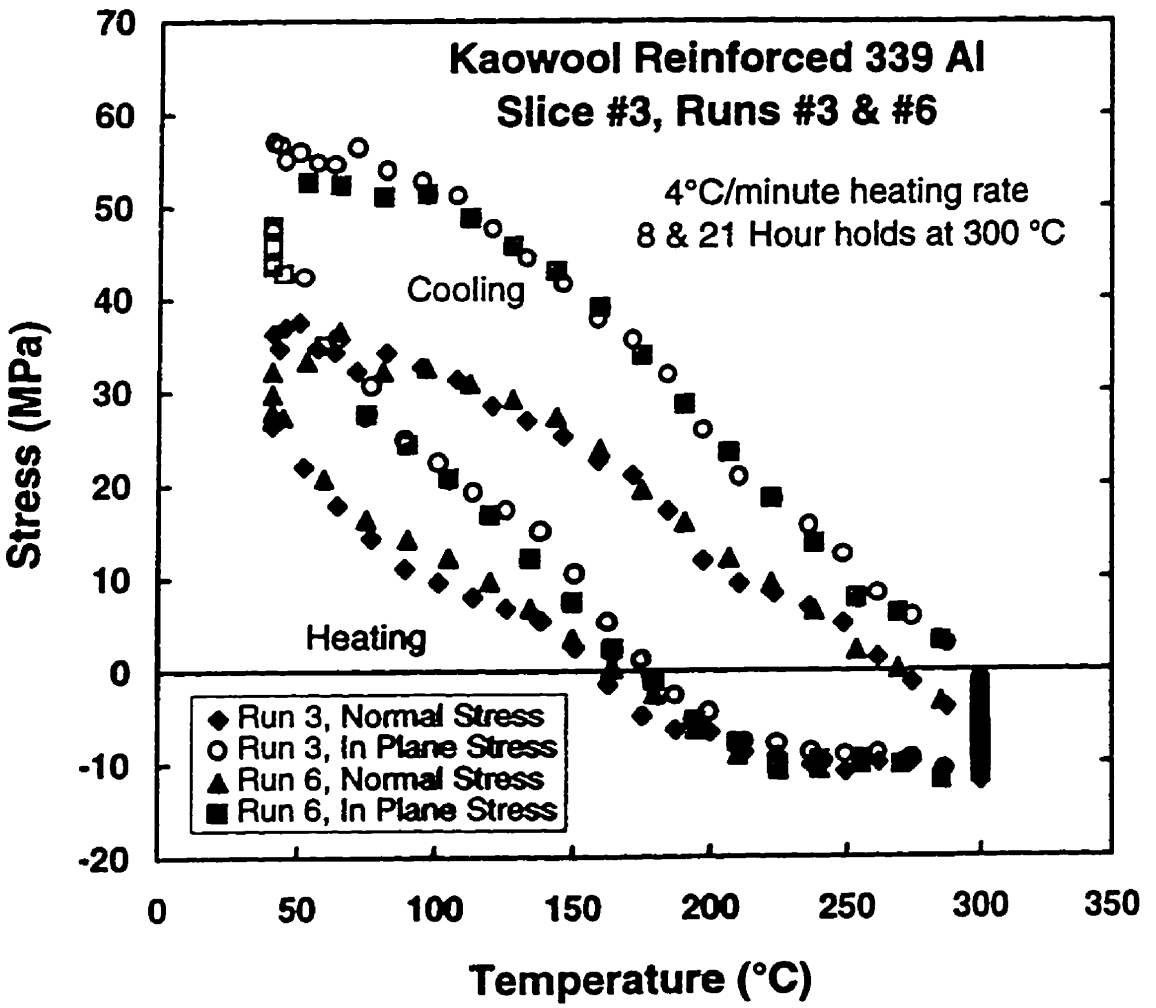

Figure 4.9: Stress vs. temperature data from Clarke & Saimoto.[17]

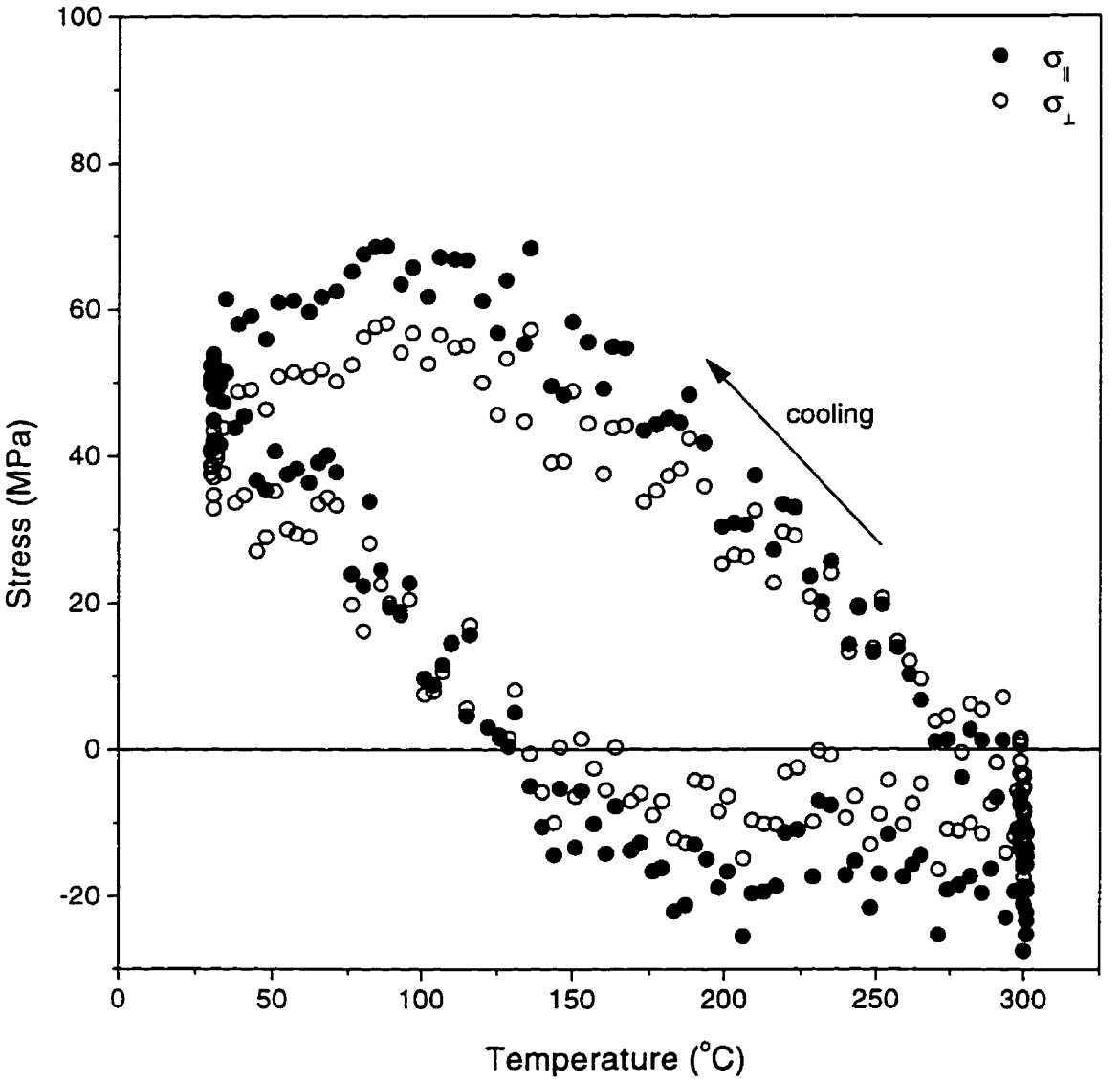

Figure 4.10: Stress vs. temperature data from run 17: 5°C/min heating and cooling rates.

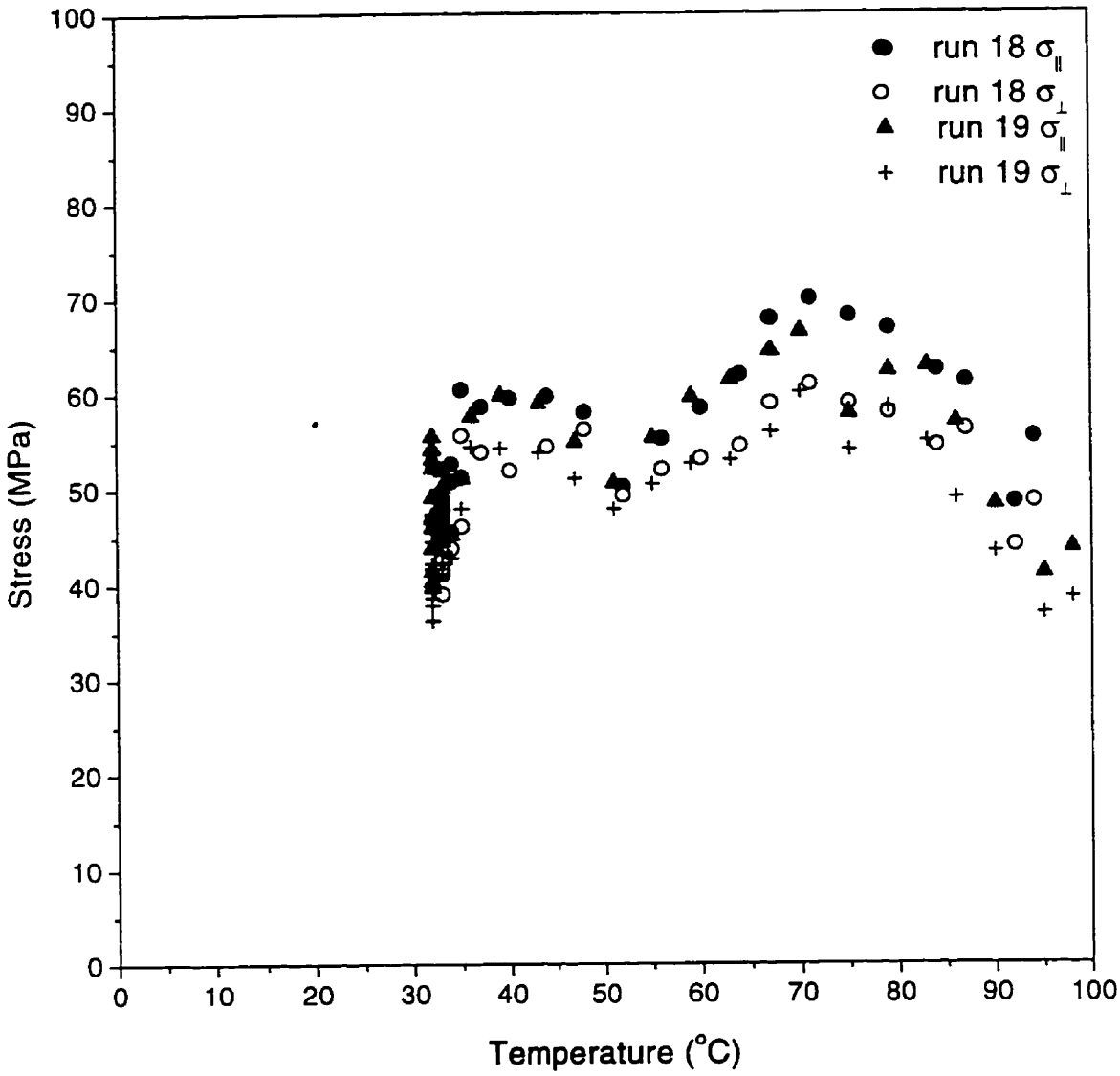

Figure 4.11: Stress vs. temperature data for cooling from 100°C to ambient temperature for runs 18 and 19

distribution. The precipitates most likely form on dislocations as coherent particles during cooling. Due to the stress field of a coherent precipitate, the formation kinetics are strongly influenced by the stress fields due to the fibres. Because of the larger spacing between the particles in the short annealing time case, dislocations could more easily break free from them. In the case of the long anneals, the precipitates would not have these heterogeneous sites and hence would likely be smaller and more finely distributed pinning the dislocations more strongly. This would result in the plateau observed in the Clarke & Saimoto data.[17] The possibility of a misalignment in their study could explain the lower stresses and hence the plateau could be as high as the 80MPa peak observed in this study.

4.5 Single ψ angle runs

These runs were performed measuring only one ψ reflection and since 2 ψ reflections are required to obtain the strain state, pairs of runs are analyzed to calculate the stress state. This technique can permit measurement pairs to be obtained for the two ψ reflections at very similar times in each cycle. Hence if there is no irreversible microstructural change from cycle to cycle, then such pairs can be treated as a constant structure measurement. The structure was predicted to be similar from cycle to cycle based on the results of the previous study. Figure 4.9, discussed above, shows the results from Clarke & Saimoto's[17] runs 3 and 6. The stresses obtained from both cycles are essentially identical, suggesting that the structure from cycle to cycle may be similar and hence two cycles run one after another may be considered as a quasi isostructure test.

The <001> fibre texture of the reinforced specimens have strong intensity at ψ_1=25.2° and ψ_2=72.5° for the (311) reflection. The odd numbered runs

measured the diffracted peak at the ψ_1 orientation, and the even numbered ones the ψ_2 reflections.

Since all the reduced data from each cycle is given in **Appendix 2**, the data presented in this section and subsequent ones show the data from the runs performed using the same technique (only one ψ reflection per run versus both reflections in each run) on the same plot for identical parts of the temperature cycle. Above each stress vs. time plot is a schematic representation of the thermal cycle with the specific region presented in the graph highlighted. The single reflection per cycle method has the virtue of speed, since ψ does not have to change between measurements, but the drawback is that the microstructure may be different between the two cycles.

4.5.1: Stabilization at 100°C on heating from ambient temperature

In each cycle, the specimen was heated from ambient temperature to 100°C and held for 20 minutes to stablize the microstructure. The early cycles, 1–8 were performed using a measurement time of 3 seconds for each peak measurement and the random errors and statistical counting errors resulted in a large scatter, hence this data is presented in **Appendix 2** only. Subsequent runs used a longer counting time of 5 seconds and this was found to yield a reduced scatter. Figure 4.12 shows the in–plane stress vs. time for the runs 9&10, 11&12 and 13&14 measured during the stabilization at 100°C after slow heating (5°C/min) from ambient temperature. The corresponding normal stresses are shown in Figure 4.13. The figures show that the stress does not relax with time. This indicates that the response to the temperature increase is purely elastic. This agrees with the linear behaviour observed in this temperature regime during the slow rate cycles which have been discussed above. The scatter in the data is due primarily to the temperature control: the very low thermal mass of the specimen and stage necessary for the rapid

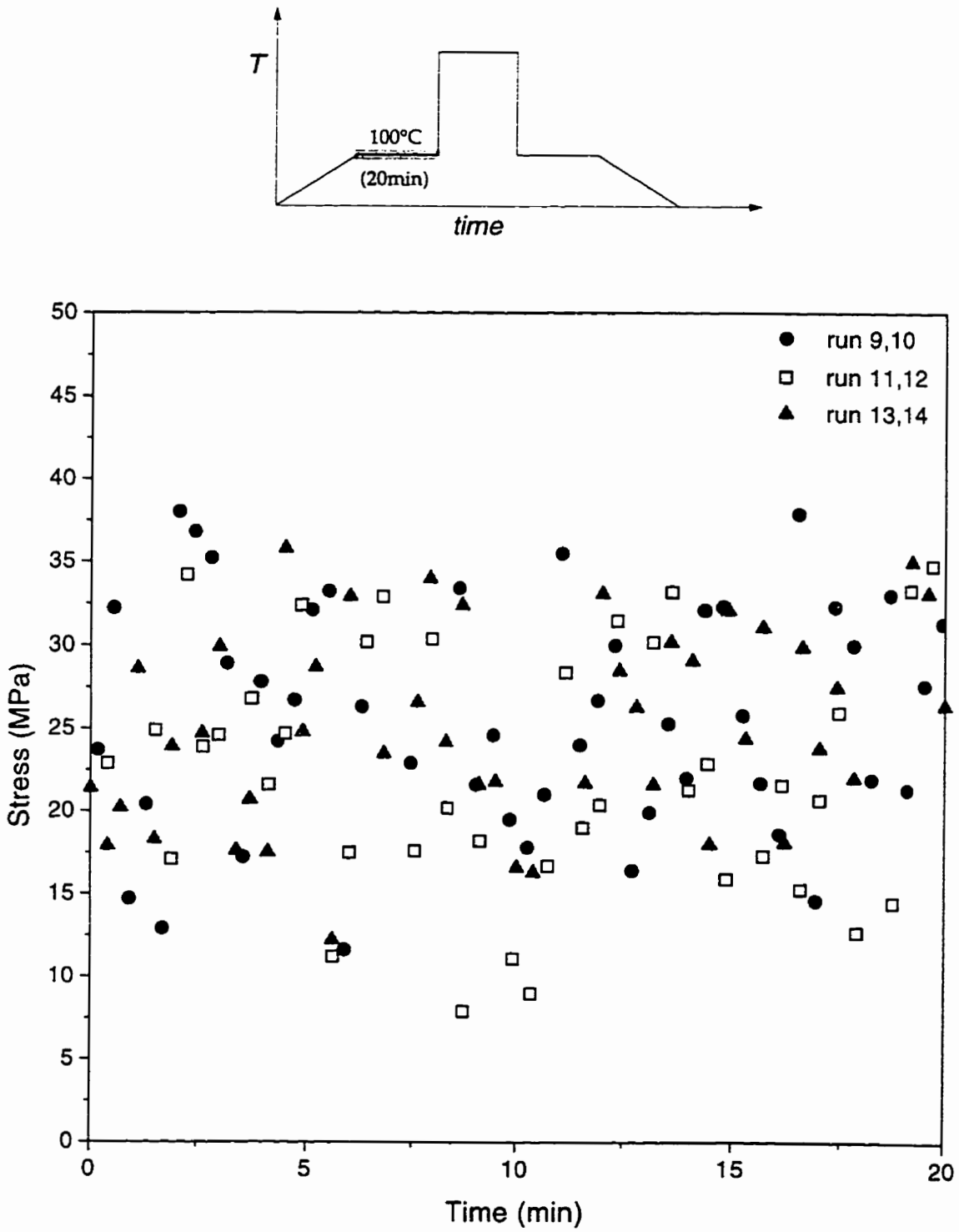

Figure 4.12: Isothermal in plane stress at 100°C on heating from ambient temperature for three symmetric sets, 9&10, 11&12 and 13&14.

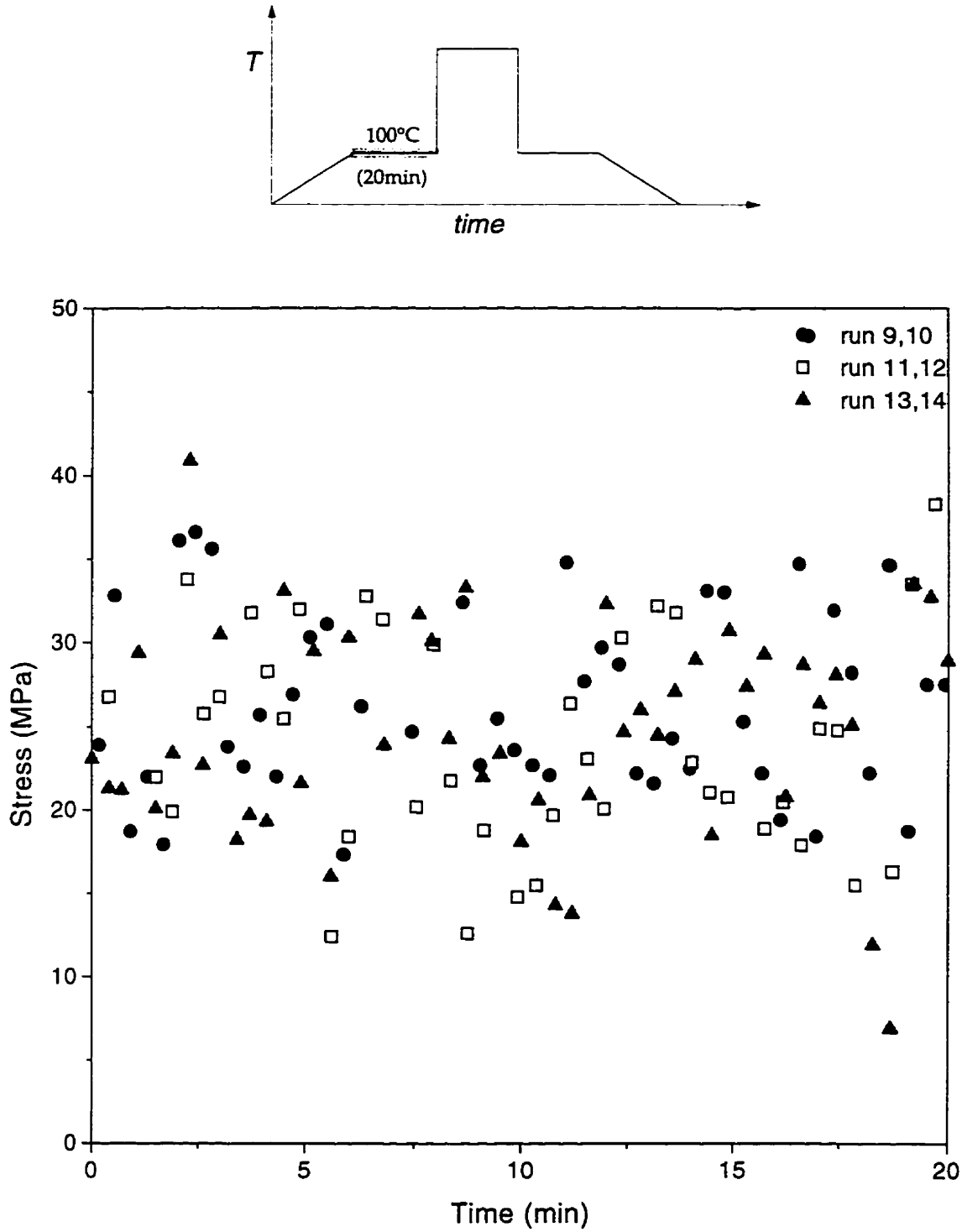

Figure 4.13: Isothermal normal stress at 100°C on heating from ambient temperature for three symmetric sets, 9&10, 11&12 and 13&14.

cycling also makes temperature control difficult since the response time is very short. The temperature controller must therefore have a very small time constant to keep fluctuations in temperature to a minimum. The temperature control was observed to be approximately ±1.5°C, and this results in an estimated error in the stress values of ±7MPa.

4.5.2: Anneal at 300°C on rapid heating from 100°C

The slow cycle measurements indicated that a stress relieving mechanism begins to operate near 200°C and that there is a stress relaxation at 300°C. No reliable strain measurements could be made during the rapid heating of the fast cycles, but stresses obtained at 300°C in the fast cycles appear to relax. The in–plane stresses deduced from the single ψ cycles 9&10, 11&12 and 13&14 are shown in Figure 4.14 and the corresponding normal stresses in Figure 4.15. From the two figures, there appears to be a relaxation of the compressive stresses as indicated by the wide band with a small, positive slope. This band was estimated by taking the data set 11&12 and performing a linear regression and attaching ±7 MPa error bars to this fit. Comparing the in–plane stresses with the normal ones, it can be seen that the normal stresses are about 65% of the in–plane stresses. This observation in itself indicates that a shear stress $(\sigma_{\parallel}-\sigma_{\perp})/2$ exists, but is not the driving force for the relaxation. From the simulation discussed in **§4.1**, the stress state near an interface was shown to be nearly uniaxial and that this stress is greater than the mean stress obtained from the x–ray data. Hence rather than estimating the shear stress from the difference between the in–plane and normal stresses, the shear stress should be estimated assuming a uniaxial stress whose magnitude is the mean stress scaled by the ratio defined in equation (4.3). Since the volume fraction of the reinforcement phase is greater in this system and due to the different morphology, the ratio is difficult to estimate. An 'order of magnitude' estimate of the shear stress should be obtainable however using the value of

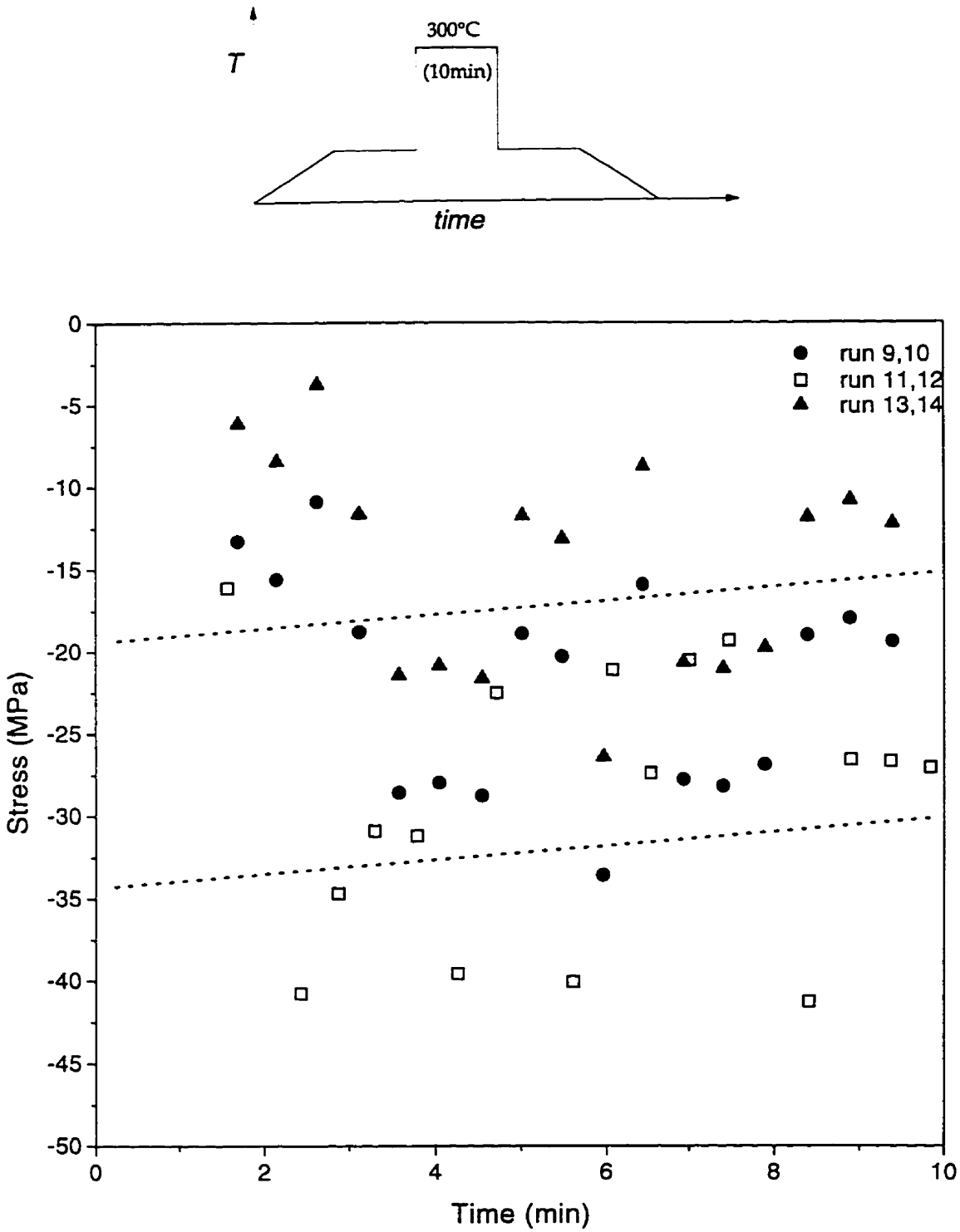

Figure 4.14: Isothermal in-plane stress at 300°C on rapid heating from 100°C for three symmetric sets, 9&10, 11&12 and 13&14. The dashed lines indicate the upper and lower bounds of the relaxation trend.

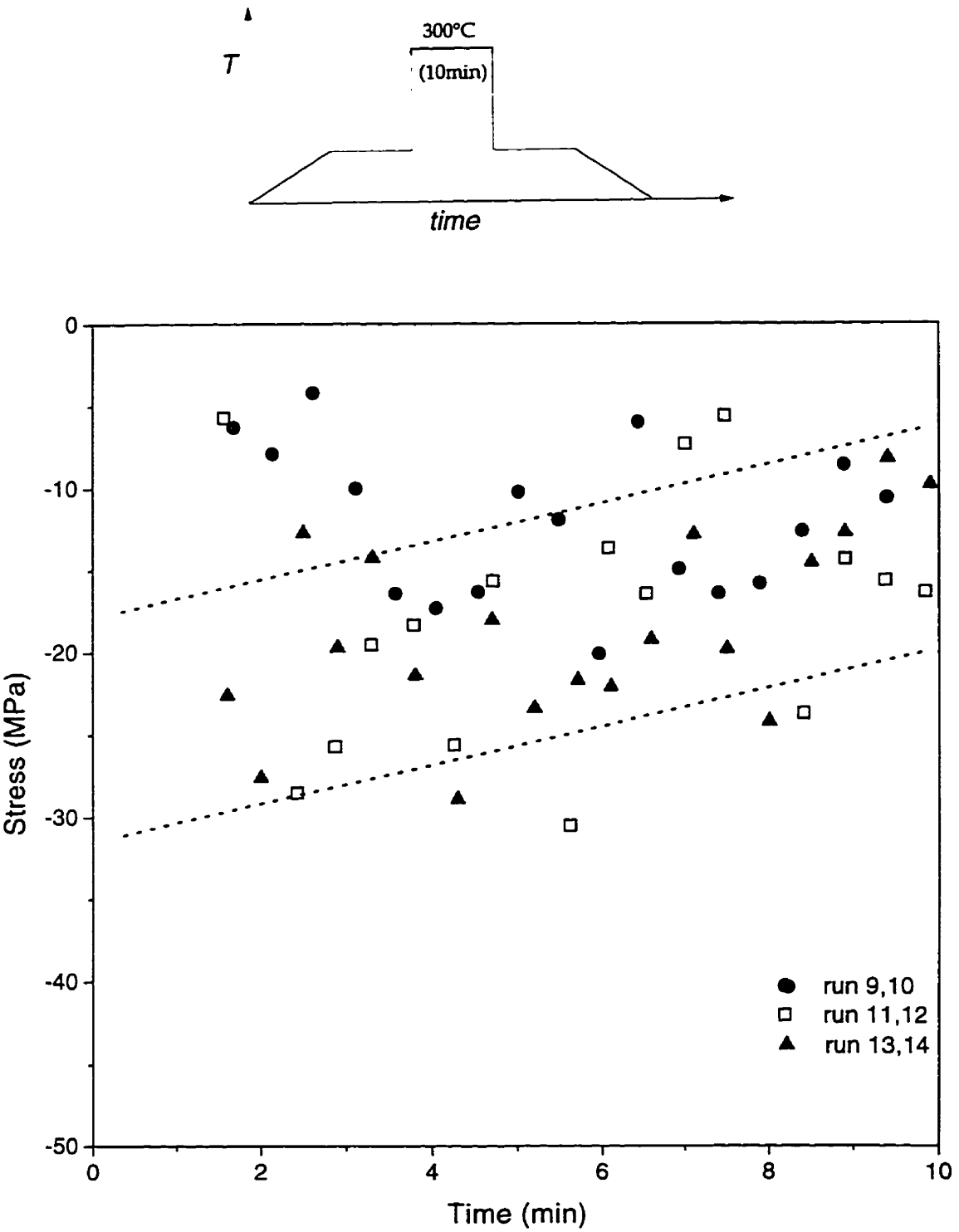

Figure 4.15: Isothermal normal stress at 300°C on rapid heating from 100°C for three symmetric sets, 9&10, 11&12 and 13&14. The dashed lines indicate the upper and lower bounds of the relaxation trend.

the strain ratio calculated in §4.1. A 'normalized' shear stress (τ/μ) is thus estimated to be ~10^{-3}. Examining the Frost–Ashby deformation map[56] for pure Al, reproduced in Figure 4.16, it can be seen that the predicted strain rate is approximately 10^{-1} s^{-1}. A strain rate near the interface can be estimated by scaling the mean strain rate observed by the same strain ratio, $\Re_\varepsilon$. The strain rate was obtained by fitting a linear curve through the in–plane stress data from cycles 13 & 14 and is ~10^{-5} s^{-1}. This indicates that the alloying additions greatly improve the creep resistance.

The relaxation of these stresses must be achieved by dislocation generation and motion. While dislocation glide can only be induced by shear stresses, the stress state in the matrix also includes a hydrostatic component which must also be relaxed. This can also be achieved by a dislocation mechanism: climb of edge dislocations. Edge dislocations have a hydrostatic component to the their stress field, which changes sign across the slip plane. While the net hydrostatic stress field due to a single edge in an infinite matrix must integrate to zero, the stress field of a dipole or prismatic loop may have a net tensile or net compressive stress field around it. The sign of the field is dependent on the character of the dipole or prismatic loop, that is whether the loop or dipole bounds an interstitial disc or a vacancy disc. Figure 4.17 shows schematically the stress field due to an edge dislocation and the configurations predicted for a matrix in hydrostatic compression (present at 300°C) and for a matrix in hydrostatic tension (at low temperatures).

4.5.3: Stress development at 100°C after quenching from 300°C

Quenching the specimen from 300°C to 100°C in the required time of less than 1 minute was found to occur without a forced cooling technique. As mentioned earlier, the temperature control was found to be underdamped and on some runs, an overshoot of no more than 2°C was observed which recovered in 5 to 10 seconds. The in–plane stresses obtained from 9&10, 11&12 and 13&14 are plotted in Figure 4.18 and the corresponding normal stresses in

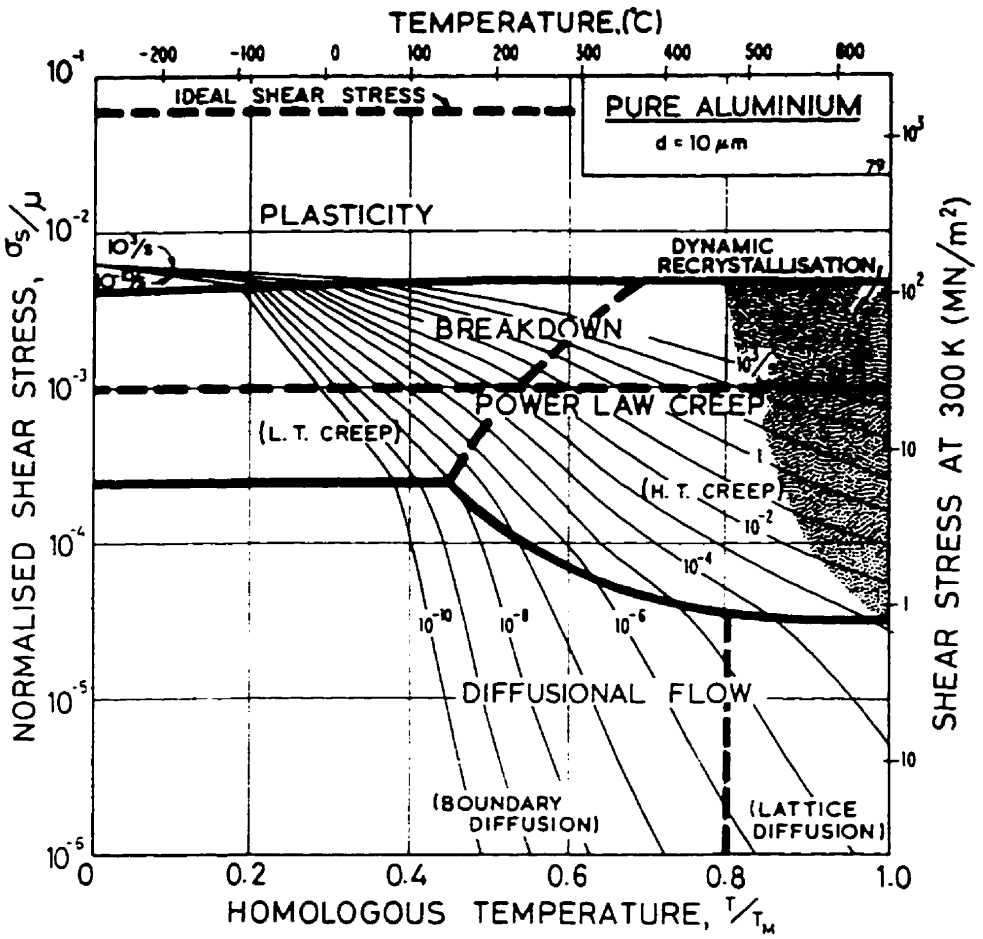

Figure 4.16: Frost–Ashby Deformation–Mechanism map for pure aluminum with a 10μm grain size. After Frost & Ashby[56]

a

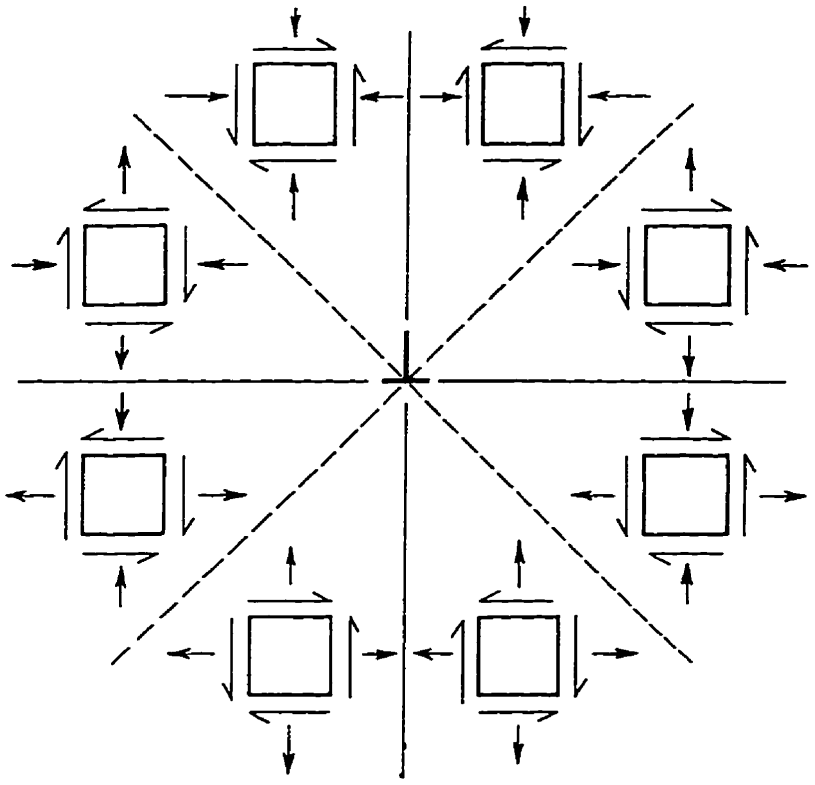

b

Predicted configuration at 300°C,
increased volume of tensile stress field

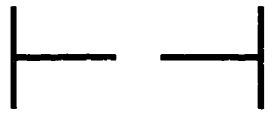

Predicted configuration at 100°C,
increased volume of compressive stress field

Figure 4.17: (**a**) schematic representation of the stress field surrounding an edge dislocation, after Hirth & Lothe,[57] and (**b**) the predicted dislocation dipole and prismatic loop configurations at 100°C and 300°C.

Figure 4.19. For these cycles, relaxations are not readily apparent and can be attributed to two possibilities: first that the relaxation mechanism is accomodated during the quench; and the second is that the apparent lack of a relaxation is an artifact of the measurement technique. The mean plastic strain rate during cooling can be estimated by calculating the misfit strain ($\Delta\alpha\Delta T$) and dividing it by the cooling time. The mean strain rate is therefore estimated to be $\dot{\varepsilon} = 5 \times 10^{-5} s^{-1}$. This is clearly sufficiently slow for dislocation glide and climb to occur. The scatter present in the data is again primarily due to the difficulty in controlling the temperature. If the lack of a relaxation is an artifact of the measurement technique, that is the assumption that the microstructure is constant from cycle to cycle is not valid, then the slower technique of alternately measuring the peak position for both ψ reflections may reveal a different behaviour. To examine this, subsequent runs (runs 15–19) were performed using this second technique.

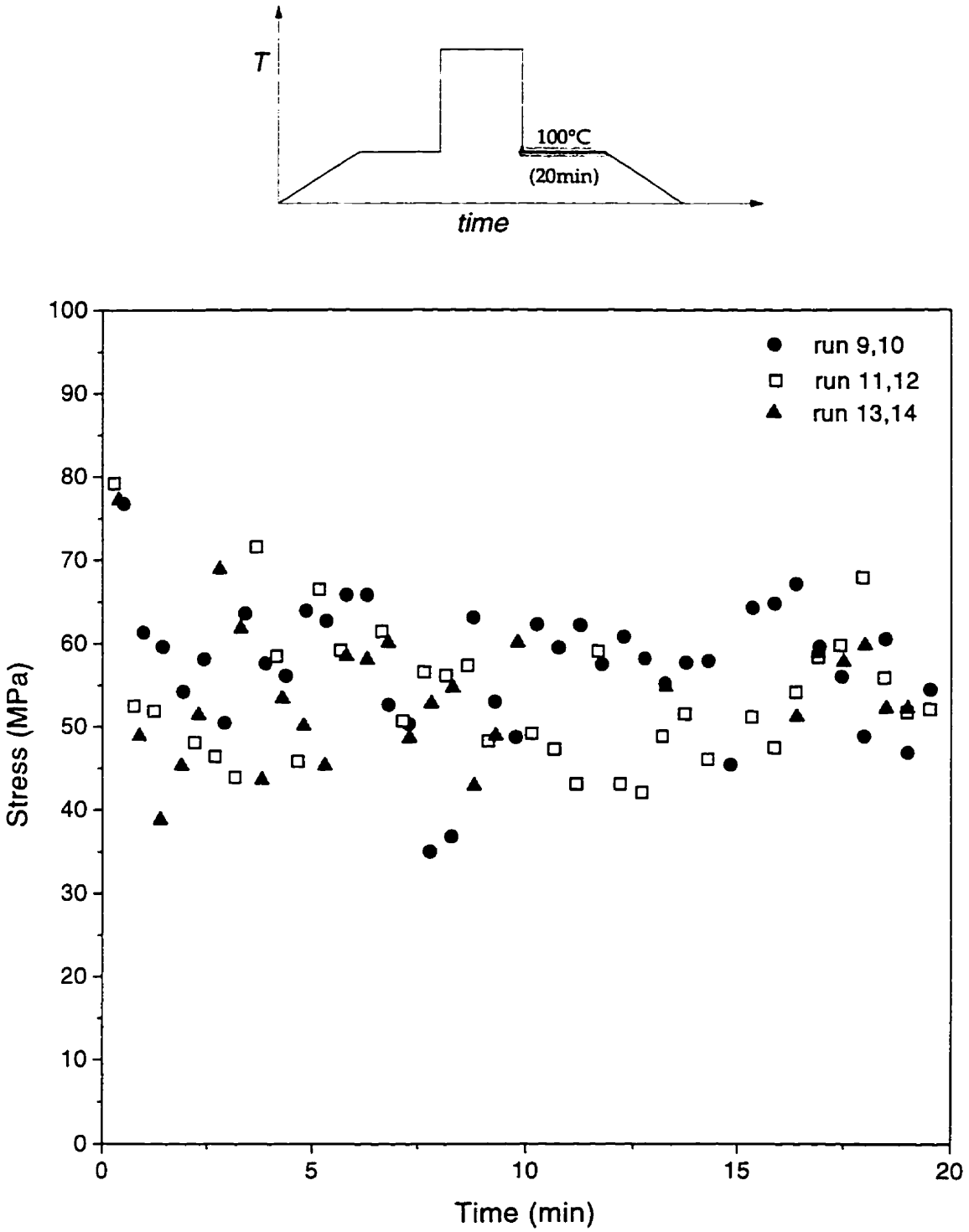

Figure 4.18: Isothermal in plane stress at 100°C on rapid cooling from 300°C for three symmetric sets, 9&10, 11&12 and 13&14.

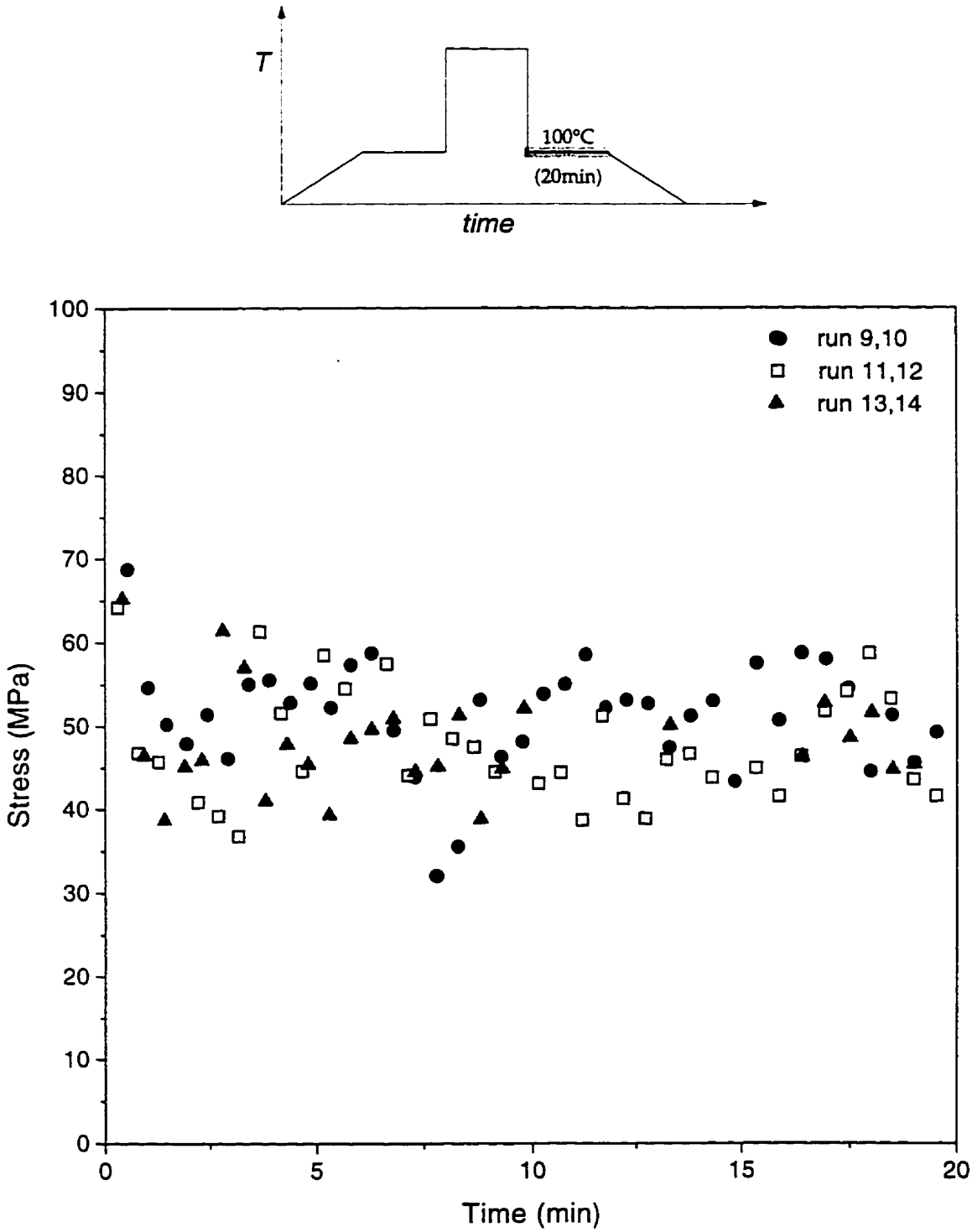

Figure 4.19: Isothermal normal stress at 100°C on rapid cooling from 300°C for three symmetric sets, 9&10, 11&12 and 13&14.

4.6 Double ψ angle runs 15 and 16

To obtain the quasi–isostructure pairs of ψ reflections, the complementary peak positions measured immediately before and after any given data point was averaged to estimate the value that would be obtained by a true isostructure measurement.

The temperature cycles in these runs were not the single fast cycles performed in the earlier cycles, but instead multiple cycles between 100°C and 300°C were performed to examine the behaviour without the plastic behaviour observed at low temperature (below 100°C) in the earlier runs. Runs 15 and 16 were both performed with two rapid cycles and runs 18 and 19 (discussed below in §4.7) examined the residual stress behaviour before and after 10 rapid cycles with very short hold times: 3 minutes at 300°C and 8 minutes at 100°C. In addition to the dynamic behaviour of the residual stresses at these temperatures, the behaviour of the stresses during heating and cooling would be of interest. The previous tests were unable to gain reliable information due to the difficulty in matching times and temperatures during the rapid heating and cooling. Hence for runs 15 and 16, the heating and cooling steps were interrupted for 3 minutes at 200°C to estimate the magnitude of the hysteresis between the heating and cooling. Again however, reliable data was difficult to achieve and hence is not discussed in this section.

4.6.1: Stabilization at 100°C on heating from ambient temperature

Identically to the runs described above, the microstructure was stabilized at 100°C on heating from ambient temperature. The stresses for runs 15 and 16 are plotted in Figure 4.20. While the data from run 16 are in agreement with the elastic decrease in stress observed in this region in the continuous slow rate runs discussed above, the stresses in run 15 decrease with time. This

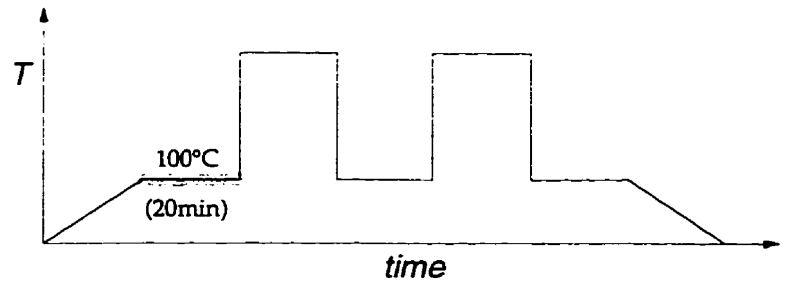

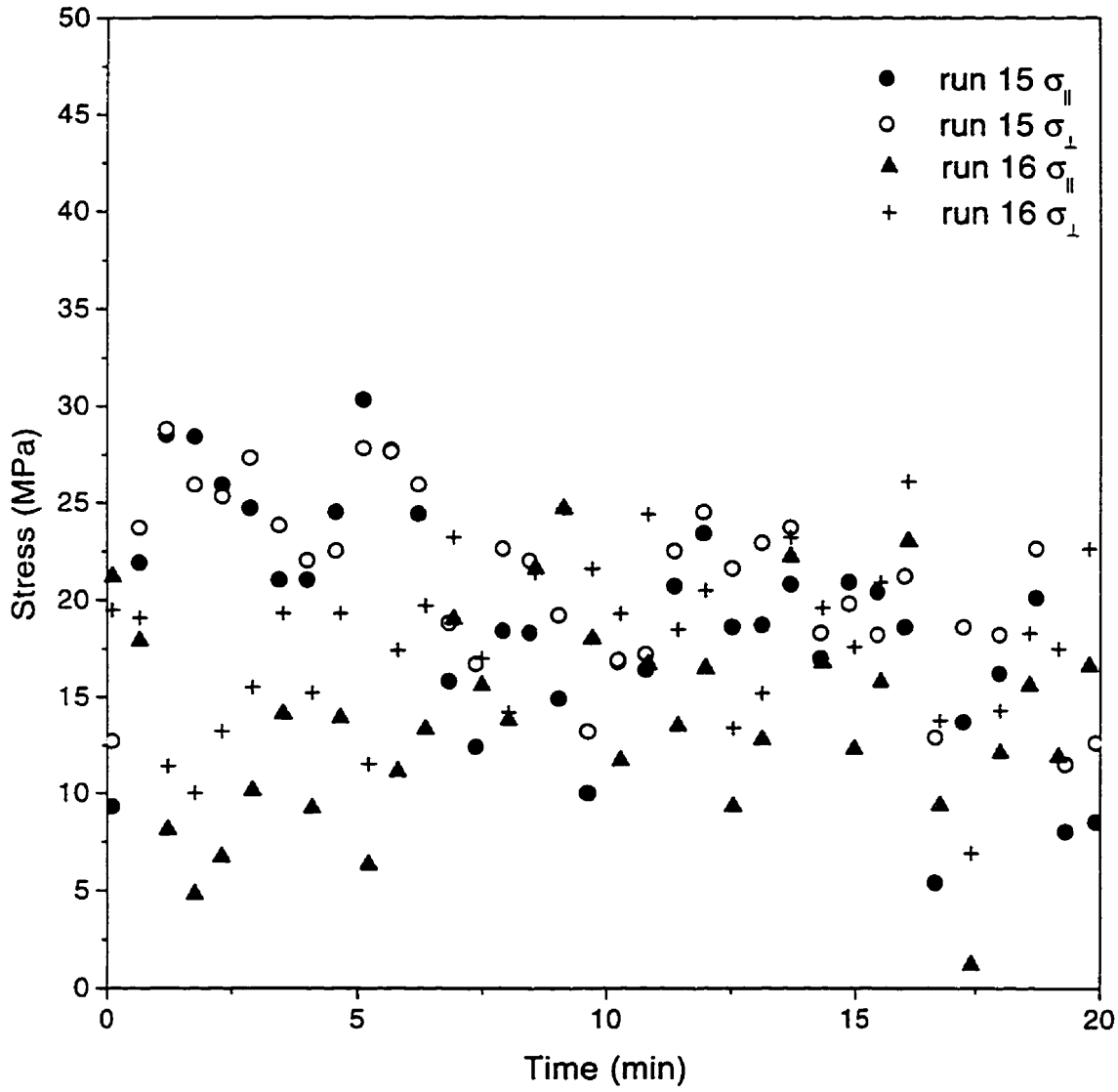

Figure 4.20: Isothermal in plane and normal stress at 100°C on slow heating from ambient temperature for runs 15 & 16.

anomalous behaviour is most likely an experimental artifact due perhaps to the difficulty in finely controlling the temperature. The other runs (9–14 discussed above and 18 & 19 discussed below) all show the elastic behaviour of a constant stress with time.

4.6.2: Anneal at 300°C on rapid heating from 100°C

To examine the residual stress behaviour at 300°C in sufficient detail with the slower data collection rate imposed by the double ψ method, the annealing time was increased from the 10 minutes used in the earlier runs to 20 minutes. The in–plane and normal stresses for runs 15 and 16 at 300°C after the stabilization at 100°C are shown in Figure 4.21. The run 16 data decreases with time is similar to the behaviour observed in the earlier cycles. The run 15 data however, seems to be constant with time and shows more scatter than run 16 does. The run 16 data can be analyzed following the same method used for the 13&14 pair of runs. From the slope of the in–plane stress vs. time curve, and the strain ratio derived in §4.1, the strain rate is ~10^{-6} s^{-1} for a 'normalized' shear stress ~10^{-3}. Again this indicates that the alloying additions improve the creep resistance.

4.6.3: Stress development at 100°C after quenching from 1st 300°C

Considering now the residual stress behaviour at 100°C after the quench from 300°C, the stresses in runs 15 and 16 after the the first anneal at 300°C (discussed in the previous section) are now examined. The stresses at this point in the cycles for both runs are plotted in Figure 4.22. In both there is a distinct initial relaxation which was not observed in the earlier runs (9–14). The long time changes, using a linear regression with ±7 MPa indicate a negative slope as expected. The sudden appearance of this can be explained by three general possibilities: firstly that the relaxations observed are due to the development of 'damage' in the matrix which strongly pins dislocations; and the second is that the single ψ, two run technique could not resolve the relaxation due to a possible

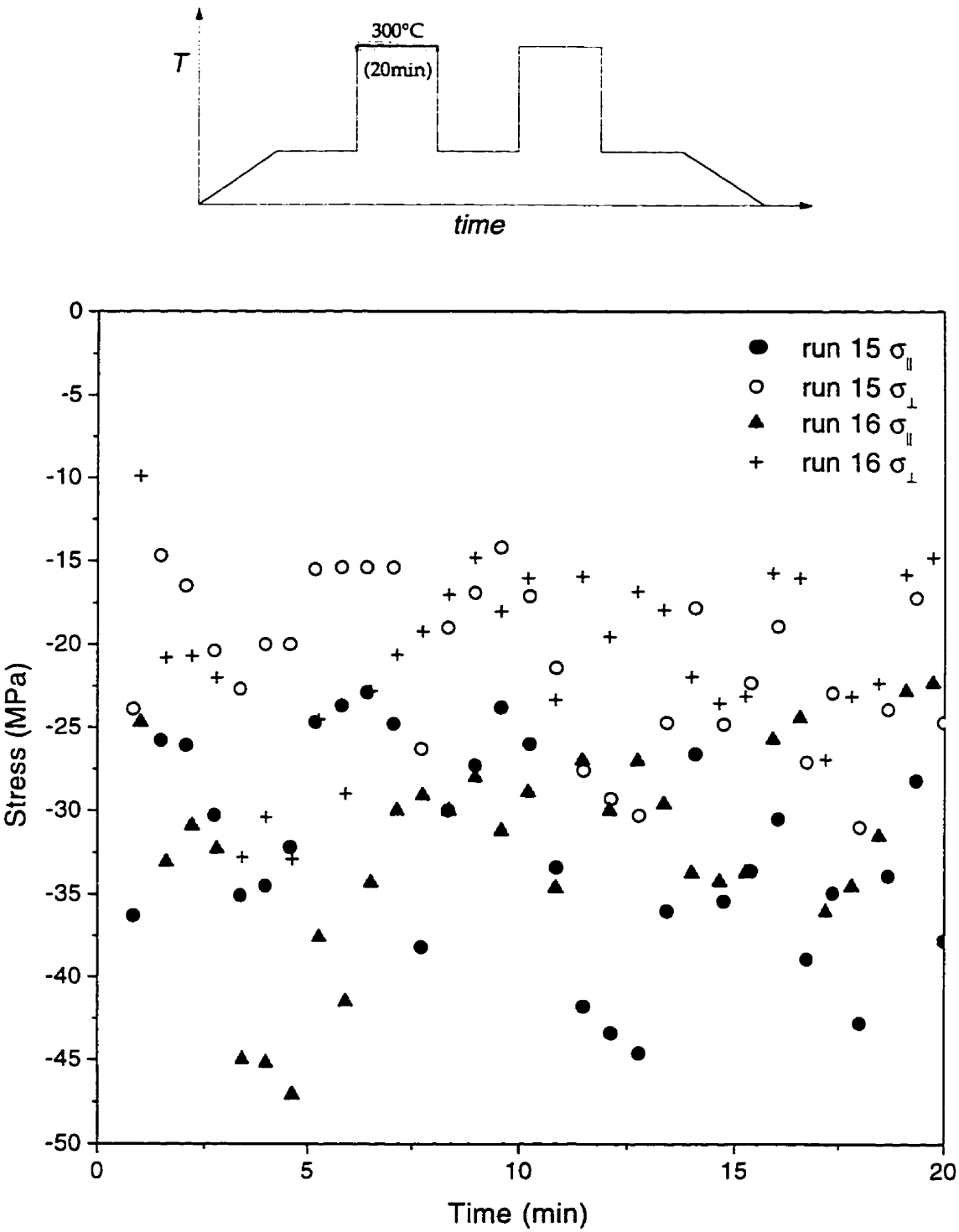

Figure 4.21: Isothermal in plane and normal stress at 300°C on rapid heating from 100°C for runs 15 & 16.

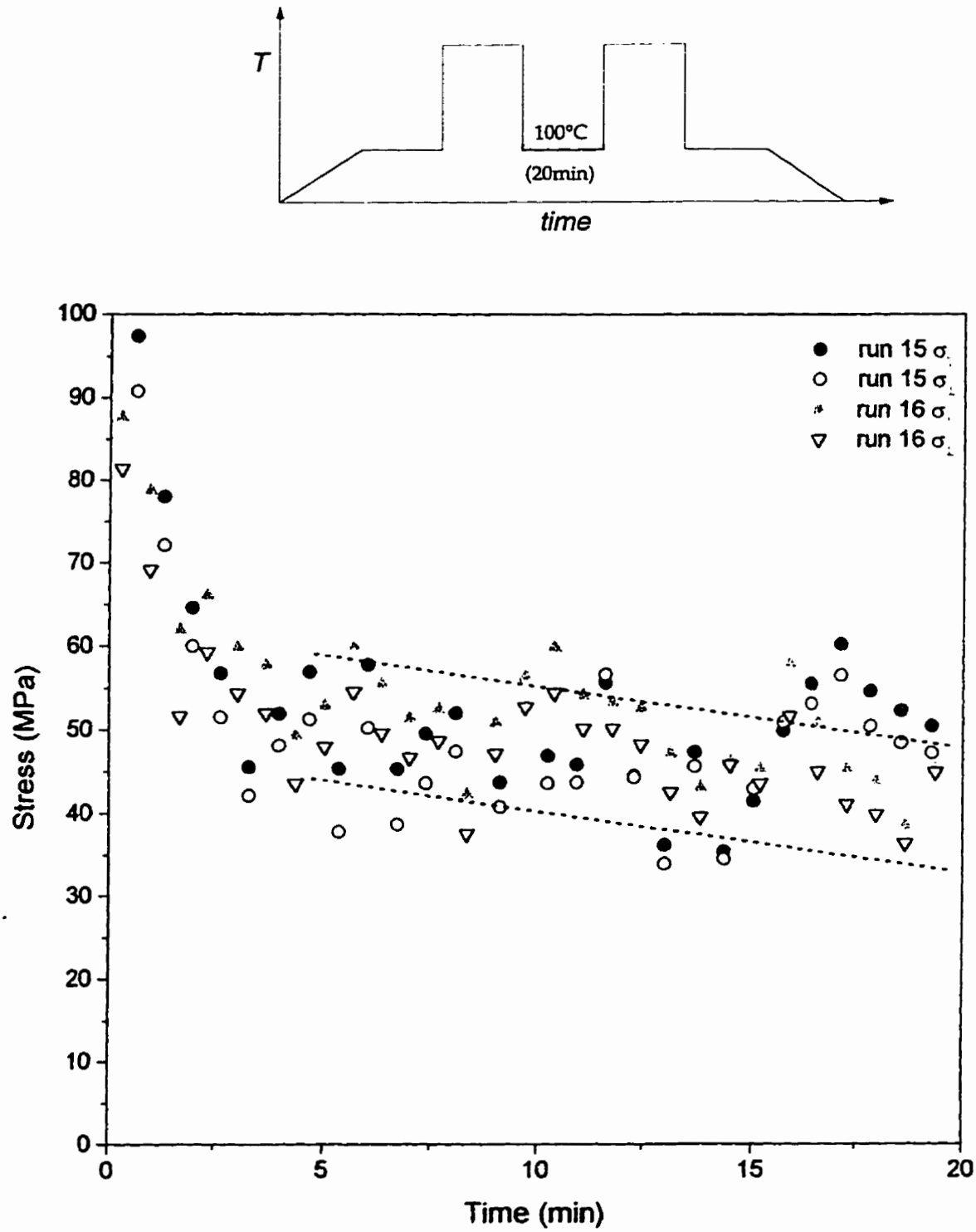

Figure 4.22: Isothermal in-plane and normal stress at 100°C on quenching from 300°C for runs 15 & 16.

difference in structure between each run. The third possibility is that interrupting the quench at 200°C for the three minutes resulted in a different structure and hence the different behaviour. As will be discussed in §4.7, similar behaviour was observed in run 19 which did not have the interruption in the heating and cooling at 200°C and hence this third notion is an unlikely cause. Considering therefore only the first two, these are two limits and the observed behaviour is likely a combination of both effects.

4.6.4: Anneal at 2nd 300°C on rapid heating from 100°C

The specimen was rapidly reheated to 300°C at the end of the 20 minute relaxation previously discussed for both runs 15 and 16. The stresses obtained for the second rapid cycle in runs 15 and 16 are plotted in Figure 4.23 and show similar behaviour to the first ones, but the stresses for run 16 are about 5MPa higher. While this is within the estimated error, the difference is consistent and therefore possibly true. If this is true then it may suggest that the rapid cycling also influences the structure at high temperatures. That is, the microstructure is becoming more resilient to the stress state.

4.6.5: Stress development at 100°C after quenching from 2nd 300°C

The residual stresses after quenching from the second 300°C anneal (with the interruption at 200°C) are shown in Figure 4.24 and again show similar behaviour to the data presented in Figure 4.22. Undulations in stress with time are observed whose magnitudes exceed the estimated error in stress values in both cases and while these are likely due to temperature fluctuations, a microstructural change could be responsible. Such a change could be the formation of coherent precipitates which produce a hydrostatic tensile stress field. The formation of these could be delayed due to the large hydrostatic stress field already present and would only grow when the stress field has been reduced. The increase in stress observed then is due to the

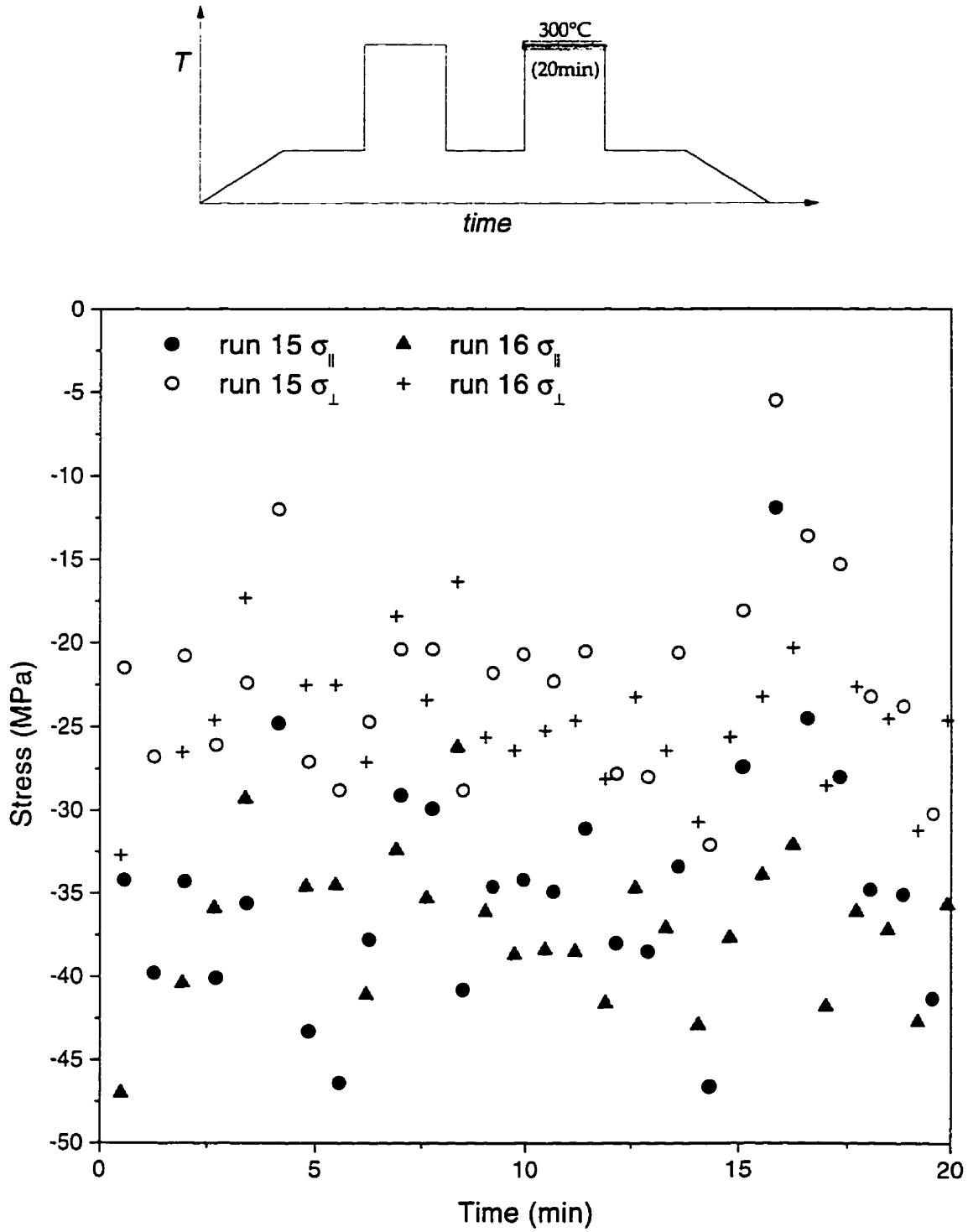

Figure 4.23: Isothermal in plane and normal stress at 300°C on rapid heating from 100°C for the second cycle of runs 15 & 16.

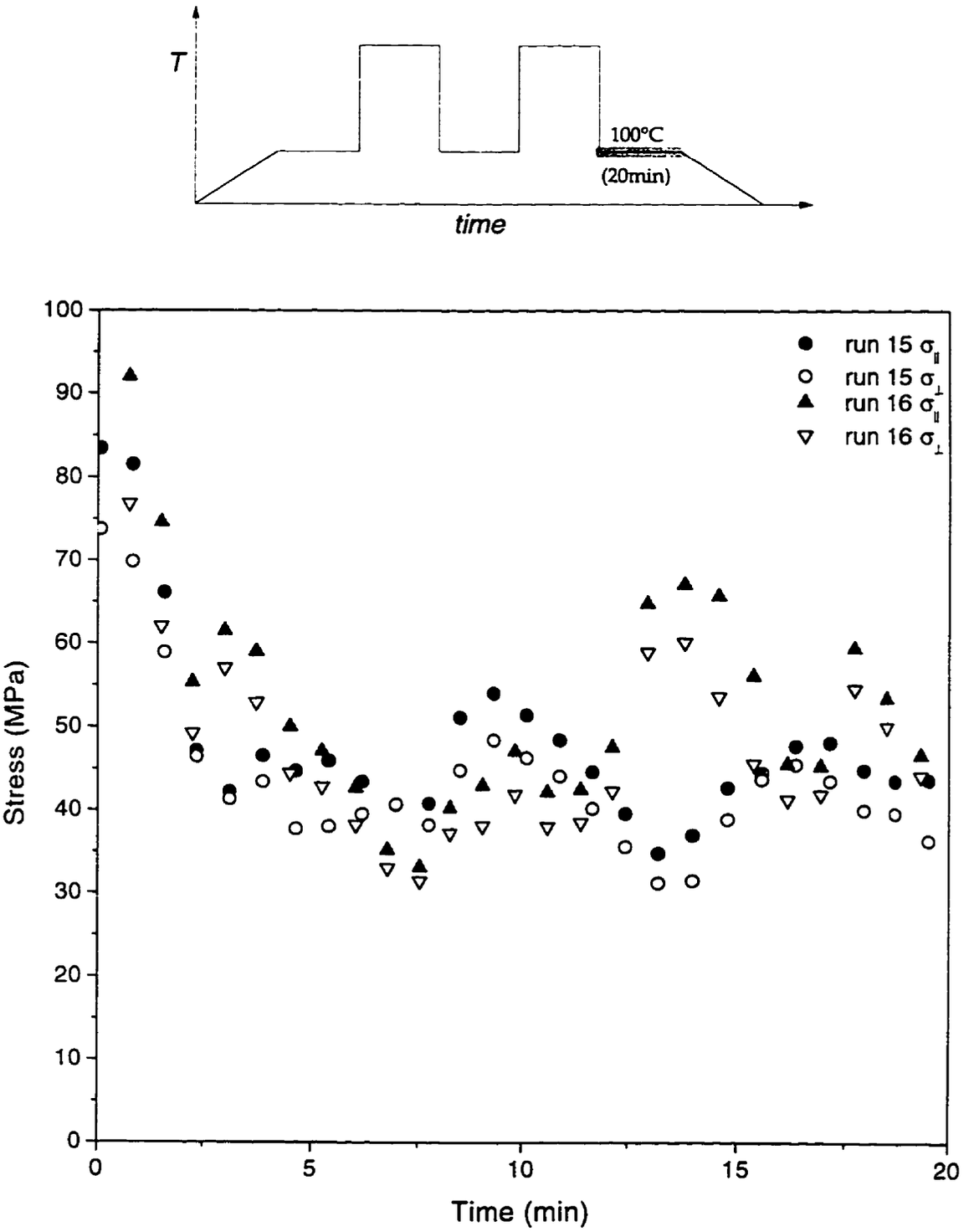

Figure 4.24: Isothermal in plane and normal stress at 100°C on quenching from 300°C for the second cycle of runs 15 & 16.

increased stress field surrounding the coherent particles. However, this hypothesis cannot be confirmed with the current data and would require a dynamic electron microscopy study to observe the kinetics of the precipitation.

4.7 Double ψ angle runs 18 and 19

The two runs discussed in this section examined the behaviour of the residual stresses before and after a series of 10 rapid cycles with shorter dwell times at 300°C (3 minutes) and 100°C (8 minutes). The reader is reminded that run 17 was a slow rate cycle (5°C/min heating and cooling) and thus the structure in run 18 is potentially very different from that of run 19 and runs 15 & 16.

4.7.1: Stabilization at 100°C on heating from ambient temperature

The residual stress development at 100°C after slowly heating (5°C/min) from ambient temperature for run 18 is shown in Figure 4.25 and indicates the expected constant behaviour associated with the elastic decrease in stress, and the results from run 19 are similar (Figure 4.26). Since this is still within the elastic region, no difference in structure should be observed here. The microstructural differences are evident only by differences in the plastic behaviour.

4.7.2: Anneal at 300°C on rapid heating from 100°C

The residual in–plane and normal stresses obtained during the first 300°C hold for run 18 are shown in Figure 4.27. The stresses are also reduced compared to runs 15&16, but do seem to show a relaxation with time. The different behaviours observed suggest that the microstructure has been significantly changed by the slow rate cycle.

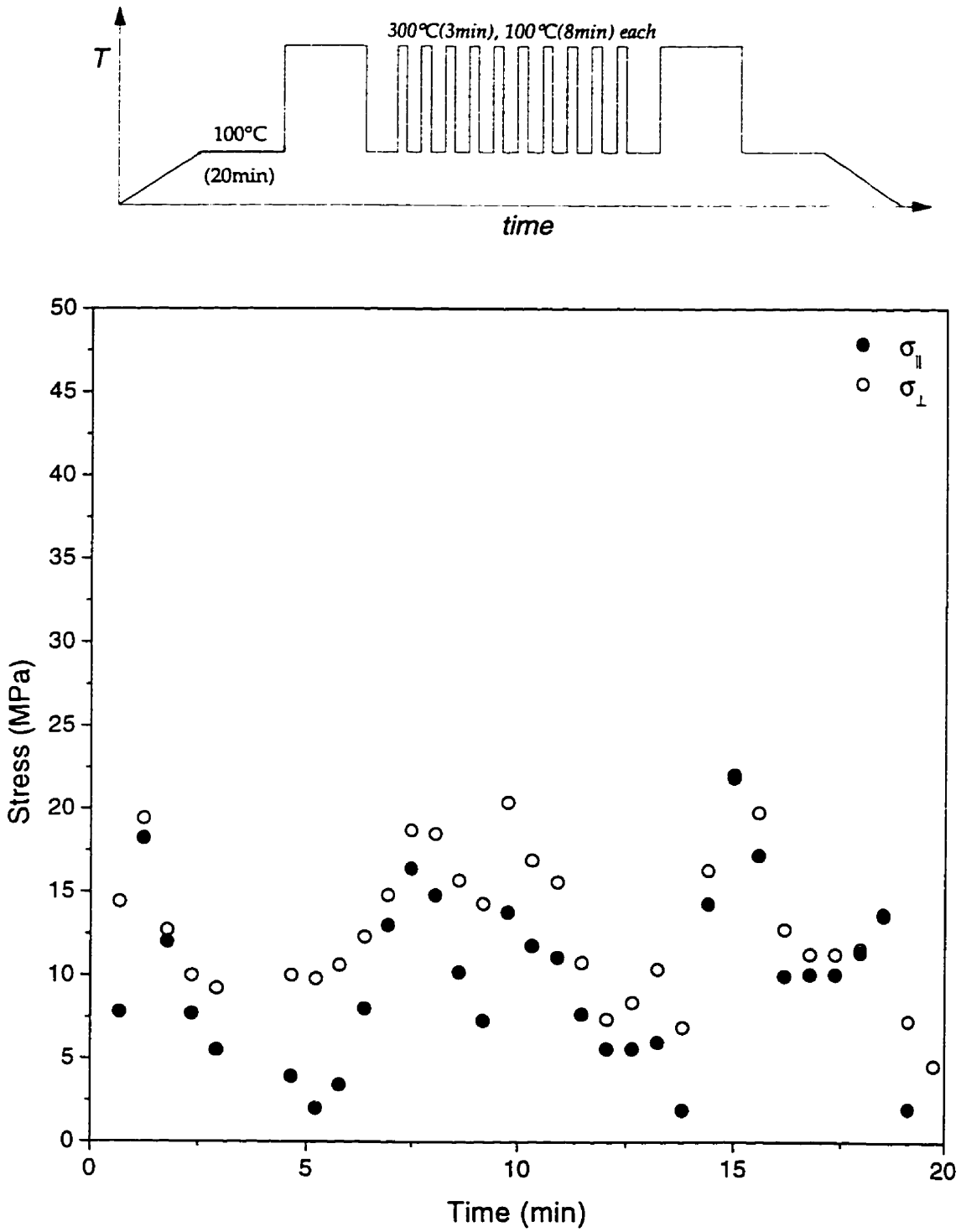

Figure 4.25: Isothermal in plane and normal stress at 100°C on slow heating from ambient temperature for run 18.

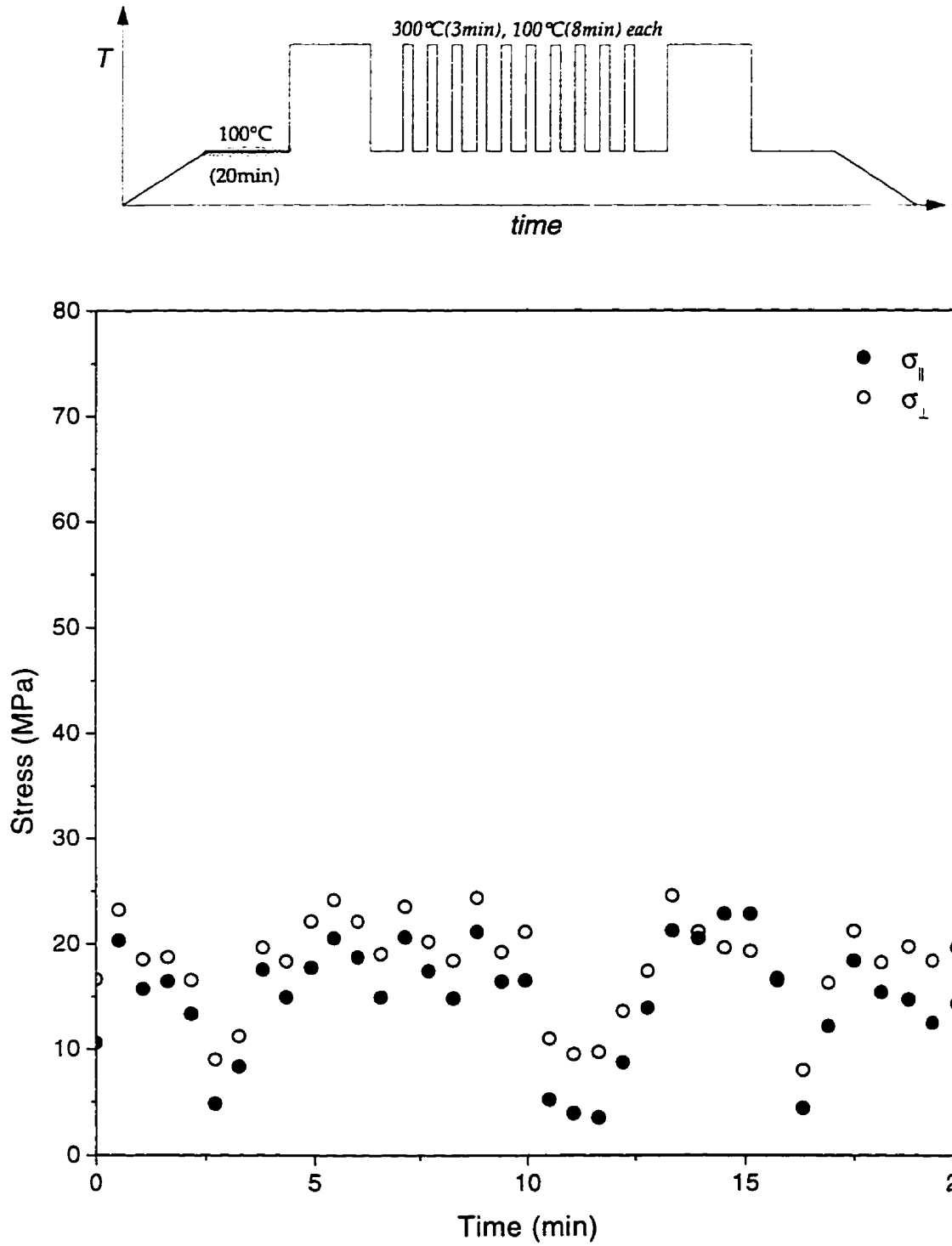

Figure 4.26: Isothermal in plane and normal stress at 100°C on slow heating from ambient temperature for run 19.

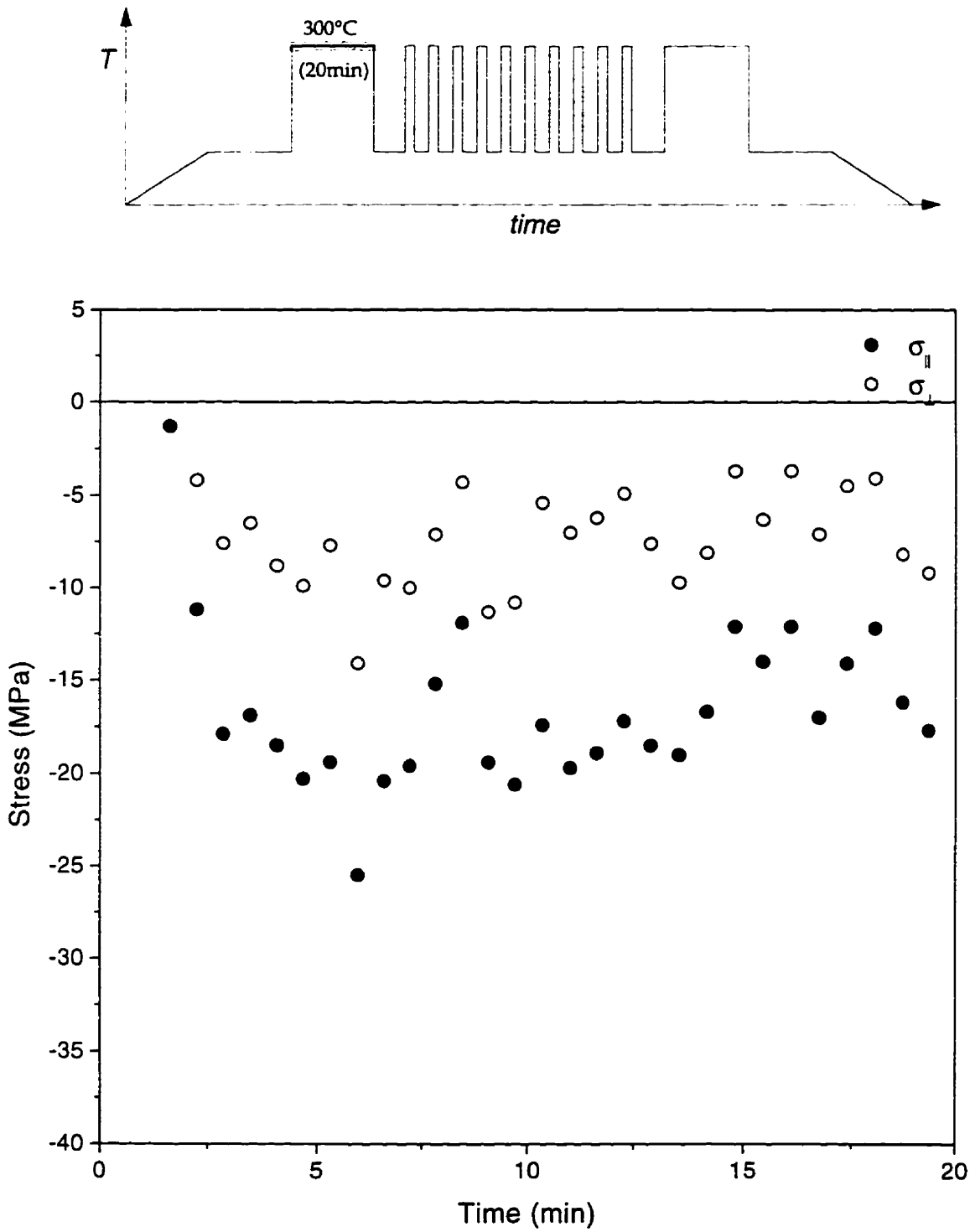

Figure 4.27: Isothermal in plane and normal stress at 300°C on rapid heating from 100°C for run 18.

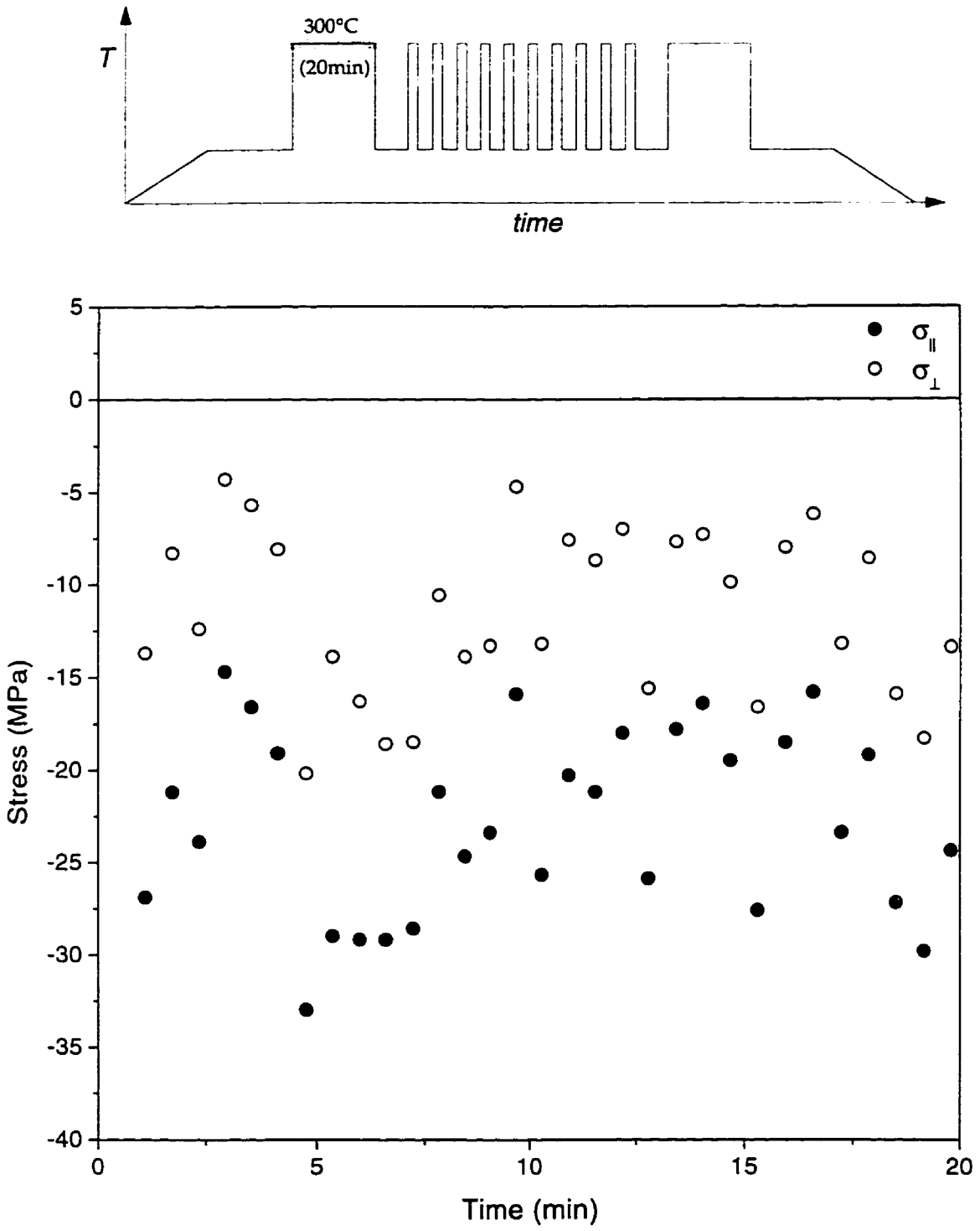

Figure 4.28: Isothermal in plane and normal stress at 300°C on rapid heating from 100°C for run 19.

Since there were many cycles in run 18, the results from run 19 could be expected to behave similarly to those of runs 15 and 16. The stresses at the first 300°C in run 19 are shown in Figure 4.28 and are more similar to the results from run 18 in magnitude (approximately 5MPa stronger), but is approximately constant with time rather than the decrease observed in run 18. While there had been fewer cycles up to 300°C prior to the data presented in Figure 4.28 (counting the heat treatment cycles in run 18 only) compared to runs 15 and 16, perhaps the most significant difference is that specimen had returned to ambient temperature only at the end of run 18, wheras before runs 15 and 16, the specimen had returned to ambient temperatures many more times. This possibly suggests that the behaviour at low temperatures is very important in the microstructural development. Further evidence for this hypothesis will be presented below.

4.7.3: Stresses at 100°C on quenching from 300°C, run 18

The stresses determined at 100°C after quenching from 300°C for run 18 are shown in Figure 4.29 and are clearly different from those observed in runs 15 and 16. The lack of a relaxation in this case is most likely due to a change in microstructure during run 17. The slow cycle anneals the damaged microstructure developed by the previous runs. The difference between the slow rate runs and the rapid ones is not purely due to a different dislocation network, but instead must be related to precipitation kinetics. This is supported by the above calculation which showed that the mean strain rate during the rapid cycling is only ~$10^{-5}s^{-1}$. Since this is certainly slow enough for dislocation glide and climb to occur, the difference in the observed behaviours must be due to precipitates pinning dislocations.

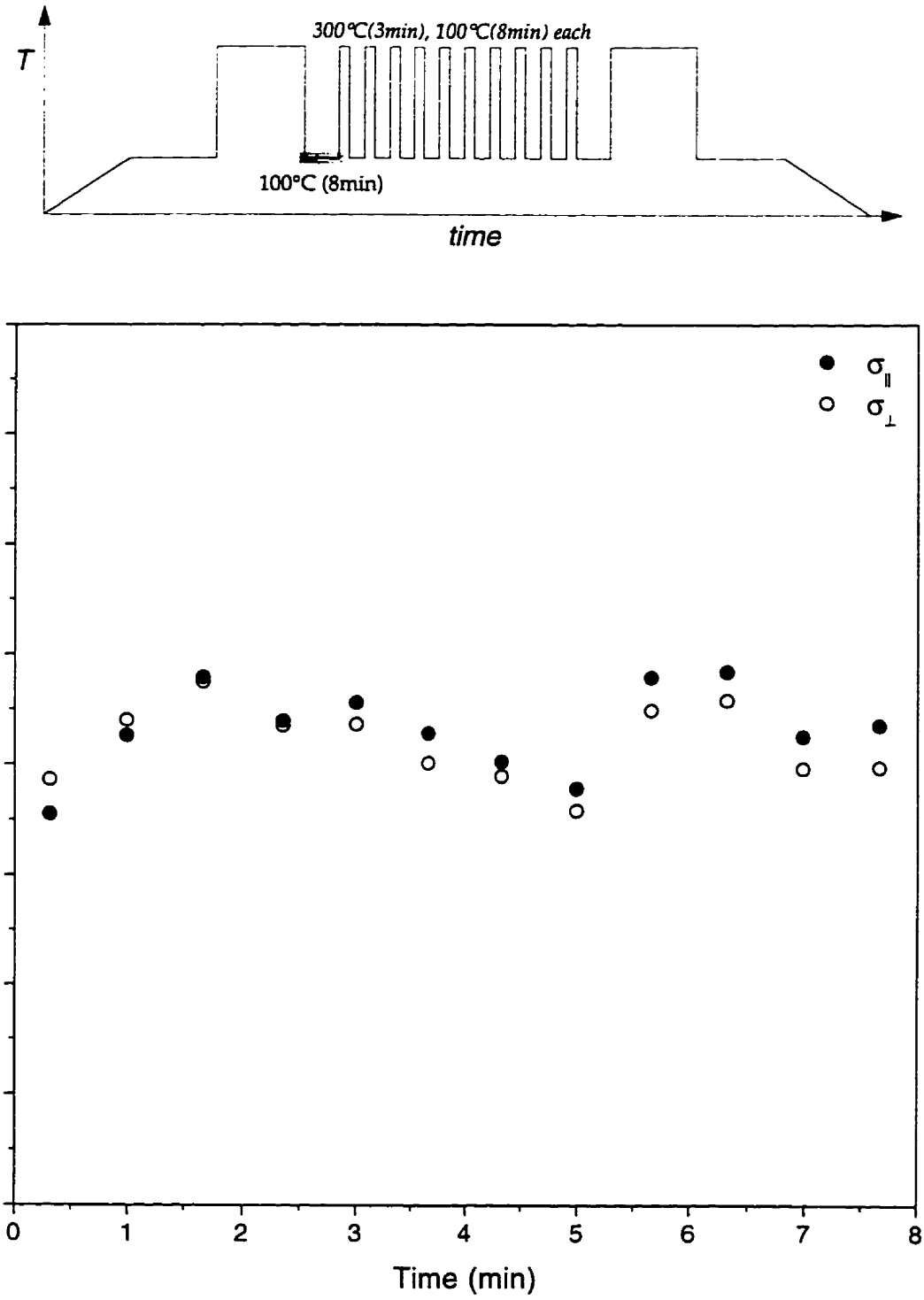

Figure 4.29: Isothermal in plane and normal stress at 100°C on rapid cooling from 300°C for run 18 prior to the 10 very rapid cycles.

4.7.4: Stresses at 100°C ending the rapid cycles: run 18

X–ray measurements were discontinued during the 10 very rapid cycles, and resumed at the last 100°C relaxation. The residual stresses obtained from run 18 for this stage of the heat treatment are shown in Figure 4.30. The behaviour is similar to the previous one indicating that plastic flow occurs during cooling to accomodate the mistfit between the matrix and the reinforcement. The slight increase in stress observed is possibly due to the formation of coherent precipitates which add to the tensile stress field, however since the increase is only slightly greater than the estimated error of ±7MPa, this interpretation is only weakly supported.

4.7.5: Stresses at 300°C after the rapid cycles: run 18

The 300°C annealing step after the 10 rapid cycles for run 18 shows that the stresses, plotted in Figure 4.31, behave similarly to the 100°C step discussed above. That is, the stresses in the first 7 minutes increase and then remain constant. This behaviour may again be due to a precipitation related phenomenon. Here those precipitates which had produced a hydrostatically tensile stress field may be redissolving, resulting in a more compressive stress in the matrix.

4.7.6: Stresses at 100°C prior to cool down: run 18

Lastly, the dynamic behaviour of the stresses at 100°C after quenching from 300°C are considered. The stresses, presented in Figure 4.32, are constant with time, indicating that the necessary plastic flow has again been accomodated during the cooling. Comparing this data to the previous 100°C hold (Figure 4.30) the constant stress values observed here suggest that the microstructure here is rather different. This is likely due to the longer hold at 300°C.

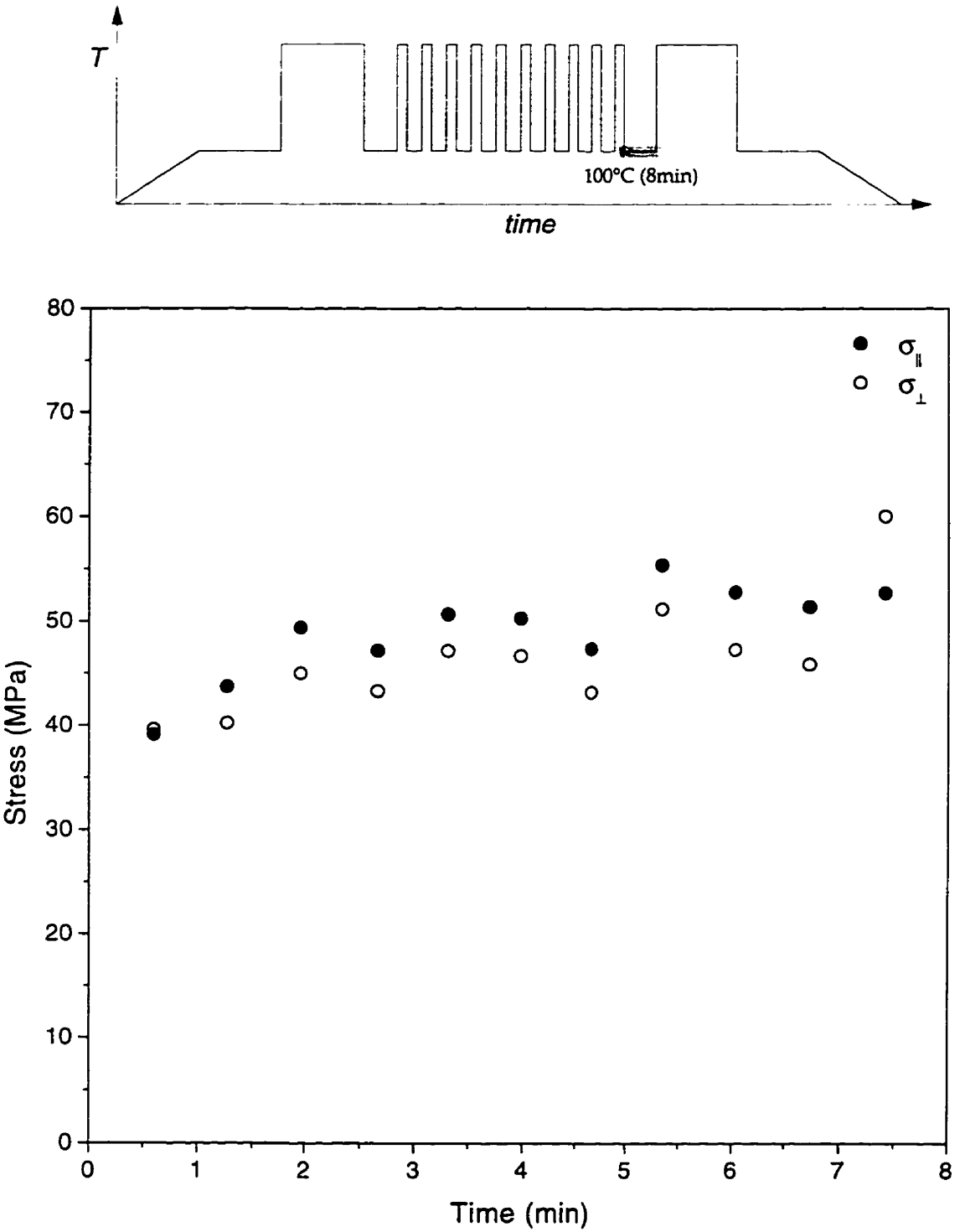

Figure 4.30: Isothermal in plane and normal stress at 100°C on rapid cooling from 300°C for run 18 at the end of the 10 very rapid cycles.

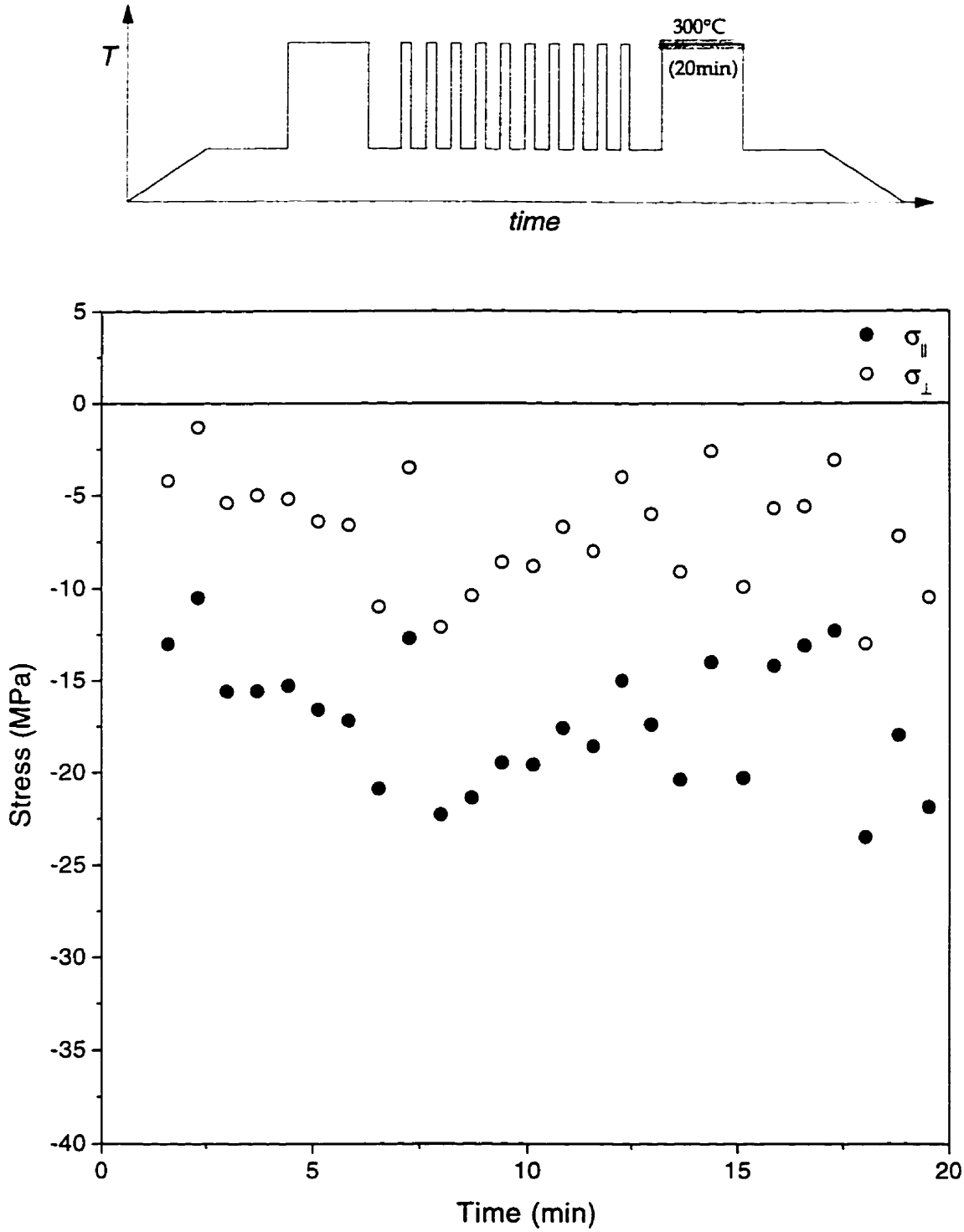

Figure 4.31: Isothermal in plane and normal stress at 300°C on rapid heating from 100°C for run 18 after the 10 very rapid cycles.

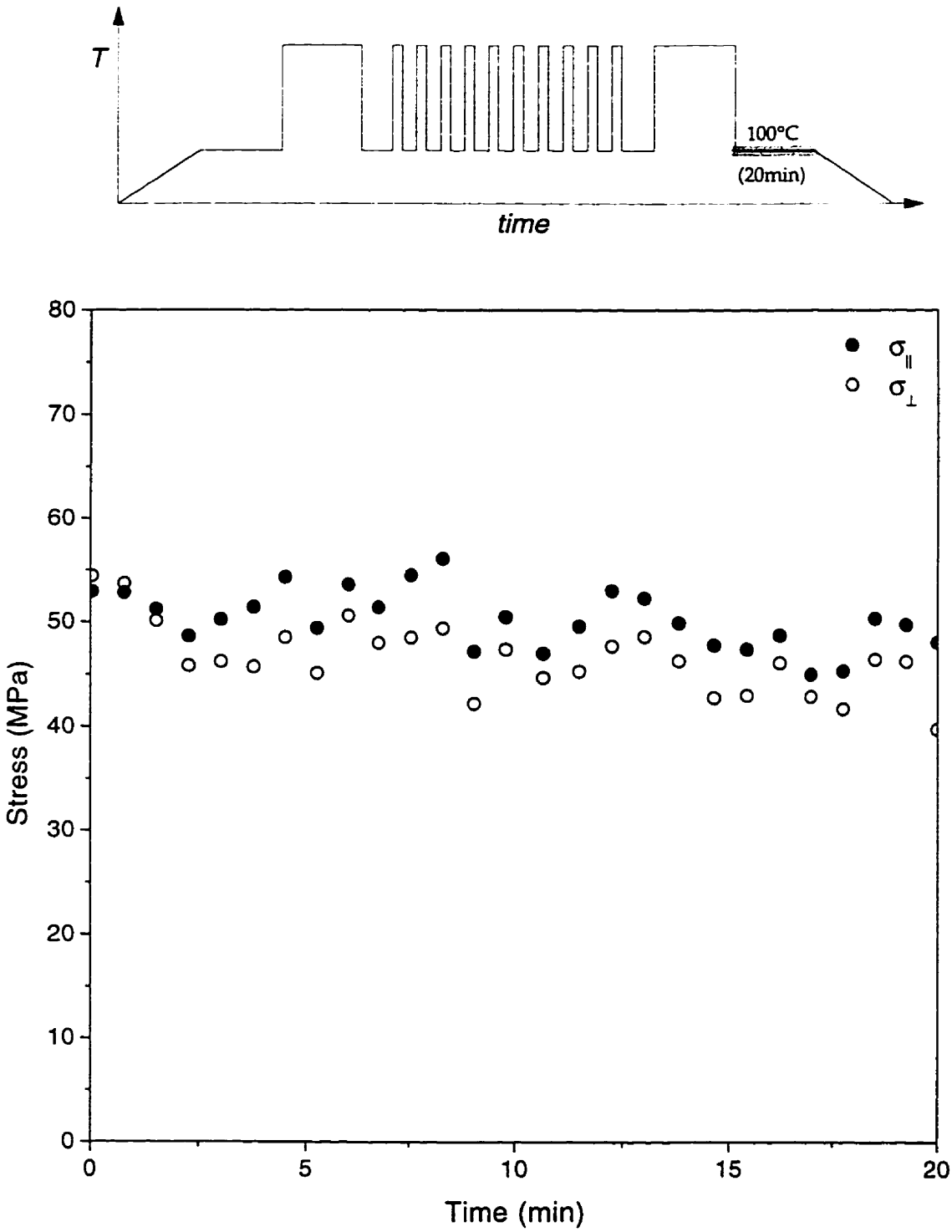

Figure 4.32: Isothermal in plane and normal stress at 100°C on rapid cooling from 300°C for run 18 at the end of the 12th cycle.

4.7.7: Stresses at 100°C after quenching from 1st 300°C: run 19

Since the thermal history of run 19 compared to that of run 18 is very different, only run 18 has been considered in the discussion above with the exception of the stabilization at 100°C and the 300°C anneal immediately afterwards. Having presented the results of run 18, the stresses obtained from run 19 shall be presented and compared with those obtained from run 18 and runs 15 & 16.

Examining the stresses obtained after quenching from the first 300°C anneal to 100°C shown in Figure 4.33, some relaxation is observed. The hump in stress after 5 minutes is likely due to a fluctuation in the temperature control, which is also shown in this figure. The difference between the 10th and 11th cycles of run 18 with this one before 10 cycles in run 19 is that the sample was cooled to ambient temperature prior to reheating. Thus it appears that the deformation behaviour between 100°C and ambient temperature after 10 cycles is quite different from that after slow cycling such as run 17.

4.7.8

Considering now the stress behaviour after the 10 cycles, Figure 4.34 shows the in–plane and normal stresses at the end of the 10th cycle. There is now a more distinct relaxation indicating that there is still some microstructural development during the rapid cycling. As mentioned earlier, the precipitate distribution may be responsible for the greatly reduced dislocation mobility. The role that precipitates could play in the micromechanics of the relaxation is further discussed in §4.8.

4.7.9

The stresses obtained during the 20 minute anneal at 300°C after the 10 cycles in run 19 are shown in Figure 4.35 and are very similar to the stresses before the 10 cycles (Figure 4.28).

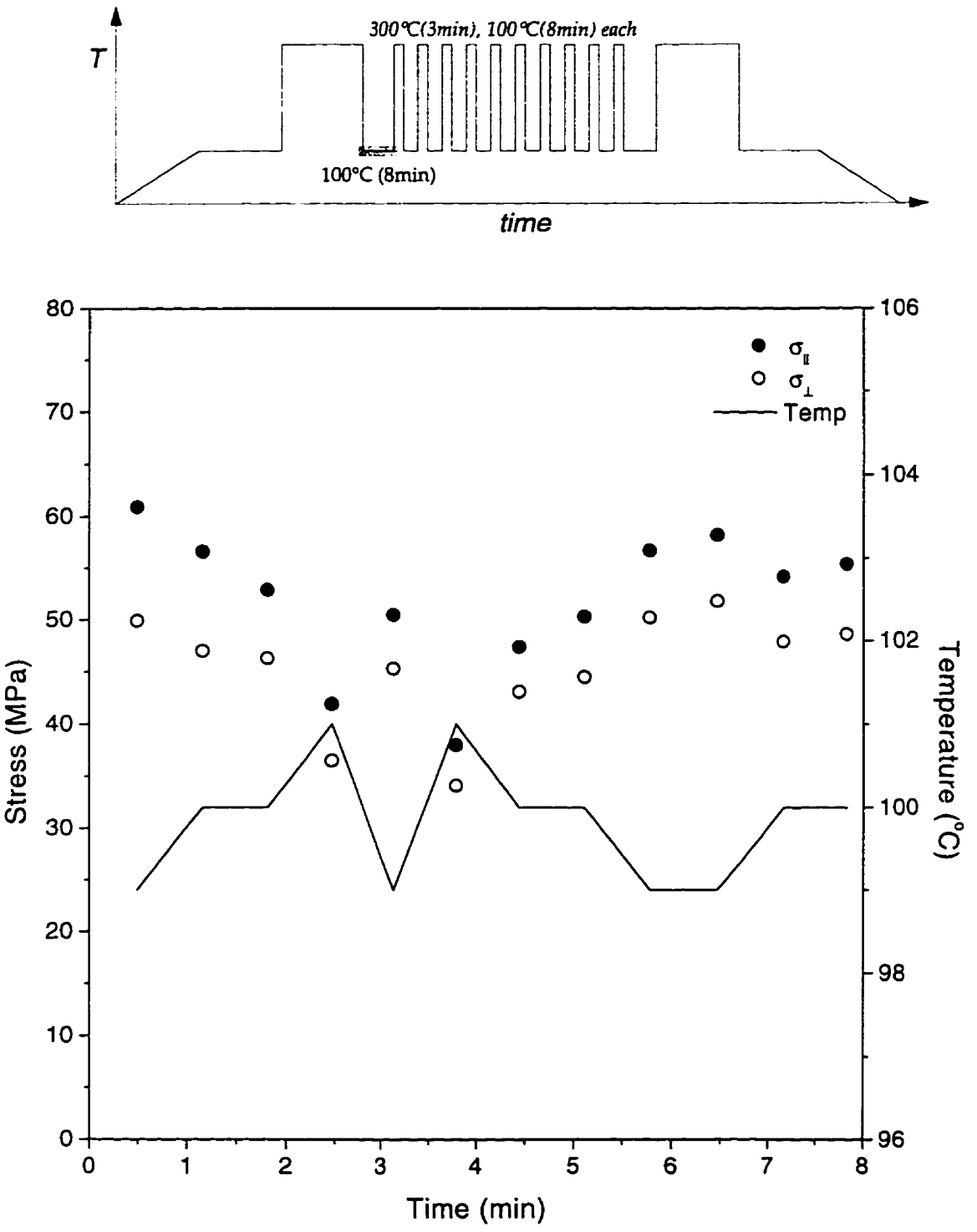

Figure 4.33: Isothermal in plane and normal stress at 100°C on rapid cooling from 300°C for run 19 prior to the 10 very rapid cycles.

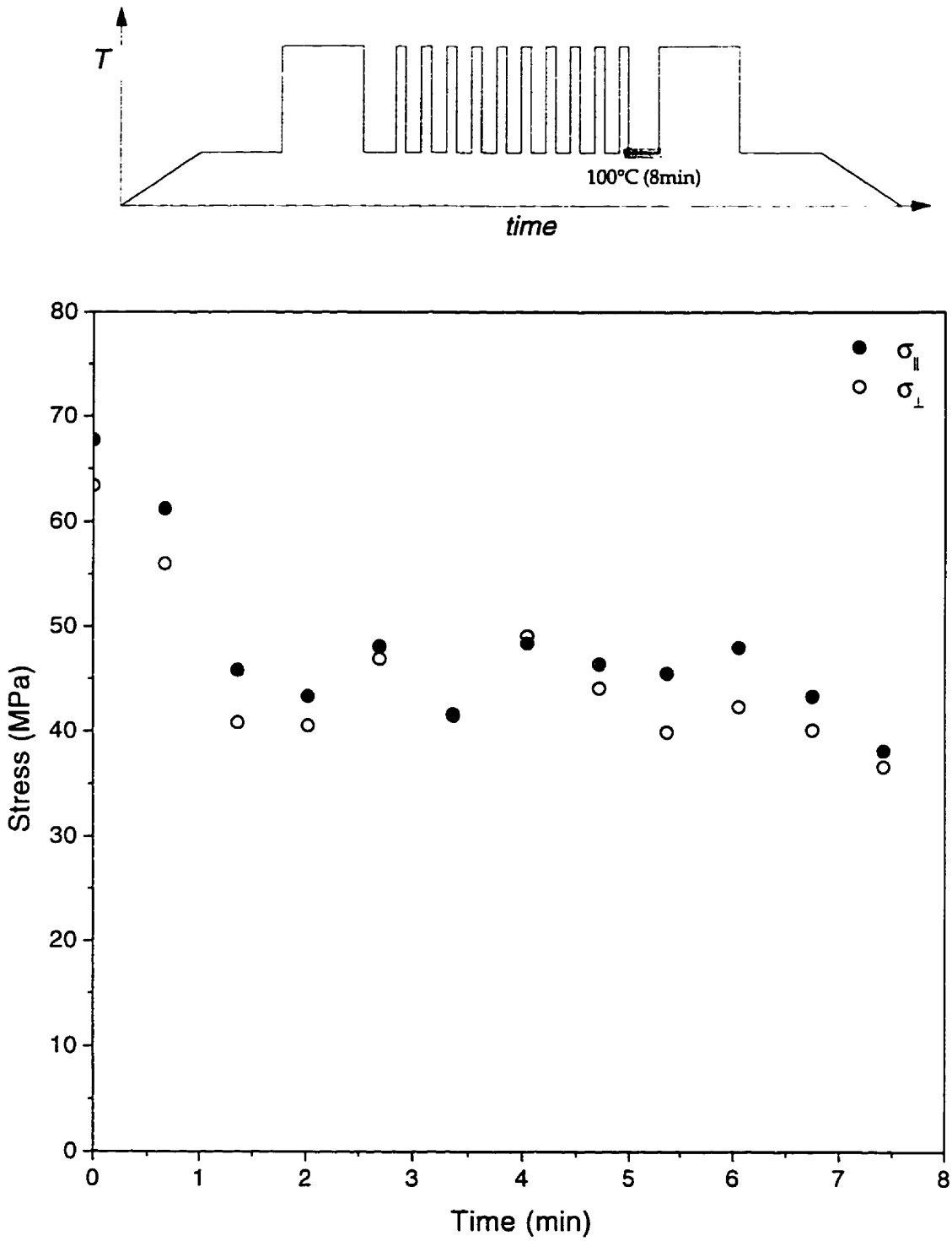

Figure 4.34: Isothermal in plane and normal stress at 100°C on rapid cooling from 300°C for run 19 at the end of the 10 very rapid cycles.

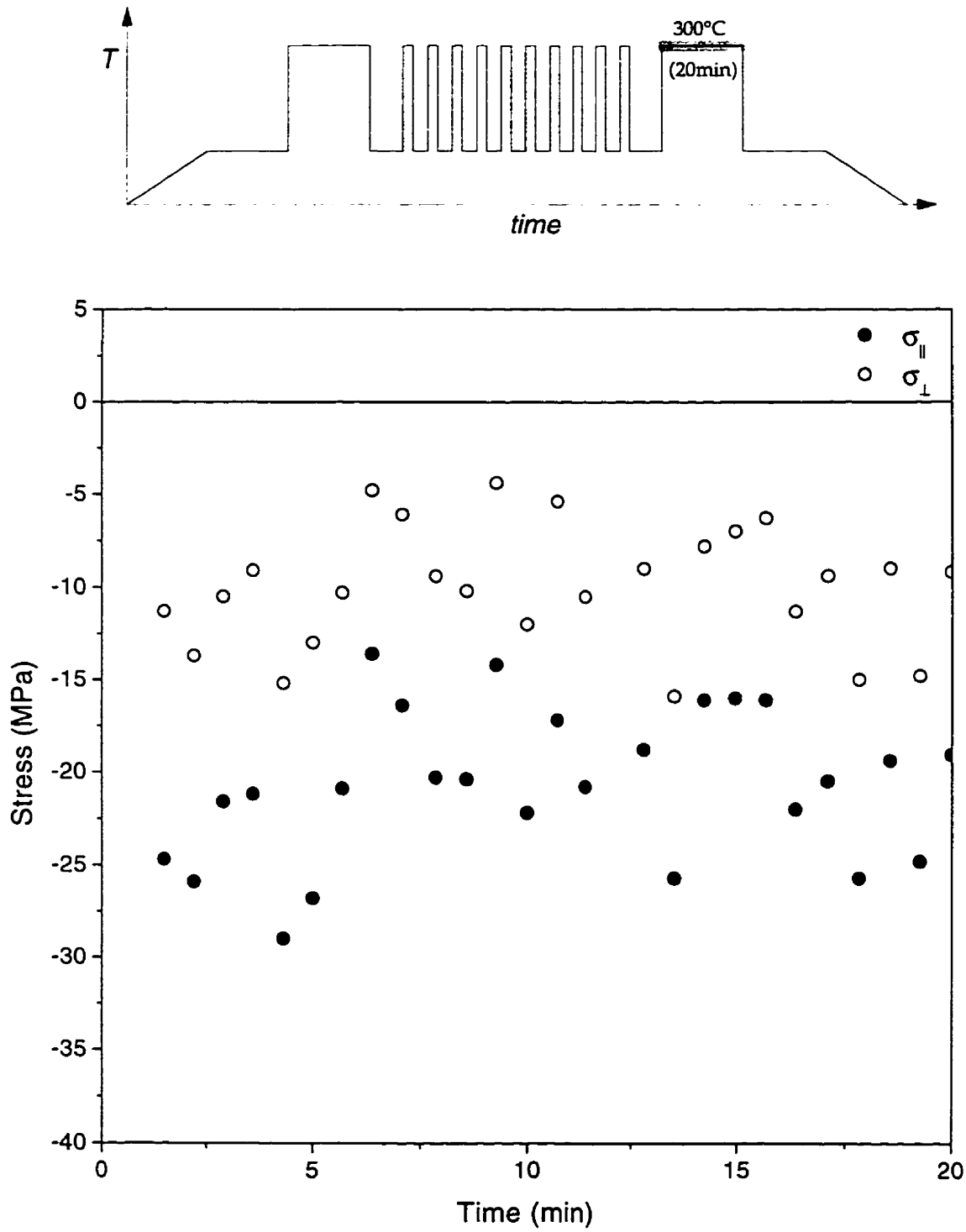

Figure 4.35: Isothermal in plane and normal stress at 300°C on rapid heating from 100°C for run 19 after the 10 very rapid cycles.

4.7.10: Stress development at 100°C after the longer hold at 300°C for run 19

Lastly, the final relaxation at 100°C prior to cooling to ambient temperature is examined and the isothermal stress vs. time plot is presented in Figure 4.36. The relaxation observed here is similar to those observed in cycles 15 and 16 (Figures 4.22 and 4.24). The difference between this relaxation and the one at the end of the 10 cycles is most likely to the hold time at 300°C of 20 minutes compared to the 3 minutes during the fast cycling. The size and distribution of the precipitates would be different for the two cases due to the kinetics of the dissolution and precipitation. The longer time at 300°C would result in more precipitates redissolved and the remaining ones would be smaller than for a 3 minute hold. Thus quenching from the shorter annealing time is predicted to result in a coarser distribution of larger precipitates.

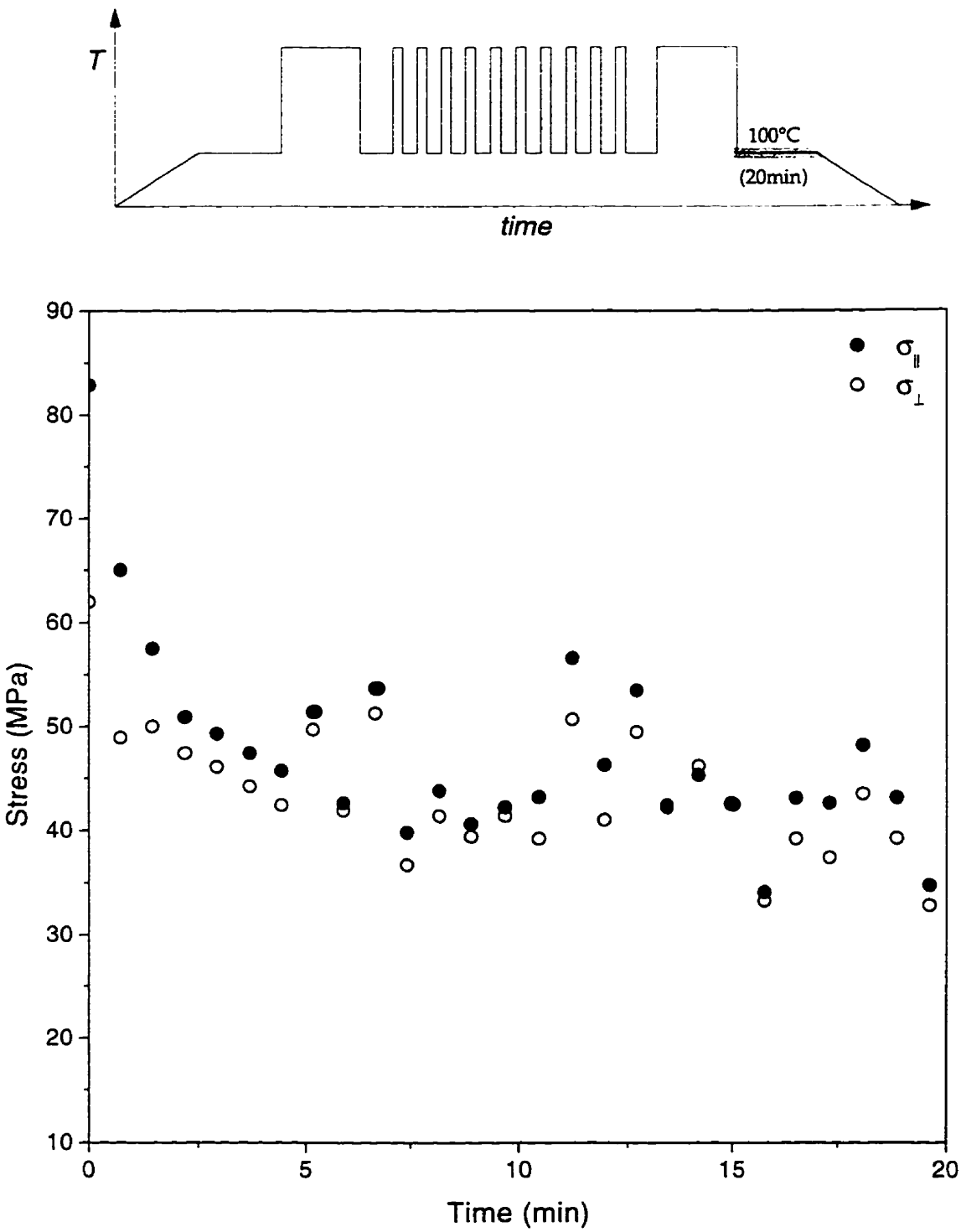

Figure 4.36: Isothermal in plane and normal stress at 100°C on rapid cooling from 300°C for run 19 at the end of the 12th cycle.

4.8 Possible Dislocation Pinning Mechanism for the Relaxation Rates Observed

As discussed above, the mean strain rate during the quench from 300°C to 100°C is a relatively slow $10^{-5}s^{-1}$. Dislocation glide should easily be achieved, and dislocation climb is also possible at this strain rate. Since in cycles 15,16 and 19 a large relaxation is observed at 100°C after quenching from the high temperature annealing, there must be some microstructural feature which strongly pins the dislocations. Secondly, since the relaxations did not appear in run 18, which followed a slow rate cycle, the pinning mechanism can be removed. These two observations, and the low temperature cooling behaviour discussed in §4.4, suggest that a precipitation mechanism is a possible one.

The difference in low temperature behaviour between the present study and the previous one[17] was attributed to the kinetics of precipitation: the much longer anneals at 300°C in the previous study may have completely dissolved the precipitates wheras in the current study, only the smaller precipitates are dissolved. The remaining ones can then act as nuclei and the precipitate distribution on cooling becomes one of large particles coarsely distributed. The coarse distribution is less effective at pinning dislocations and hence the yield stress is reduced.

This does not yet explain the relaxation behaviour observed at 100°C after quenching from 300°C. The results obtained in run 18 indicate that the dislocation pinning mechanism can be removed by a slow rate cycle since relaxations were not observed here. Precipitation is a diffusion controlled process and the driving force for nucleation and growth of a precipitate is not due to the activity of the solute species in the matrix alone, but is the minimization of the free energy. The free energy also includes a strain energy term which may alter the equilibrium precipitate concentration. Coherent

precipitates which are misfitting in the matrix have a stress field surrounding the particle. Thus, for example, a large misfitting particle would not be expected to grow if the matrix is already under a hydrostatic tensile stress since the strain energy of the system would increase by the growth of the particle. A small misfitting particle, however, which generated a compressive stress field would be expected to grow readily in this example.

Stress fields are not associated with incoherent precipitates and hence the thermodynamics of the growth or dissolution of an incoherent precipitate would not be affected by an external stress. Such particles would therefore be more stable during the cycling of the thermal mismatch stresses in the MMC being studied.

Precipitates can easily nucleate and grow as coherent particles on a dislocation by the Cottrell–Bilby mechanism.[58] Precipitates relieving the strain field of dislocations was first observed in 1978 by Allen and vander Sande[59] using weak beam TEM and has also been observed in an Al 0.14wt% Cr alloy by Lagacé and Saimoto in 1986.[60] The solute atoms can diffuse quickly along the dislocation and hence the growth or dissolution rate is rather fast. The pipe diffusion of solutes to or from a precipitate suggests that the coherent particles could grow or dissolve during the rapid thermal cycling driven by the stresses due to the ceramic fibres.

The relaxation behaviour can now be examined using this background to determine whether a precipitation mechanism can account for the relaxations observed. Since the stress relaxation effect does not appear after the 10th or 11th cycle in run 18, the metallurgical structure responsible cannot be due solely to the rapid cycling but must also be due to the stored work structure during cooling to ambient temperature. Moreover this stored work structure is resilient to fast thermal cycling. Hence the probable origin of this phenomenon must be due to the precipitation kinetics rather than the

plasticity condition. The compostion of the as–cast matrix may decompose at near ambient temperature due to transition precipitates for which the Al–Cu system is well known. The fine precipitate distribution and the solute concentration in the matrix depends on the prior thermal–mechanical processing. Thus the microstructure with greater solute in solution (large degree of supersaturation) can precipitate out by heterogeneous precipitation on dislocations as they are generated at high stresses (low temperatures). As the stresses increase these precipitates will become detached from the dislocations and become incoherent and more resistant to resolution when reheated. On the other hand for slow heating cycles, the solute can migrate to pre–existing precipitates and a fine dispersion would not be present. This difference in microstructure could account for the observed relaxation difference. If indeed this model is applicable, then one should expect differences in the stress changes during cooling from and heating to 100°C for the cases of runs 18 and 19.

The critical stage at which the damage becomes evident is likely due to the condition at which the fine dispersion of precipitates become incoherent. While they are coherent, the elastic field due to the crystallographic mismatch is influenced by the longer range stress field from the ceramic reinforcement phase. In this state they will dissolve or precipitate depending on the sign of the long range field with respect to the misfit of the precipitate. When the precipitate becomes incoherent, it no longer has an elastic stress field in the matrix and hence is less influenced by the stress field from the reinforcement. That is, the stress field does not influence the free energy of growth for such a precipitate. Since the stability of coherent particles are more influenced by temperature changes, their aging behaviour will be reflected in the variation of flow stress resulting in the large relaxations observed. The incoherent precipitates on the other hand are no longer attached to a dislocation and

hence precipitate size changes by pipe diffusion is not available and hence the precipitates are more stable during temperature cycling.

This notion, if applicable, can also account for the hump in stress observed during cooling from 100°C to ambient temperature. The stress decrease is due to the release of elastic energy when the precipitates become incoherent. This is possibly due to a change in character of the precipitates present: that is, they may have changed from coherent precipitates to incoherent ones. Since incoherent particles do not have an elastic stress field due to the crystallographic mismatch, such precipitates would become less susceptible to stress influenced resolution and dissolution.

This discussion has shown that the relaxation behaviour observed may be explained by the pinning of dislocations by a fine dispersion of incoherent particles. These can be redissolved during slow thermal cycling, which results in the development of coherent particles forming on dislocations during subsequent rapid cycling. After many cycles, a dislocation and particle structure has developed such that the particles become unpinned from the dislocation and are then incoherent with the matrix. These are stable to subsequent thermal cycling. The low temperature decrease in stress during cooling can also be expained by the change in character of the precipitates from coherent ones with an elastic field (possibly tensile) to incoherent ones with no stress field. The drop in stress is thus not a softening of the matrix but due instead to the decrease in the elastic strain energy from the particles. The dislocation density can increase while the mean elastic stress can still decrease.

The data obtained during this study cannot conclusively confirm this hypothesis and would require an in situ transmission electron microscope study to examine directly the kinetics of the precipitation processes in this system.

Chapter 5
Conclusions and Recommendations for Future Research

5.1 Summary

Residual stresses were measured dynamically by x–ray diffraction during rapid thermal cycling of a metal matrix composite. This was achieved using a linear position sensitive detector to reliably measure the diffracted peak in 5 seconds. Systematic errors due to crystallographic texture were reduced by rocking the specimen about the θ axis during data collection. A method was developed to align large grained specimens with the goniometer centre so that accurate lattice parameter measurements can be made with such materials. This technique was applied to the stress free standard specimen which was found to have a grain size of approximately 2mm.

A novel high temperature stage was developed to have a low thermal mass for rapid thermal cycling and a low expansion for reliable x–ray measurements over a wide temperature range. The stage was found to have a thermal expansion less than the measurement capabilities of the calibration procedure, indicating that normal displacements of the stage was less than 5μm. Temperature control was achieved using an infrared spot heater, a type K thermocouple welded to the specimen and a programmable temperature controller, resulting in temperature control of ±1.5°C. The low thermal mass permitted heating rates of better than 200°C/min from 100°C to 300°C and air cooling rates such that the specimen could be cooled from 300°C to 100°C in approximately 50 to 55 seconds.

This experimental design was used to measure the dynamic behaviour of residual stresses in a 23%(vol.) Kaowool short fibre reinforced AA339 Al alloy during rapid thermal cycling.

The mean residual stresses measured by the diffraction technique were interpreted by comparison with an elastic model of cuboidal inclusions periodically distributed in an infinite matrix. The model showed that the stresses near the interface between the two phases are larger than the mean stresses. The stress near the interface is approximately uniaxial and is 8× larger than the mean stress for the special case modelled. The volume averaged shear stesses were found to vanish, supporting the assumptions in the stress state used to analyze the x–ray data.

The relaxation behaviour observed was attributed to the development of a fine, incoherent precipitate structure which strongly pinned dislocation glide and climb. This structure is formed during rapid cycling if the precipitates break free from the dislocations where they may readily nucleate and grow as initially coherent ones. When they break free from the dislocation, the growth rate or dissolution rate is reduced by the slower lattice diffusion compared to pipe diffusion. These incoherent precipitates are now stable during rapid cycling with short hold times at 300°C. The high stresses at low temperatures play an important role in releasing the dislocations from the coherent precipitates. The stress drop observed below 80°C on cooling is attributed to the decrease in the elastic strain energy by the particles becoming detached from the dislocations and becoming incoherent. During a slow heating and cooling rate cycle the precipitates may redissolve, eliminating the particle dispersion developed during the rapid cycles.

5.2 Recommendations for Future Work

This model cannot be confirmed by the present data, hence future work should include an insitu transmission electron microscopy study to observe directly the kinetics of the precipitation. The use of a high voltage TEM is recommended to better approximate the stress state in the bulk.[37] Improvements in the x–ray measurements can be realized by improving the temperature control by using a controller with a faster time constant. Lastly, microbeam x–ray experiments may be able to measure the residual stresses near the interface between the reinforcement and the matrix. This could improve the estimate of the ratio between the mean stress and maximum stress derived in the simulation.

References

[1] T.W. Clyne & P.J. Withers, An Introduction to Metal Matrix Composites, Cambridge University Press, Cambridge (1993).

[2] I.C. Noyan & J.B. Cohen, Residual Stress: Measurement by Diffraction and Interpretation, Springer–Verlag: New York NY (1987).

[3] B.D. Cullity, Elements of X–Ray Diffraction, 2nd Ed., Addison Wesley: Don Mills, ON (1978) p87.

[4] I.C. Noyan & J.B. Cohen, p119.

[5] I.C. Noyan, *Met. Trans. A*, **14A** (1983) pp249–258.

[6] I.C. Noyan, *Met. Trans. A*, **14A** (1983) pp1907–1914.

[7] Ch. Genzel, *Phys. Stat. Sol (a)*, **146** (1994) pp629–637.

[8] Ch. Genzel, *Phys. Stat. Sol (a)*, **156** (1996) pp353–363.

[9] T. Sasaki, M. Kuramoto & Y. Yoshioka, *Adv. X–Ray Analysis*, **27** (1984) 121.

[10] I.C. Noyan & J.B. Cohen, p140.

[11] M. Ohtsuka, H. Matsuoka, Y. Hirose & H. Ishii, *Adv. X–Ray Analysis*, **38** (1995) pp463–470.

[12] P. Predecki, X. Zhu & B. Ballard, *Adv. X–Ray Analysis*, **36** (1993) pp237–245.

[13] P. Predecki, B. Ballard & X. Zhu, *Adv. X–Ray Analysis*, **36** (1993) pp247–255.

[14] B.L. Ballard, P.K. Predecki & D.N. Braski, *Adv. X–Ray Analysis*, **37** (1994) pp189–196.

[15] T.H. Hanabusa, K. Nishioka, H. Fujiwara, *Z. Metallkde.*, **74** (1983) 307.

[16] A.P. Clarke, *Ph.D. Thesis*, Queen's University (1993).

[17] A.P. Clarke & S. Saimoto, *in Micromechanics of Advanced Materials*, ed. Chu, Liaw, Arsenault, Sadananda, Chan, Gerberich, Chau, Kung, Pub. TMS (1995) pp191–196.

[18] H.J. Bunge, Texture Analysis in Materials Science (Mathematical Methods), Butterworth (1982).

[19] P. Van Houtte & L. de Buyser, *Acta Metall. Mater.*, **41** (1993) pp323–336.

[20] M.A. Korhonen & C.A. Paszkiet, *Scripta Metall.*, **23** (1989) pp1449–1454.

[21] L. Castex, J.L. Lebrun & S. Bras, *Adv. X–Ray Analysis*, **24** (1981) 139.

[22] G.F. Knoll, Radiation Detection and Measurement, John Wiley & Sons, Toronto (1979), chapter 6.

[23] J. Hendrix, *Advances in Polymer Science*, **67** (1985) pp60–97.

[24] B.D. Cullity, Elements of X–Ray Diffraction, Addison Wesley (1978) pp204–207.

[25] M.R. James & J.B. Cohen, *J. Appl. Cryst.*, **12** (1979) pp339–345.

[26] J.J. Heizmann & C. Laruelle, *J.Appl. Cryst.*, **19** (1986) pp467–472.

[27] L. Wcislak & H.J. Bunge, *Textures & Microstructures: ICOTOM 9*, **14–18** (1991) pp257–271.

[28] L. Wcislak, H.J. Bunge, M. Haase & C. Nauer–Gerhardt, *Adv. X–Ray Anal.*, **35A** (1992) 309.

[29] F. Seitz, *Phys. Rev.*, **79** (1950) p723.

[30] F.R.N. Nabarro, *Phys. Rev.*, **79** (1950) p894.

[31] G.C. Weatherly, *Phil. Mag.*, **17** (1968), pp791–799.

[32] A. Kelly, Strong Solids, Clarendon Press, Oxford (1966) *also*
A. Kelly & N.H. MacMillan, Strong Solids 3rd Edition, Oxford University Press, New York (1986), pp24–34.

[33] M.F. Ashby & L. Johnson, *Phil. Mag.*, **20** (1969) pp1009–1022.

[34] M.E. Gulden & W.D. Nix, *Phil Mag.*, **18** (1968) pp217–228.

[35] I.M. Brown, G.R. Woolhouse & U. Valdrè, *Phil Mag.*, **17** (1968) pp781–789.

[36] R.J. Arsenault & R.M. Fisher, *Scripta Metall.*, **17** (1983) 67.

[37] R.J. Arsenault & N. Shi, *Mat. Sci. & Eng.*, **81** (1986) 175.

[38] M. Vogelsang, R.J. Arsenault & R.M. Fisher, *Met. Trans. A*, **17A** (1986) pp379–389.

[39] R.J. Arsenault, L. Wang & C.R. Feng, *Acta Metall. Mater.*, **39** (1991) pp47-57.

[40] M. Taya & T. Mori, *Acta Metall.*, **35** (1987) pp155–162.

[41] S. Shibata, M. Taya, T. Mori & T. Mura, *Acta Metall. Mater.*, **40** (1992) pp3141–3148.

[42] M. Taya & T. Mori, *J. Eng. Mat. Tech.*, **116** (1994) pp409–413.

[43] D.C. Dunand & A. Mortensen, *Scripta Metall. Mater.*, **25** (1991) pp761–766.

[44] D.C. Dunand & A. Mortensen, *Acta Metall. Mater.*, **39** (1991) pp1417–1429.

[45] D.C. Dunand & A. Mortensen, *Acta Metall. Mater.*, **39** (1991) pp1405–1416.

[46] H.L. Cox, *Brit. J. Appl. Phys.*, 3 (1952) pp72–79.

[47] W.D. Nix, *Met. Trans. A*, **20A** (1989) 2217.

[48] T. Malis, D.J. Lloyd & K. Tangri, *Phys. Stat. Sol. (a)*, **11** (1972) pp275–286.

[49] A.P. Clarke, G. Langelaan, S. Saimoto, *Mat. Res. Soc. Symp. Proc.* ,**356** (1994) pp609–614.

[50] G. Langelaan, S. Saimoto, M. Moske, *Mat. Res. Soc. Symp. Proc.* , **428** (1996) pp537–542.

[51] EG&G Ortec, Maestro II v1.11 Software Operator's Manual.

[52] I.C. Noyan & J.B. Cohen, p132.

[53] T. Mura, Micromechanics of Defects in Solids, Martinus Nijhoff Publishers, The Hague (1982) pp17–18.

[54] J.D. Eshelby, *Proc. Roy. Soc. A*, **241** (1957) pp376–396.

[55] W.D. Kingery, H.K. Bowen & D.R. Uhlman, Introduction to Ceramics, 2nd Ed., John Wiley & Sons, New York (1976).

[56] H.J. Frost & M.F. Ashby, Deformation-Mechanism Maps: The Plasticity and Creep of Metals and Ceramics, Pergamon Press, Toronto (1982).

[57] J.P. Hirth & J. Lothe, Theory of Dislocations, John Wiley & Sons, Toronto (1982).

[58] A.H. Cottrell & B.A. Bilby, *Proc. Phys. Soc. Lond.*, **A267** (1949), pp49–62.

[59] R.M. Allen & J.B. vander Sande, *Met. Trans. A*, **9A** (1978) pp1251–1258.

[60] H. Lagacé & S. Saimoto, *in Defect Forum*, (1986).

[61] P.M. Sutton, *Phys. Rev.*, **91** (1953) pp816–821.

Appendix 1
Derivation of the Single Crystal Analysis

Following the derivation of Korhonen and Paszkiet,[20] who showed that for a biaxial stress state a fibre textured Al film on Si could be treated as a single crystal, the analysis here is expanded to a triaxial stress state. In the system being studied, the texture has been found to be a <001> fibre texture with the fibre axis parallel to the surface normal. This is consistent with the columnar region of a casting. It is assumed in this analysis that the principal directions of the stress are parallel to the <100> directions and that the stress in the plane of the specimen (the (001) plane) is uniform and that the stress normal to the surface is similar in magnitude to the in–plane stress. Since the in–plane stress is uniform and the texture is symmetrical about the specimen normal, the [100] and [010] directions are arbitrary. The stresses and strains are thus:

$\sigma_{[100]}=\sigma_{[010]}=\sigma_1$

$\sigma_{[001]}=\sigma_3$

$\varepsilon_{[100]}=\varepsilon_{[010]}=\varepsilon_1$

$\varepsilon_{[001]}=\varepsilon_3$

ε_ψ=strain measured at the orientation ψ.

The measured parameter, ε_ψ, must be converted to the principal stresses which are the desired parameters. Thus the co–ordinates must be rotated from the specimen axes to the laboratory axes and represent ε_ψ in terms of the principal strains. Since the both the texture and the stress are symmetrical about the specimen normal, rotations about the [001] axis can be neglected. For simplicity, align the ψ rotation axis to the [010]. The strain ε_ψ for some tilt ψ then becomes

$$\varepsilon_\psi = \varepsilon_3 \cos^2\psi + \varepsilon_1 \sin^2\psi . \qquad \text{(A1.1)}$$

Substituting the relations for ε_3 and ε_1 from Hooke's Law and simplifying,

$$\varepsilon_\psi = S_{11}\sigma_3 + 2S_{12}\sigma_1 + \left(S_{11}(\sigma_1 - \sigma_3) + S_{12}(\sigma_3 - \sigma_1)\right)\sin^2\psi . \qquad \text{(A1.2)}$$

where S_{ij} are the elastic compliances. Hence, the strain state is linear with $\sin^2\psi$ and the stress state can be determined by measuring the strain in two ψ orientations only. Since the stress in the (001) plane is uniform, measurements in only one φ orientation are necessary. The stresses can be calculated by measuring the slope of the d vs. $\sin^2\psi$ plot and by determining the intercept (ψ=0):

$$\frac{\partial \varepsilon_\psi}{\partial \sin^2\psi} = S_{11}(\sigma_1 - \sigma_3) + S_{12}(\sigma_3 - \sigma_1), \text{ and} \qquad \text{(A1.3a)}$$

$$\varepsilon_{\psi=0} = S_{11}\sigma_3 + 2S_{12}\sigma_1 . \qquad \text{(A1.3b)}$$

Since this result assumes that the specimen is a single crystal, the measurements can only be made at the ideal orientations. This treatment should also apply to other textures, but care must be taken that the orientations used are the ideal orientations for the texture component being examined. In principle, therefore, this technique can be used to determine the residual stresses in each texture component of a complex textured material. In practice however, this becomes difficult as some components may have reflections very close to each other in (φ,ψ) space.

Lastly, the single crystal elastic compliances must be rotated to align with the texture. Since the texture in this study is an <001> fibre texture, no rotation is necessary. The values of the elastic compliances used were the temperature dependent compliances measured by Sutton[61] and are reproduced in Figure A1.1 together with a polynomial fit.

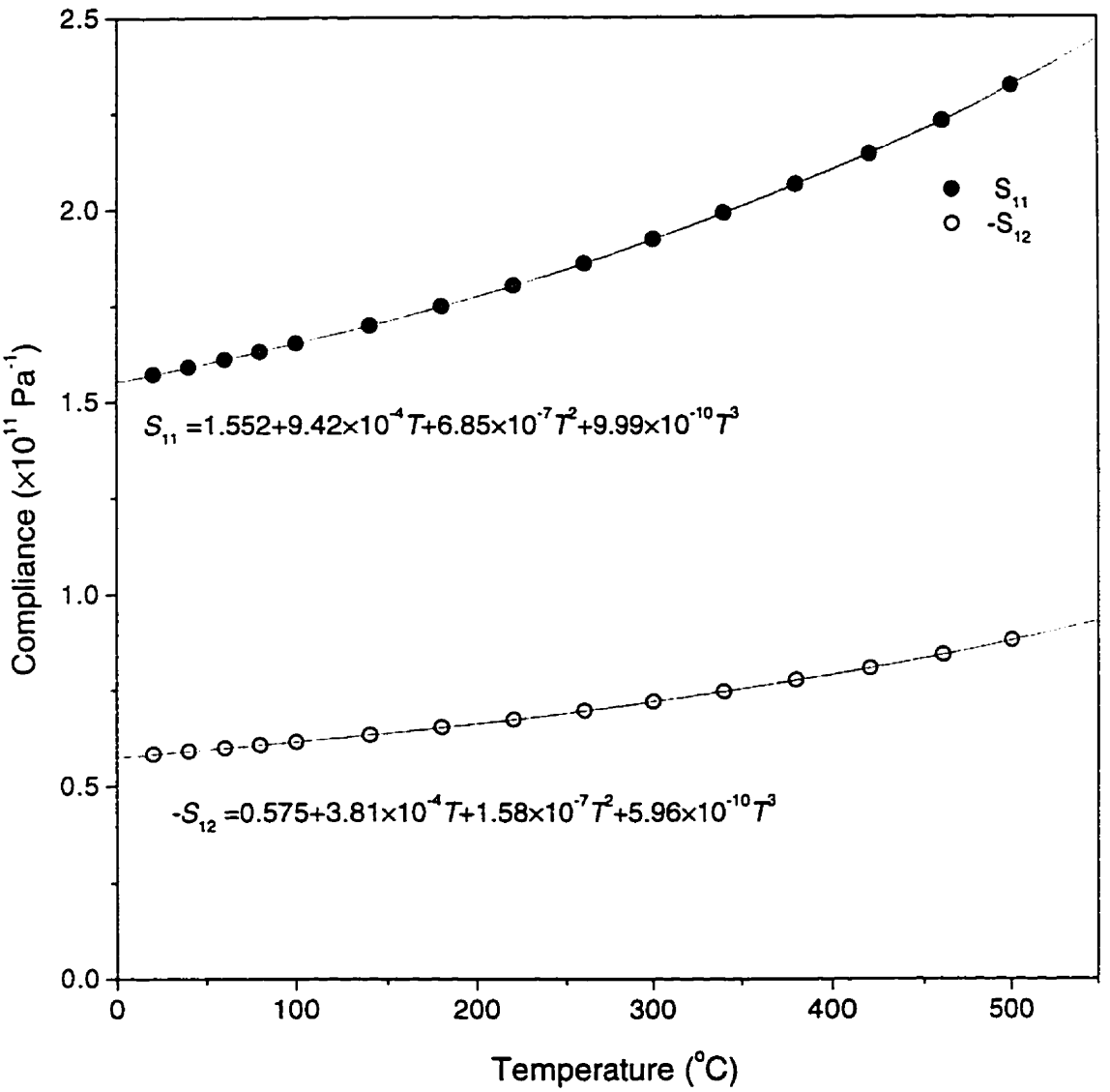

Figure A1.1: Single Crystal Elastic Compliances vs. Temperature
Data measured by P.M. Sutton.[61]

Appendix 2
Stress vs. Time and Stress vs. Temperature Plots of All Data Reduced in this Study

This appendix contains the stress vs. temperature and stress vs. time data reduced in this study. Data from runs 4,5,6 could not be reduced due to experimental difficulties with software. The temperature control for runs 1–3 was found to under–estimate the temperature by approximately 15%. This was due to a poor thermocouple connection with the specimen. The temperature shown for these graphs is therefore the estimated temperature. The temperatures in the other plots are 'as measured'.

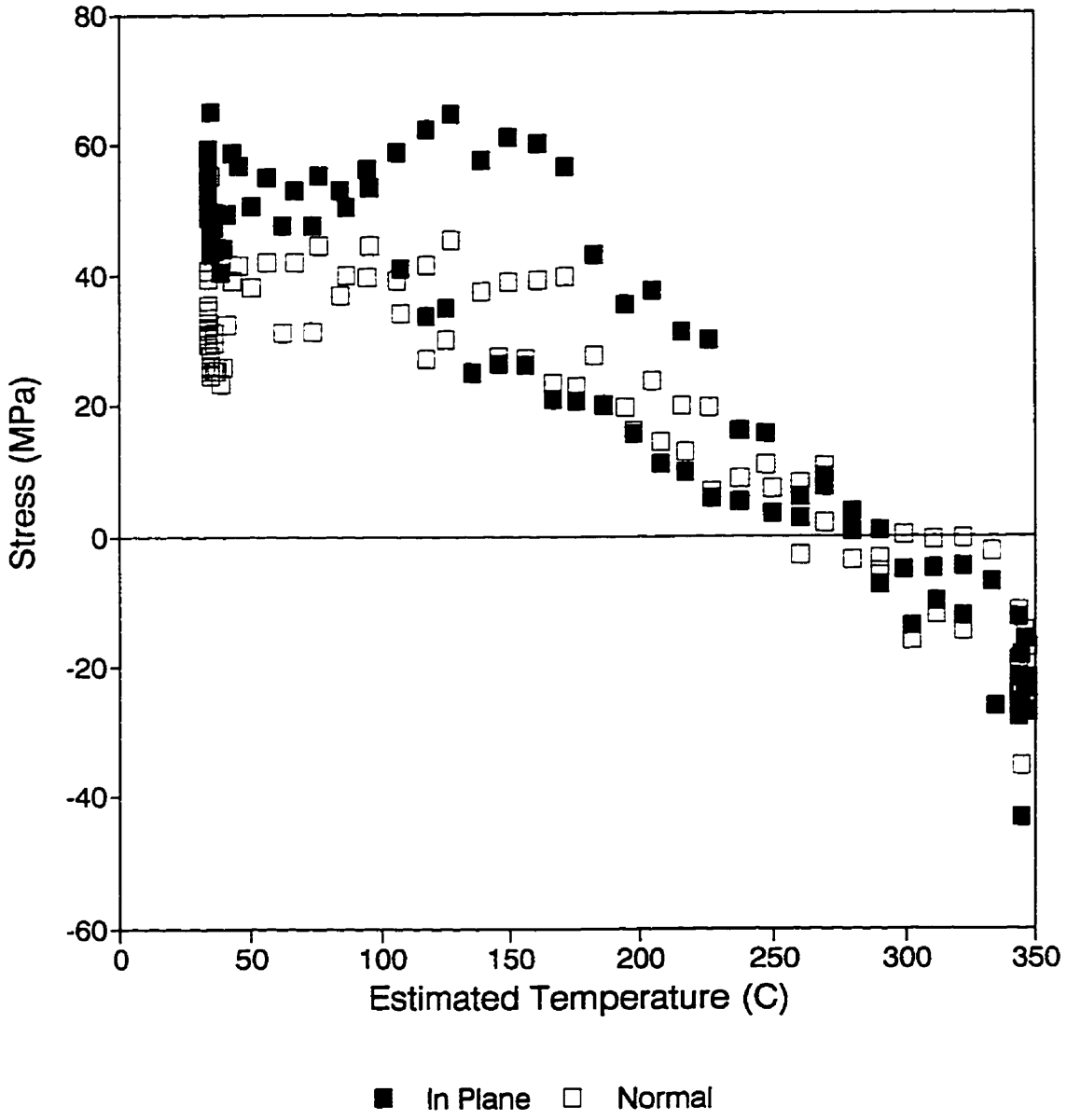

Figure A2.1: Stress vs. temperature data for run #1, a slow cycle run with 5°C/min heating and cooling rates.

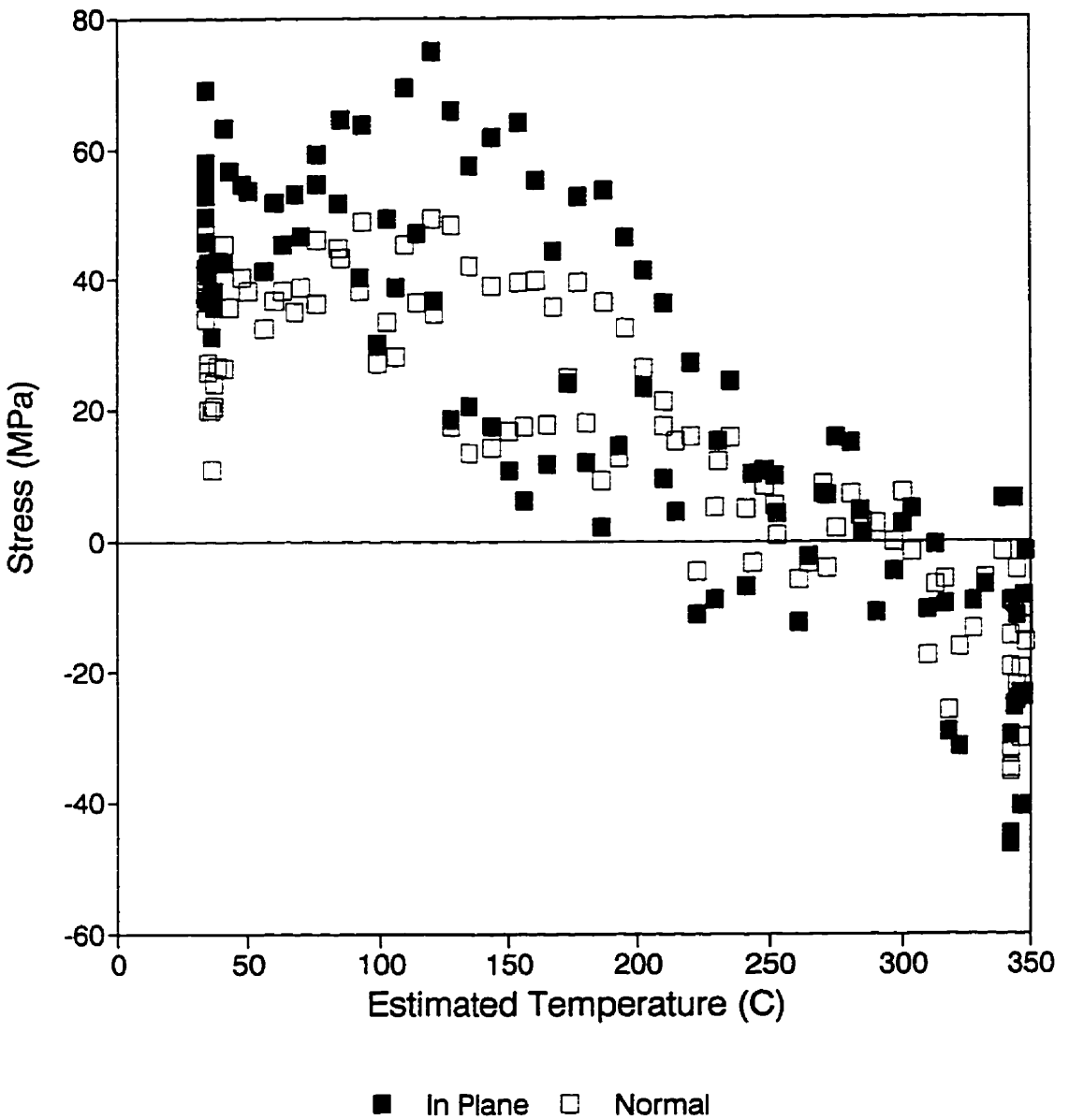

Figure A2.2: Stress vs. temperature data for run #2, a slow cycle run with 5°C/min heating and cooling rates.

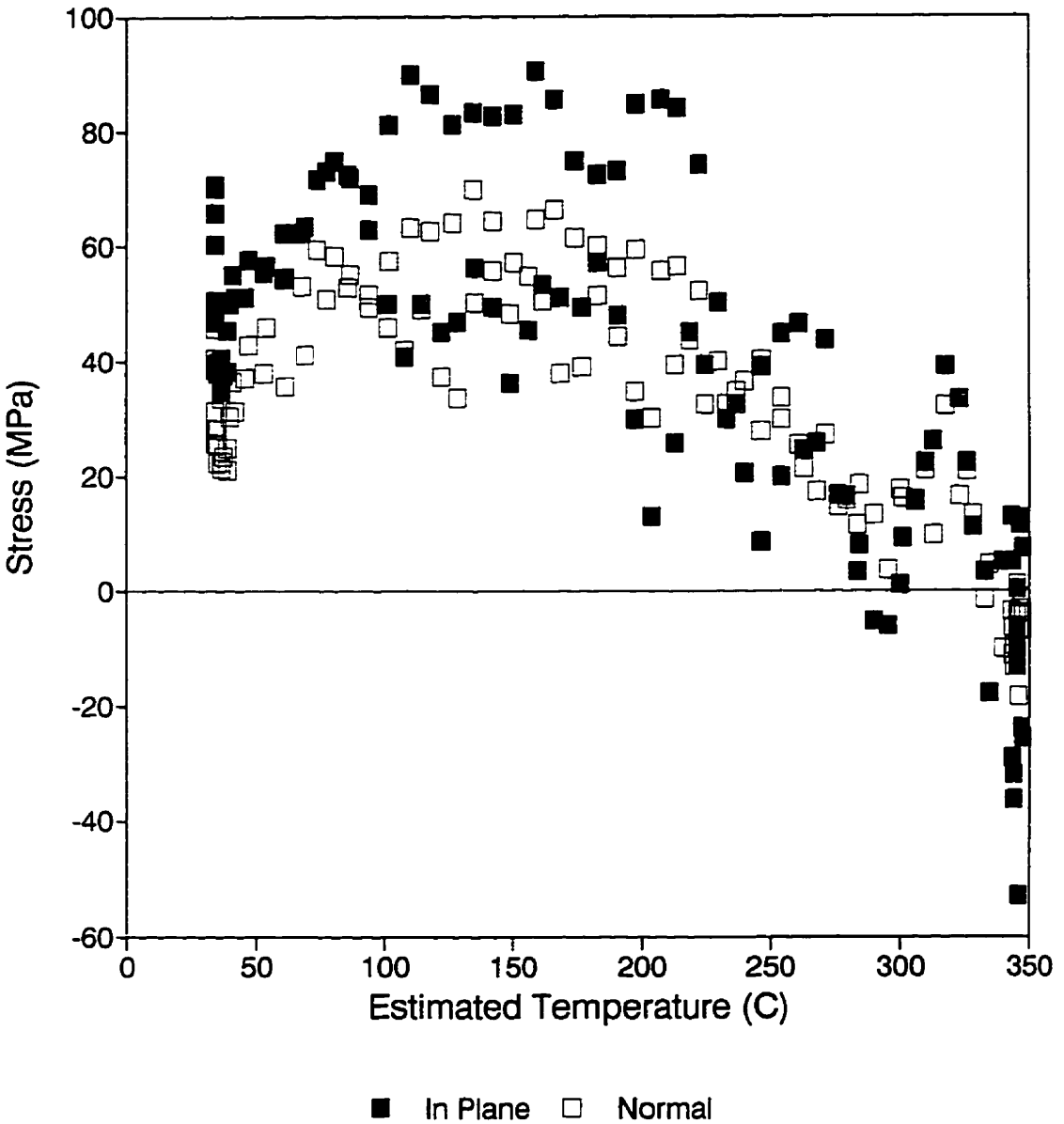

Figure A2.3: Stress vs. temperature data for run #3, a slow cycle run with 5°C/min heating and cooling rates.

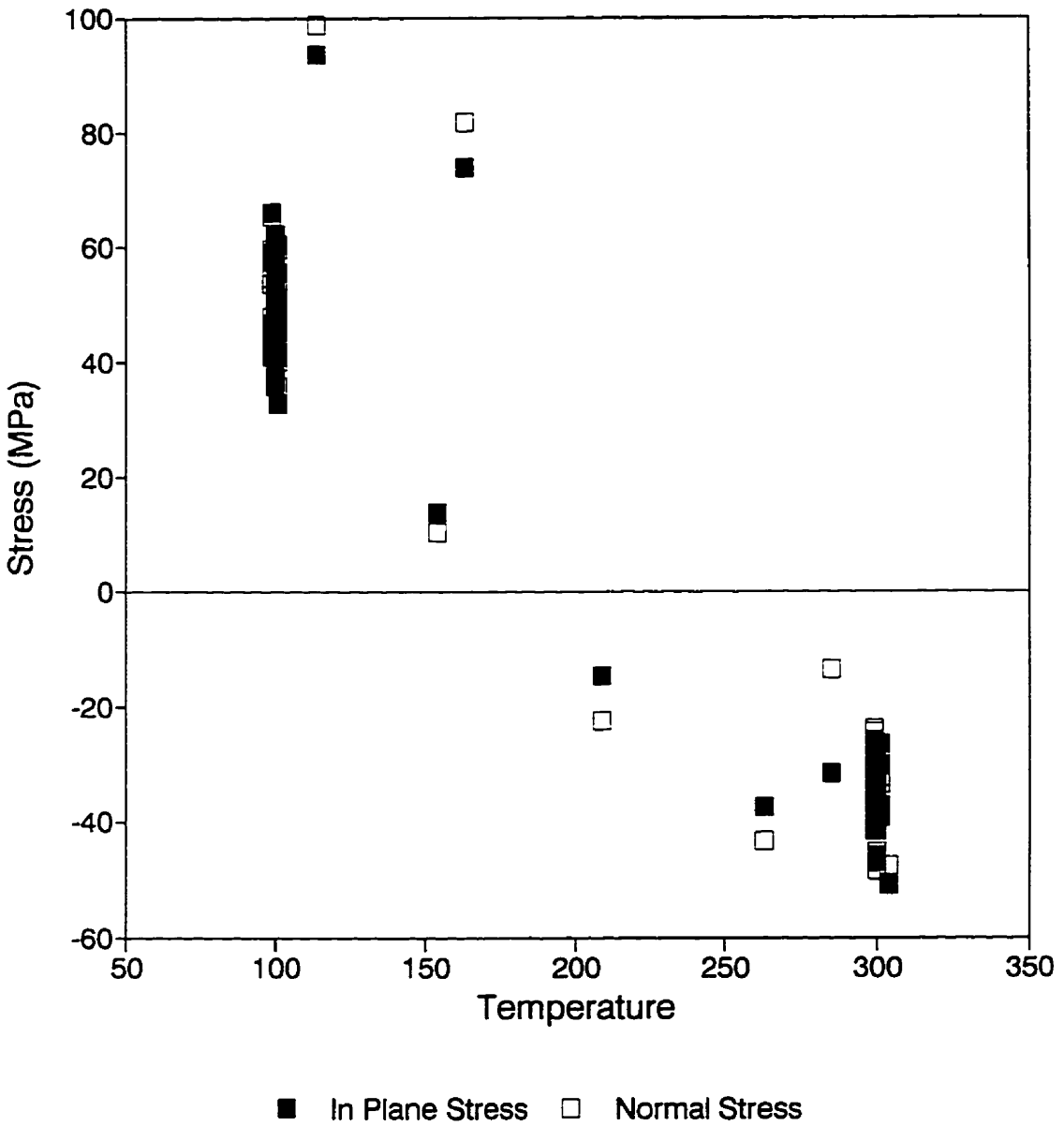

Figure A2.4: Stress vs. temperature data for the symmetric pair of runs 7 & 8. Data was collected during rapid heating from 100°C to 300°C and also during the quench. Data was not collected at temperatures below 100°C.

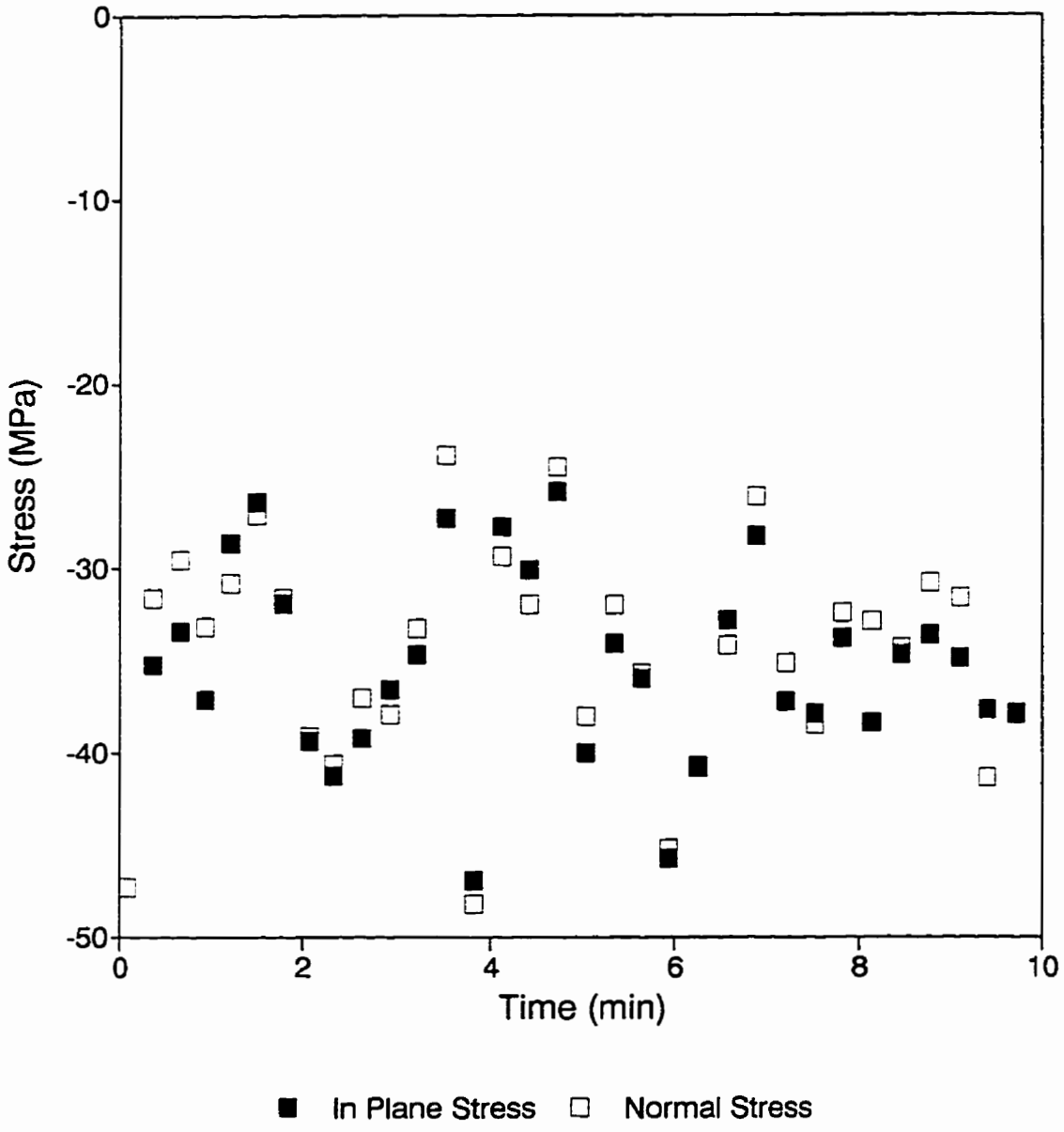

Figure A2.5: Stress vs. time data for the symmetric pair 7&8 at 300°C after rapid heating from 100°C.

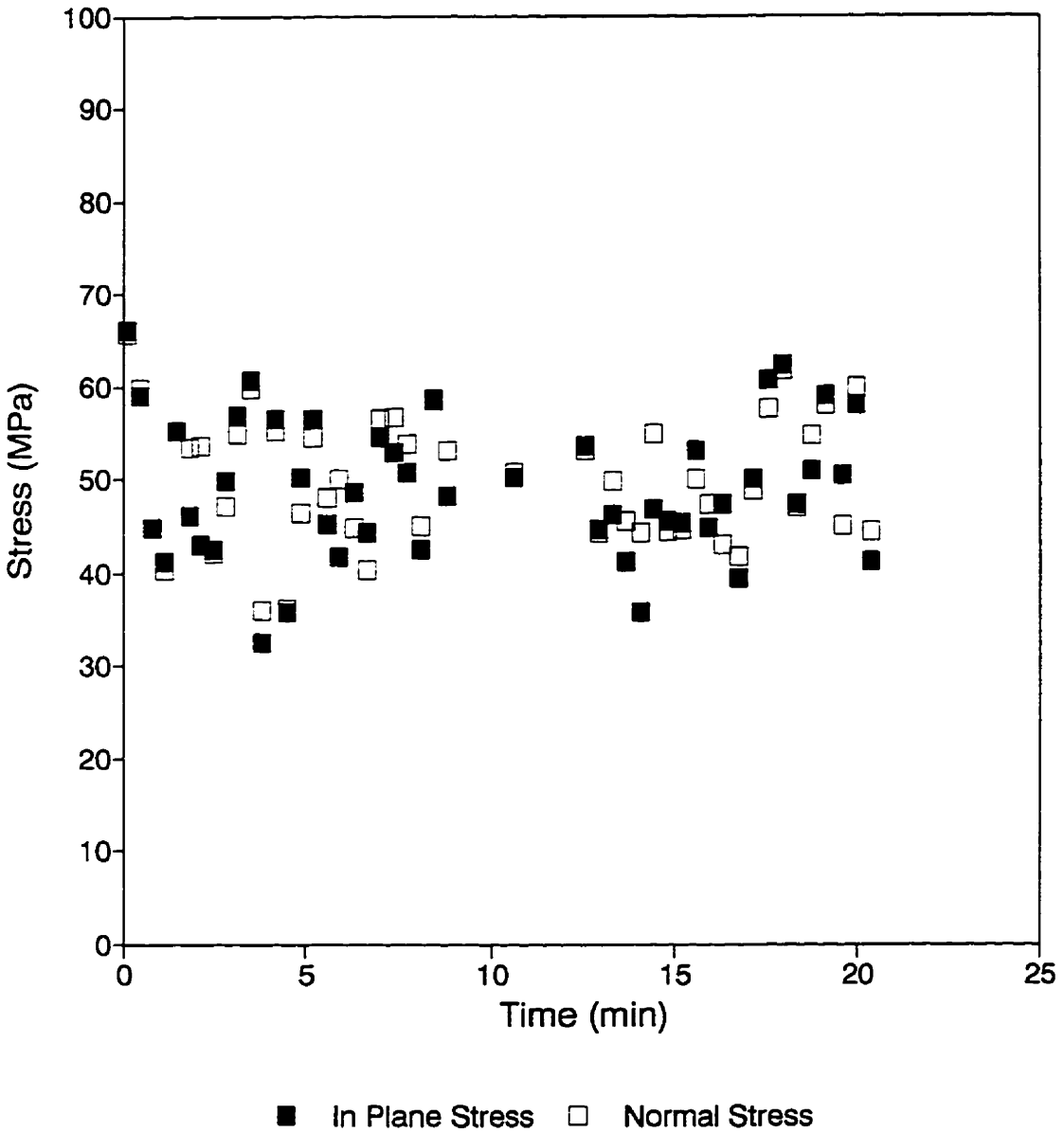

Figure A2.6: Stress vs. time data for the symmetric pair 7&8 at 100°C after rapid cooling from 300°C.

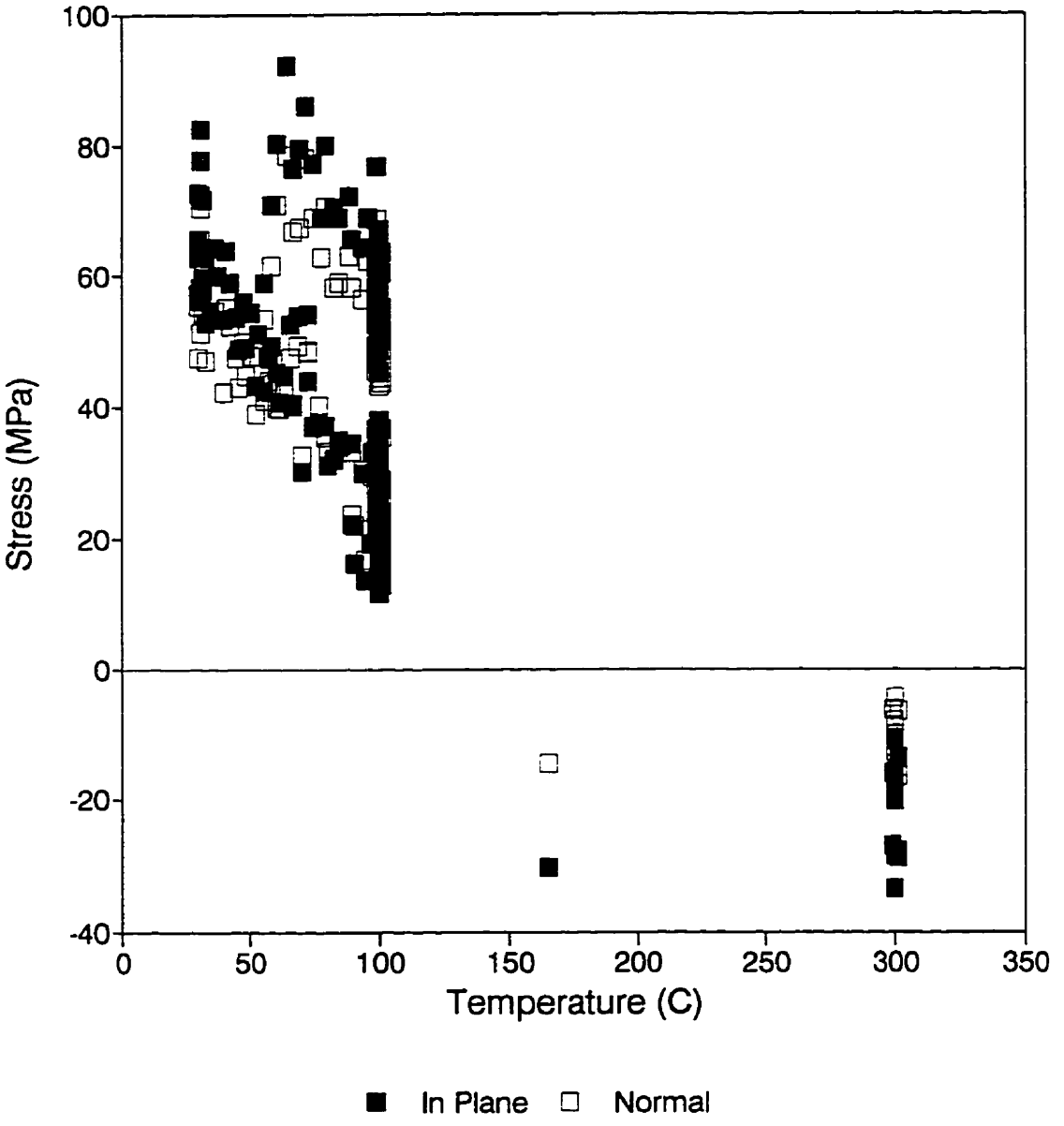

Figure A2.7: Stress vs. temperature data for the symmetric pair 9&10 showing the complete thermal cycle.

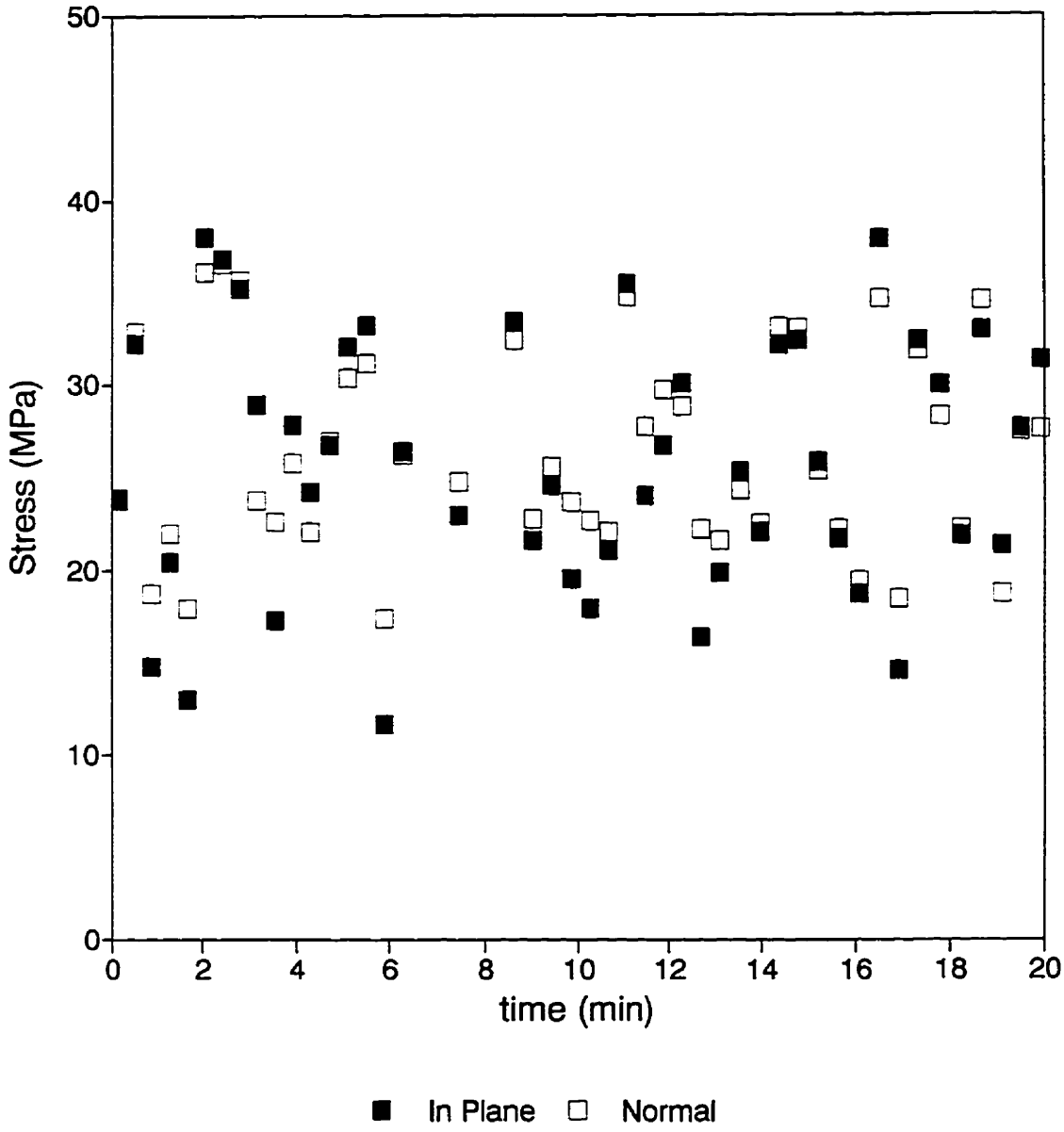

Figure A2.8: Stress vs. time data for the symmetric pair 9&10 at 100°C after slow heating from ambient temperature.

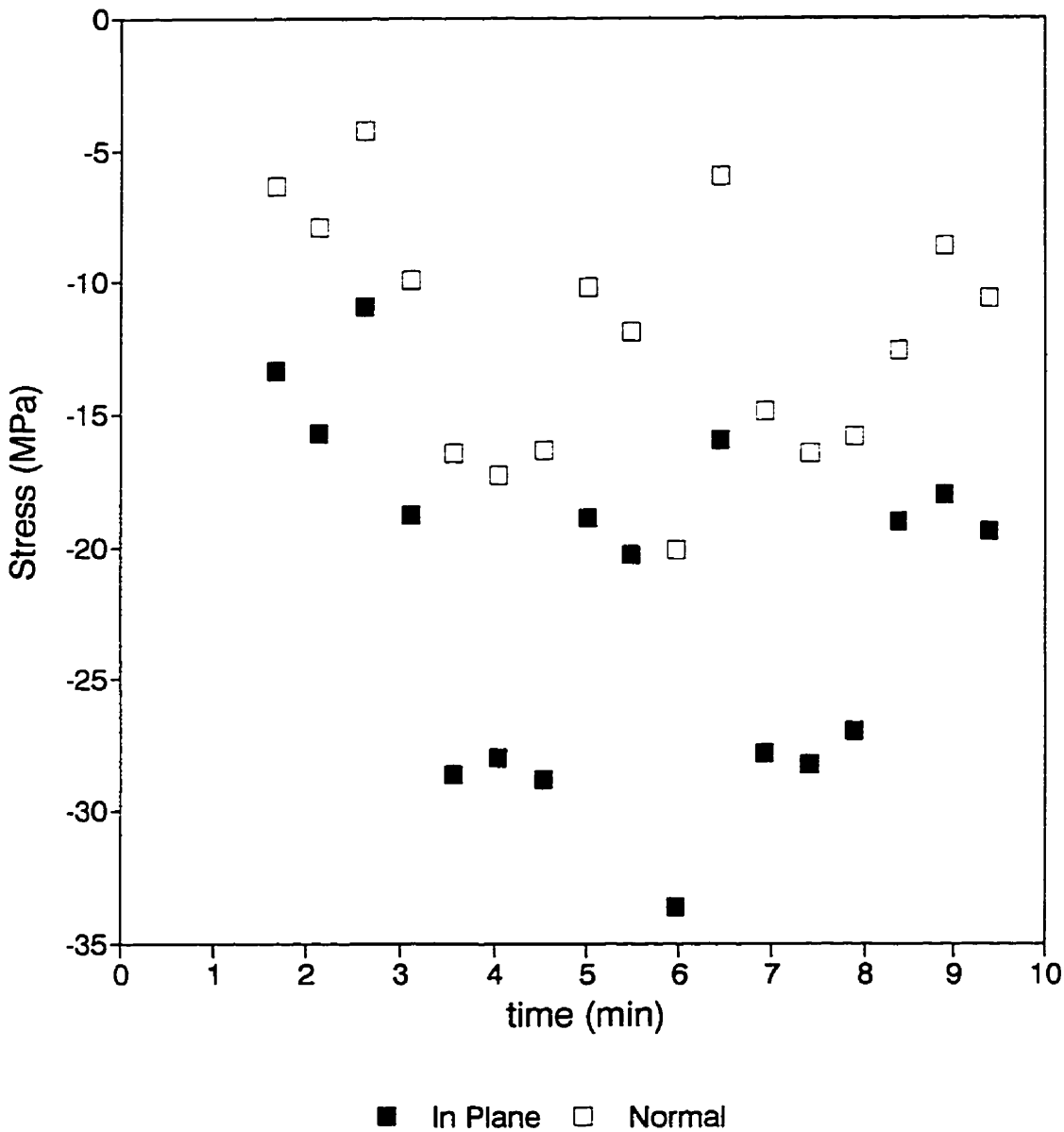

Figure A2.9: Stress vs. time data for the symmetric pair 9&10 at 300°C after rapid heating from 100°C.

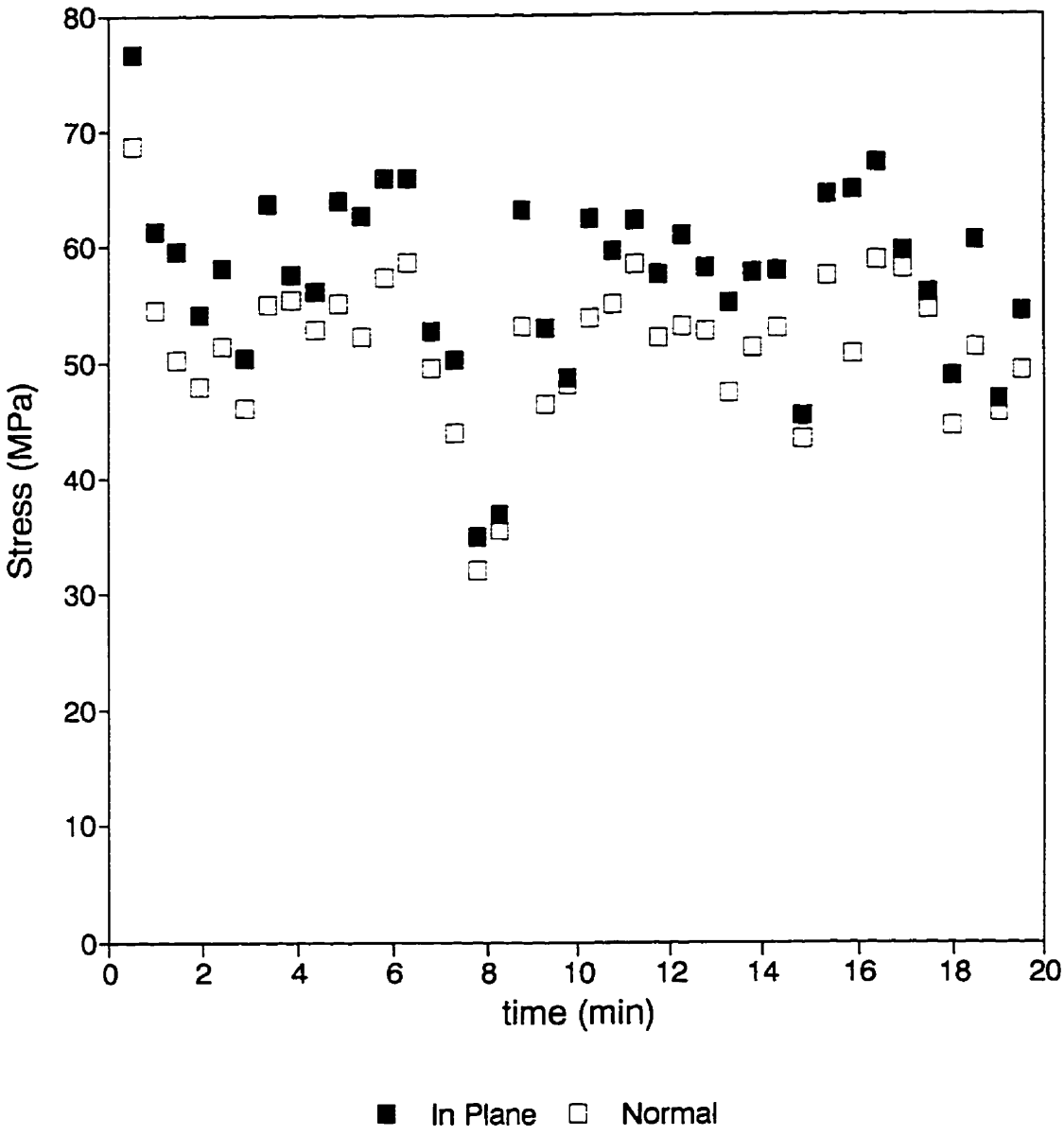

Figure A2.10: Stress vs. time data for the symmetric pair 9&10 at 100°C after rapid cooling from 300°C.

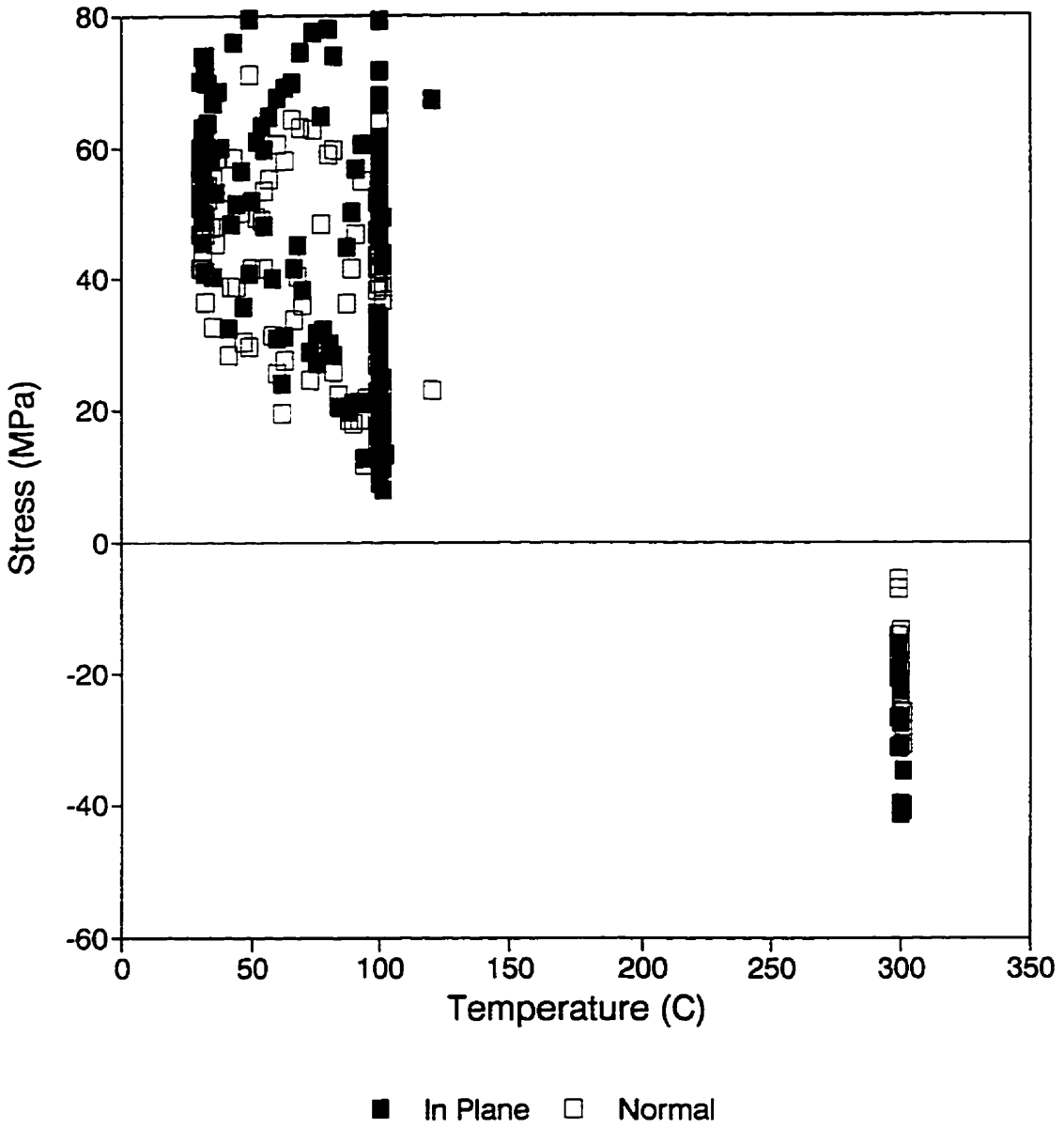

Figure A2.11: Stress vs. temperature data for the symmetric pair 11&12 showing the complete thermal cycle.

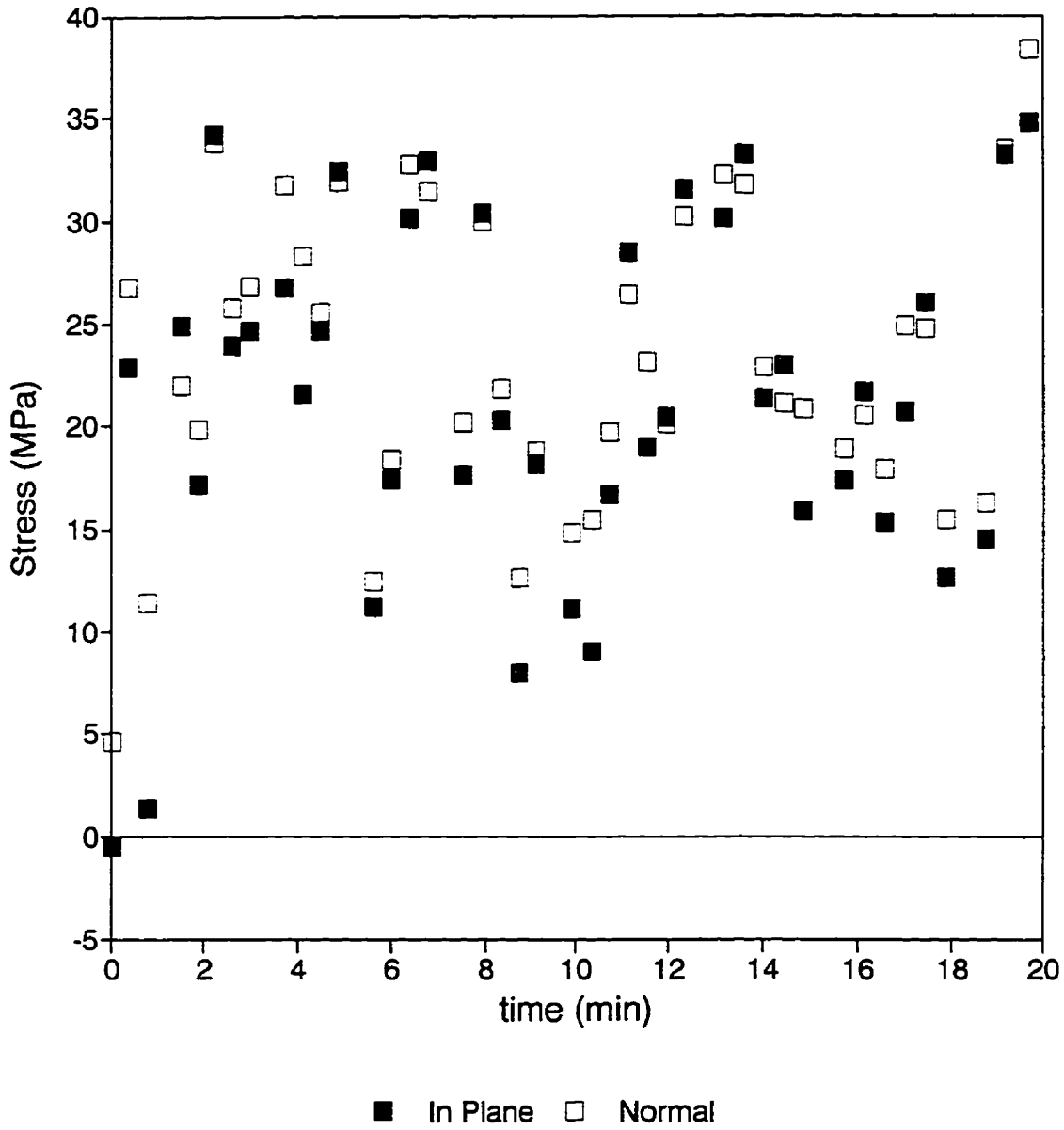

Figure A2.12: Stress vs. time data for the symmetric pair 11&12 at 100°C after slow heating from ambient temperature.

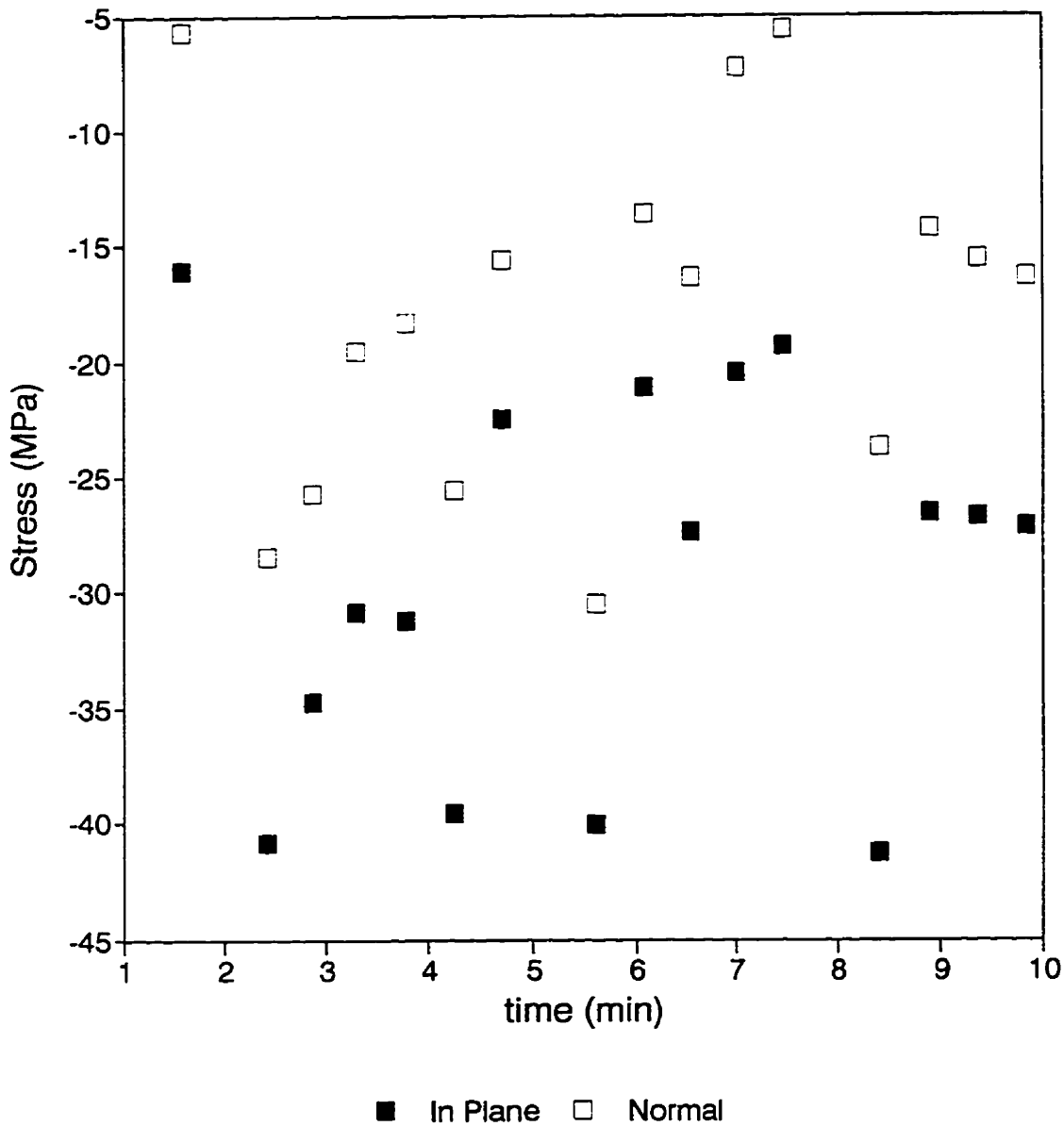

Figure A2.13: Stress vs. time data for the symmetric pair 11&12 at 300°C after rapid heating from 100°C.

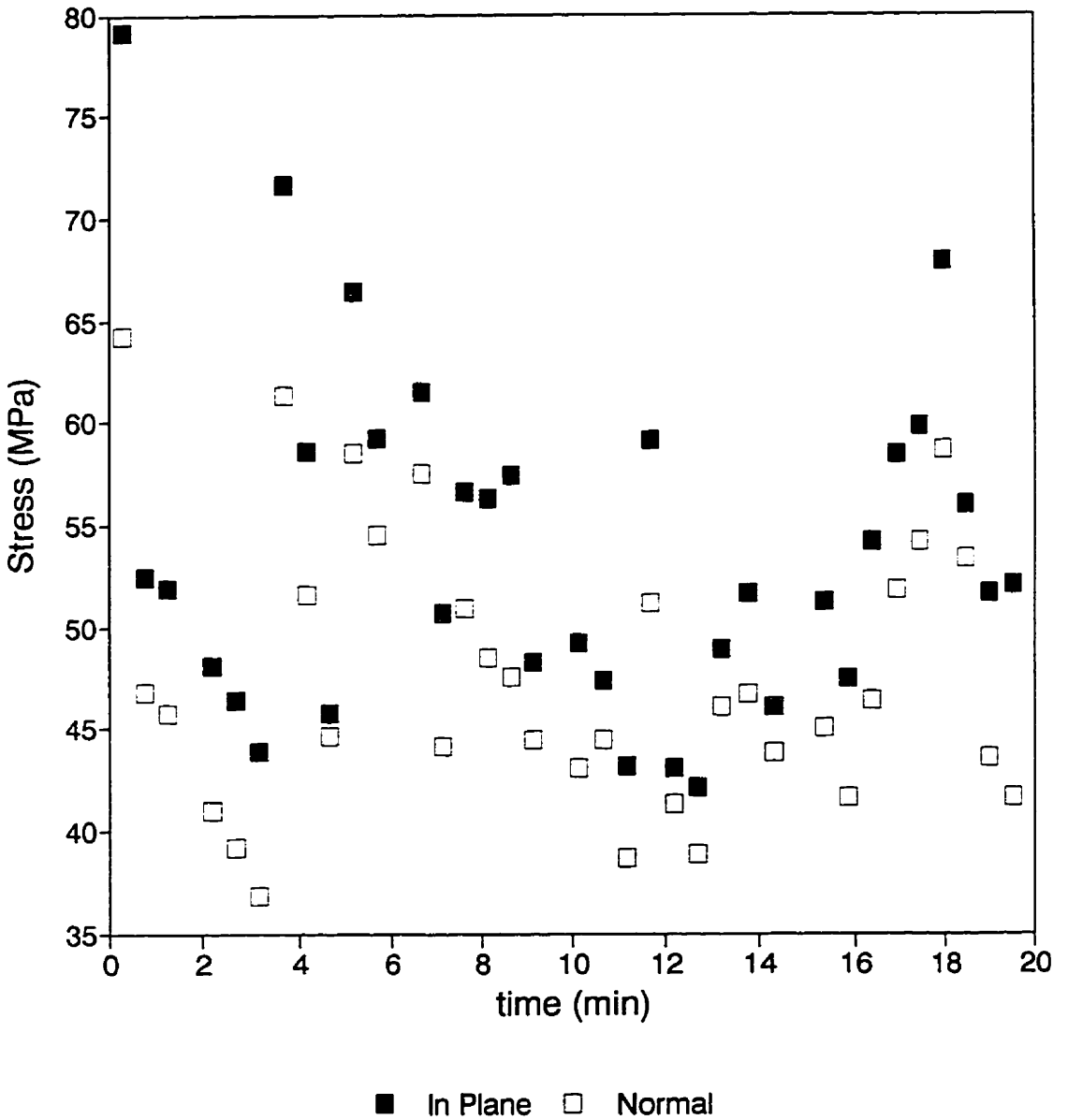

Figure A2.14: Stress vs. time data for the symmetric pair 11&12 at 100°C after rapid cooling from 300°C.

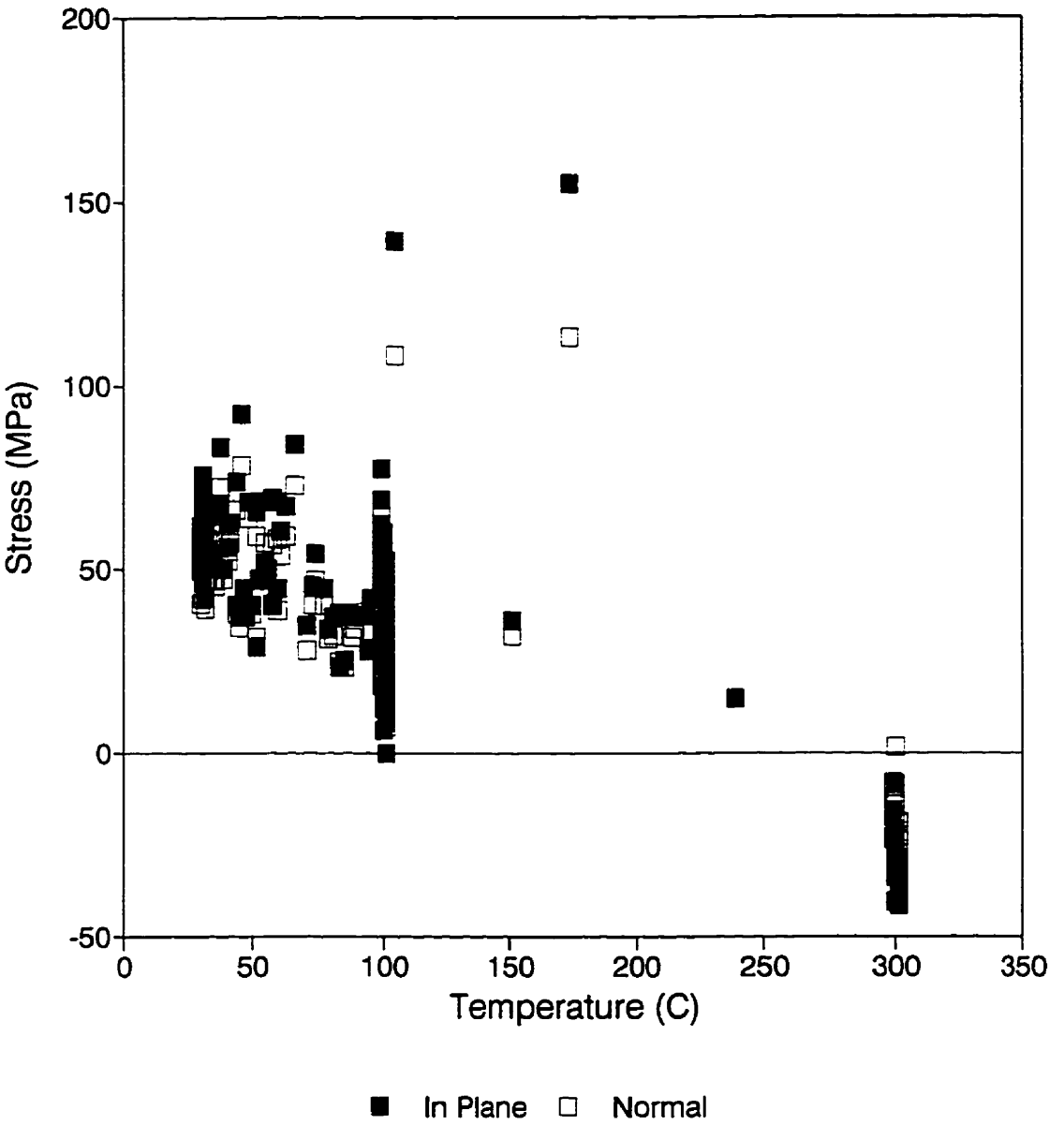

Figure A2.15: Stress vs. temperature data for the symmetric pair 13&14 showing the complete thermal cycle.

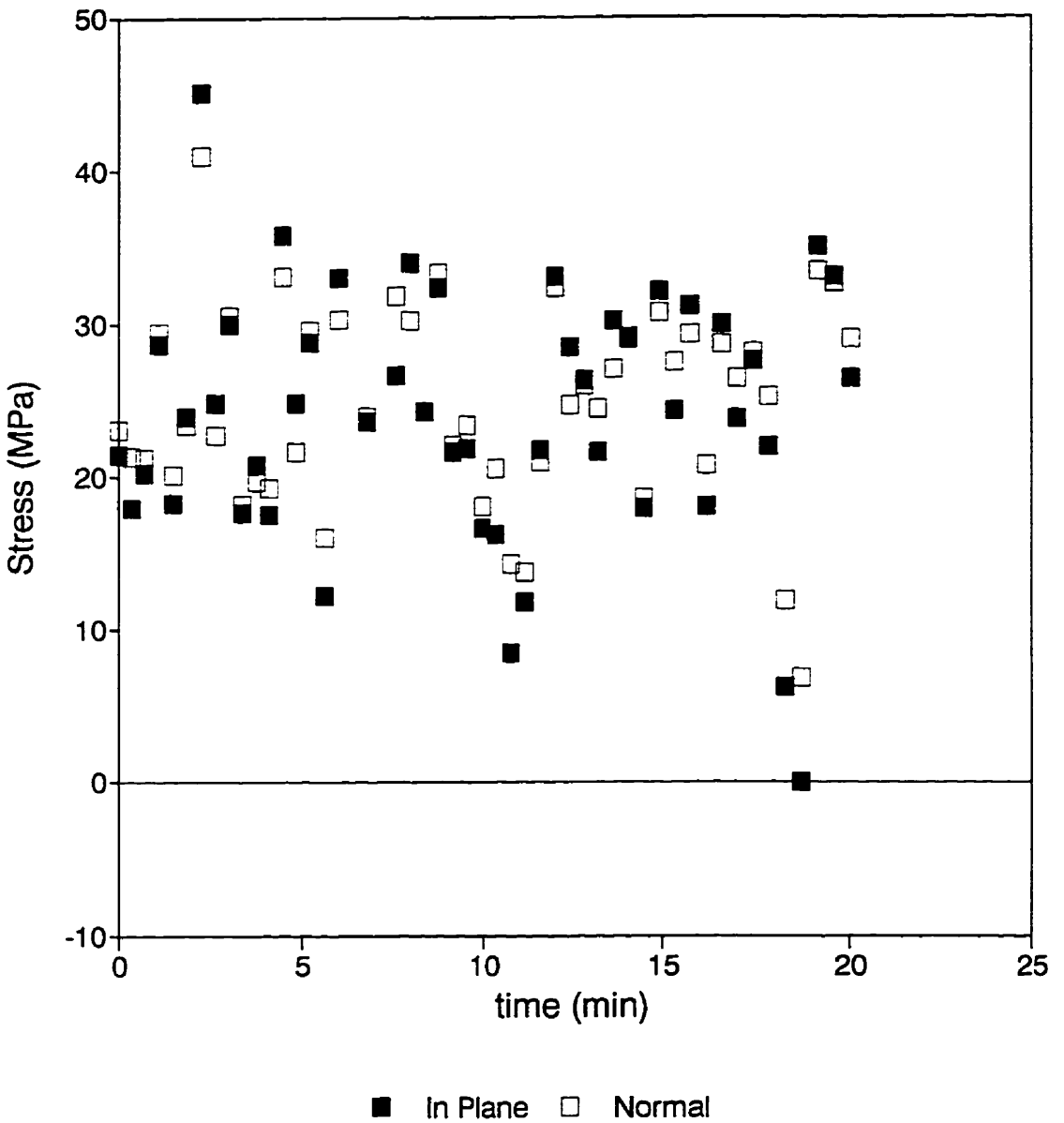

Figure A2.16: Stress vs. time data for the symmetric pair 13&14 at 100°C after slow heating from ambient temperature.

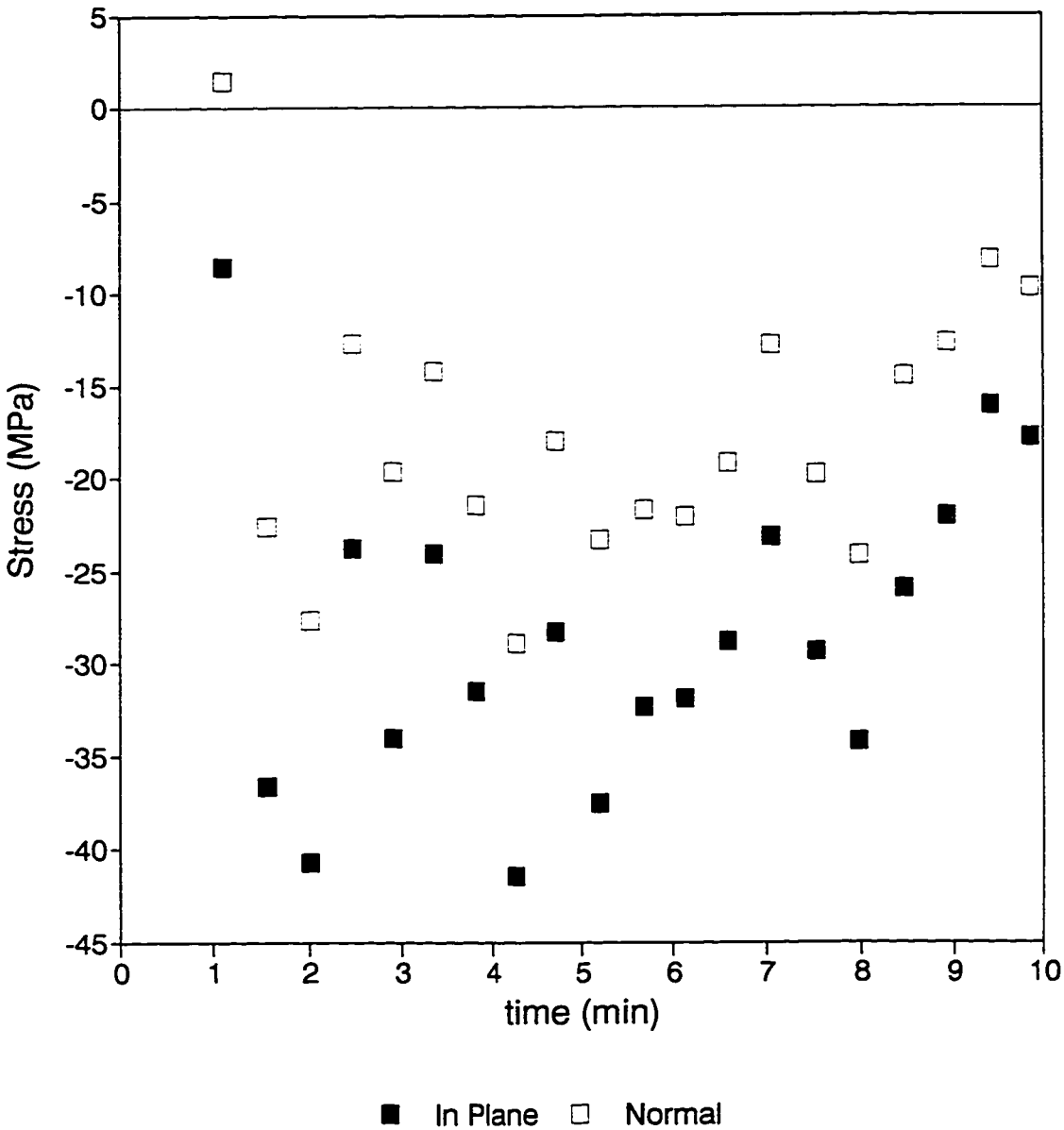

Figure A2.17: Stress vs. time data for the symmetric pair 13&14 at 300°C after rapid heating from 100°C.

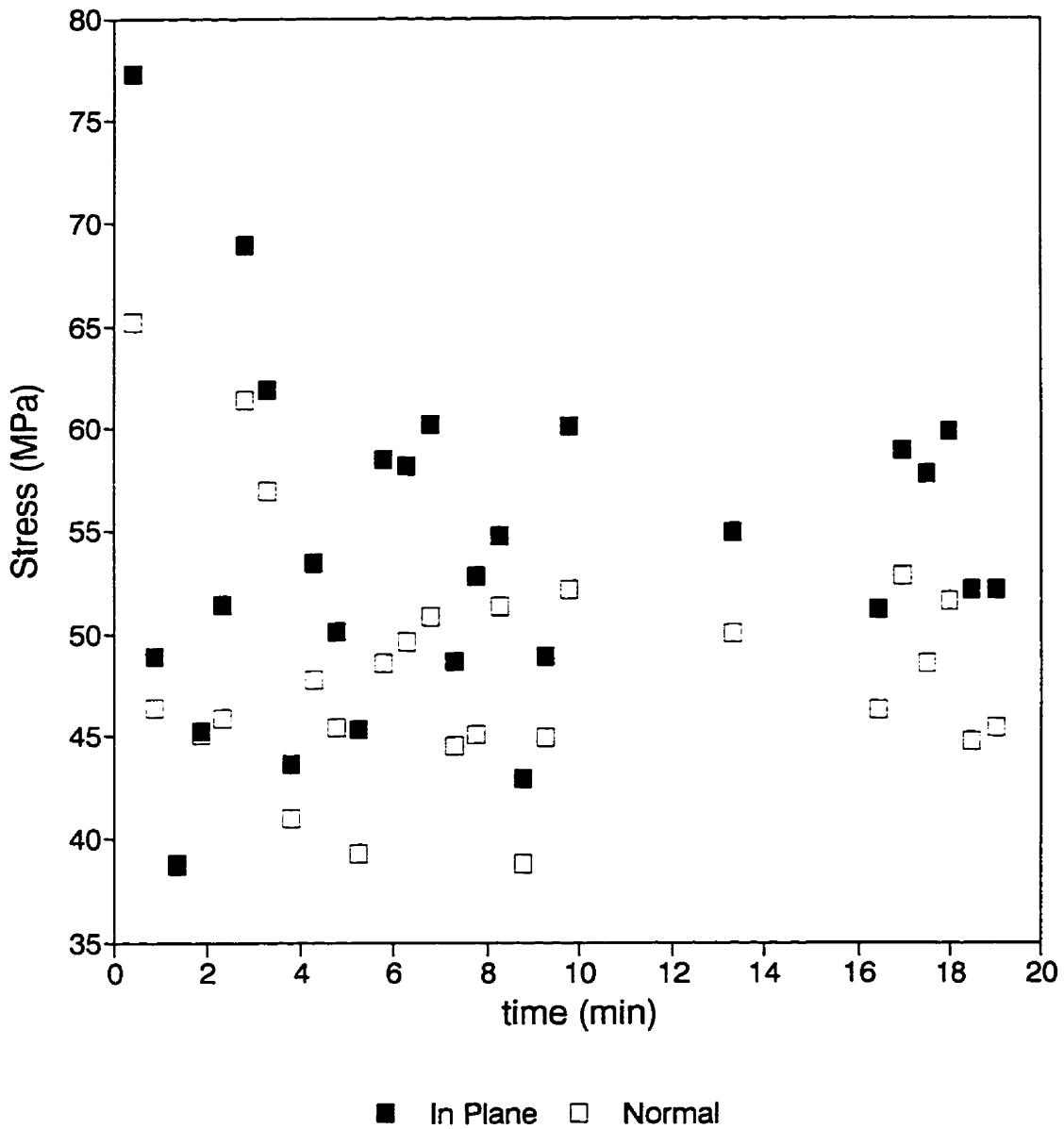

Figure A2.18: Stress vs. time data for the symmetric pair 13&14 at 100°C after rapid cooling from 300°C.

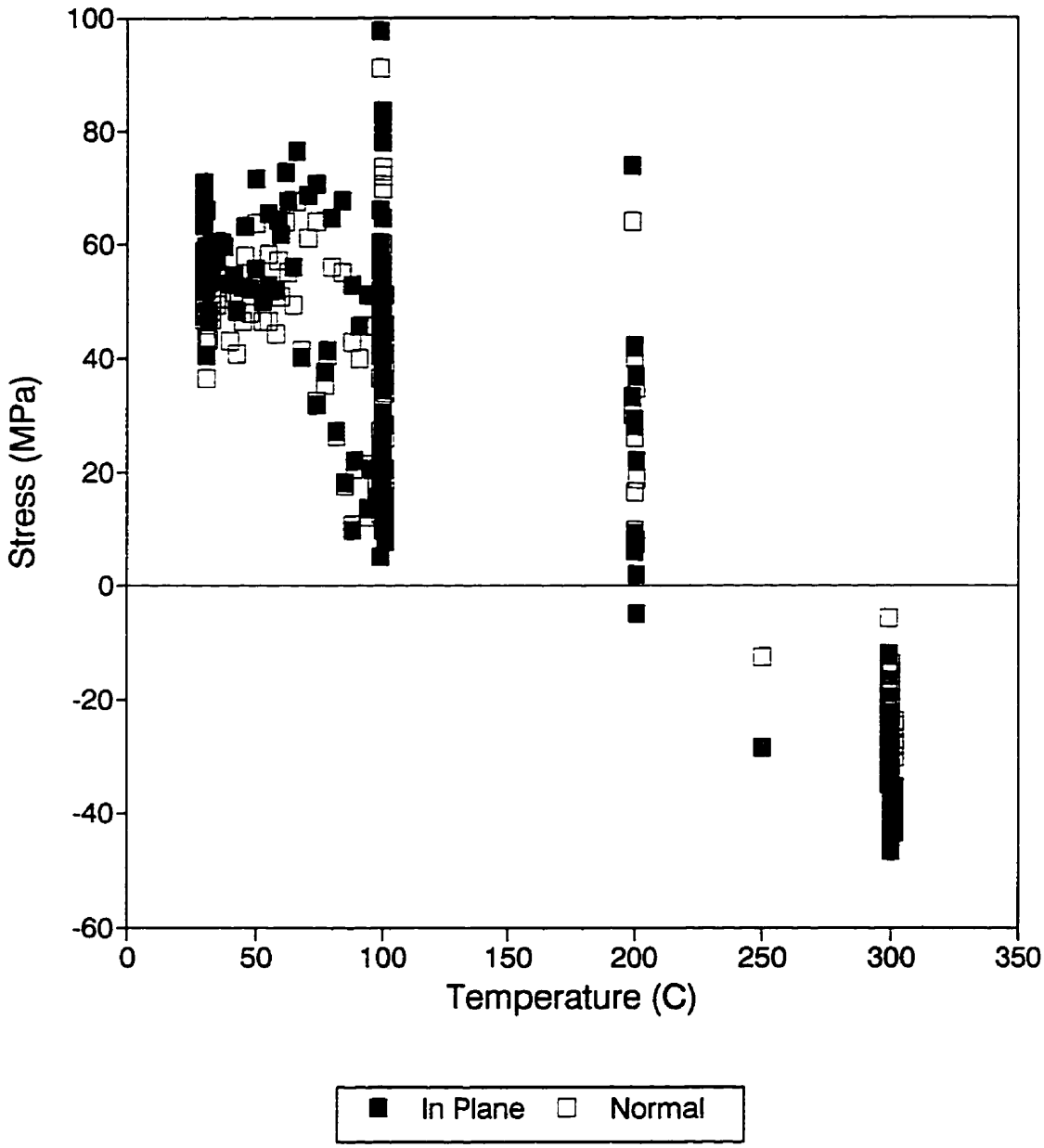

Figure A2.19: Stress vs. temperature data for run 15 showing the complete thermal cycle.

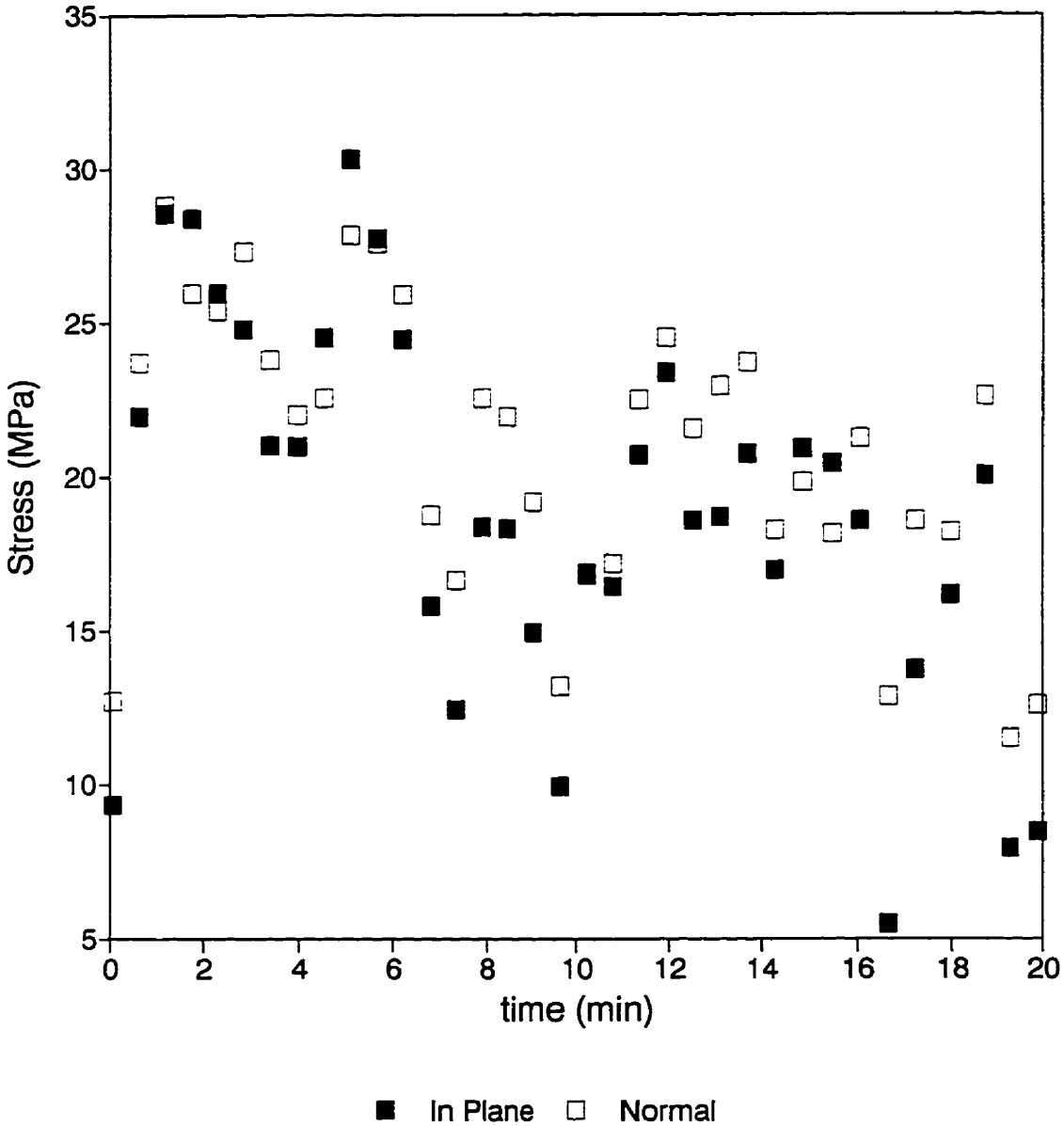

Figure A2.20: Stress vs. time data for run 15 at 100°C after slow heating from ambient temperature.

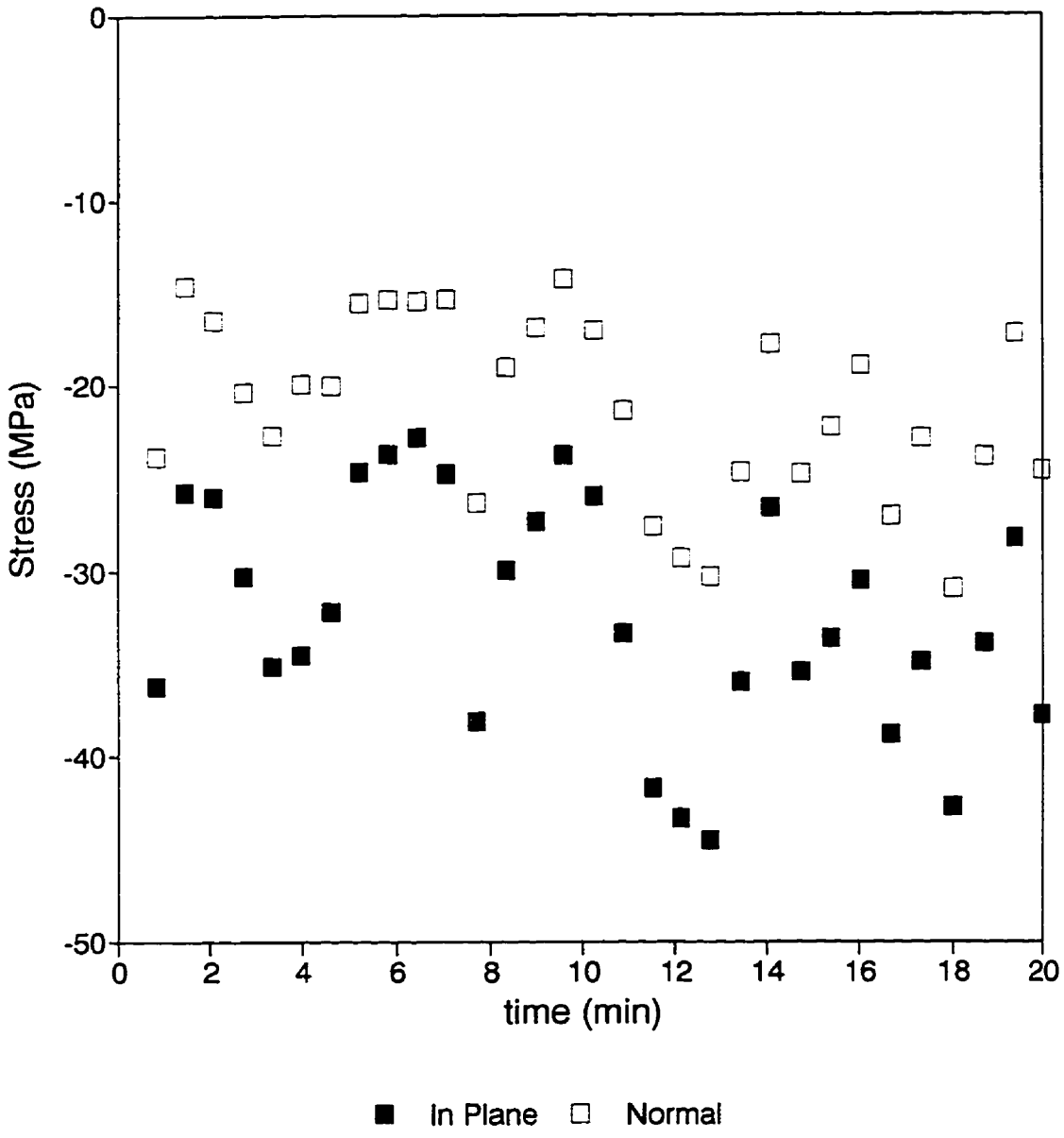

Figure A2.21: Stress vs. time data for run 15 at 300°C after rapid heating from 100°C.

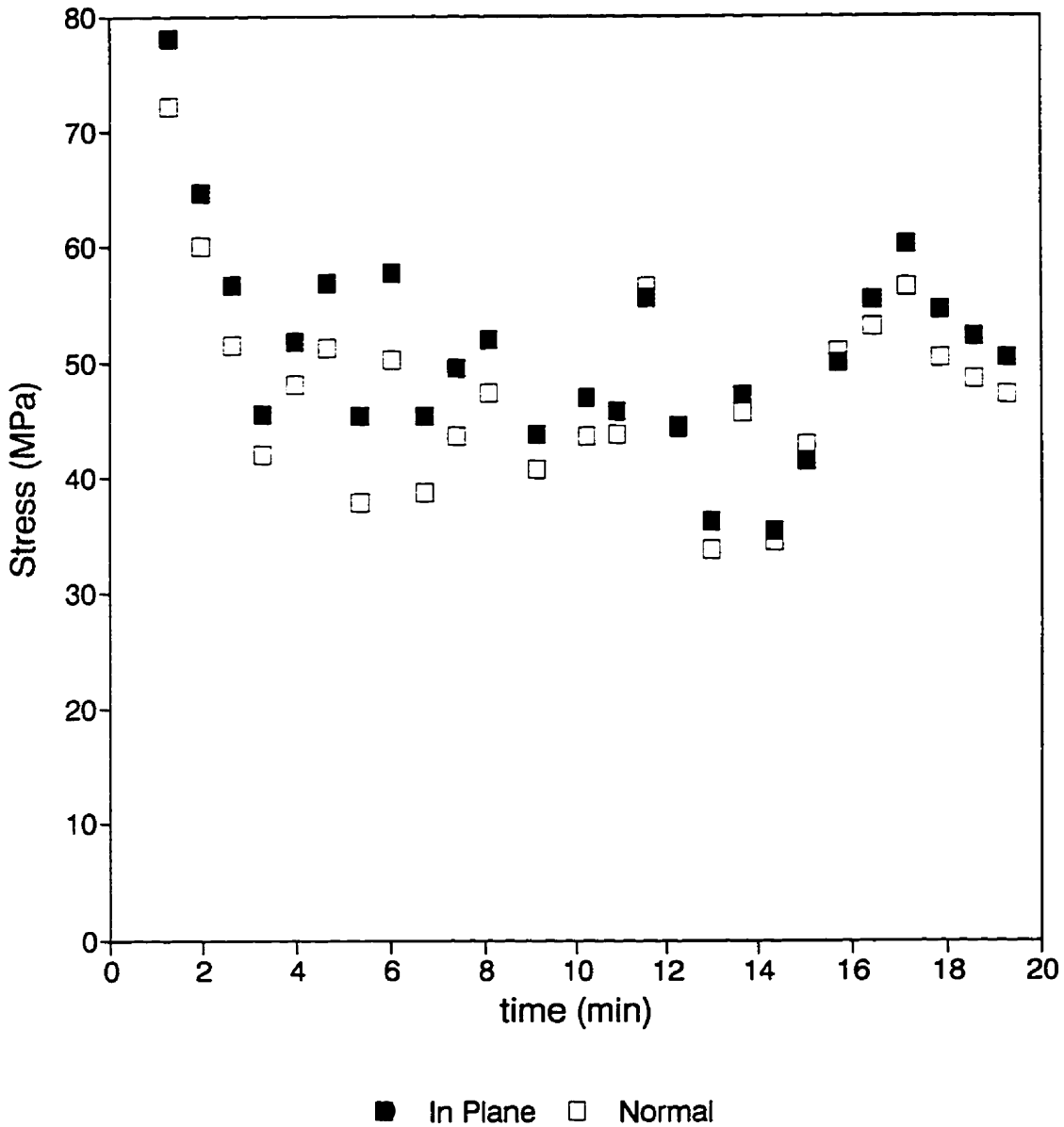

Figure A2.22: Stress vs. time data for run 15 at 100°C after rapid cooling from 300°C.

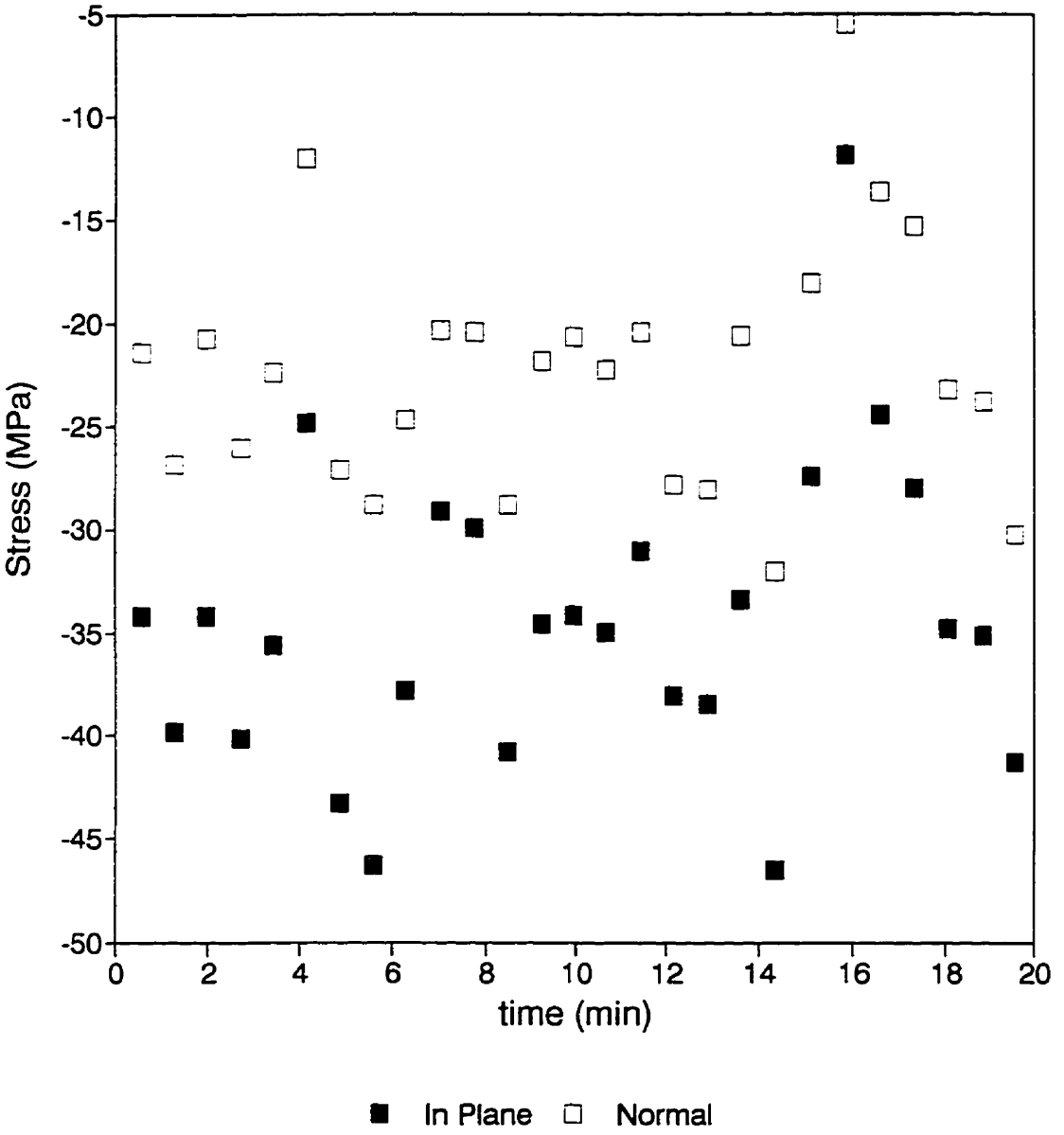

Figure A2.23: Stress vs. time data for run 15 at 300°C after rapid heating from 100°C in the second cycle.

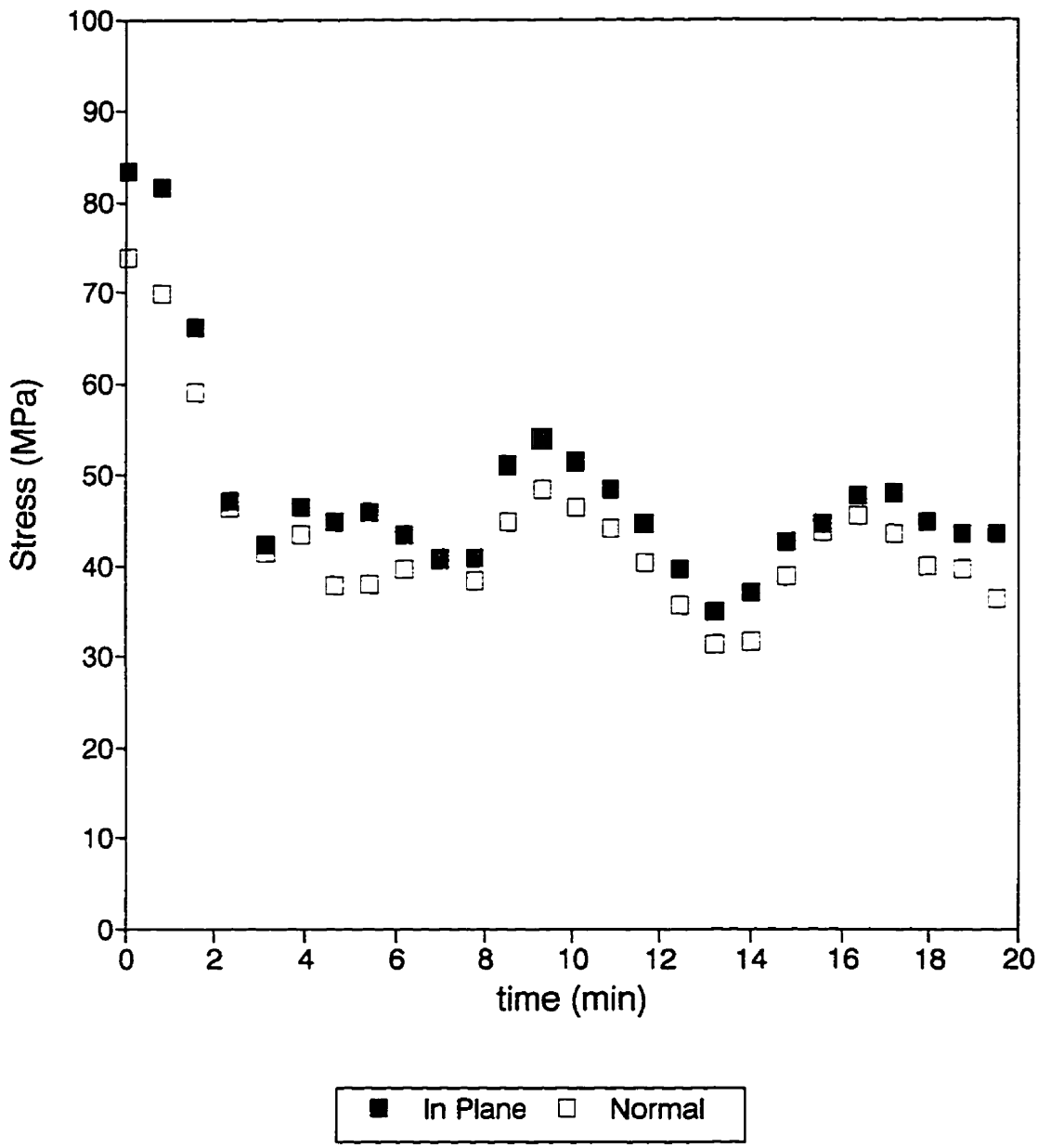

Figure A2.24: Stress vs. time data for run 15 at 100°C after rapid cooling from 300°C at the end of the second cycle.

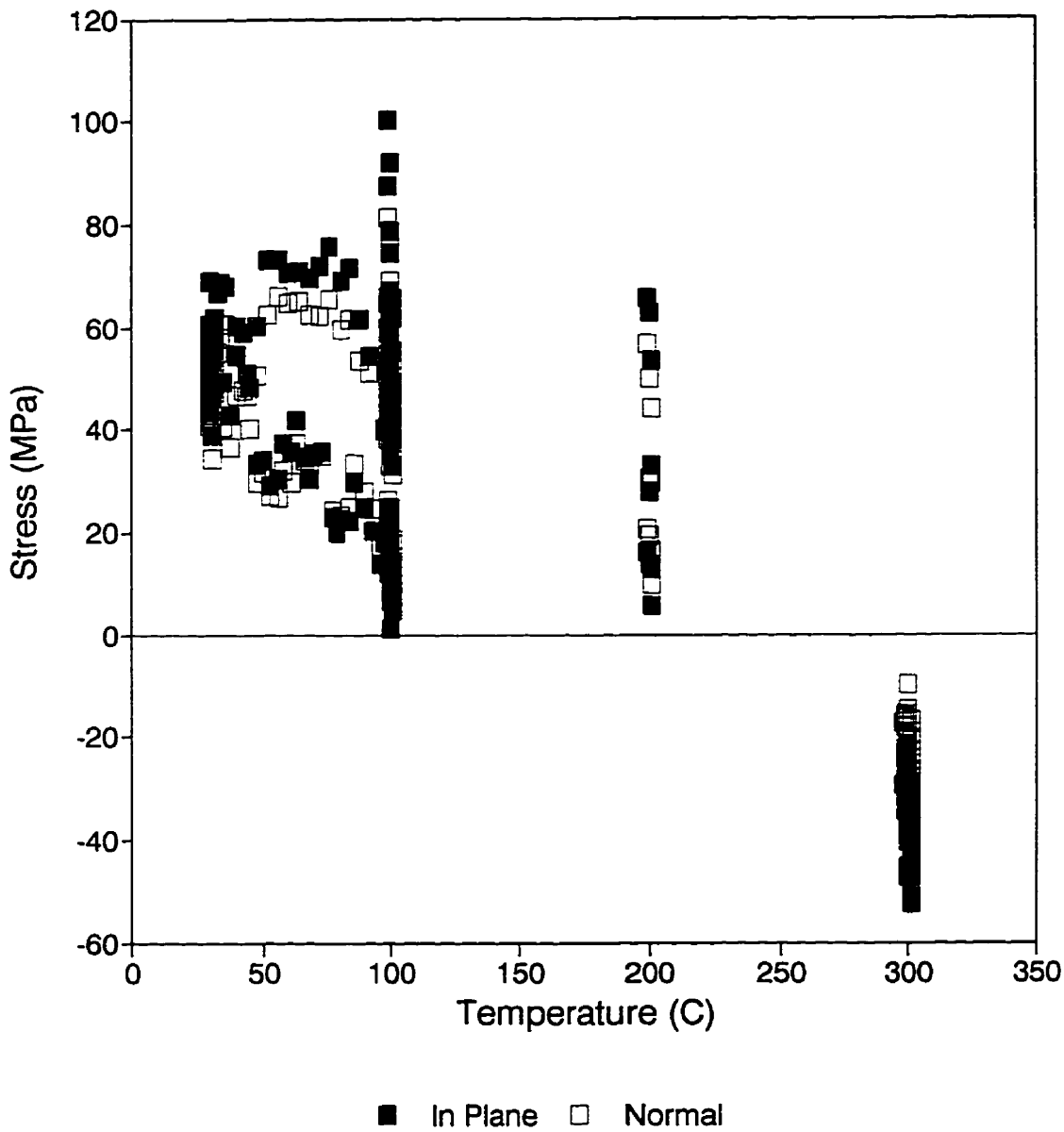

Figure A2.25: Stress vs. temperature data for run 16 showing the complete thermal cycle.

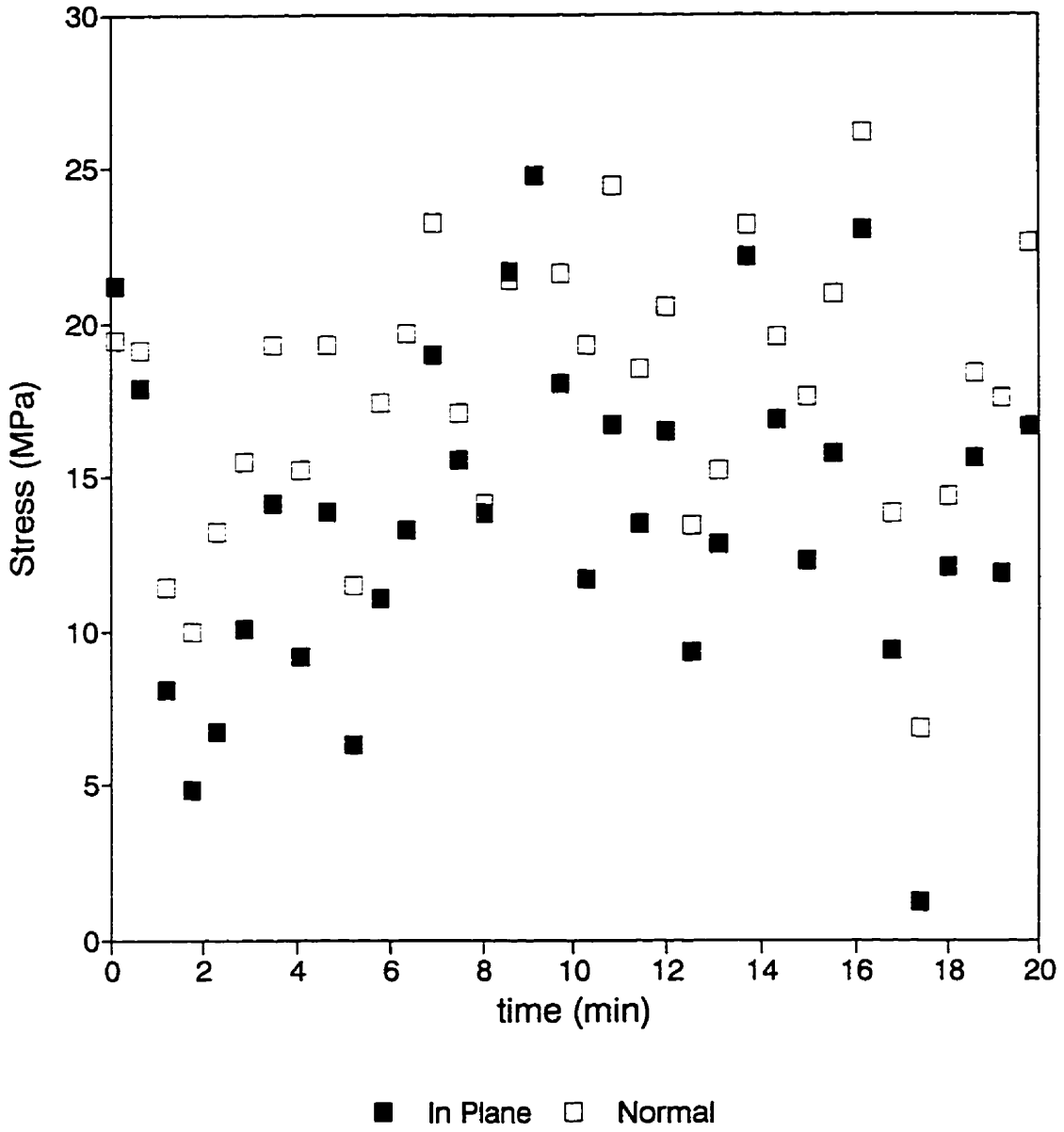

Figure A2.26: Stress vs. time data for run 16 at 100°C after slow heating from ambient temperature.

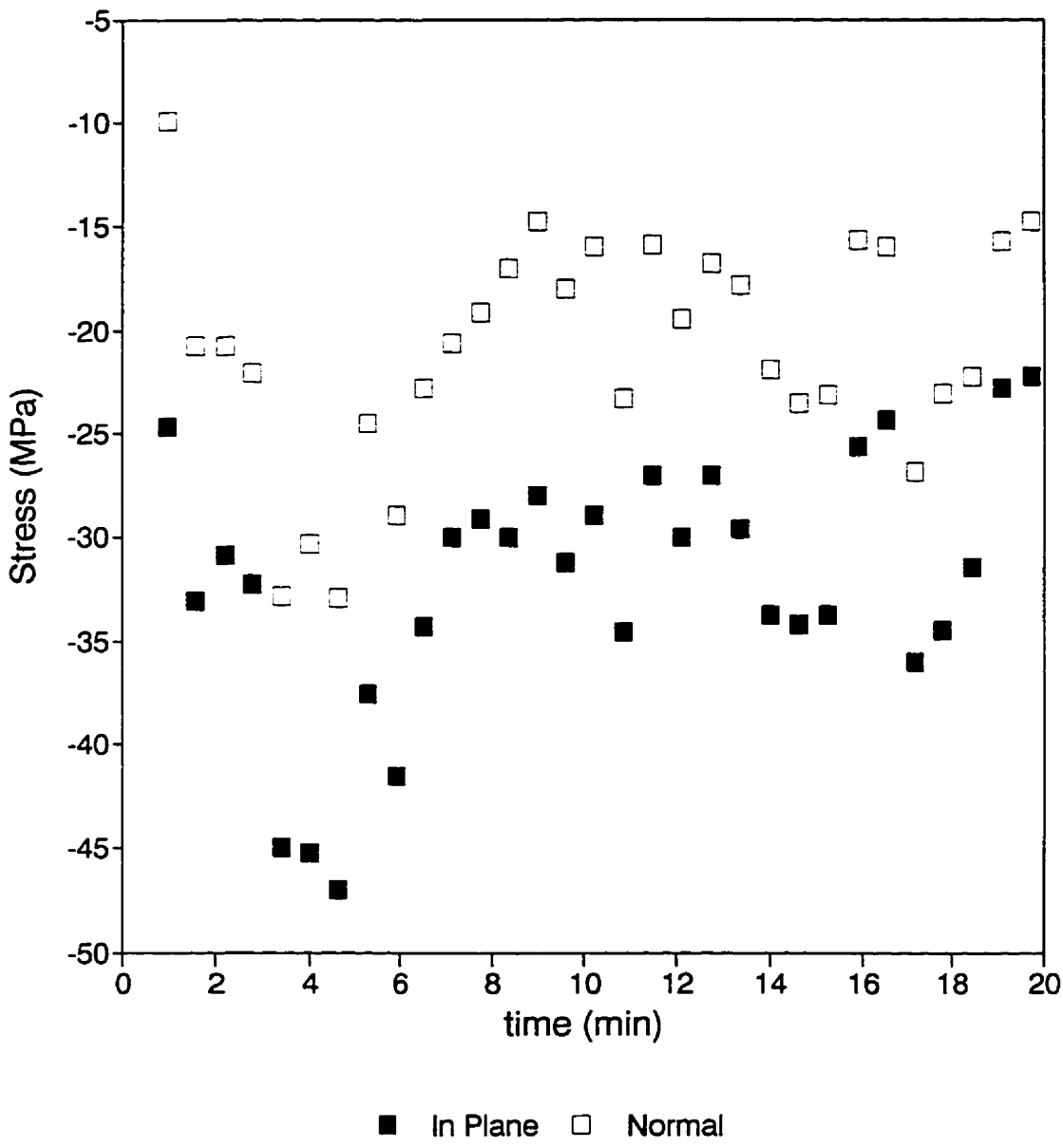

Figure A2.27: Stress vs. time data for run 16 at 300°C after rapid heating from 100°C.

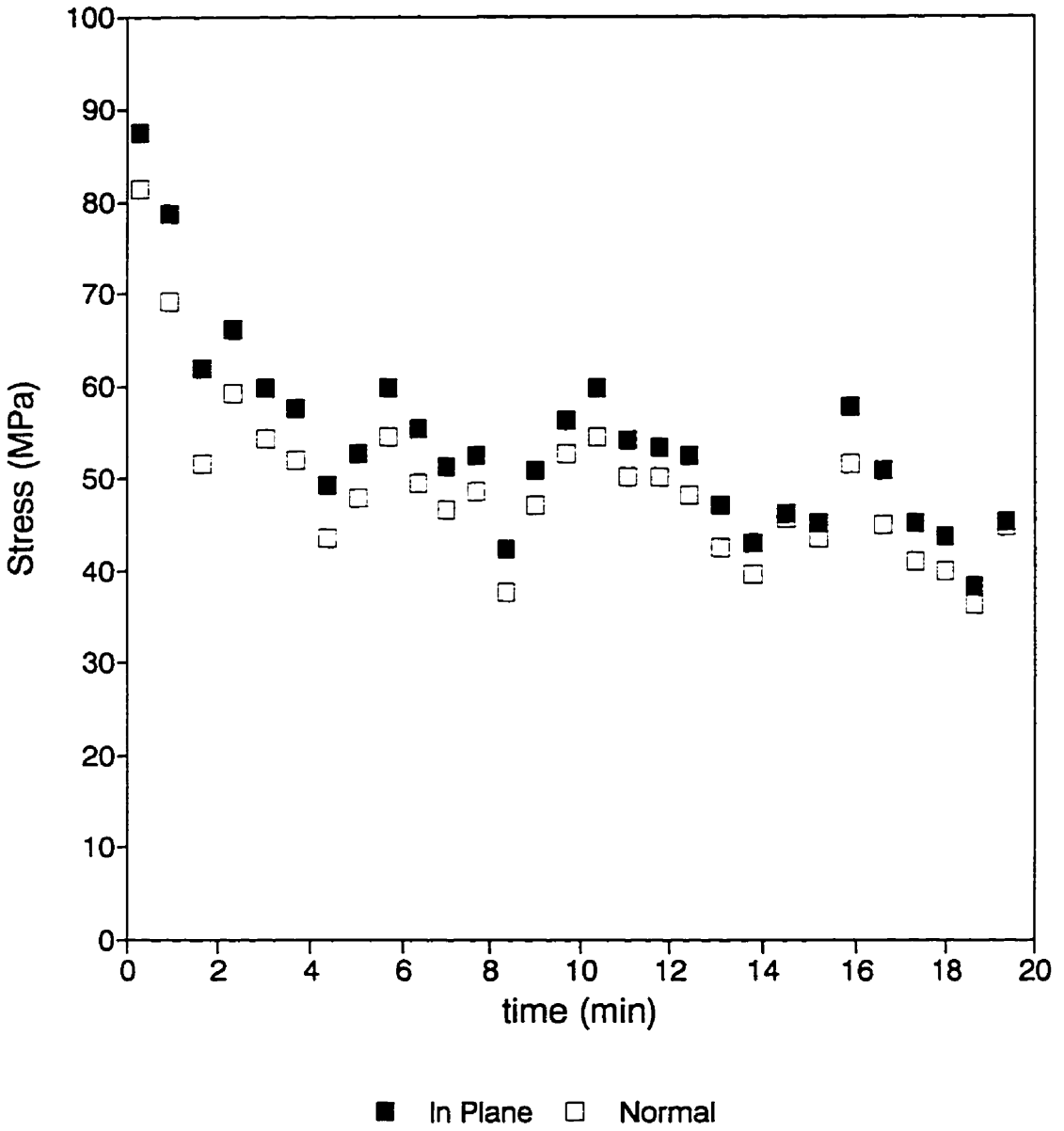

Figure A2.28: Stress vs. time data for run 16 at 100°C after rapid cooling from 300°C.

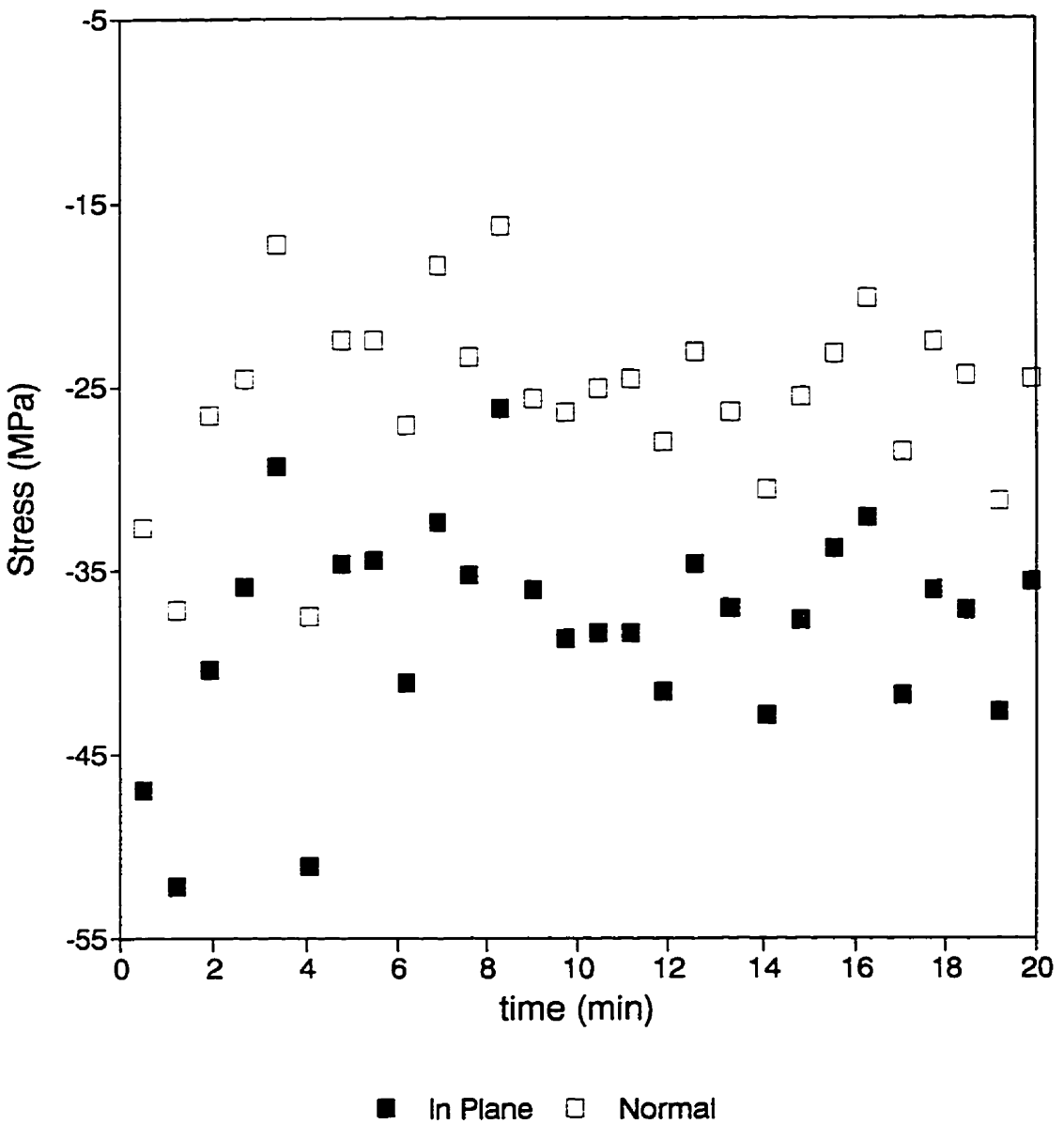

Figure A2.29: Stress vs. time data for run 16 at 300°C after rapid heating from 100°C in the second cycle.

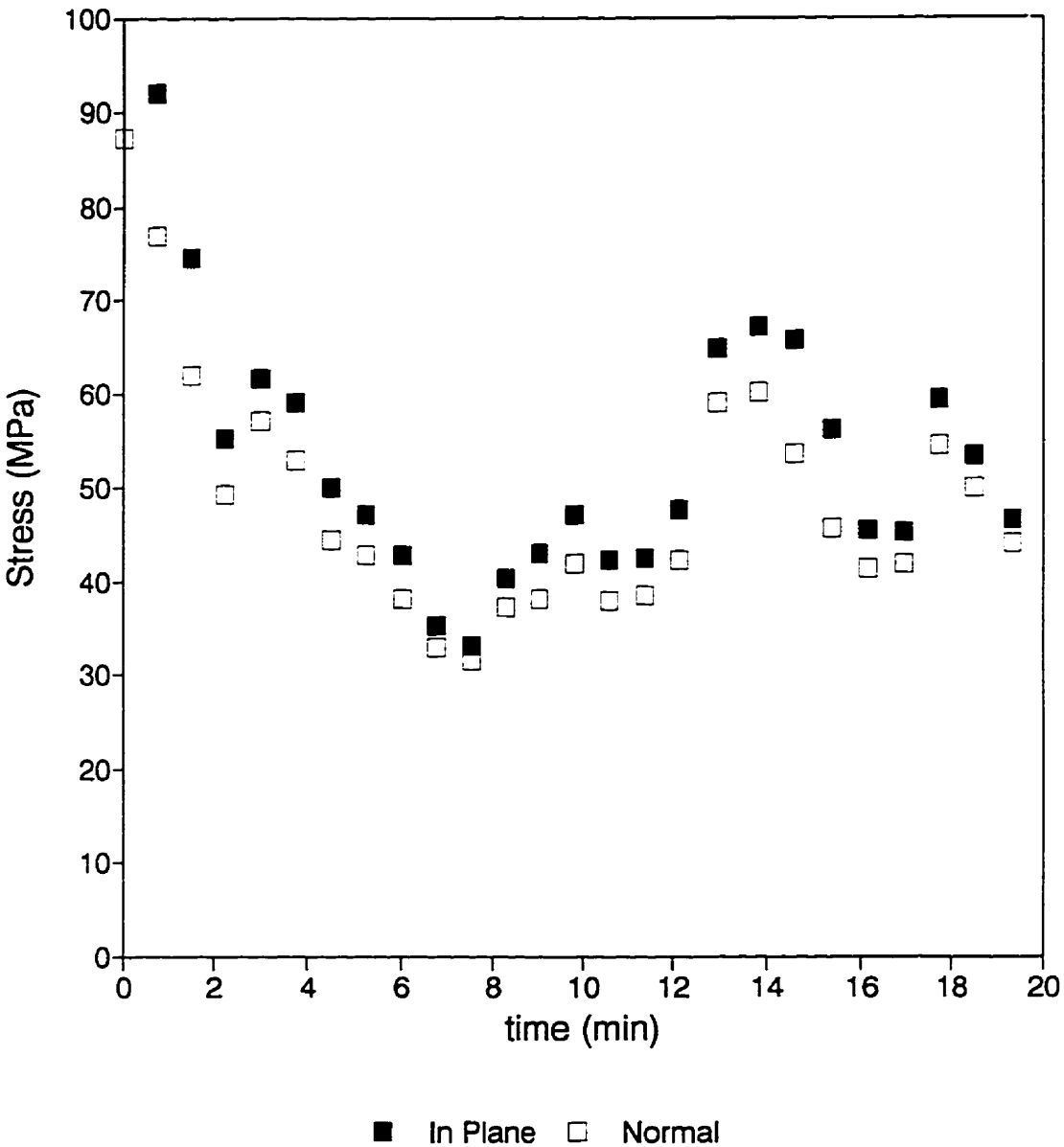

Figure A2.30: Stress vs. time data for run 16 at 100°C after rapid cooling from 300°C at the end of the second cycle.

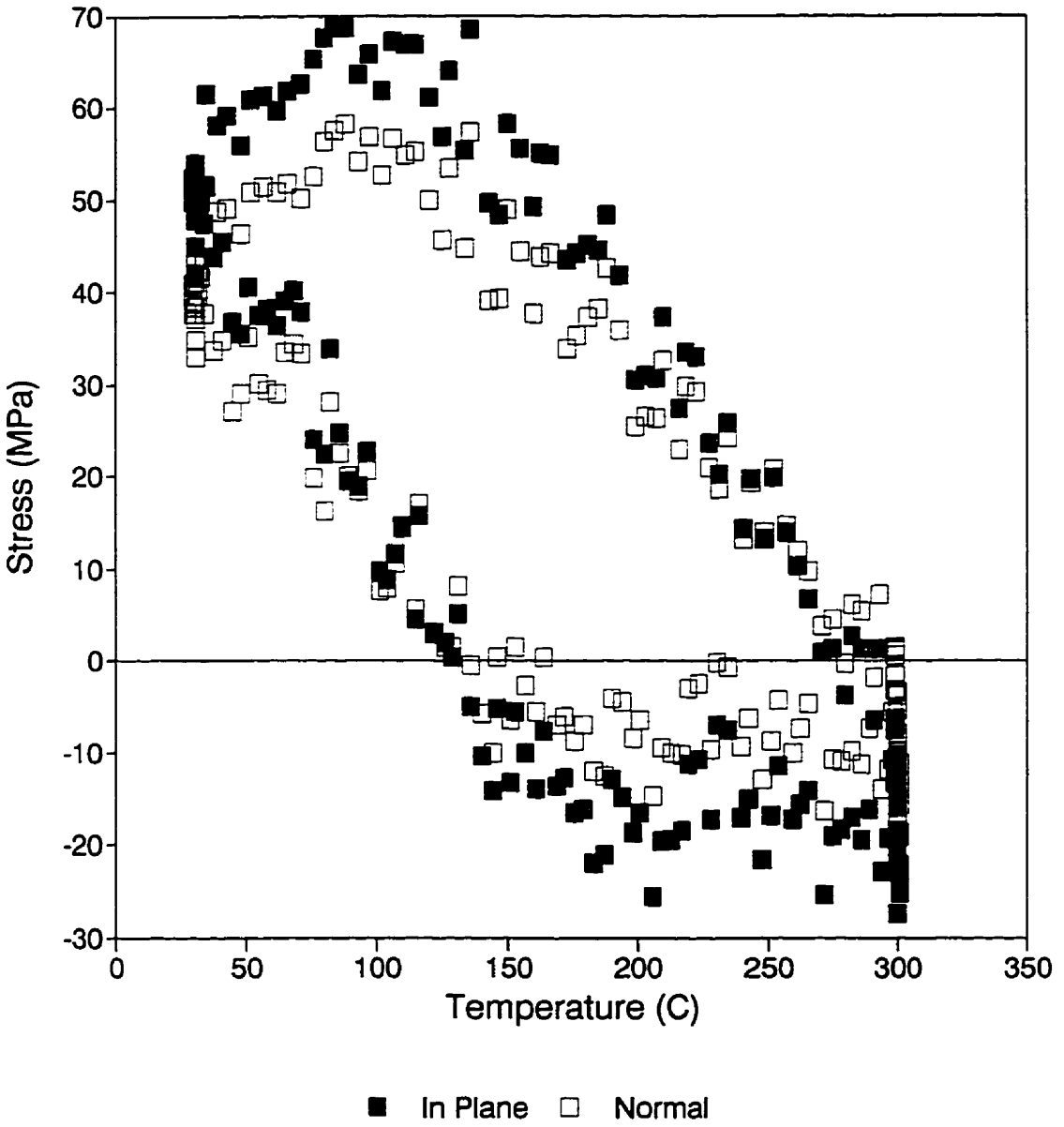

Figure A2.31: Stress vs. temperature data for run #17, a slow cycle run with 5°C/min heating and cooling rates.

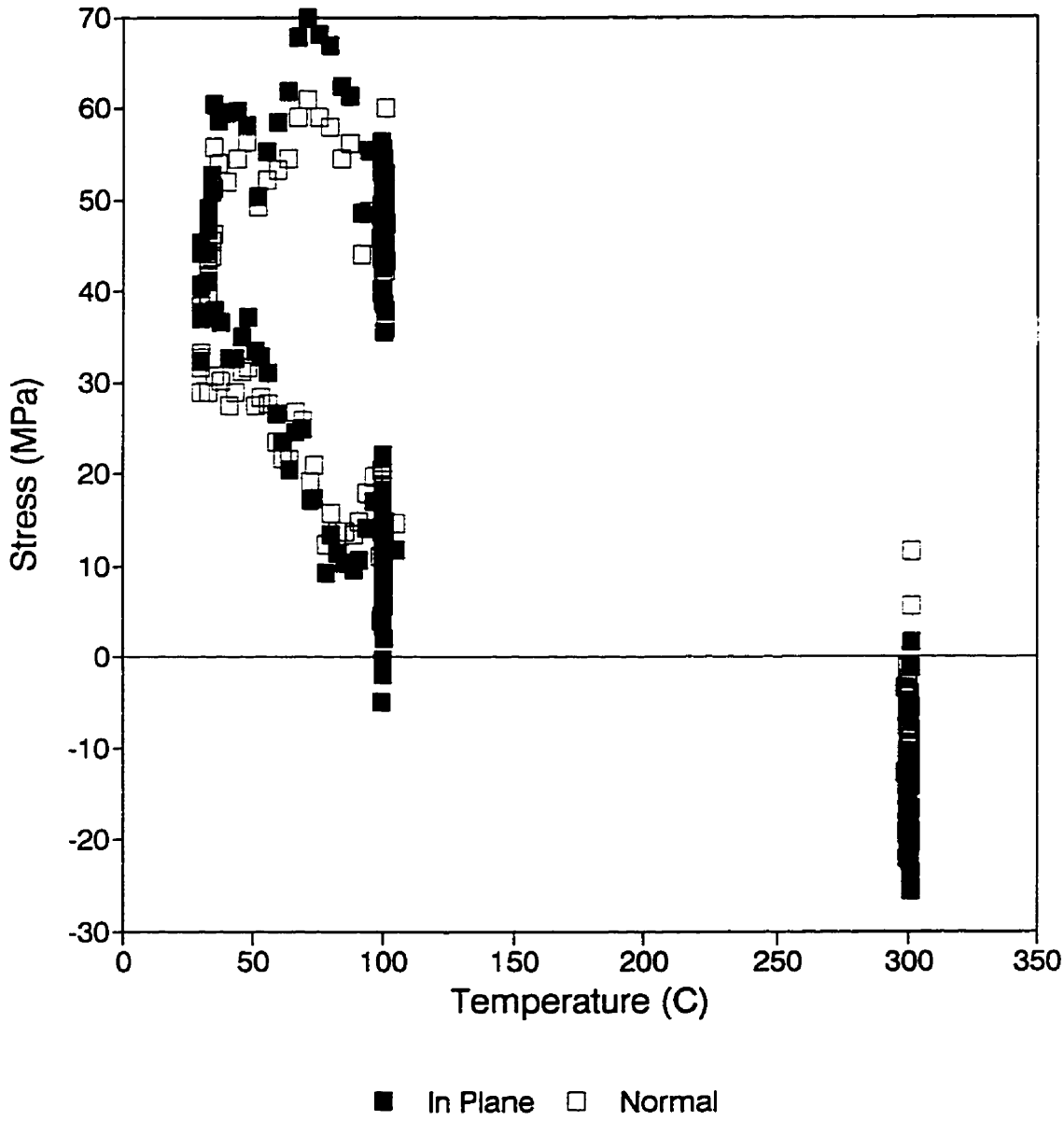

Figure A2.32: Stress vs. temperature data for run #18, showing all the data collected in this run.

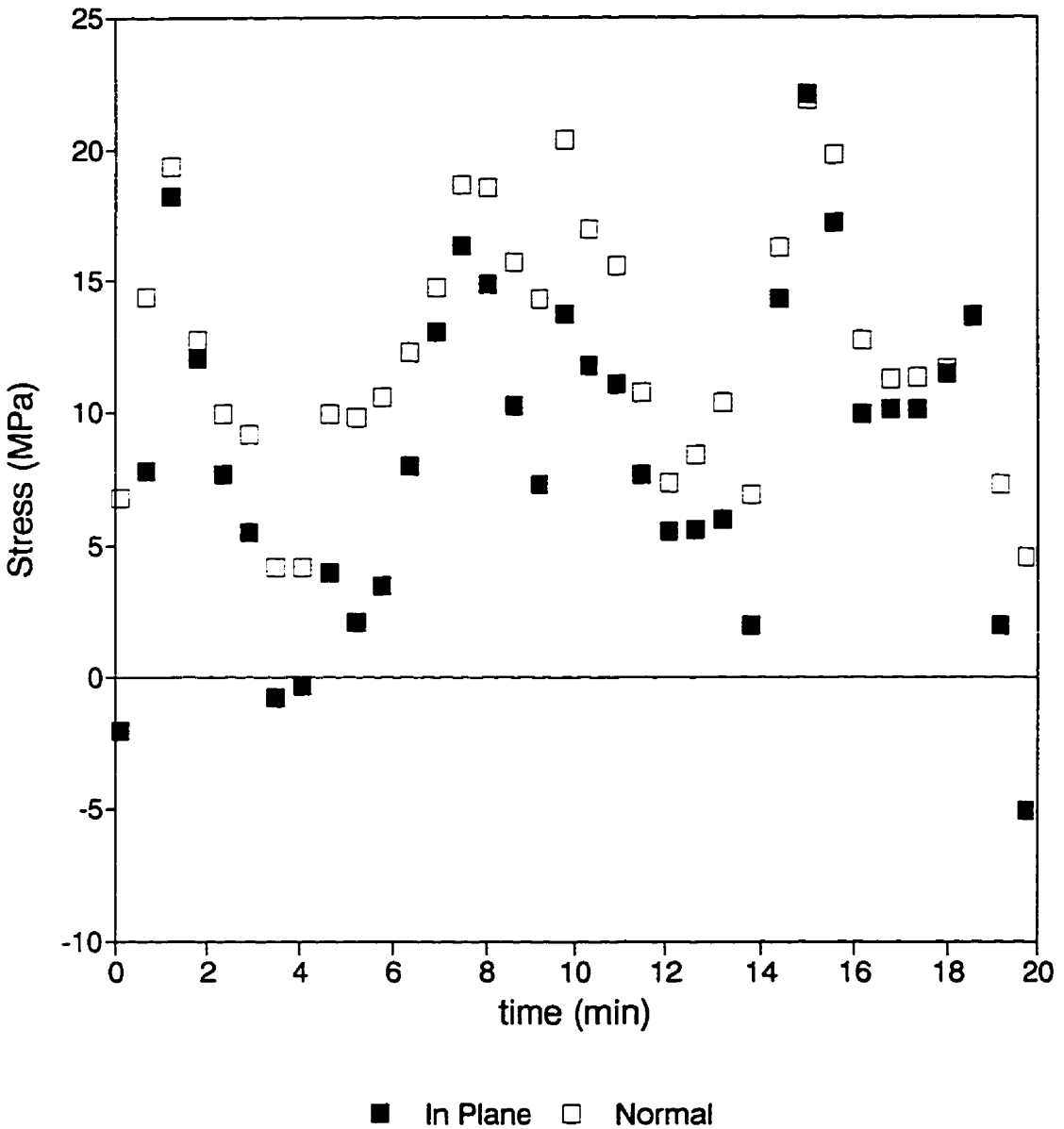

Figure A2.33: Stress vs. time data for run 18 at 100°C after slow heating from ambient temperature.

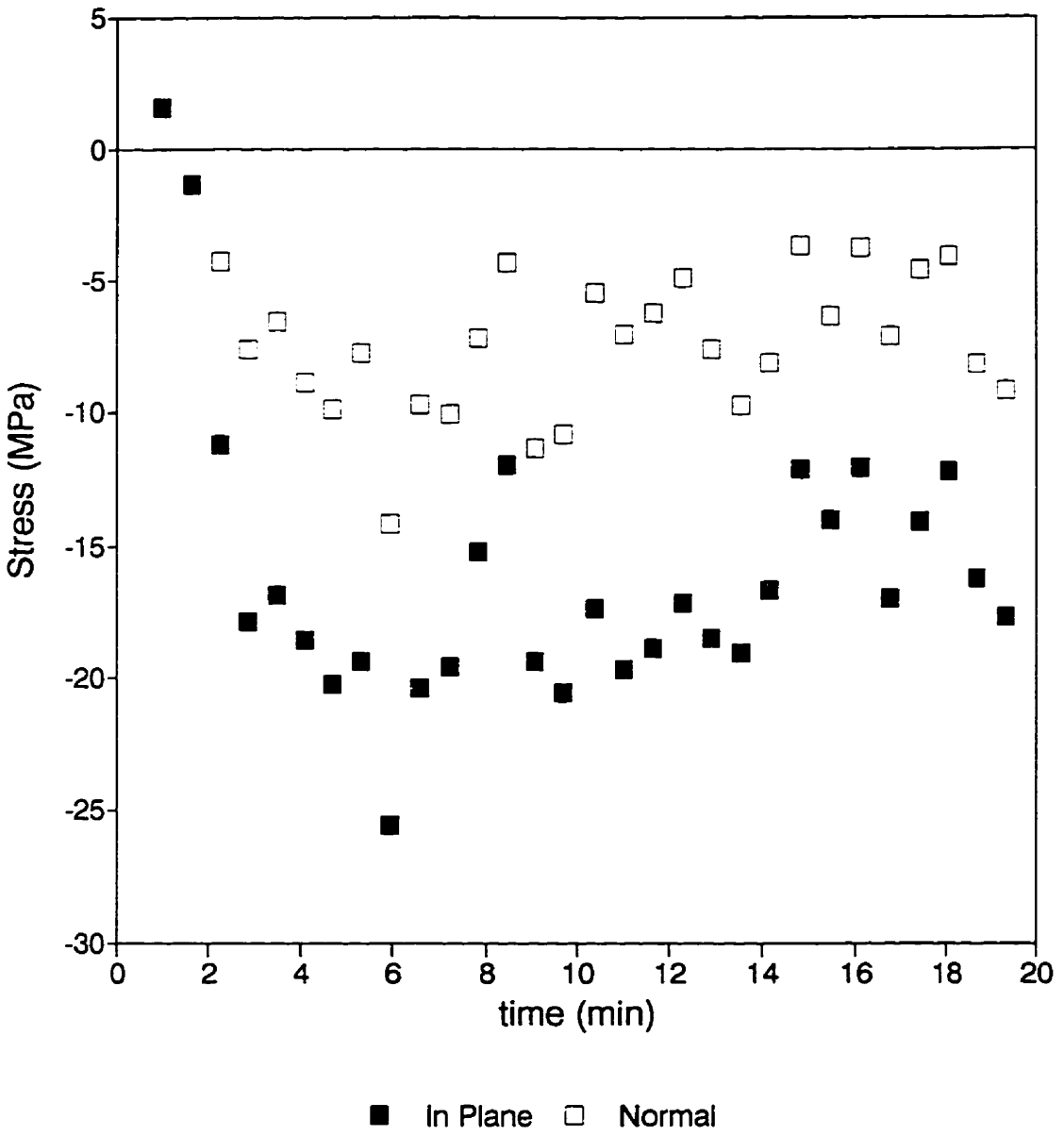

Figure A2.34: Stress vs. time data for run 18 at 300°C after rapid heating from 100°C.

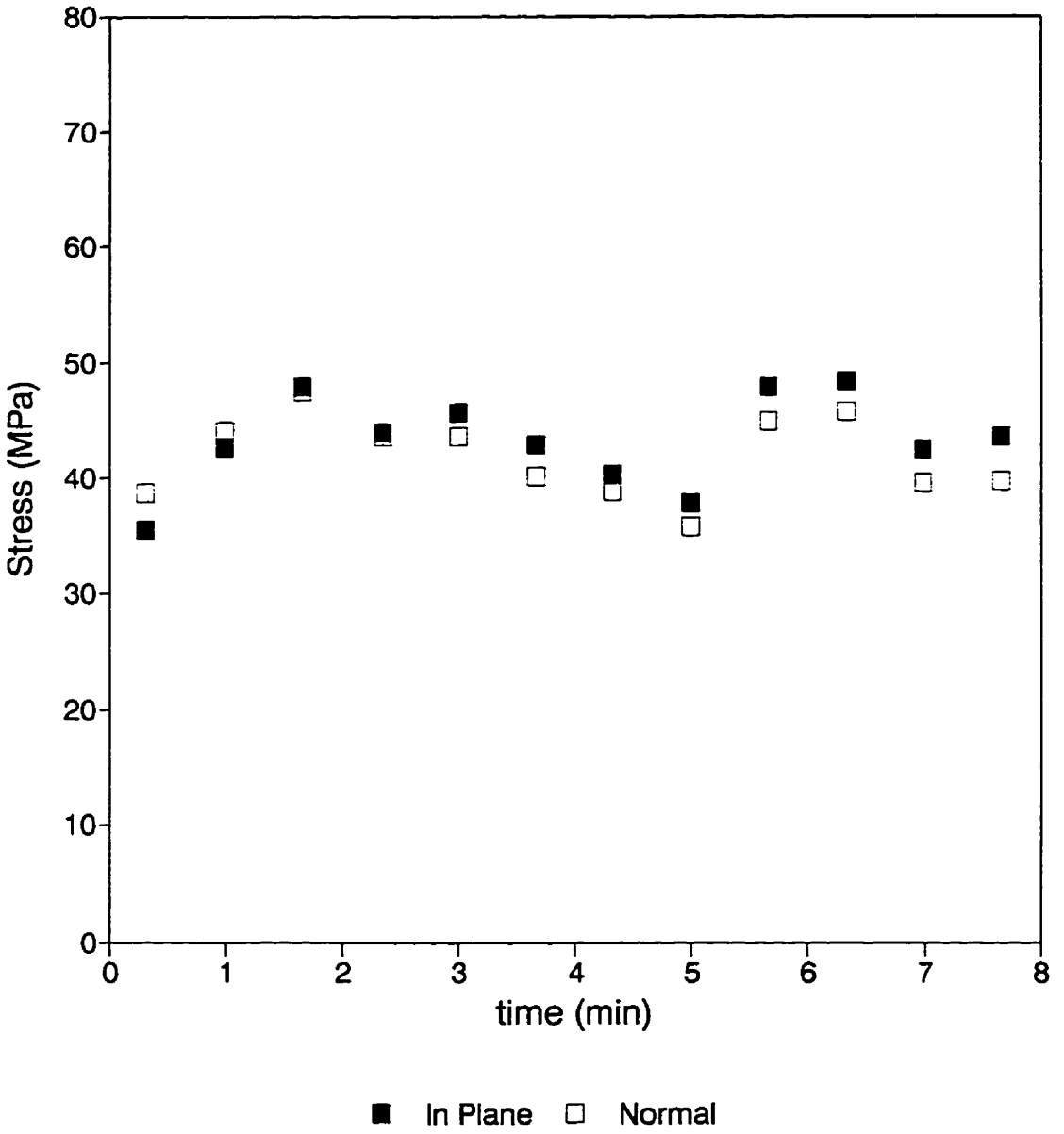

Figure A2.35: Stress vs. time data for run 18 at 100°C after rapid cooling from 300°C prior to the 10 very rapid cycles.

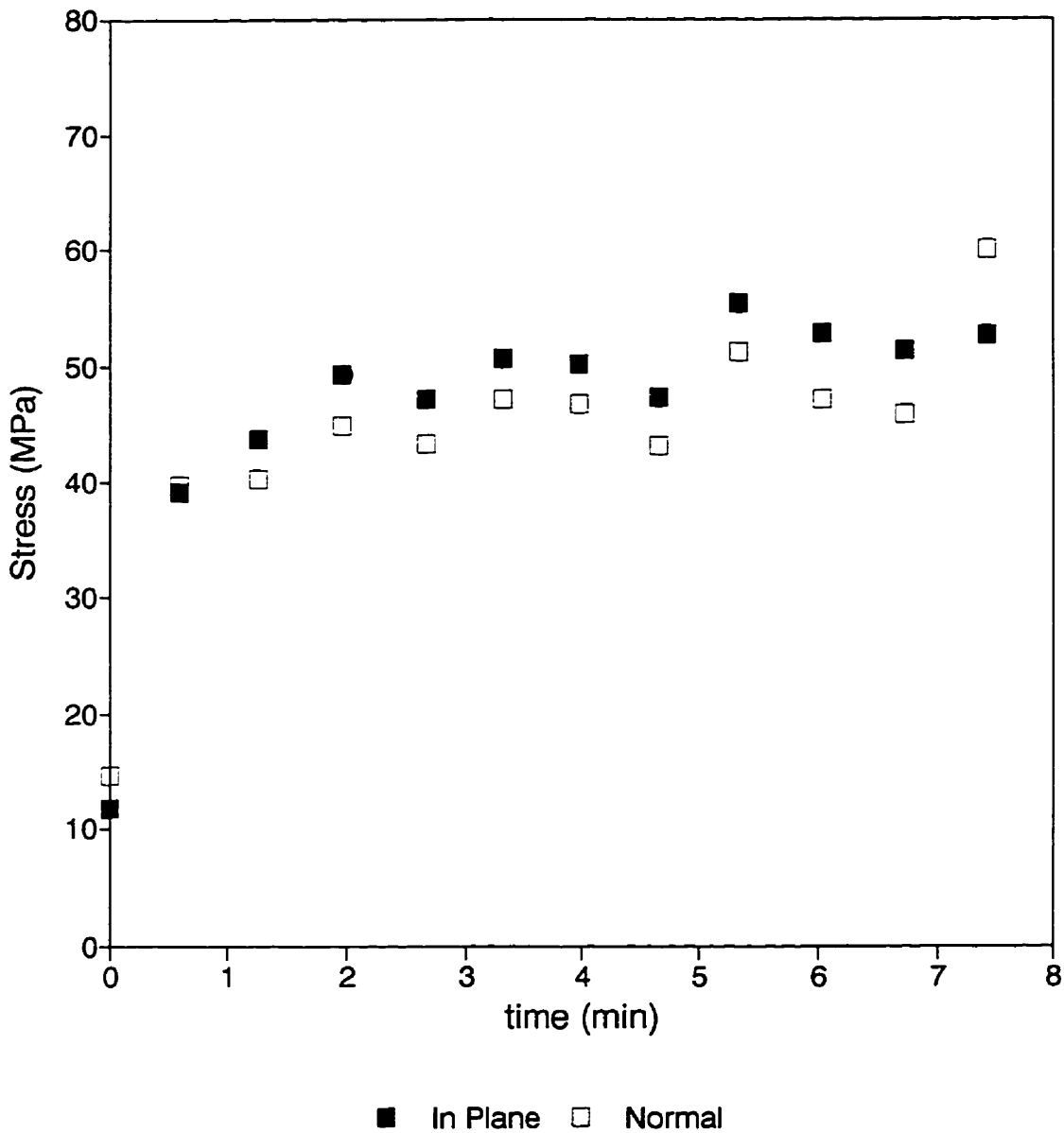

Figure A2.36: Stress vs. time data for run 18 at 100°C after rapid cooling from 300°C at the end of the 10th very rapid cycle.

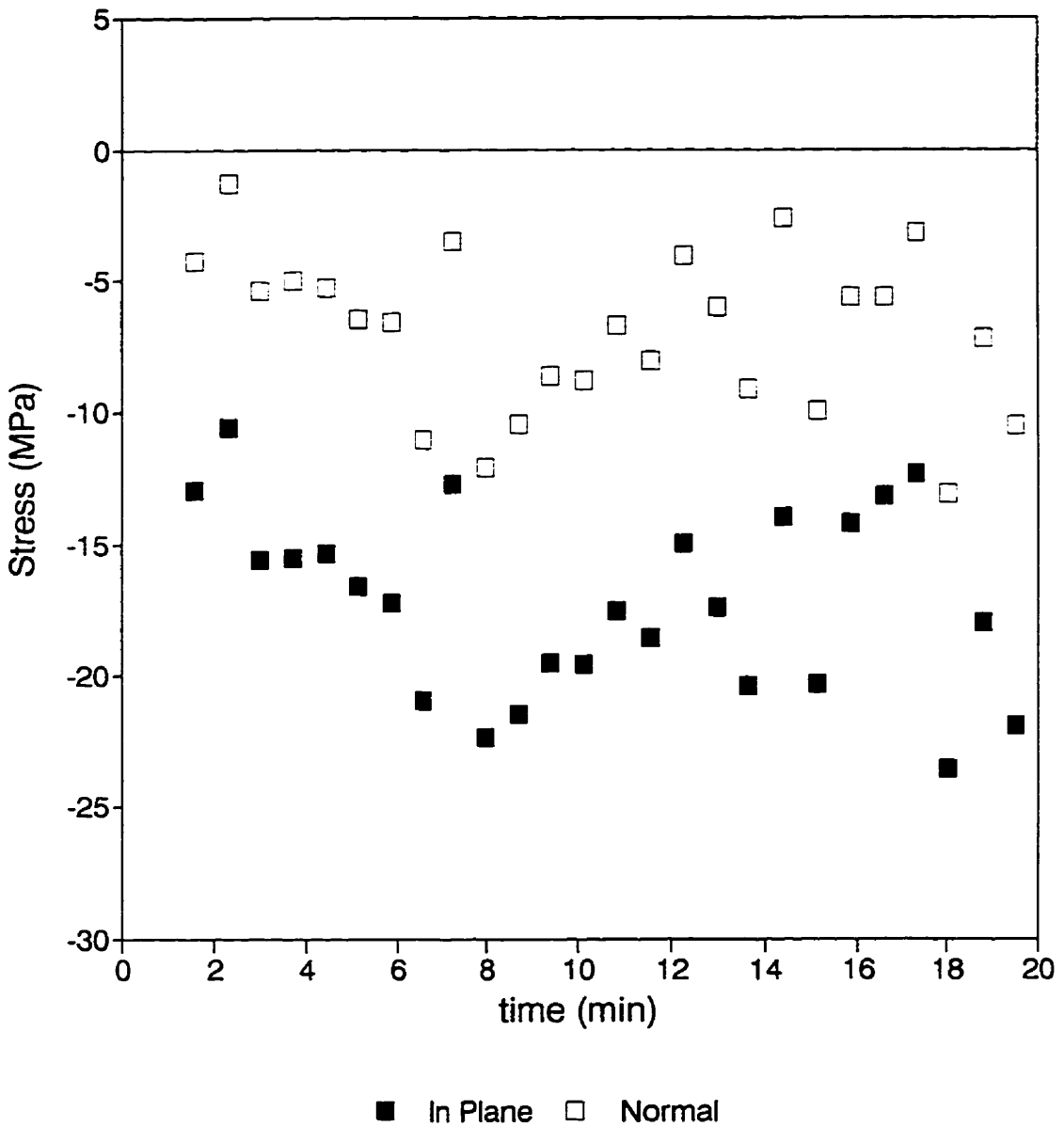

Figure A2.37: Stress vs. time data for run 18 at 300°C after rapid reheating from 100°C after the 10th rapid cycle..

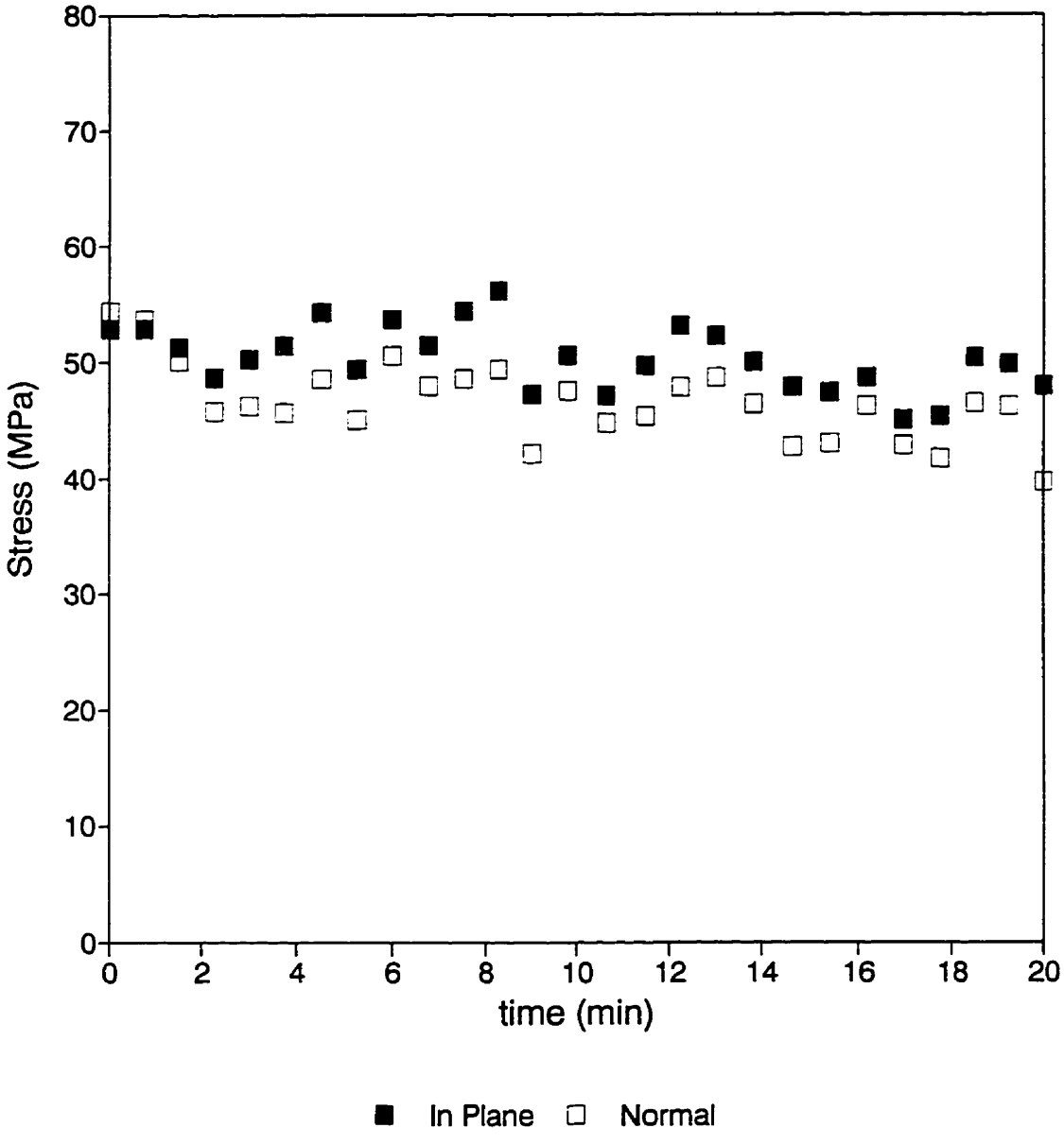

Figure A2.38: Stress vs. time data for run 18 at 100°C after rapid cooling from 300°C at the end of the final cycle prior to cooling to ambient temperature.

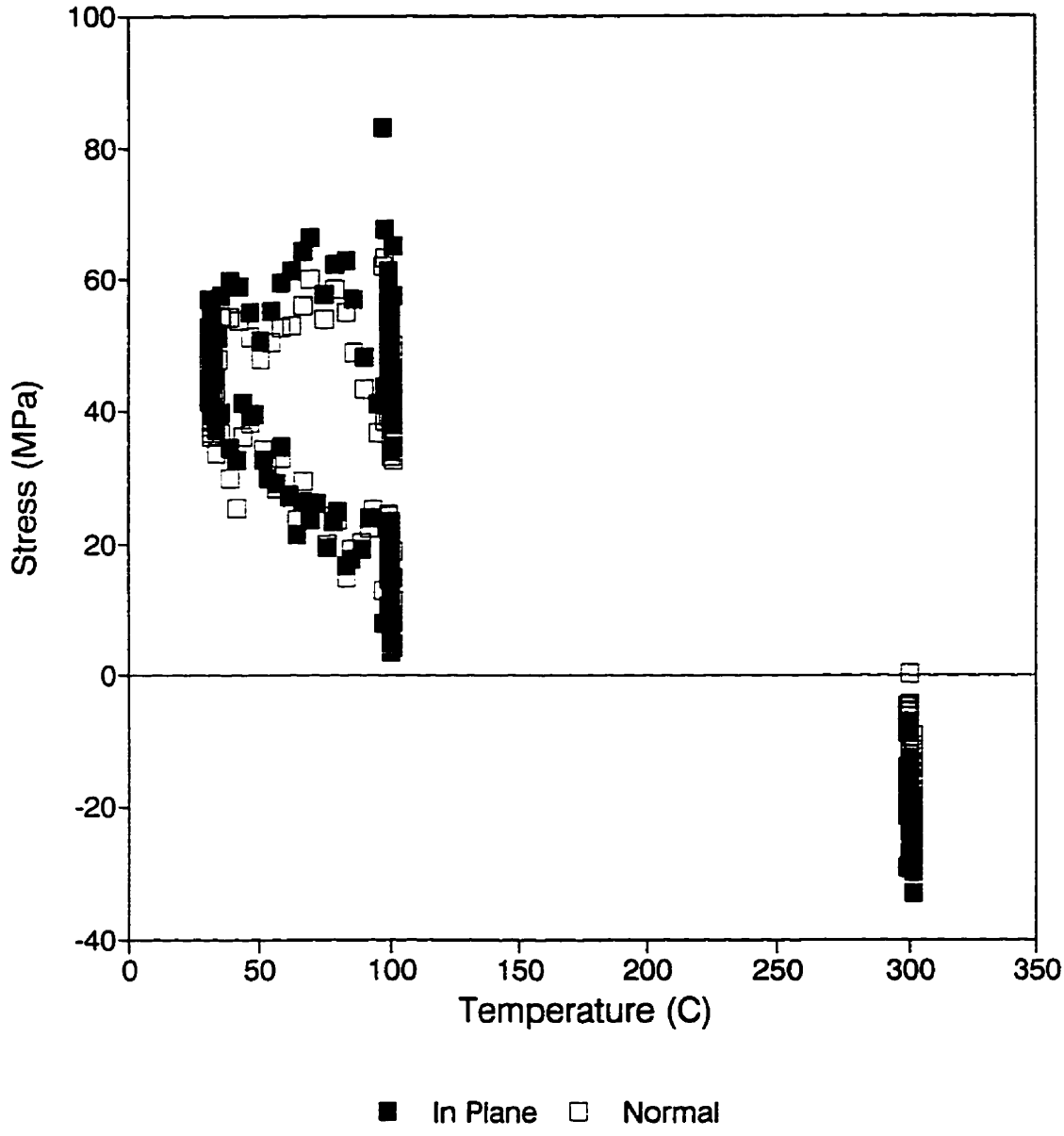

Figure A2.39: Stress vs. temperature data for run #19, showing all the data collected in this run.

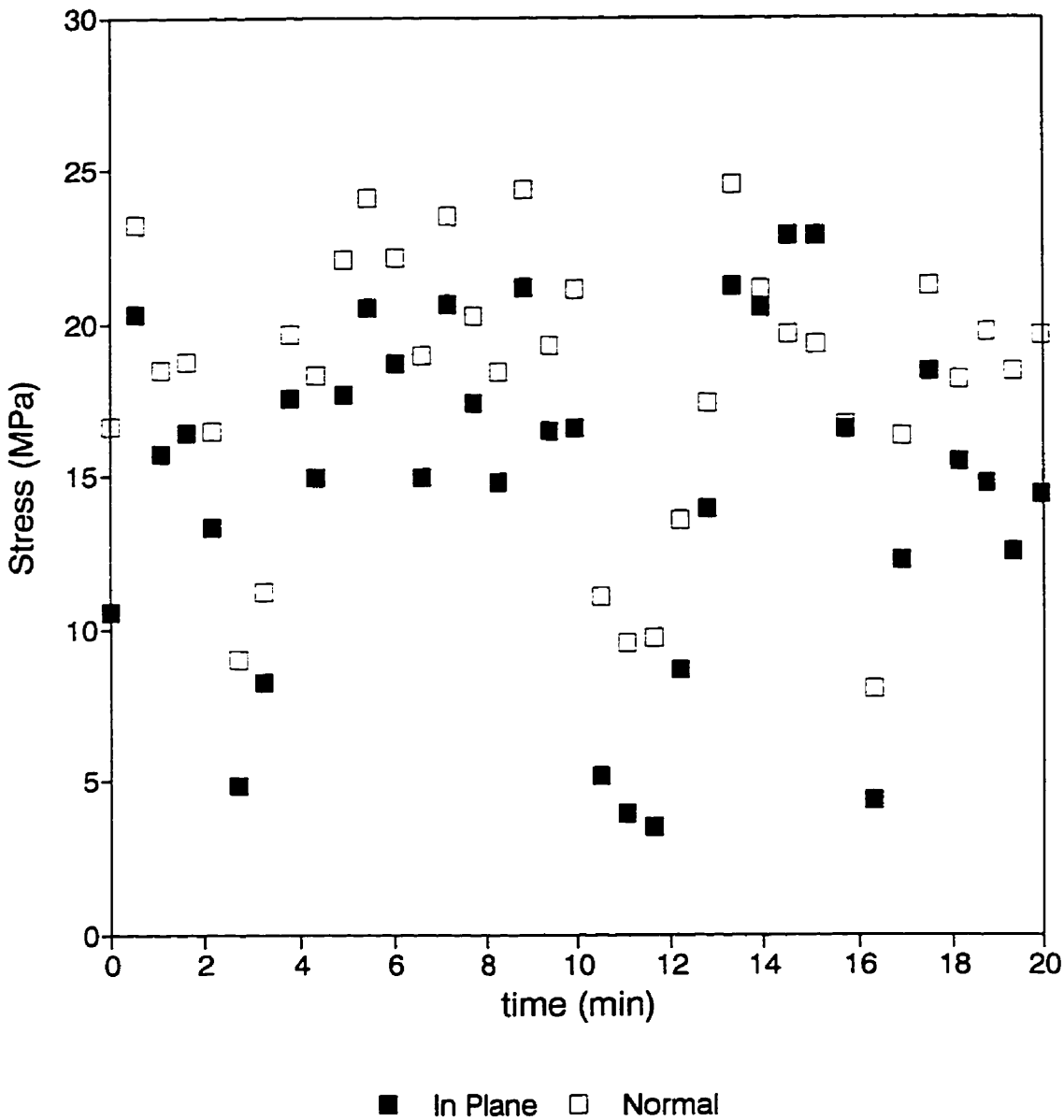

Figure A2.40: Stress vs. time data for run 19 at 100°C after slow heating from ambient temperature.

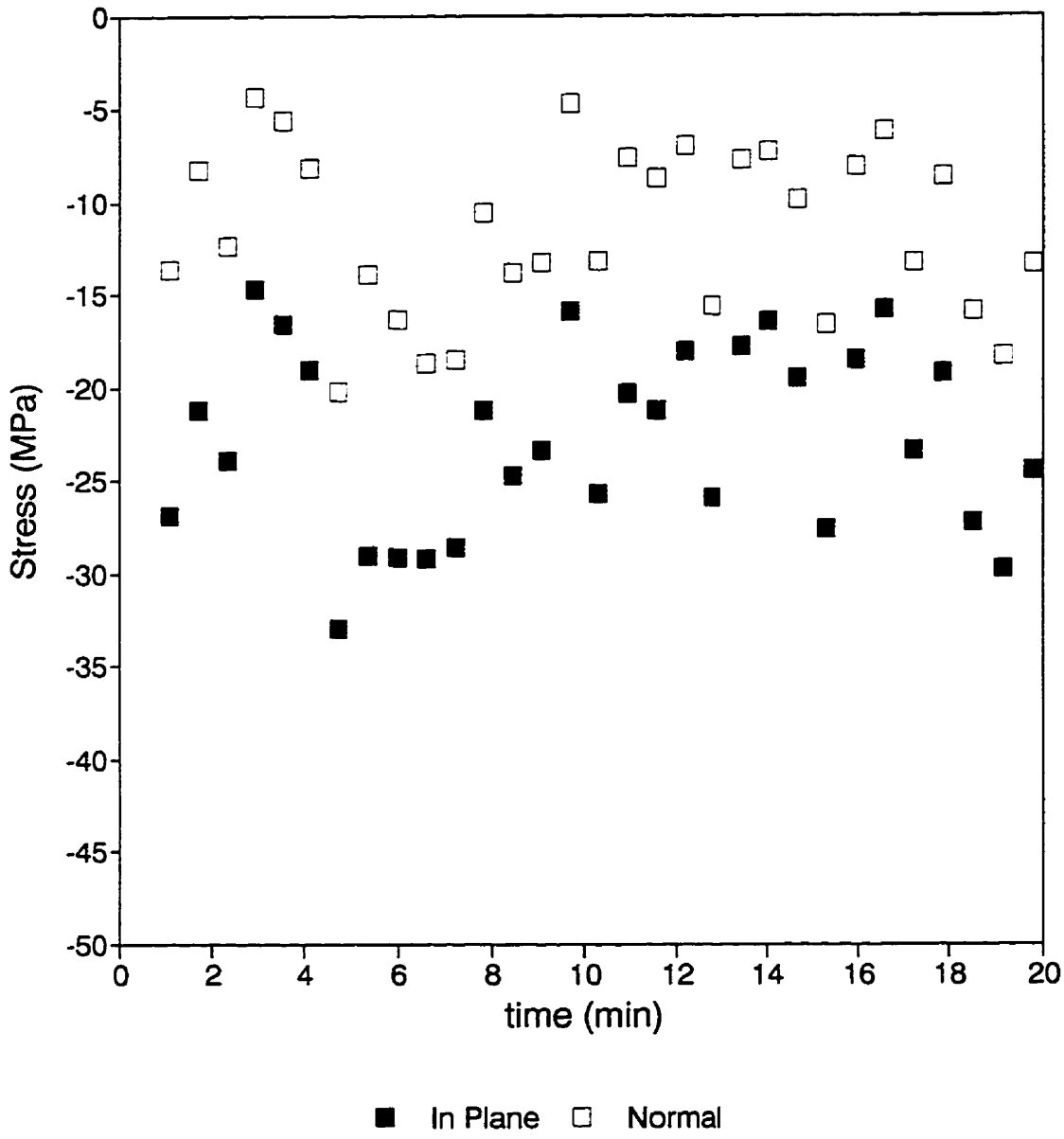

Figure A2.41: Stress vs. time data for run 19 at 300°C after rapid heating from 100°C.

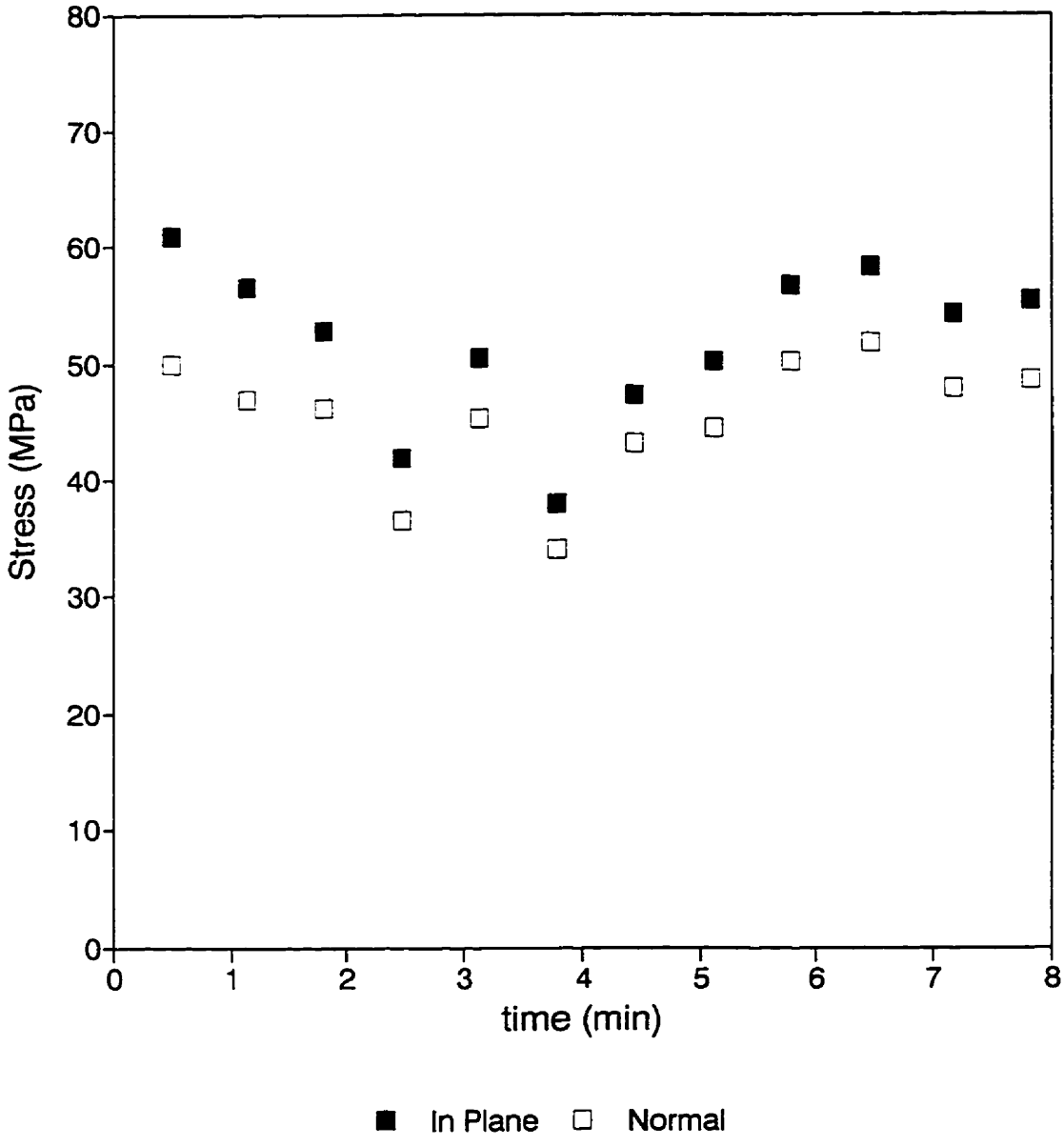

Figure A2.42: Stress vs. time data for run 19 at 100°C after rapid cooling from 300°C prior to the 10 very rapid cycles.

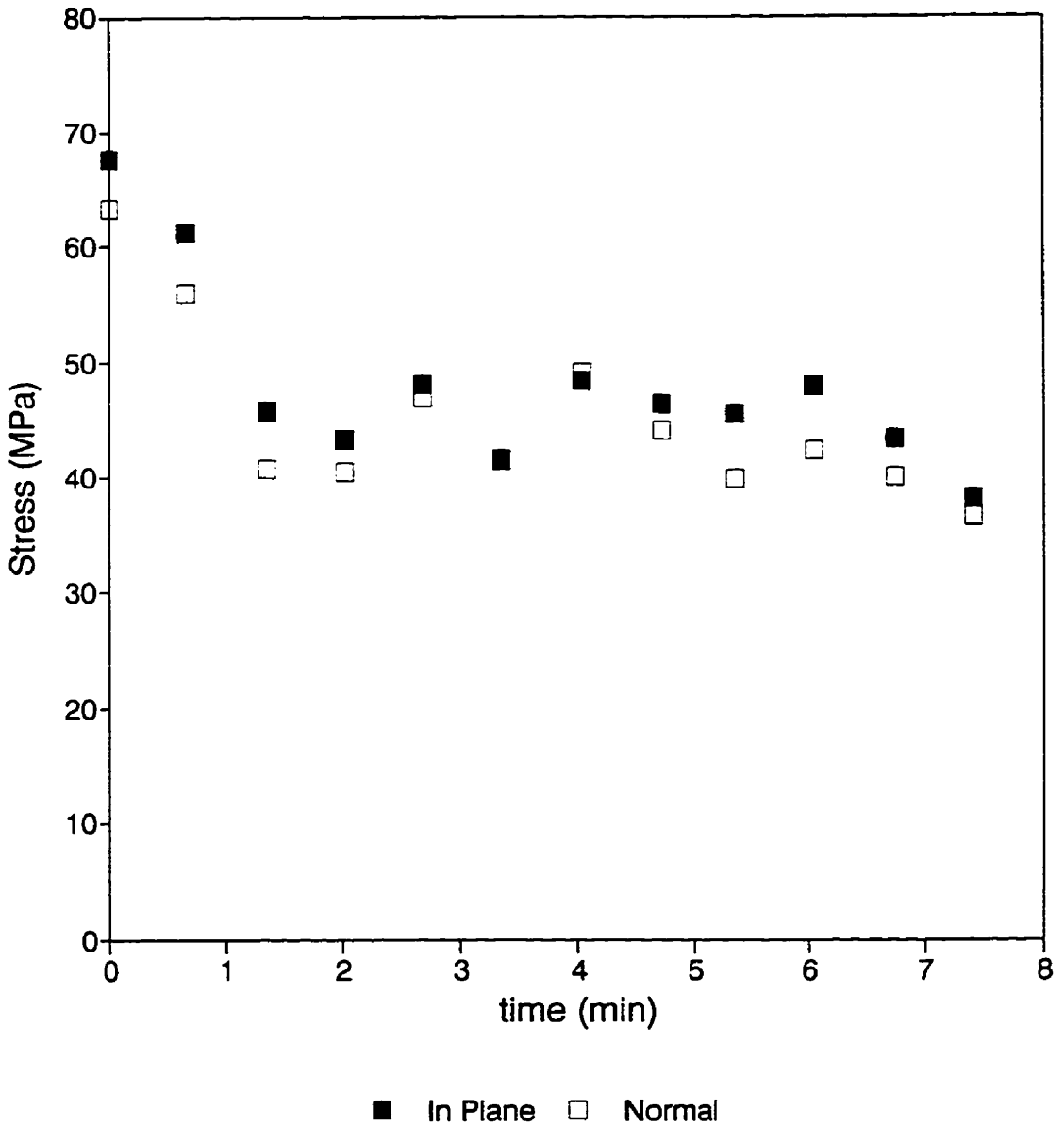

Figure A2.43: Stress vs. time data for run 19 at 100°C after rapid cooling from 300°C at the end of the 10th very rapid cycle.

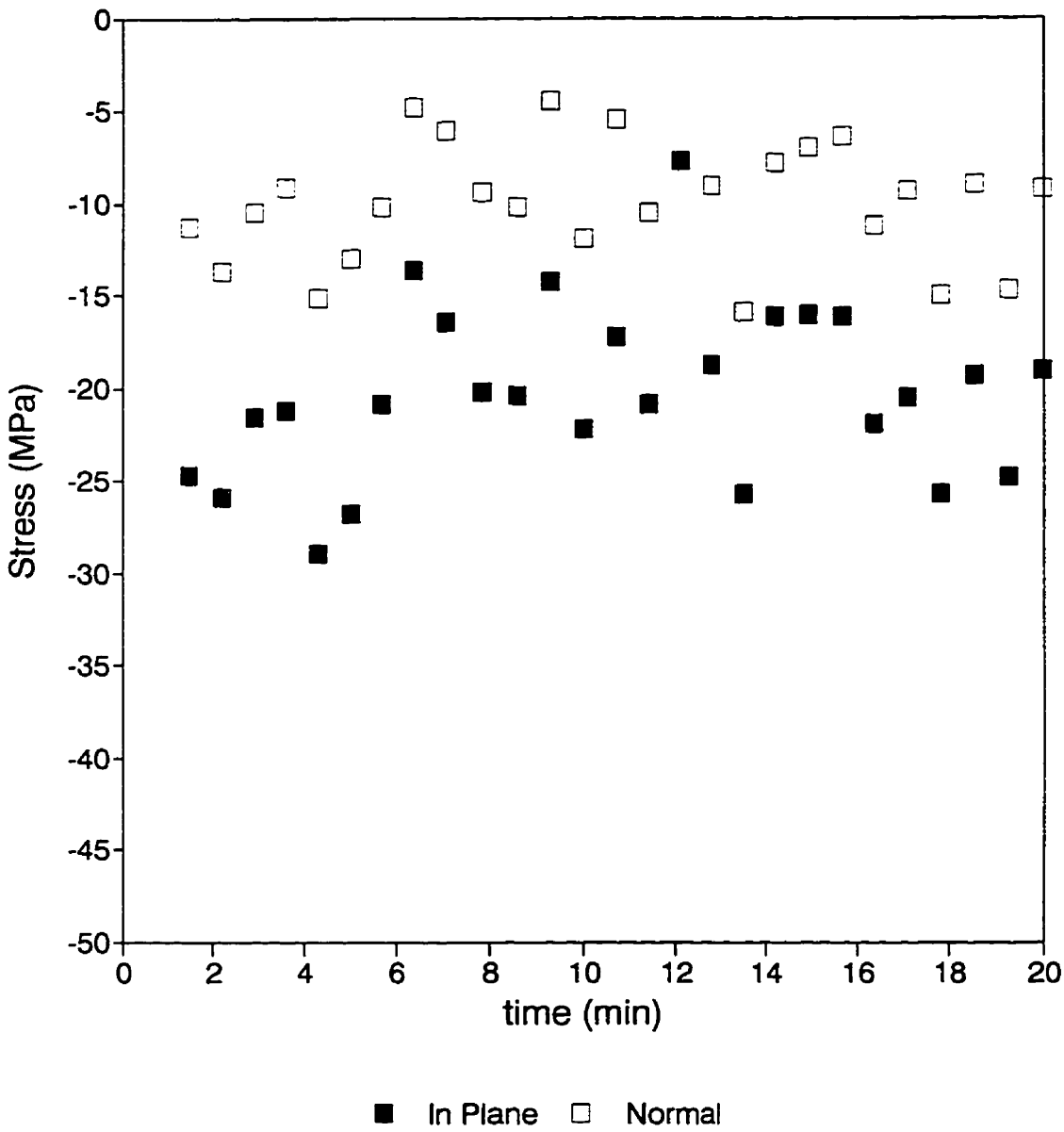

Figure A2.44: Stress vs. time data for run 19 at 300°C after rapid reheating from 100°C after the 10th rapid cycle..

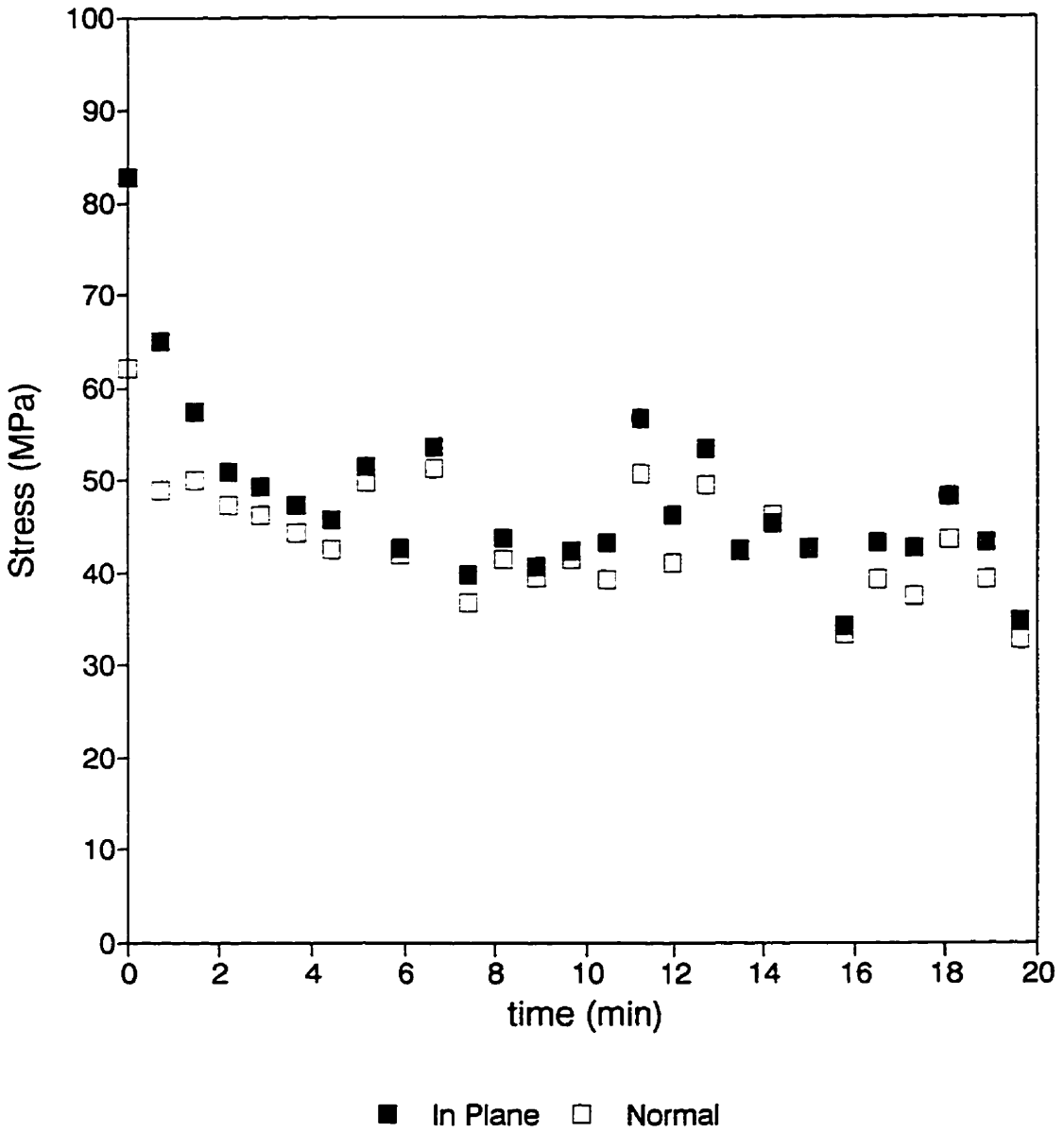

Figure A2.45: Stress vs. time data for run 19 at 100°C after rapid cooling from 300°C at the end of the final cycle prior to cooling to ambient temperature.

Appendix 3
Alignment and Calibration Procedures

This appendix details the procedures for aligning and calibrating the apparatus for both residual strain measurements and for pole figure measurements. Specimen and beam alignment procedures are discussed first and are followed by the technique used to calibrate the angular resolution of the TEC 205 detector and the correct centre channel.

A3.1 Set up of the Apparatus

A3.1.1: Installing the specimen holders

The sample holders have a threaded ring nut that threads onto the mounting of the goniometer. Examination of the back of the holder shows this ring and a mounting plate with a notch. This notch fits into the key on the goniometer mounting. Proper mounting of the sample holder requires that the notch fits into the key, and it can be determined by gently attempting to rotate the sample holder on the mounting. The holder should not rotate more than a few degrees. This is the only play in the mounting, and is not a serious problem.

To mount the texture device, the brushes for the oscillating motor must first be screwed onto the mounting. The brushes are held on by two screws. There is a large spacer which accompanies this, and the small piece of paper should be wedged between the spacer and the brush mounting.

The pole figure stage must be correctly mounted on the goniometer and the motor must oscillate properly throughout a full rotation. Improper mounting of the motor brushes will be evident by a grinding sound at some φ orientations and/or stopping of the motor .

A3.1.2: Positioning the scintillation counter

The following discussion applies to the use of the scintillation counter, which is currently necessary for beam alignment and for pole figure measurement. For the alignment of the specimen and the beam, best results are obtained with the detector at the residual strain measurement position (the rear tape markings on the left side of the detector arm should align). The detector slits should be set to 1mm wide, and should be approximately centered. The slits are controlled by the micrometer screws on the right side of the detector. Clockwise pressure is the convention for positioning if the slits need to be adjusted. The slit height will probably not need to be adjusted and should be about 10mm. This set up results in a narrower peak and hence the peak position can be estimated with greater precision and accuracy.

After the alignment procedure has been completed, the detector must be moved to the pole figure position and the detector slits widened to 3mm. The front pair of tape markings should align. This makes the system less sensitive to shifts in peak position and hence more accurate texture measurements can be made. The wide slits also improve pole figure measurement, since a larger portion of the integrated intensity is collected. For low angle reflections, the peak is often narrow enough that the complete integrated intensity is registered.

A3.2 Checking the Alignment

! N.B.

Prior to aligning the zero expansion high temperature stage, the specimen oscillation should be running for at least 15 minutes to allow for thermal expansion of the motor stage to equilibrate.

!

A3.2.1: Using the program 'STEELSTR'

The program used to perform the alignment is STEELSTR. This program measures the diffraction peak position at a user defined number of ψ angles, equispaced in $\sin^2\psi$ space. The program displays on the screen a plot of apparent strain vs. $\sin^2\psi$. The object of the alignment procedure is to obtain a horizontal line i.e. no apparent strain. On obtaining this, there is no peak shift as a function of ψ, thus the real peak intensity can be measured at all orientations during the pole figure. The alignment procedure described here is intended for the random textured, stress free Al standard specimen. It can in principle be used with other specimens, if the stress state is well known and any texture present is not too strong.

The program can be started from any directory by simply typing STEELSTR. The program automatically opens the shutter. This will happen only if the shutter switch is set to external, and the motor power supply is turned on.

The program prompts the user for the following information:

1. general description
2. the filename to save the data collected
3. the height of the intensity scale on the screen {2000}
4. the number of φ orientations, set = 1
5. the Lorentz-Gaussian fitting term {7}
6. the current θ value {29}
7. the current 2θ value {58}
8. the actual 2θ position, should be same as 2θ value {58}
9. the number of reflections (number of Bragg peaks) set = 1
10. *confirm the above recorded entries*
11. an estimate of the 2θ peak position {58.6}

12. position of the first background measurement {57.0}
13. position of the second background measurement {60.0}
14. the estimated width of the peak, window width {0.75}
15. the counting time for each point, the time factor {5} sec.
16. the *hkl* value of the Bragg peak, using Miller notation {111}
17. the number of ψ directions (arm number) max 2: set =1 for ψ–down only, set =2 for ψ–down and ψ–up
18. for each arm number: the first $\sin^2\psi$ value, the final $\sin^2\psi$ value, and the $\sin^2\psi$ increment

    The maximum value for ψ-up is 0.75, on ψ-down 0.8 is sufficient

    Incrementing by 0.2 gives enough data points while keeping experiment times reasonable
19. the number of points used to measure the peak position {11}
20. press ENTER twice to begin the experiment

Numbers in {} are typical values for a measurement using the Al (111) peak.

After the first scan, the user is prompted to press ENTER to continue. This allows the user to ensure that everything has been entered correctly without waiting for the program to complete the experiment. The program plots on screen each data point as it is collected, the previous set of data points and the curve fitted to them. On the bottom of the screen are displayed the fitting parameters calculated for the data. The results of the calculated apparent strain are also displayed as a line drawn from the right to the left of the screen. The first line drawn is blue and represents the results from the ψ–down arm, if the arm number entered was 2, then a second line is drawn in red for the ψ–up arm.

A3.2.2: Alignment criteria

The alignment is sufficiently accurate for a pole figure when the two lines are essentially parallel and horizontal. This is also good accuracy if the alignment has been performed at a low angle reflection and stress measurements will be be performed at high angle reflections. That the two lines follow the same path indicates that the beam is correctly aligned to the goniometer centre. Once this has been achieved, it is sufficient to align the specimen using only ψ–down.

A3.3 Correcting a Misalignment

There are two components to the alignment, as stated above, the beam position and the sample position. The beam position is adjusted by turning the screws on the incident slits nearest the specimen, while a thumbscrew on the specimen mount controls the sample position. Sections **§A3.3.1** and §A3.3.2 discuss how to correct beam and specimen alignment errors respectively, and §A3.3.3 discusses how to obtain the correct 2θ zero position.

A3.3.1: Beam alignment

Beam misalignments are corrected using the micrometer controlled primary beam slits. These are housed in the slit box nearest the specimen in the beam path from the x–ray source. The pair of micrometer screws on the top of the slits control the vertical slits. The dial nearest the operator controls the top slit. It is important to note that turning either of the dials clockwise tends to narrow the slit spacing: i.e. turning either or both slits sufficiently clockwise will close the slits completely. Based on this, it is clear that the dials must be turned equal amounts in opposite directions when adjusting the beam position.

The Huber slits allow precise adjustment of beam position and of the detector's slit width and position. The micrometers on the slits provide 500μm of movement per turn. Hence each major division represents a 50μm displacement. Beam position can be achieved to better than 5μm if carefully adjusted. The dials on the top of the slits control vertical width and position, while the dials on the side of the slit box control horizontal width and position. Using the spare slits allows the operator to confirm that the each micrometer is turned in the appropriate direction.

The relative position of the beam can be determined from the apparent strain data. If the ψ-up data is more apparently tensile (higher on the screen) than the ψ-down data, then the beam is too low. If the red line is below the blue line on the screen, then the ψ-up data is more compressive and the beam is too high.

The beam position is generally rather close to the centre and hence individual adjustments should be kept less than a maximum of 50μm in either direction. The convention of adjusting the dials to the desired value in a clockwise direction eliminates backlash and is consistent with current practice. Adjustments of about 10 to 20μm are typically sufficient to get close alignment.

It is very important that the beam's vertical width remains the same. Thus the user must be careful to adjust each slit properly by determining the necessary direction which each micrometer must be rotated. In the x-ray enclosure is a spare slit box which can be used as a reference to ensure that each dial is turned in the proper direction.

Example: In order to adjust a beam that is too high, the front micrometer (controlling the top slit) must be rotated clockwise, while the rear micrometer must be rotated counter clockwise, overshooting the desired position, and

then rotated clockwise to the proper position. Again, the operator must be careful to adjust each micrometer by the same amount to keep the vertical width of the slits constant.

A3.3.2: Specimen *z*–alignment

The thumb screw on the specimen mount for the z–adjustment is right hand threaded and has a set screw as an indicator of its position. Rotation of the thumb screw clockwise makes any apparent stress more tensile. One full rotation of the thumb screw results in a change in peak position of the Al (111) peak by about 0.1° 2θ at ψ=0. While the sample position does affect the measured position of the peak, the primary purpose of adjusting the thumb screw is to eliminate apparent stresses.

A3.3.3: Detector 2θ alignment

After all apparent strains due to sample position and beam position have been removed, any 2θ offset may now be corrected. Use the program BACK2PNT or BACK2TEC if using the TEC 205 (section **§A3.4**) to determine a reliable value of the lattice parameter using a high angle reflection. For Al, the (222) or the (311) give good results. From this, adjust the 2θ by manually offsetting the 2θ motor and using BACK2PNT to change the motor reading until the lattice parameter measured at the low angle reflection matches the high angle value.

A3.3.4: Examples of misalignments and a good alignment

Figure A3.1 below show hypothetical results for various types of misalignments and indicates the corrections necessary.

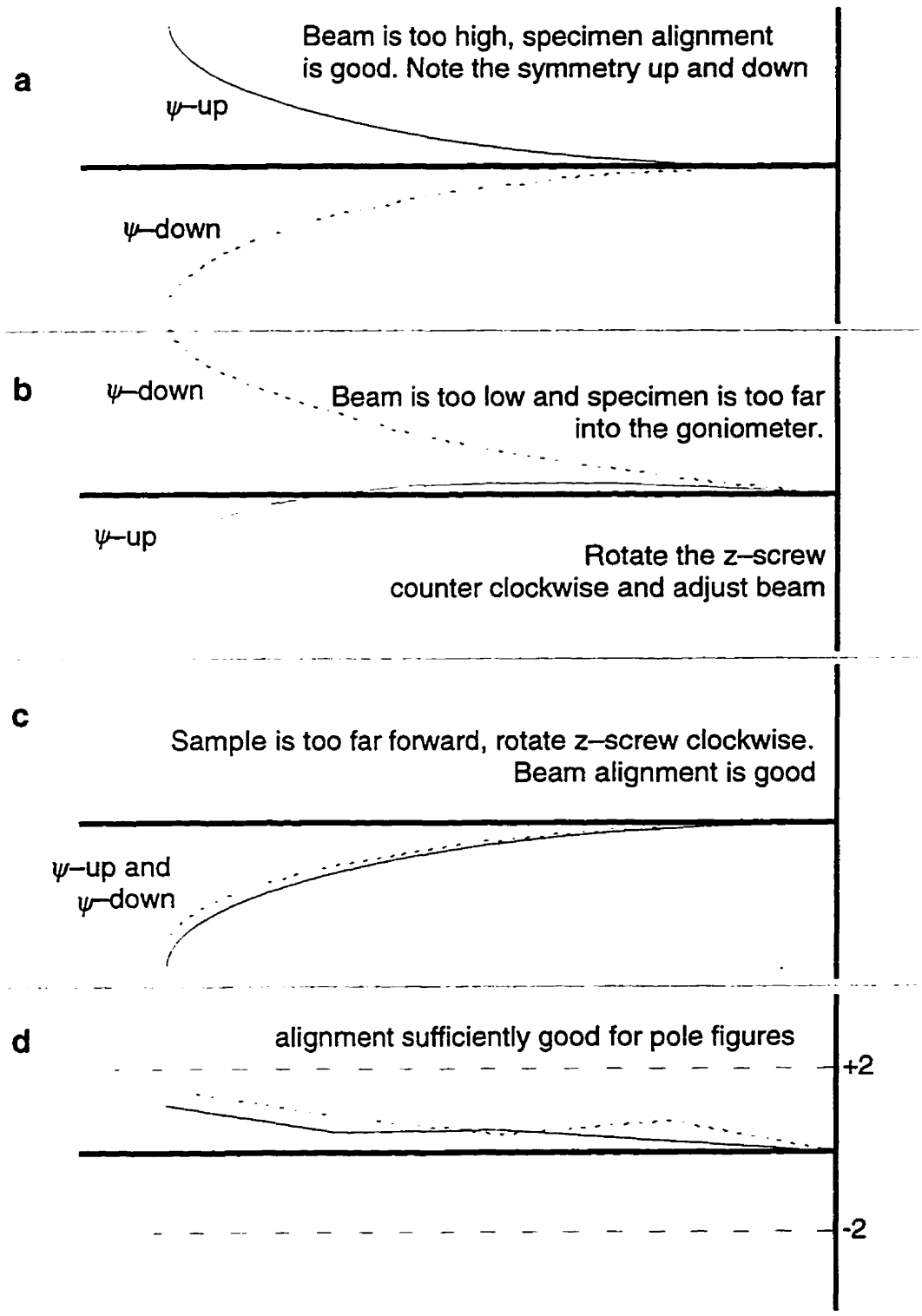

Figure A3.1a–d: Examples of misalignments and the corresponding corrections necessary

A3.4 Strain Measurement Programs

When BACK2PNT or BACK2TEC is run, the first steps consist of entering the information required to scan for the peaks. The following is the outline of the information the user is required to enter.

1. General description of the sample, and the experiment
2. Name of file for data to be saved to
3. Vertical scale of screen plot (counts)
4. Number of points to measured per peak
5. The χ value
6. Number of reflections
7. Current position of the θ and 2θ arms
8. Whether the χ arm needs to be moved before scanning
   (by how much)

for each reflection,

9. The estimate of the location
10. The distance outside the scan window for the background points
11. The scan window width
12. The counting time (time factor, tc) for each point
13. The sum of the squares of the *hkl* indices
14. The Lorentz factor

and finally

15. The χ distance between the reflections in degrees
16. The total run time of the experiment in minutes.

The general description should not exceed about 40 characters in length, although there is no real limit. The file name must follow standard DOS conventions; i.e. 8 characters and a 3 character optional extension.

The vertical scale serves only as a real time tool in observing the peak. It **does not** affect the calculation to determine peak location. The scale is in number of counts. The scale chosen should reflect the expected intensity of the signal. The intensity will depend on the volume fraction of the component of the sample being studied, the thickness of the sample and the counting time for each data point.

The number of points is the number of scan positions the detector will use in the window to determine the peak location. The default value of 11 is usually adequate. Note that this does not include the two background points outside the scan window. More data points may be needed if there is a double peak on a wide window.

The χ value is the current position of the χ angle. This can be read from the MCU above the computer.

The number of reflections is the number of reflections per scan cycle. It is 2 for stress determination at 2 χ angles. If only one peak is needed, then the value is 1. For example, when performing an alignment on textured samples for the hot stage only one peak at a time is usually more efficient.

The current position of the θ and 2θ arms can be read on the MCU's above the computer. These should match the values quoted by the computer. If the MCU values are incorrect (i.e. when the MCU has been turned off, the values read zero) then they can be changed by editing the values in the computer, and then telling the computer to change the MCU readings.

Next, the program will ask whether the ψ angle needs to be changed, if so by how much. The value you enter will be the ψ **distance**. The convention is that a **positive** value is **down**.

The next set of prompts are repeated for each reflection:

The first asks you for an estimate of the peak location. An estimate to the **nearest 0.1° is required.** A more precise estimate may be given, but is not necessary as the program will centre the scan on the peak based on an extrapolation from the previous three peak locations.

The next prompt is the angular distance outside the scan window the background points are to be taken. The default values of 0.5° are usually adequate, but sometimes a wider or narrower spread may be desired. As a caveat, it should be noted that the background positions should be kept close the scan window, otherwise, the background measured will not correspond to the actual background levels in the scan window!

The width of the scan window is the next entry to be made, and this should be an estimate of the width of the peak. The width depends on the peak location: at lower angles (<90°) the windows can be kept narrow (<1°). While at higher angles (>120°), where the peaks are broader due to $K_{\alpha 1}$ and $K_{\alpha 2}$ splitting, the window should be wider. Appropriate widths at high angles are ~2 to 3° or more for the scintillation counter or ~1.5° for the PSPC.

The time factor (tc) is the counting time in seconds for each point measured. This is dependent on the intensity of the signal. For very high intensities, lower counting rates are more practical. At high 2θ and/or ψ angles, the intensity is usually fairly low and longer counting times are required for the program to fit a curve with reasonable accuracy. The tc should also reflect the heating rate where appropriate: it is important that the peak be scanned over a reasonably small temperature range (<10°C max.). This is to prevent peak broadening during the scan. This is especially important on cooling.

Next you are required to enter the *hkl* value. In these programs, it is the sum of the squares of the Miller indices.

The Lorentz factor is an estimate of the shape of the tails of the peak: whether it is more Lorentzian or more Gaussian. The value of this is dependent on the angle of the reflection and on the amount of stored work in the specimen. Heavily deformed specimens will have a broader peak than well annealed ones. The LG parameter should be about 5 for most cases.

This is repeated for the other reflection (if applicable), and then you will be asked for the ψ distance between the two points. The program will always tell the MCU to go **down** first, and hence, your choice of the order in which you enter the two reflections should be dictated by their relative peak locations on the ψ axis. If you have entered only one reflection, then the ψ distance should remain zero.

The run time is the total time you wish to repeat the scanning process. This is in minutes, and your run time should be several minutes longer than the heat treatment cycle (if applicable) to allow a set of scans to be completed before the heat treatment begins. Having a complete set of peaks at the starting temperature is important in estimating the temperature of the peaks in the analysis.

After this has been entered and verified, the program displays that the program is ready to begin in green characters at the bottom left hand corner. Check that the MCU's are all on auto setting, that the Plexiglas windows are closed, and that the shutter is set to external and the specimen oscillator motor is on.

Press [ENTER], and the program will begin scanning. When the program has finished, a prompt is shown in green that the program has completed, and pressing [ENTER] will exit the program.

A3.5 Running the Random Standard

The random standard is used to weight the intensity data from a pole figure. The procedure is very similar to running a pole figure. The following describes the use of the program and the subsequent analysis and modification of the data. Currently, pole figures are measured using the Bicron scintillation counter, and all the information below applies to this detector only.

Prior to running the powder program,
ensure that the detector is in the forward position!

A3.5.1: Using the program 'POWDER'

The program, POWDER, must be run from the C:\BASIC directory. The program automatically opens the shutter at the beginning of the program and initiates the oscillation of the sample. The following discusses each step of the user interface in the program.

1. general description of the sample
2. set up: unless special conditions, indicate that it is the standard set up
3. file name: think of something useful i.e. jun11pow.der for a powder run on June 11
4. θ, 2θ readings and actual 2θ position: just like STEELSTR
5. number of pole figures to be run
6. the *hkl* for each pole figure
7. standard setup: press y for yes. Non standard powders are beyond the scope of this manual for the time being
8. *confirm the above recorded entries*

9. Do you wish to scan for peak locations? Enter 'y' unless you already know the peak locations and background values
10. for each pole figure, enter peak estimate (2TH), window width (WNDOW), the number of points in the window (NPTS), and the height of the scale on the screen (YMAX)
11. Each scan is performed, at the end of each scan, check to make sure that the peak position and the background values are reasonable. If they are not, they may be changed after all scans have been completed.
12. After all the peak location scans, the program displays the peak locations and the background values for each pole figure. It prompts the user whether the values are acceptable or whether they need to be changed. Change the values if necessary.
13. It is not usually necessary to measure the background values during the pole figure and it will take up extra time.
13. Begin the pole figures. This takes about 1h45m

A3.5.2: Checking the data

After the powder pole figure has been completed, run Quattro Pro. Import the data as a comma and quote delimited file. The first group of numbers in each block are the background values. The second block are the peak intensities recorded with the background subtracted. Move the data into rows, one for each pole figure. Plot the data in each row on an x-y graph. The x scale should extend from 0 to 90°. The first column is the intensity at ψ=0, and each subsequent column is incremented by 5°, the last is ψ=80. Add two extra columns to the x scale row for 85 and 90°.

At the low ψ angles, large deviations (more than 10 counts or so) should be corrected to better match the intensities of neighbouring points. There are generally very few corrections at the higher ψ angles (with the exception of

the (311) data to be discussed below). If there are any deviations, again these can be corrected.

All of the data should tend to zero intensity at ψ=90. Unfortunately, the (311) data does not do this. Suitable numbers should be chosen for the last 6 or 7 data points such that the (311) behaves like the rest of the data. Properly corrected data should look like something like the figure below.

Note all of the corrections the you have made, since the spreadsheet cannot be saved in the proper format. The corrections to the data must be done in a suitable editor such as the MS Word word processor on the computer.

To run word, quit Quattro and type 'word'. Once the program has loaded, press ESC to go to the menus. Press 't' for transfer, then '*l*' for load and then enter the name of the powder file. Edit the file to make the changes that were necessary. To save the file, press ESC, t, s and ensure that the file saves as an UNFORMATTED file. This is the same as a text file. Quit MS Word: ESC, q.

To ensure that the spacing between each data point is correct (this is very important!!!) print the file on the screen using the command TYPE *filename.ext*. All of the data should be neatly aligned in rows and columns. If it is not, go back to MS Word and insert or remove spaces where required. Pressing the 'PAUSE' key immediately after entering the command to the display the file, will allow you to see the first set of data.

If the data is not lined up in rows and columns, then the pole figure program, AAAPOLE, will crash.

If everything is OK, then go to the C:\ANDERS directory and copy the old random file, presumably RANDAL.PWD, to RANDOLD.PWD. Copy the powder file you made and corrected in the C:\BASIC directory to C:\ANDERS\RANDAL.PWD. Display the RANDAL file on the screen using the TYPE command again to ensure that the RANDAL file has the same data as your powder file.

Appendix 4
Detector Electronics Settings

The amplifier gain values and delay settings for each instrument used in analyzing the signals from the detector are listed in this appendix.

Ortec 575 Amplifier #1

Coarse Gain:	10.0
Fine Gain:	0.5
Output:	POS, BIPOLAR

Ortec 575 Amplifier #2

Coarse Gain:	10.0
Fine Gain:	0.5
Output:	POS, BIPOLAR

Ortec 551
Timing Single Channel Analyzer #1

Upper Limit:	10.0 V
Lower Limit:	0.0 V
Delay:	1.0 μs
Window:	NOR
Output:	NEG

Ortec 551
Timing Single Channel Analyzer #2

Upper Limit:	10.0 V
Lower Limit:	0.0 V
Delay:	2.68 μs
Window:	NOR
Output:	NEG

Ortec 533 Dual Sum and Invert Amplifer

No adjustable settings

Ortec 551 Timing Single Channel Analyzer #3 (Energy discriminator)

Upper Limit:	1.0 V
Lower Limit:	0.05 V
Delay:	1.0 μs
Window:	NOR
Output:	POS

Ortec 457 Biased Time to Pulse Height Converter

Range:	5.0 μs
Coarse Gain:	5
Fine Gain:	0.54
Bias:	0.8 V
Gate:	Coincident

Ortec 919 Multichannel Analyzer

1024 Channels

Input #1
ADC LLD: 0.0 V (0.865 V for the Bicron scintillation counter)

Tennelec 940A High Voltage Power Supply

TEC 205: +1650 V
Bicron: +985 V